

Electromagnetic Computation for Eddy Current Inspection

A thesis submitted to The University of Manchester for the degree of

Doctor of Philosophy

in the Faculty of Science and Engineering

2021

Ruochen Huang

School of Electrical and Electronic Engineering

LIST OF CONTENTS

LIST OF CONTENTS	1
LIST OF FIGURES	5
LIST OF TABLES	12
NOMENCLATURE	14
ABSTRACT.....	15
DECLARATION	17
COPYRIGHT STATEMENT	18
ACKNOWLEDGEMENTS	19
PUBLICATIONS.....	20
Chapter 1 Introduction	22
1.1 Motivation.....	22
1.2 Aim and Objectives.....	23
1.3 Contributions.....	24
1.4 Organization of thesis	25
References.....	27

Chapter 2 Background	29
2.1 Eddy current testing	29
2.1.1 Pulsed eddy current testing	30
2.1.2 Single/multi-frequency eddy current testing.....	30
2.1.3 Lift-off Effect.....	31
2.2 Electromagnetic simulation for eddy current problems.....	32
2.2.1 Analytical methods	32
2.2.2 Numerical methods	33
2.2.3 Acceleration for the numerical methods	34
2.3 Applications based on eddy current testing	35
2.3.1 Thickness measurement	35
2.3.2 EM properties measurement	36
2.3.4 Crack detection	38
Reference	39
Chapter 3 Support theory	51
3.1 The inductance calculation based on Dodd & Deeds model	51
3.1.1 Inductance calculation for co-axial sensor probe.....	51
3.2 FEM based eddy current computation solver	55
Reference	63

Chapter 4 Overview of papers	65
4.1 Analytical methods for eddy current testing.....	66
4.1.1 The modified analytical method for metallic plates with finite planar dimension.....	66
4.1.2 A novel lift-off compensation technique on phase signature.....	82
Appendix.....	93
4.2 FEM solver for eddy current computation.....	98
4.2.1 Acceleration based on perturbed matrix inversion	98
4.2.2 Accelerated calculation for the algebraic system due to small perturbation	106
Reference	118
Chapter 5 Thickness measurement of metallic plates with finite planar dimension using eddy current method.....	121
Chapter 6 Measurement of permeability for ferrous metallic plates using a novel lift- off compensation technique on phase signature	130
Chapter 7 A Novel Perturbed Matrix Inversion Based Method for the Acceleration of Finite Element Analysis in Crack-Scanning Eddy Current NDT	138
Chapter 8 A novel acceleration method for eddy current crack computation using finite element analysis.....	146
Chapter 9 Conclusions and future works	170
9.1 Conclusions.....	170

9.1.1 Analytical solution based on Dodd and Deeds plate model	170
9.1.2 Finite element method.....	172
9.2 Future works	174
Reference	175

LIST OF FIGURES

Figure 2.1 The working principle of the eddy current testing [7].....	29
Figure 3.1 A coil above an infinite conductive plate	51
Figure 3.2 Schematic diagram of the sensor system above the infinite non- magnetic metallic sample plate (a) real part (b) imaginary part	54
Figure 3.3 Linear interpolation functions in one dimensional element [3].....	56
Figure 3.4 The numbering scheme for tetrahedral elements [4]	57
Figure 3.5 (a) The tetrahedral element (b) The vector shape function of edge 23 (c) The vector shape function of edge 34 (d) The vector shape function of edge 24	58
Figure 3.6 Second-order interpolation functions (a) N021023 (b) N012023 (c) N020124 (d) N010224 (e) N002134 (f) N001234	60
Figure 4.1 Illustration of the integrational path for the proposed method (a) An infinite plate where r ranges from 0 to ∞ (b) A finite plate where r ranges from 0 to r_s	66
Figure 4.2 Air-cored sensor above the tested plate(a) schematic setup (b) actual setup	71
Figure 4.3 Experimental setup (a) measurement setup (b) circular sample plates	71
Figure 4.4 The simulated model (a) the plate with a radius of 20 mm (84 k elements) (b) the plate with a radius of 100 mm (142 k elements).....	73

Figure 4.5 (a)The inductance change caused by copper plates with sample radius of 20 mm (b) The change of $R\omega - 1$ caused by copper plates with sample radius of 20 mm (c)The inductance change caused by copper plates with sample radius of 100 mm (c) The change of $R\omega - 1$ caused by copper plates with sample radius of 100 mm.....	74
Figure 4.6 (a) The inductance change caused by copper plates with the radius of 17.5 mm (b) $R\omega - 1$ caused by copper plates with the radius of 17.5 mm.....	76
Figure 4.7 (a) The inductance change caused by copper plates with the radius of 22.5 mm (b) The change of $R\omega - 1$ caused by copper plates with the radius of 22.5 mm.....	77
Figure 4.8 (a) The inductance changes under various radius of the copper samples (b) The change of $R\omega - 1$ under various radius of the copper samples.....	78
Figure 4.9 Relationship between αr_s and the reciprocal of sample radius.....	79
Figure 4.10 The change of $R\omega - 1$ under varying thickness samples.....	81
Figure 4.11 Estimated thickness by Dodd Deeds analytical solution and modified analytical solution	82
Figure 4.12 EM Sensor	83
Figure 4.13 The procedure of impedance phase compensating deduction	85
Figure 4.14 Measurement setup a) EM air-cored Sensor configuration b) SI 1260 impedance analyser	89
Figure 4.15 Real and imaginary part of inductance under varying lift-offs - 0.8 mm, 2.3 mm, and 3.8mm (a) real part (b) imaginary part	90

Figure 4.16 Trend of inductance term L_0/L_m (for DP 600 specimen) for different lift-offs	91
Figure 4.17 Compensation performance both on simulations and measurements with 0.8, 2.3, 3.8 mm lift-offs	92
Figure 4.18 Model Geometry (a) metal plate (b) metal plate with the defect	99
Figure 4.19 Sensor Configuration.....	100
Figure 4.20 The real part of the inductance due to the aluminium and copper plate without defect.....	101
Figure 4.21 The imaginary part of the inductance caused by the aluminium and copper plate without defect.....	101
Figure 4.22 Computation results for the aluminum plate with different depths of defect, lift-off is 0.05 mm	103
Figure 4.23 Computation results for the copper plate with different depths of defect, lift-off is 0.05 mm	103
Figure 4.24 Computation results for the copper plate with different lift-offs ...	104
Figure 4.25 Computation time of PMI method and CGS method for different scanning sample numbers	105
Figure 4.26 Computation time of PMI method and CGS method under different frequencies	105
Figure 4.27 The configuration of EM sensor probe.....	110
Figure 4.28 Crack shapes (a) Triangle (b) Rectangle (c) Circular sector (d) X shape	110

Figure 4.29 Eddy current (a) without crack and with crack (b) triangle (c) rectangle (d) circular sector (e) X shape	114
Figure 4.30 Relative residual under different element number	115
Figure 4.31 The sensor probe scans across the crack along (a) x axis (b) y axis	116
Figure 4.32 Experimental setup	117
Figure 4.33 Measured and simulated results under different depths	118

Chapter 5

Figure 1 A coil above an infinite conductive plate	123
Figure 2 Illustration of the integrational path for the proposed method (a) An infinite plate where r ranges from 0 to ∞ (b) A finite plate where r ranges from 0 to r_s	124
Figure 3 Air-cored sensor above the tested plate (a) schematic setup (b) actual setup.....	125
Figure 4 Experimental setup (a) measurement setup (b) circular sample plates..	125
Figure 5 The simulated model (a) the plate with a radius of 20 mm (84 k elements) (b) the plate with a radius of 100 mm (142 k elements)	125
Figure 6. (a) The inductance change caused by copper plates (b) The change of $R\omega^{-1}$ caused by copper plates.....	126
Figure 7 (a) The inductance change caused by copper plates with the radius of 17.5 mm (b) $R\omega^{-1}$ caused by copper plates with the radius of 17.5 mm.....	126

Figure 8 (a) The inductance change caused by copper plates with the radius of 22.5 mm (b) The change of $R\omega^{-1}$ caused by copper plates with the radius of 22.5 mm.....	127
--------------------------------------------------------------------------------------------------------------------------------------------------------------------------------	-----

Figure 9 (a) The inductance changes under various radius of the copper samples (b) The change of $R\omega^{-1}$ under various radius of the copper samples.....	127
-----------------------------------------------------------------------------------------------------------------------------------------------------------------	-----

Figure 10 Relationship between α_{r_s} and the reciprocal of sample radius

Figure 11 The change of $R\omega^{-1}$ under varying thickness samples.....	128
-----------------------------------------------------------------------------	-----

Figure 12 Estimated thickness by Dodd Deeds analytical solution and modified analytical solution.....	128
-------------------------------------------------------------------------------------------------------	-----

Chapter 6

Figure 1. EM Sensor.....	131
--------------------------	-----

Figure 2. The procedure of impedance phase compensating deduction.....	132
------------------------------------------------------------------------	-----

Figure 3. Measurement setup a) EM air-cored Sensor configuration b) SI 1260 impedance analyser.....	133
-----------------------------------------------------------------------------------------------------	-----

Figure 4. Real and imaginary part of inductance under varying lift-offs - 0.8 mm, 2.3 mm, and 3.8mm (a) real part (b) imaginary part.....	134
-------------------------------------------------------------------------------------------------------------------------------------------	-----

Figure 5. Trend of inductance term L_0/L_m (for DP 600 specimen) for different lift-offs.....	134
-------------------------------------------------------------------------------------------------	-----

Figure 6. Compensation performance both on simulations and measurements with 0.8, 2.3, 3.8 mm lift-offs	135
---------------------------------------------------------------------------------------------------------------	-----

Chapter 7

Figure 1. Model Geometry (a) metal plate (b) metal plate with the defect	141
Figure 2. Sensor Configuration.....	141
Figure 3. The real part of the inductance due to the aluminium and copper plate without defect.....	142
Figure 4. The imaginary part of the inductance caused by the aluminium and copper plate without defect.....	142
Figure 5. Computation results for the aluminum plate with different depths of defect, lift-off is 0.05 mm.....	142
Figure 6. Computation results for the copper plate with different depths of defect, lift-off is 0.05 mm.....	142
Figure 7. Computation results for the copper plate with different lift-offs.....	143
Figure 8. Computation time of PMI method and CGS method for different scanning sample numbers.....	143
Figure 9. Computation time of PMI method and CGS method under different frequencies.....	143

Chapter 8

Figure 1. The configuration of EM sensor probe.....	155
Figure 2. Crack shapes (a) Triangle (b) Rectangle (c) Circular sector (d) X shape	156

Figure 3. Eddy current (a) without crack and with crack (b) triangle (c) rectangle (d) circular sector (e) X shape.....	157
Figure 4. Relative residual under different element number.....	158
Figure 5. The sensor probe scans across the crack along (a) x axis (b) y axis.....	161
Figure 6. Experimental setup.....	162
Figure 7. Measured and simulated results under different depths.....	163

LIST OF TABLES

Table 4.1 Sensor Parameters.....	72
Table 4.2 Peak frequency of Dodd Deeds analytical solution and modified analytical solution for the aluminium plates	81
Table 4.3 Actual and estimated thickness using aluminium plates	82
Table 4.4 Probes properties.....	83
Table 4.5 Properties of Duplex-phase specimens	92
Table 4.6 Relative permeability measurements for different lift-offs	92
Table 4.7 Sensor Parameters.....	100
Table 4.8 CGS method and PMI method computation time for different defect depths	106
Table 4.9 Coil Parameters.....	110
Table 4.10 The accelerated rate and deviation of the inductance change due to the sample plate under different element number.....	114
Table 4.11 The computation time for one step	116
Table 4.12 Experiment sensor parameters	117

Chapter 5

Table 1. Sensor parameters.....	125
---------------------------------	-----

Table 2. Peak frequency of Dodd Deeds analytical solution and modified analytical solution for the aluminium plates.....	127
--------------------------------------------------------------------------------------------------------------------------	-----

Table 3. Actual and estimated thickness for the aluminium plates.....	127
-----------------------------------------------------------------------	-----

Chapter 6

Table 1. Probes properties.....	133
---------------------------------	-----

Table 2. Properties of Duplex-phase specimens.....	134
----------------------------------------------------	-----

Table 3. Relative permeability measurements for different lift-offs.....	136
--------------------------------------------------------------------------	-----

Chapter 7

Table 1. Sensor parameters.....	141
---------------------------------	-----

Table 2. CGS method and PMI method computation time for different defect depths.....	143
--------------------------------------------------------------------------------------	-----

Chapter 8

Table 1. Coil parameters	157
--------------------------------	-----

Table 2. The accelerated rate and deviation of the inductance change due to the sample plate under different element number.....	161
----------------------------------------------------------------------------------------------------------------------------------	-----

Table 3. The computation time for one step.....	162
-------------------------------------------------	-----

Table 4. Experiment sensor parameters.....	163
--------------------------------------------	-----

NOMENCLATURE

Abbreviations and Acronyms

EM	Electromagnetic
FEM	Finite Element Method
BEM	Boundary Element Method
GMR	Giant Magnetoresistive
NDT	Non-destructive Testing
ECT	Eddy Current Testing
PECT	Pulsed Eddy Current Testing
TREE	Truncated Region Eigenfunction Expansion
ZCF	Zero-Crossing Frequency
SDP	Subdomain Perturbation

ABSTRACT

Eddy current testing, as one of the promising techniques in non-destructive testing, is widely applied in various industrial applications achieving high accuracy and contactless to the target. In the testing process, electromagnetic calculations are crucial to evaluate the performance of sensor probes and inversion algorithms. Electromagnetic calculation can be summarised mainly into two categories: analytical methods and numerical methods.

For the analytical methods, Dodd and Deeds analytical solutions have served to calculate the eddy current problems for several decades, but it can only be applied to infinite plates. In this research, based on the finding that the sample radius is related to the integration range, the modified analytical method is proposed which is capable of calculating the problems for the case where the radius of the sample plate does not satisfy the assumption of infinity.

Further, for the measurement of ferrous plate magnetic permeability, it suffers from the lift-off effect. With increased lift-off, the phase of the measured impedance for steel plates reduces. Meanwhile, the magnitude of the impedance signal decreases. Based on these facts, a novel algorithm is developed to reduce the error of impedance phase for ferrous steels due to sensor lift-offs. By utilising the compensated phase, the prediction for the permeability can be more precise.

The finite element method, as a numerical method, is a versatile tool for eddy currents simulations. However, the computation speed of eddy current three-dimensional modelling is rather slow. Therefore, two methods to accelerate the customised solver for crack detection are proposed. Numerical tests and experiments have been carried out to verify the proposed methods. From the flow patterns of eddy currents and the calculated inductance change, the effectiveness and robustness of the accelerated solver

are proved. Numerical tests show that the computation time can be reduced significantly by utilising the accelerated approaches.

DECLARATION

No portion of the work referred to in this thesis has been submitted in support of an application for another degree of qualification of this or any other university or other institution of learning.

COPYRIGHT STATEMENT

i. The author of this thesis (including any appendices and/or schedules to this thesis) owns certain copyright or related rights in it (the “Copyright”) and he has given The University of Manchester certain rights to use such Copyright, including for administrative purposes.

ii. Copies of this thesis, either in full or in extracts and whether in hard or electronic copy, may be made only in accordance with the Copyright, Designs and Patents Act 1988 (as amended) and regulations issued under it or, where appropriate, in accordance with licensing agreements which the University has from time to time. This page must form part of any such copies made.

iii. The ownership of certain Copyright, patents, designs, trade marks and other intellectual property (the “Intellectual Property”) and any reproductions of copyright works in the thesis, for example graphs and tables (“Reproductions”), which may be described in this thesis, may not be owned by the author and may be owned by third parties. Such Intellectual Property and Reproductions cannot and must not be made available for use without the prior written permission of the owner(s) of the relevant Intellectual Property and/or Reproductions.

iv. Further information on the conditions under which disclosure, publication and commercialisation of this thesis, the Copyright and any Intellectual Property and/or Reproductions described in it may take place is available in the University IP Policy (see <http://documents.manchester.ac.uk/DocuInfo.aspx?DocID=487>), in any relevant Thesis restriction declarations deposited in the University Library, The University Library’s regulations (see <http://www.manchester.ac.uk/library/aboutus/regulations>) and in The University’s policy on Presentation of Theses.

ACKNOWLEDGEMENTS

Ph.D. researches in these three years are precious and they would be a treasure throughout my whole life. I am grateful to those who supported and helped in these years.

Firstly, I would like to express my sincere thanks and profound gratitude to my supervisor, Dr. Wuliang Yin, who gave me encouragement, patience, and support throughout the entire development of the project. The achievements made until now could not leave the guidance from him. Apart from these, he also teaches me those which are beyond books.

I would also like to extend my appreciation to Dr. Mingyang Lu, for providing valuable suggestions and patient assistance in simulations and publications; Dr. Hanyang Xu, for helping with measurements; and colleagues in SISP group in University of Manchester for helping me in various other aspects.

Furthermore, I would like to express my thanks to my best friend and colleague, Miss Ziqi Chen, for her company and care in daily life. Her suggestions and discussions in both life and researches are appreciated.

Lastly, my thanks go to my beloved parents, for their selfless support and encouragement. Without their support and patient company, I could not have made this progress. Deeply grateful for their cultivation, I can have this opportunity to achieve my own value.

PUBLICATIONS

M. Lu, **R. Huang**, W. Yin, Q. Zhao, A. Peyton, “Measurement of permeability for ferrous metallic plates using a novel lift-off compensation technique on phase signature,” *IEEE Sensors Journal*, vol. 19, no. 17, 2019.

R. Huang, M. Lu, A. Peyton, W. Yin, “A Novel Perturbed Matrix Inversion Based Method for the Acceleration of Finite Element Analysis in Crack-Scanning Eddy Current NDT,” *IEEE Access*, vol. 8, 2020.

J.R.S. Avila, M. Lu, **R. Huang**, Z. Chen, S. Zhu, W. Yin, “Accurate measurements of plate thickness with variable lift-off using a combined inductive and capacitive sensor,” *NDT & E International*, vol. 110, 2020.

S. Zhu, **R. Huang***, J. R. Salas Avila, Y. Tao, Z. Zhang et al., “Simultaneous measurements of wire diameter and conductivity using a combined inductive and capacitive sensor,” *IEEE Sensors Journal*, 2020.

R. Huang, M. Lu, A. Peyton, W. Yin, “Thickness measurement of metallic plates with finite planar dimension using eddy current method,” *IEEE Transaction on Instrumentation and Measurement*, vol. 69, no. 10, pp. 8424-8431, Oct. 2020.

Z. Jin, Y. Meng, R. Yu, **R. Huang***, et al., “Methods of Controlling Lift-Off in Conductivity Invariance Phenomenon for Eddy Current Testing,” *IEEE Access*, vol. 8, pp. 122413-122421, 2020.

R. Huang, M. Lu, Z. Zhang, Q. Zhao, et al., “Measurement of the Radius of Metallic Plates Based on a Novel Finite Region Eigenfunction Expansion (FREE) Method,” *IEEE Sensors Journal*, vol. 20, no. 24, pp. 15099-15106, 15 Dec.15, 2020.

M. Lu, X. Meng, **R. Huang**, L. Chen, A. Peyton and W. Yin, “Measuring Lift-Off

Distance and Electromagnetic Property of Metal Using Dual-Frequency Linearity Feature,” *IEEE Transactions on Instrumentation and Measurement*, vol. 70, pp. 1-9, 2021.

R. Huang, M. Lu, X. He, A. Peyton and W. Yin, “Measuring Coaxial Hole Size of Finite-Size Metallic Disk Based on a Dual-Constraint Integration Feature Using Multifrequency Eddy Current Testing,” *IEEE Transactions on Instrumentation and Measurement*, vol. 70, pp. 1-7, 2021.

M. Lu, X. Meng, **R. Huang**, L. Chen, A. Peyton and W. Yin, “Inversion of Distance and Magnetic Permeability Based on Material-Independent and Liftoff Insensitive Algorithms Using Eddy Current Sensor,” *IEEE Transactions on Instrumentation and Measurement*, vol. 70, pp. 1-9, 2021.

M. Lu, X. Meng, **R. Huang***, L. Chen, *et al.*, “Thickness measurement of circular metallic film using single-frequency eddy current sensor,” *NDT & E International*, vol. 119, pp. 102420, 2021.

M. Lu, X. Meng, **R. Huang**, L. Chen, Z. Tang, *et al.*, “Determination of Surface Crack Orientation Based on Thin-Skin Regime Using Triple-Coil Drive–Pickup Eddy-Current Sensor,” *IEEE Transactions on Instrumentation and Measurement*, vol. 70, pp. 1-9, 2021.

G. Hu, **R. Huang***, M. Lu, L. Zhou, W. Yin, “Measurement of radius of a metallic ball using eddy current testing based on peak frequency difference feature”, *Measurement*, vol. 184, 2021.

R. Huang, M. Lu, Z. Chen, Y. Shao, G. Hu, A. Peyton, W. Yin, “A novel acceleration method for eddy current crack computation using finite element analysis”, *NDT & E International*, **submitted**.

Chapter 1 Introduction

In this chapter, the motivation of the research is presented, followed by the aim and objectives. Contributions throughout the research and the organization of the thesis are also summarised in the following sections.

1.1 Motivation

Non-destructive testing techniques have been applied in the fields of aerospace [1-3], rail transport [4-5], and pipeline testing [6-7]. Due to its advantage of high sensitivity and strong adaptability to the specimen, eddy current testing is widely used in thickness measurement, liquid level measurement, and defect detection, etc [8-12]. Generally, as a key indicator, the change of the coil impedance of sensor probe is observed in the measurements which results from the interaction between the primary magnetic field and the secondary magnetic field due to the eddy currents in the conductive samples.

Eddy current computation plays an essential role in the development of eddy current techniques, which can provide theoretical support of investigating eddy current phenomena and comparison with measurements. Many works use analytical methods to analyse the performance of the electromagnetic (EM) sensor probe and measure the material properties, i.e., electrical conductivity and magnetic permeability. Dodd and Deeds analytical solution [13] has been widely applied in the calculation of the eddy current problems, which offers formulations of some special models, i.e., plate model and cylindrical model. However, there are some difficulties to adopt the analytical method into practical testing, including crack detection with various EM sensor setups and arbitrary geometries of test objects, still remaining for further investigation and exploration.

The advent of the high-speed and high-capacity electronic computers offers another

possibility to address the eddy current problem. As one of the powerful numerical tools, finite element method (FEM) has been well developed for steady-state, time-varying field problems and nonlinear problems from two-dimensional calculation to three-dimensional calculation [14-15]. The accuracy of FEM is highly related to the discretisation of the whole mesh model. In order to achieve high quality solutions, the dense model is commonly chosen which results in a high cost of computation. Besides, accelerating the computation speed of eddy current three-dimensional finite element modelling is also crucial in producing large amount of data for feeding into deep learning algorithms. Therefore, the acceleration for the finite element analysis is worth exploring in solving the eddy current problems, especially for inspecting conductive structure with the surface crack.

1.2 Aim and Objectives

The aim of the research focuses on EM calculations for eddy current problems by developing new analytical method for the case where samples have finite dimensions, exploring the compensation algorithm for the permeability inversion and studying FEM-based modelling solver for simulation of eddy current sensor inspecting surface crack. The objectives are listed as follows:

1. To develop a novel theoretical approach adopted for samples with finite dimensions. Currently, the plate model proposed by Dodd and Deeds can be adopted for the infinite cases (the radius of the testing sample is normally 3-5 times larger compared with the radius of the sensor coil). In this thesis, based on this model, the measured samples that do not meet this condition is investigated by finding the relationship between the integration point in the analytical model and the radius of the sample plate from both experiments and simulations.
2. To carry out different types of measurements by utilising the proposed

theoretical method, for example, thickness measurement using the peak frequency feature.

3. To develop a compensation approach for measurements of magnetic permeability for ferrous plates. Both the magnitude and the phase of the impedance signal reduces due to the increase of the lift-off. It will result in the error in permeability prediction. Therefore, an algorithm to reduce the lift-off effect is explored.
4. To implement first/high order FEM eddy current solver for calculating eddy current problems. In the solver, it requires constructing the nodal and edge shape functions for each tetrahedral element by using local coordinate method for evaluating the element matrix and solving the whole system to obtain the simulated fields.
5. To accelerate the FEM based solver for the eddy current problems in order to reduce the computation cost for the crack detection. Due to the existence of the small crack, the entire system is slightly perturbed by the small perturbation. In this thesis, strategies of hastening the computation of inspecting surface crack due to the small perturbation are explored.

1.3 Contributions

In this thesis, the contributions in the field of eddy current testing are summarised in the following aspects:

1. Proposed a modified analytical solution for the metallic sample with a finite dimension. The novelty of this method is introducing an integral point which is found related to the radius of the sample plate so that the inductance change due to the finite sample plate can be calculated. With this method, it is capable of conducting thickness measurement for the circular samples and the thickness

can be accurately reconstructed with a small error within 2%.

2. Proposed a phase compensation algorithm for ferrous metallic plates. It corrects the phase change due to lift-off from the magnitude of the impedance signal. By utilising the measured magnitude and zero-crossing frequency, the phase with zero lift-off can be deduced. From the measurements, it shows that the error of the permeability estimation from the phase compensation is reduced.
3. Presented a novel method for accelerating eddy current calculation for crack detection using FEM and perturbed matrix inversion (PMI) method. This method based on PMI formulation only requires the inversion of a much smaller matrix and therefore improves the speed of the computation process. From the numerical tests, the computation time of the proposed method was shortened about 3 times compared with the original method.
4. Proposed a novel crack calculation acceleration method for solving the system with the perturbation due to the small crack. This method is based on the fact that the crack only causes a small perturbation in fields in the surrounding region. In the calculation, by utilising the unperturbed field, the subdomain affected by the small crack is chosen and calculated. It proved effective in greatly shortening the computation time. For larger mesh element number, with the proposed method, due to the separation of the small crack perturbation field from the unperturbed field, the computation burden is released so that the accelerated rate is more significant (i.e., 3 times for 10k elements and 34 times for 139k elements).

1.4 Organization of thesis

This section introduces the organization of this thesis. It contains 9 chapters.

Chapter 1 presents a basic introduction of the entire research, including the motivation,

aim and objectives, contributions and the outline of the thesis.

Chapter 2 demonstrates the background of this thesis by reviewing the achievement made by other researchers in the field of eddy current testing, including eddy current computation and measurements using eddy current techniques.

Chapter 3 presents the support theory of the thesis in eddy current testing, including Dodd and Deeds analytical method and the finite element method, introducing the computation of the inductance change due to the sample plate from both methods. In addition, the peak frequency feature of the inductance change is also introduced in this chapter.

Chapter 4 presents an overview of the achievements made in this thesis. It can be concluded in three folds, the development of the analytical solution for samples with finite dimension, the permeability measurement for ferrous plate using the phase signature and the acceleration of FEM based solver due to the presence of the small crack.

Chapters 5-8 present the related published works which are summarised in chapter 4.

Chapter 9 presents the conclusions of the thesis and future works are also considered in this chapter.

Overall, analytical methods and numerical methods are two kinds of basic techniques for solving the eddy currents problems. Due to the limitation of the Dodd and Deeds models that it requires the sample to be large enough to reach its assumption – infinity, it is found that the radius of the sample plate is related to the integration domain, the new analytical methods by introducing an initial integral point can be used to calculate the inductance change for finite dimension plate. Besides, during the measurement, the signal affects by the lift-off of the sensor probe. By utilising the measured data, a phase correction method to reduce the error introduced by the lift-off is proposed and the

permeability of the sample can be deduced. In addition, compared with the analytical methods, finite element method can be applied to object with any geometry, however, the disadvantage of finite element method is that it takes long time to obtain the simulated results. Therefore, two accelerated approaches are proposed for the acceleration of the FEM based solver.

References

- [1]. Y. He, F. Luo, M. Pan, F. Weng, X. Hu, J. Gao and B. Liu, “Pulsed eddy current technique for defect detection in aircraft riveted structures,” *NDT & E International*, vol. 43, no. 2, pp. 176-181, 2010.
- [2]. N. V. Nair, V. R. Melapudi, H. R. Jimenez, X. Liu *et al.*, “A GMR-Based Eddy Current System for NDE of Aircraft Structures,” *IEEE Transactions on Magnetics*, vol. 42, no. 10, pp. 3312-3314, Oct. 2006.
- [3]. Z. Zeng, X. Liu, Y. Deng, L. Udpa, L. Xuan, W. C. L. Shih and G. L. Fitzpatrick, “A Parametric Study of Magneto-Optic Imaging Using Finite-Element Analysis Applied to Aircraft Rivet Site Inspection,” *IEEE Transactions on Magnetics*, vol. 42, no. 11, pp. 3737-3744, Nov. 2006.
- [4]. M. P. Papaelias, M. C. Lugg, C. Roberts and C. L. Davis, “High-speed inspection of rails using ACFM techniques,” *NDT & E International*, vol. 42, no. 4, pp. 328 – 335, 2009.
- [5]. T. Heckel, H. M. Thomas, M. Kreutzbruck and S. R  he, “High Speed Non-Destructive Rail Testing with Advanced Ultrasound and Eddy-Current Testing Techniques,” *NDTIP Proceedings*, Prague, 2009.
- [6]. A. A. Carvalho, J. M. A. Rebello, M. P. V. Souza, L. V. S. Sagrilo and S. D. Soares. “Reliability of non-destructive test techniques in the inspection of pipelines used in the oil industry,” *International journal of pressure vessels and piping*, vol. 85, no. 11, pp. 745-751, 2008.
- [7]. Z. Xu, X. Wu, J. Li and Y. Kang, “Assessment of wall thinning in insulated

ferromagnetic pipes using the time-to-peak of differential pulsed eddy-current testing signals,” *NDT & E International*, vol. 51, pp. 24-29, 2012.

[8]. T. Yang, Q. Zhao, K.Y. How, K. Xu, M. Lu, Y. Xie and W. Yin, “Level measurement for saline with a small surface area using high frequency electromagnetic sensing technique,” *Measurement*, vol. 101, pp. 118-125. 2017.

[9]. J. C. Moulder, E. Uzal and J. H. Rose. “Thickness and conductivity of metallic layers from eddy current measurements,” *Review of scientific instruments*, vol. 63, no. 6, pp. 3455-3465, 1992.

[10]. J. Král, R. Smid, H. M. G. Ramos and A. L. Ribeiro, “Thickness measurement using transient eddy current techniques,” *2011 IEEE International Instrumentation and Measurement Technology Conference*, Binjiang, pp. 1-6, 2011.

[11]. G. Y. Tian and A. Sophian, “Defect classification using a new feature for pulsed eddy current sensors,” *NDT & E International*, vol. 38, no. 1, pp. 77-82, 2005.

[12]. F. Lucklum and B. Jakoby, “Non-contact liquid level measurement with electromagnetic–acoustic resonator sensors,” *Measurement Science and Technology*, vol. 20, no. 12, ,2009.

[13]. C. V. Dodd and W. E. Deeds, “Analytical Solutions to Eddy-Current Probe-Coil Problems,” *Journal of Applied Physics*, vol. 39, issue 6, pp. 2829 – 2838, 1968.

[14]. Y. Koutromanos, “Nonlinear Finite Element Analysis”, Virginia Polytechnic Institute and State University, Dec. 2014.

[15]. O. Biro, G. Koczka and K. Preis, “Finite element solution of nonlinear eddy current problems with periodic excitation and its industrial applications. Applied Numerical Mathematics,” *Applied Numerical Mathematics*, vol. 79, no. 100, pp: 3-17, May, 2014.

Chapter 2 Background

In this chapter, eddy current testing and its applications in industry are introduced. Firstly, the working principle of eddy current testing is stated, followed by the introduction of the electromagnetic calculation for eddy current problems. The applications using eddy current testing are also demonstrated.

2.1 Eddy current testing

With the non-contact capability and high sensitivity to the surface crack, eddy current testing has a promising prospect to interrogate the sample, which has been successfully applied in a variety of industrial applications. As shown in Figure 2.1, the working principle of the eddy current testing is that firstly an alternating current is injected into the excitation coil to generate an alternating magnetic field, then the eddy current is induced in the conductive samples. Thus, the receiving coil receives the signal contributed by both the primary magnetic field from the transmitter and that reflected from the sample. The variation of the received signal is examined and analysed to determine the underlying problems of the test sample with high detection accuracy [1-3]. By using this method, it also has the potential of process monitoring [4-6].

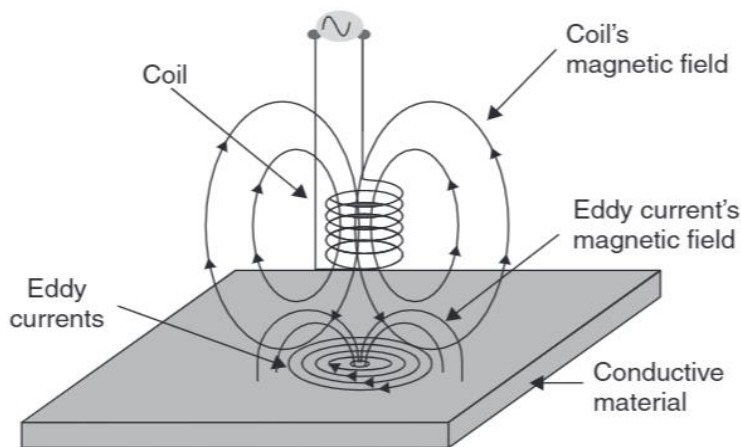


Figure 2.1 The working principle of the eddy current testing [7]

There are two mainstreams of eddy current testing techniques which are commonly used, namely pulsed eddy current testing and single/multi-frequency eddy current testing technique.

2.1.1 Pulsed eddy current testing

Pulsed eddy current testing, as a time domain method, injects a rectangular stimulus signal into the excitation coil during testing. Since the square excitation signal contains wide band of frequency data, the evaluation can be completed from frequency aspects by the decomposition process from the detected signal [8, 9]. For the excitation coil of the pulsed eddy current sensor probe, the coil size is selected to be large due to the dominated component from low frequency spectra. While from the receiving side, previously, the sensing coil are commonly implemented to detect the changing field [10-13]. Later on, it is found that it is more sensitive to detect the magnetic field by using the IC chip assembled with Hall sensor or Giant Magnetoresistive (GMR) sensor [14-17]. From the received signals, there are three important information can be extracted, which are the time to the peak value, the peak value and the lift-off point of the intersection respectively. Using these three significant features of the pulsed eddy current signal, the characteristic information of samples can be derived [18-21]. The signal from a differential-pulsed eddy current probe was used to evaluate the thickness of the metal plate in [22]. However, there was a trade-off between the peak value feature and the other two features. Until now, more features (zero crossing time, rising point, etc.) are investigated by researchers to further address the problems using pulsed eddy current testing [23, 24].

2.1.2 Single/multi-frequency eddy current testing

Compared with the pulsed eddy current testing, the single/multi-frequency eddy current testing only use one or a range of frequencies to conduct the measurements through the

consideration of the EM properties of the samples [25, 26]. For the single frequency eddy current testing methods, it is essential to choose a proper excitation frequency to optimise the performance of the sensor probe [27, 28]. Due to the skin depth effect which is related to the material properties (electrical conductivity and magnetic permeability) and the excitation frequency, the distribution of the eddy current differs from different excitation frequencies. In the aspect of the crack detection, for the inspection of the surface crack, a higher frequency is normally chosen while for the subsurface crack, a relative low frequency is used to detect deep area. However, the use of single frequency eddy current testing methods is limited so that multi-frequency eddy current testing methods emerge to overcome the constraints and provide more details from the response of the test sample [29, 30]. Therefore, the inversion of the profile of the test sample can be achieved accurately, i.e., surface inspection, EM property measurement [2-3, 31].

2.1.3 Lift-off Effect

The lift-off of the sensor probe is the distance between the sensor probe and the test sample. In the eddy current testing, the measured signal is sensitive to the lift-off of the sensor probe, resulting in unsuspected error in the inversion of material properties. In order to reduce the effect of the lift-off from testing, the approaches by using the eddy current techniques have been developed [32, 33]. Giguere, *et al.* proposed the lift-off intersection (LOI) point [10]. Many researchers were inspired by this study result [33-35] and it was also implemented in the ferromagnetic samples [32]. Yu, *et al.* found that the rising time due to different lift-offs can be reduced by subtracting the signal received by zero lift-off and crack free sample [14]. Despite the approach using the changing magnetic flux [36] is sensitive to sample plate for the small lift-off, it can be utilised for larger lift-offs. Meanwhile, the larger lift-offs can cause a relative low signal to noise ratio (SNR), the algorithm based on cumulative integration [37] can be applied to enhance the SNR during the measurement. Furthermore, special sensor setups [38-

40] and data processing strategies [41-43] to eliminate the lift-off effect are also exploited. In [44], by using the multi-frequency eddy current testing, it is found that the measured signals are independent to the lift-offs in phase spectra, which provides the possibility for the measurements that the change of the lift-off is smaller than the pole distance of the sensor probe. By utilising these novel techniques, the prediction for the sample material can be accurately achieved and make sure the prediction is within a reasonable error.

2.2 Electromagnetic simulation for eddy current problems

Eddy current testing methods require the support from simulations. To precisely simulate the eddy current problems, there are various methods and can be generally divided into two groups, that is, analytical methods and numerical methods. For the analytical methods, it is fast and convenient for the researchers to compute the electromagnetic field for specific cases. Compared with analytical methods, numerical methods have the capability to solve the eddy current problem for arbitrary cases, i.e. arbitrary geometry of test sample or crack and the sensor setup. However, in order to obtain accurate simulation results, a dense mesh model would be generated which leads to slow computation. In the following sections, both methods will be introduced in detail and the acceleration for numerical methods is also stated.

2.2.1 Analytical methods

In recent decades, many researchers have been dedicated in the development of the analytical methods. In 1960s, Dodd and Deeds proposed a series of analytical solutions for the eddy current probe-coil problems [45-46]. It is capable of calculating impedance change for the air-cored sensor probe and provides sufficient theoretical support to many works regarding eddy current problems [47-49]. By setting the boundary conditions for the magnetic field for the test sample, Theodoulidis, *et al.* introduced the summation

expressions with the usage of the eigenvalue of the Bessel function which can be used to calculate the impedance of the coil for the truncated cases, namely truncated region eigenfunction expansion (TREE) method [50]. The high computational efficiency is proved by the good performance of the magnetic field computation for the multi-layered specimens [51]. With the aid of the TREE method, Tytko *et al.* proposed a computation method suitable for both the E-cored coil with the circular air gap and the air gap of I-cored coil [52]. The formulations for typical system configurations are also provided, including ferrite-cored probe [53], rectangle planar coil [53], continuous conductivity material [55], tilted coil [56]. For the case where the coil is located at the corner of the test sample, the edge effect should also be considered. The analytical model was presented to obtain a better view of the interaction from the edge of conductor [57]. Moreover, not only the crack free model, the expressions for the crack models are also derived by the researchers. In [56], the impedance change due to the long crack can be derived by using the thin-skin theory – the skin depth is relatively small compared with the length and the width of the crack (at least three times) [58]. Based on this formulation, the analytical solution for triple-coil drive-pickup EC sensor probe was developed to identify the orientation of the surface crack [59].

2.2.2 Numerical methods

So far, when it comes to the numerical analysis for electromagnetics, diverse methods are proposed to solve for different situations of the eddy current problems, which can be roughly summarised into two groups, finite element methods and integral equation techniques. In solving the problem caused by the presence of the crack using the integral formulation, volume integral [60-63] can be considered for the scattered field. The dyadic kernel was applied by Bowler and Jenkins, the direct and reflected field can be calculated due to the perturbation of the open crack and meets the continuity for the boundary [60]. Supported by the dedicated kernel which lessens massive computations for the number of unknown variables, the eddy current problem due to the existence of

the edge crack in the conductive quarter region can be addressed [63]. Besides, the crack with negligible width can also be treated as a surface with jump in the electromagnetic field between the crack and the conductor [64]. The boundary condition for the crack in the thin skin regime introduced by Bowler and Harfield satisfied with the 2-D Laplace equation and the impedance change can be derived [65].

Several researches for the development of the finite element methods for different cases have been conducted for decades, including curved plates simulation [66], ferromagnetic modelling [67-68] and conductive defect simulation [69]. Since the received field is affected by the crack, the perturbed field can be calculated by improving the formulations in most works. In order to ease the burden from the mesh discretization, Badics, *et al.* introduced a thin sheet crack model for the crack which satisfies the condition that the crack width is much smaller than other dimensions of the crack [70]. In [71], to tackle the effect caused by the conductive crack, the parallel component of the received signal can be calculated with the condition that the width of a crack is less than the prepared database.

2.2.3 Acceleration for the numerical methods

Due to the fact that the massive computation time is required to achieve high accuracy from the simulation, reducing the running time is essential and several significant progresses have been made during these decades in this aspect. Prestored database method [67, 71-73] and FEM-BEM hybrid method [62, 71, 74-76] are popular in solving this kind of problem. A fast simulator based on the precomputed unflawed database approach was proposed in [72] for the evaluation of the crack size. Due to the advantage of its detectability, this method can be used for crack reconstruction. For FEM-BEM method, it combines the boundary element region with the finite element region to obtain a solution of the non-uniform material distribution. Du, *et al.* proposed a fast calculation solver based on the FEM-BEM method and database for ECT simulations

and the running time was significantly shortened with the guarantee of the accuracy [71]. Combining the finite element method with the existing analytical methods for the unflawed area, the distorted field due to the defect can be directly obtained [77]. The adaptive fast multipole method offers the possibility to shrink the operations in the computation process and Rubinacci, *et al.* proved its robustness in [78]. Moreover, new shape functions were presented by Morozov adapting the eddy current caused by the crack and a small part from the entire system was inverted to obtain the perturbed signal which lessens the burden of the computation [62]. Lu, *et al.* proposed an accelerated method by using the optimized initial guess from previous frequency calculation which reduces the iteration numbers for the simulation [79]. Combining Darwin approximation with the first-order subdomain perturbation (SDP) formulation, a low frequency stable formulation was proposed to simulate the near field for eddy current problem. In low frequency range, Darwin approximation can decouple the inductive and capacitive effects from the system. The computation speed improved significantly because the computation burden released from the two sub-problems (the unperturbed and perturbed field) compared with the total field simulations [80].

2.3 Applications based on eddy current testing

Eddy current testing, as one of the most universal non-destructive techniques, has extensive applications for thickness measurement, the inspection of material integrity (e.g. crack detection) and the evaluation of material properties (e.g. electrical conductivity and magnetic permeability). In the following sections, three types of measurements are stated with the support of the eddy current testing in pursuit of a better inspection of the test sample.

2.3.1 Thickness measurement

Due to the presence of the thick coating, the lift-off effect in pulsed eddy current testing

can be reduced by using the reference signals and normalization process [33] and it is found that the sensitivity of the sensor coil would be boosted with higher lift-off under a certain range of the coil gap [81]. With the support of the look-up table, Tai *et al.* developed a pulsed eddy current technique-based equipment to measure the sample thickness [47]. In [82], Fan, *et al.* proposed that the thickness can be evaluated by using the phase of the pulsed eddy current signal which was observed independently to the lift-off.

The potential of multi-frequency eddy current testing has also been explored. It has been found that the phase signature from the sensing coil can be used to measure the thickness of the metal sample [83-84]. In [85], with the robust feature between the peak frequency of the inductance change and the sample thickness, the error of the reconstructed thickness could be achieved within 3%. Models and signal processing methods are also introduced to estimate the thickness of the sample. Fan, *et al.* proposed the model-based inversion by incorporating the non-ideal behaviour of the eddy current sensor proved its reliability in terms of lift-off elimination to deduce the thickness of the plate [86]. A novel triple planar coil was been designed for the thickness measurement in [87]. The proposed algorithm used single frequency measurement approach could improve the testing efficiency which has a potential to apply for real-time measurements.

In this thesis, the thickness measurement for the conductive plate with finite dimension can be predicted by utilising the modified analytical method with an introduced initial integral point. There is a linear trend between the reciprocal of the integral point and the plate radius. With the aid of the peak frequency of the inductance change, the thickness of the conductive plate can be estimated.

2.3.2 EM properties measurement

A precise estimation of the electrical conductivity and the magnetic permeability of the

test sample is essential in many applications. Combining the experimental measurements and the digital data processing by utilising the linear combination of Walsh functions, the experimental method proposed by Egorov *et al.* provides high accuracy and reliable classification of the material properties in the process of aluminium alloy testing [88]. Halleux *et al.* developed an equivalent simplified physical model for the electrical conductivity measurement and it can be applied in a wide range of metallic samples [89]. Moreover, a robust method by using frequency-dependent eddy current measurements was presented by Moulder *et al.* to determine the electrical conductivity of the uniform conductive layers [90]. Conductivity profiling from inductance spectroscopic measurements [91] and the conductivity measuring instrument for semi-conductors [92] also have been explored.

In terms of permeability measurements, it is still challenging to determine the permeability of the material due to the influence of the environment condition and the material conductivity on the response signal. A novel method that can measure the conductivity and permeability of the metal samples simultaneously was proposed by Ma, *et al.* [3]. The conductivity can be obtained by the impedance change of the signal while the permeability can be measured by utilising the imaginary part of the signal. The results were proved to be accurate but the frequency range is limited for estimating permeability. Yu *et al.* proposed the conductivity invariance phenomenon and developed a device to determine the permeability by decoupling the influence of the conductivity and permeability [93-94]. Besides, a novel algorithm to compensate for the zero-crossing frequency point caused by the lift-off effect was proposed by Lu *et al.* and the error caused by the lift-off can be reduced to 7.5% [42, 95].

In this thesis, due to the fact that the phase error caused by the lift-offs is non-negligible under more precise non-contact measurement with significant lift-offs, a novel approach to obtain the correct phase change is developed and therefore the permeability of the sample can be estimated more accurately.

2.3.4 Crack detection

Surface crack detection is one of the most essential issues for researchers and engineers to improve the service life of the equipment. A small crack can lead to an unreliable structure which can greatly shorten the service life of the equipment. Eddy current techniques developed for the detection of the crack can effectively prevent unnecessary loss and damage. With the presence of the surface crack, the induced eddy current is disturbed so that the crack can be detected from the received signal. The crack types in the rail can be distinguished by utilising the magnitude and phase of the received signal [96]. It is found that they are related to the surface roughness and crack respectively. The design of the sensor structure is also essential to improve the sensitive and the performance in the process of the inspection, i.e. inclined angle sensor probe [97], multi-line excitation coil [98], hybrid differential and absolute probe [99] and orthogonal coils [100].

From the detection, it should be capable of obtaining both the geometry and the orientation of the crack. To obtain the orientation of the crack, crack imaging is a direct method to acquire the position in the test sample. In [101], it shows that, from the collected surface data, the plotted imaging can clearly identify the position of the crack. Besides, various excitation profiles of the EC inspection have been proposed to quantitatively determine the position and size of surface cracks [102-104]. Xu, *et al.* proposed a novel rotating focused eddy current technique which can be used to detect arbitrary orientation of the crack. Under this excitation strategy, it suggested that the magnitude of the signal stays unchanged for different crack orientations which can be used to estimate the depth of the crack. Besides, there is a decreasing trend between the orientation of the crack and the phase of the signal. Based on these features, both the depth and the orientation of the crack can be deduced [102]. Moreover, the effect of the lift-off can also affect the performance of the sensor probe. The phase imaging is more effective compared with magnitude imaging under small variation of the lift-off [105].

Yu, *et al.* found that the rising time due to different lift-offs can be reduced by subtracting the signal received by zero lift-off and crack free sample. Taking the merit of the linear relationship between the peak value and the lift-off, the depth of the crack can be inferred with the maximum error of 6% [14]. Furthermore, the algorithms to classify the defects are also explored, i.e. multilayer perceptron neural networks [106] and K-means algorithm [107].

For crack detection, numerical simulation gives the theoretical support and suggestions before carrying out experiments (i.e. finding the optimal sensor setup and excitation frequency). However, it is rather slow to obtain the simulation results from 3D finite element model. In this thesis, in order to hasten the computation speed, the acceleration strategies for the finite element method can be used for the crack detection. Due to the small perturbation of the crack, by utilising the accelerated solver, the results can be quickly obtained by solving the inversion of a much smaller matrix which can significantly improve the simulation speed.

Reference

- [1]. D. J. Harrison, L. D. Jones, and S. K. Burke, "Benchmark problems for defect size and shape determination in eddy-current nondestructive evaluation," *Journal of Nondestructive Evaluation*, vol. 15, no.1, pp. 21–34, 1996
- [2]. A. Bernieri, G. Betta, L. Ferrigno, and M. Laracca, "Crack Depth Estimation by Using a Multi-Frequency ECT Method," *IEEE Transactions on Instrumentation and Measurement*, vol. 62, no. 3, pp. 544-552, Mar. 2013.
- [3]. X. Ma, A. J. Peyton, and Y. Y. Zhao, "Eddy current measurements of electrical conductivity and magnetic permeability of porous metals," *NDT & E International*, vol. 39, no. 7, pp. 562-568, 2006.
- [4]. S. Miyazawa, H. Yoshida, and Y. Murakoshi, "Monitoring of metal-powder diameter by eddy-current sensor," *Journal of materials processing technology*, vol. 63,

no. 1-3, pp. 303-306, 1997.

[5]. C. Schmidt, C. Schultz, P. Weber, and B. Denkena, "Evaluation of eddy current testing for quality assurance and process monitoring of automated fiber placement," *Composites Part B: Engineering*, vol. 56, pp. 109-116, 2014.

[6]. H. A. Sodano, "Development of an automated eddy current structural health monitoring technique with an extended sensing region for corrosion detection," *Structural Health Monitoring*, vol. 6, no. 2, pp. 111-119, 2007.

[7]. P. Rizzo, "Sensing solutions for assessing and monitoring railroad tracks," *Sensor Technologies for Civil Infrastructures*, vol. 2, pp. 497-524, 2014.

[8]. G. Y. Tian, Y. He, I. Adewale, and A. Simm, "Research on spectral response of pulsed eddy current and NDE applications," *Sensors and Actuators A: Physical*, vol. 189, pp. 313-320, 2013.

[9]. M. S. Safizadeh, B. A. Lepine, D. S. Forsyth, and A. Fahr, "Time-frequency analysis of pulsed eddy current signals," *Journal of Nondestructive Evaluation*, vol. 20, no. 2, pp. 73-86, 2001.

[10]. S. Giguere, B. A. Lepine, and J. M. S. Dubois. "Pulsed eddy current technology: characterizing material loss with gap and lift-off variations," *Research in Nondestructive Evaluation*, vol. 13, no. 3, pp. 119-129, 2001.

[11]. B. A. Lepine, J. S. R. Giguere, D. S. Forsyth, A. Chahbaz, and J. M. S. Dubois, "Interpretation of pulsed eddy current signals for locating and quantifying metal loss in thin skin lap splices," *AIP Conference Proceedings*, vol. 615, no. 1, pp. 415-422, May 2002.

[12]. Y. He, F. Luo, X. Hu, B. Liu, and J. Gao, "Defect identification and evaluation based on three-dimensional magnetic field measurement of pulsed eddy current," *Insight-Non-Destructive Testing and Condition Monitoring*, vol. 51, no. 6, pp. 310-314, 2009.

[13]. Y. He, F. Luo, M. Pan, X. Hu, J. Gao, and B. Liu, "Defect classification based on rectangular pulsed eddy current sensor in different directions," *Sensors and Actuators*

A: *Physical*, vol. 157, no. 1, pp. 26-31, 2010.

[14]. Y. Yu, Y. Yan, F. Wang, G. Tian, and D. Zhang, "An approach to reduce lift-off noise in pulsed eddy current nondestructive technology," *NDT & E International*, vol. 63, pp. 1-6, 2014.

[15]. J. Kim, G. Yang, L. Udpa, and S. Udpa, "Classification of pulsed eddy current GMR data on aircraft structures," *NDT & E International*, vol. 43, no. 2, pp. 141-144, 2010.

[16]. G. Yang, A. Tamburrino, L. Udpa, S. S. Udpa, Z. Zeng, Y. Deng, and P. Que, "Pulsed Eddy-Current Based Giant Magnetoresistive System for the Inspection of Aircraft Structures," *IEEE Transactions on Magnetics*, vol. 46, no. 3, pp. 910-917, March 2010.

[17]. T. Clauzon, F. Thollon, and A. Nicolas, "Flaws characterization with pulsed eddy currents NDT," *IEEE Transactions on Magnetics*, vol. 35, no. 3, pp. 1873-1876, May 1999.

[18]. A. Sophiana, G. Y. Tiana, D. Taylora, and J. Rudlinb, "A feature extraction technique based on principal component analysis for pulsed Eddy current NDT," *NDT & E International*, vol. 36, no. 1, pp. 37-41, Jan. 2003.

[19]. D. Vasic, V. Bilas, and D. Ambrus, "Pulsed eddy-current nondestructive testing of ferromagnetic tubes," *IEEE Transactions on Instrumentation and Measurement*, vol. 53, no. 4, pp. 1289-1294, Aug. 2004.

[20]. I. Z. Abidin, C. Mandache, G. Y. Tian, and M. Morozov, "Pulsed eddy current testing with variable duty cycle on rivet joints," *NDT & E International*, vol. 42, no. 7, pp. 599-605, 2009.

[21]. Y. He, G. Tian, H. Zhang, M. Alamin, A. Simm, and P. Jackson, "Steel corrosion characterization using pulsed eddy current systems," *IEEE Sensors Journal*, vol. 12, no. 6, pp. 2113-2120, June 2012.

[22]. Y. Shin, D. Choi, Y. Kim, and S. Lee, "Signal characteristics of differential-pulsed eddy current sensors in the evaluation of plate thickness," *NDT & E International*, vol.

42, no. 3, pp. 215-221, 2009.

[23]. X. Chen, D. Hou, L. Zhao, P. Huang, and G. Zhang, "Study on defect classification in multi-layer structures based on Fisher linear discriminate analysis by using pulsed eddy current technique," *NDT & E International*, vol. 67, pp. 46-54, 2014.

[24]. G. Y. Tian and A. Sophian, "Defect classification using a new feature for pulsed eddy current sensors," *NDT & E International*, vol. 38, no. 1, pp. 77-82, 2005.

[25]. M. Lu, X. Meng, R. Huang, L. Chen, A. Peyton, W. Yin, and Z. Qu, "Thickness measurement of circular metallic film using single-frequency eddy current sensor," *NDT & E International*, vol. 119, 2021.

[26]. T. Chady, M. Enokizono, and R. Sikora, "Neural network models of eddy current multi-frequency system for nondestructive testing," *IEEE transactions on Magnetics*, vol. 36, no. 4, pp. 1724-1727, 2000.

[27]. C. Ye, A. Rosell, M. Haq, E. Stitt, L. Udpa, and S. Udpa, "EC probe with orthogonal excitation coils and TMR sensor for CFRP inspection," *International Journal of Applied Electromagnetics and Mechanics*, vol. 59, no. 4, pp. 1247-1255, 2019.

[28]. M. Fan, Q. Wang, B. Cao, B. Ye, B. A. I. Sunny, and G. Tian, "Frequency optimization for enhancement of surface defect classification using the eddy current technique," *Sensors*, vol.16, no. 5, 2016.

[29]. A. Bernieri, G. Betta, L. Ferrigno, and M. Laracca, "Multi-frequency Eddy Current Testing using a GMR based instrument," *International Journal of Applied Electromagnetics and Mechanics*, vol. 39, no. 1-4, pp. 355-362, 2012.

[30]. B. van den Bos, S. Sahlen, and J. Andersson, "Automatic scanning with multi-frequency eddy current on multi-layered structures," *Aircraft Engineering and Aerospace Technology*, 2003.

[31]. T. Reyno, P. R. Underhill, T. W. Krause, C. Marsden, and D. Wowk, "Surface profiling and core evaluation of aluminum honeycomb sandwich aircraft panels using multi-frequency eddy current testing," *Sensors*, vol. 17, no. 9, pp. 2114, 2017.

- [32]. D. Wen, M. Fan, B. Cao, B. Ye, and G. Tian, "Extraction of LOI Features from spectral pulsed eddy current signals for evaluation of ferromagnetic samples," *IEEE Sensors Journal*, vol. 19, no. 1, pp. 189-195, 1 Jan.1, 2019.
- [33]. G. Y. Tian and A. Sophian, "Reduction of lift-off effects for pulsed eddy current NDT," *NDT & E International*, vol. 38, no. 4, pp. 319-324, 2005.
- [34]. C. Mandache and J. H. V. Lefebvre, "Transient and harmonic eddy currents: Lift-off point of intersection," *NDT & E International*, vol. 39, no. 1, pp. 57-60, Jan. 2006.
- [35]. G. Y. Tian, Y. Li, and C. Mandache, "Study of lift-off invariance for pulsed eddy-current signals," *IEEE transactions on Magnetics*, vol. 45, no. 1, pp. 184-191, Jan. 2009.
- [36]. J. Li, X. Wu, Q. Zhang, P. Sun, "Measurement of lift-off using the relative variation of magnetic flux in pulsed eddy current testing," *NDT & E International*, vol. 75, pp. 57-64, 2015.
- [37]. C. Huang and X. Wu, "An improved ferromagnetic material pulsed eddy current testing signal processing method based on numerical cumulative integration," *NDT & E International*, vol. 69, pp. 35-39, 2015.
- [38]. H. Hoshikawa and K. Koyama, "A new eddy current surface probe without lift-off noise," *10th APCNDT Proceedings*, Brisbane, Australia, pp. 275-8575, 2001.
- [39]. W. Yin and K. Xu, "A Novel Triple-Coil Electromagnetic Sensor for Thickness Measurement Immune to Lift-Off Variations," *IEEE Transactions on Instrumentation and Measurement*, vol. 65, no. 1, pp. 164-169, Jan. 2016.
- [40]. M. Lu, X. Meng, R. Huang, L. Chen, A. Peyton and W. Yin, "Liftoff Tolerant Pancake Eddy-Current Sensor for the Thickness and Spacing Measurement of Nonmagnetic Plates," *IEEE Transactions on Instrumentation and Measurement*, vol. 70, pp. 1-9, 2021.
- [41]. D. Kim, L. Udpa, and S. S. Udpa, "Lift-off invariance transformations for eddy current nondestructive evaluation signals," *AIP Conference Proceedings*, vol. 615, pp. 615-622, 2002.

- [42]. M. Lu, W. Zhu, L. Yin, A. J. Peyton, W. Yin and Z. Qu, "Reducing the Lift-Off Effect on Permeability Measurement for Magnetic Plates From Multifrequency Induction Data," *IEEE Transactions on Instrumentation and Measurement*, vol. 67, no. 1, pp. 167-174, Jan. 2018.
- [43]. X. Meng, M. Lu, W. Yin, A. Bennecer and K. J. Kirk, "Inversion of Lift-Off Distance and Thickness for Nonmagnetic Metal Using Eddy Current Testing," *IEEE Transactions on Instrumentation and Measurement*, vol. 70, pp. 1-8, 2021.
- [44]. W. Yin, R. Binns, S. J. Dickinson, C. Davis and A. J. Peyton, "Analysis of the Liftoff Effect of Phase Spectra for Eddy Current Sensors," *IEEE Transactions on Instrumentation and Measurement*, vol. 56, no. 6, pp. 2775-2781, Dec. 2007.
- [45]. C. V. Dodd, W. E. Deeds, J. W. Luquire and W. G. Spoeri, "Some Eddy-Current Problems and Their Integral Solutions", *Oak Ridge National Laboratory*, April 1969.
- [46]. C. V. Dodd, and W. E. Deeds. "Analytical solutions to eddy-current probe-coil problems," *Journal of applied physics*, vol. 39, no. 6, pp. 2829-2838, 1968.
- [47]. C. C. Tai, J. H. Rose, and J. C. Moulder, "Thickness and conductivity of metallic layers from pulsed eddy-current measurements," *Review of scientific Instruments*, vol. 67, no. 11, pp. 3965-3972, 1996.
- [48]. N. Bowler, and Y. Huang, "Electrical conductivity measurement of metal plates using broadband eddy-current and four-point methods," *Measurement Science and Technology*, vol. 16, no. 11, pp. 2193, 2005.
- [49]. M. Lu, X. Meng, R. Huang, L. Chen, A. Peyton and W. Yin, "Inversion of Distance and Magnetic Permeability Based on Material-Independent and Liftoff Insensitive Algorithms Using Eddy Current Sensor," *IEEE Transactions on Instrumentation and Measurement*, vol. 70, pp. 1-9, 2021.
- [50]. T. Theodoulidis and E. E. Kriezis, "Eddy current canonical problems (with applications to nondestructive evaluation)," Tech Science Press, 1st edition, Apr. 2006.
- [51]. Y. Li, T. Theodoulidis and G. Y. Tian, "Magnetic field-based eddy-current modeling for multilayered specimens," *IEEE Transactions on Magnetics*, vol. 43, no.

11, pp. 4010-4015, Nov. 2007.

[52]. G. Tytko and L. Dziczkowski, "E-Cored coil with a circular air gap inside the core column used in eddy current testing," *IEEE Transactions on Magnetics*, vol. 51, no. 9, pp. 1-4, Sept. 2015.

[53]. T. P. Theodoulidis, "Model of ferrite-cored probes for eddy current nondestructive evaluation," *Journal of applied physics*, vol. 93, no. 5, pp. 3071-3078, 2003.

[54]. J. O. Fava and M. C. Ruch, "Calculation and simulation of impedance diagrams of planar rectangular spiral coils for eddy current testing," *NDT & E International*, vol. 39, no. 5, pp. 414-424, 2006.

[55]. T. P. Theodoulidis, T. D. Tsiboukis, and E. E. Kriezis, "Analytical solutions in eddy current testing of layered metals with continuous conductivity profiles," *IEEE Transactions on Magnetics*, vol. 31, no. 3, pp. 2254-2260, 1995.

[56]. T. Theodoulidis, "Analytical model for tilted coils in eddy-current nondestructive inspection," *IEEE Transactions on Magnetics*, vol. 41, no. 9, pp. 2447-2454, Sept. 2005.

[57]. T. Theodoulidis and J. R. Bowler, "Interaction of an Eddy-Current Coil With a Right-Angled Conductive Wedge," *IEEE Transactions on Magnetics*, vol. 46, no. 4, pp. 1034-1042, April 2010.

[58]. N. Harfield and J. R. Bowler, "Theory of thin-skin eddy-current interaction with surface cracks," *Journal of applied physics*, vol. 82, no. 9, pp. 4590-4603, 1997.

[59]. M. Lu, X. Meng, R. Huang, L. Chen, Z. Tang, J. Li, A. Peyton, and W. Yin, "Determination of Surface Crack Orientation Based on Thin-Skin Regime Using Triple-Coil Drive-Pickup Eddy-Current Sensor," *IEEE Transactions on Instrumentation and Measurement*, vol. 70, pp. 1-9, 2021.

[60]. J. R. Bowler, S. A. Jenkins, L. D. Sabbagh, and H. A. Sabbagh, "Eddy-current probe impedance due to a volumetric flaw," *Journal of Applied Physics*, vol. 70, no. 3, pp. 1107-1114, 1991.

[61]. A. Skarlatos, G. Pichenot, D. Lesselier, M. Lambert, and B. Duchene, "Electromagnetic modeling of a damaged ferromagnetic metal tube by a volume

integral equation formulation,” *IEEE Transactions on Magnetics*, vol. 44, no. 5, pp. 623-632, 2008.

[62]. M. Morozov, G. Rubinacci, A. Tamburrino and S. Ventre, “Numerical models of volumetric insulating cracks in eddy-current testing with experimental validation,” *IEEE Transactions on Magnetics*, vol. 42, no. 5, pp. 1568-1576, May 2006.

[63]. J. R. Bowler, T. P. Theodoulidis, and N. Poulakis. “Eddy current probe signals due to a crack at a right-angled corner.” *IEEE Transactions on Magnetics*, vol. 48, no.12, pp. 4735-4746, 2012.

[64]. J. R. Bowler, “Eddy-current interaction with an ideal crack. I. The forward problem,” *Journal of Applied Physics*, vol. 75, no. 12, pp. 8128-8137, 1994.

[65]. J. R. Bowler and N. Harfield, “Thin-skin eddy-current interaction with semielliptical and epicyclic cracks,” *IEEE Transactions on Magnetics*, vol. 36, no. 1, pp. 281-291, Jan. 2000.

[66]. Y. Le Bihan, “3-D finite-element analysis of eddy-current evaluation of curved plates,” *IEEE Transactions on Magnetics*, vol. 38, no. 2, pp. 1161-1164, March 2002.

[67]. H. Huang, T. Takagi and T. Uchimoto, “Crack shape reconstruction in ferromagnetic materials using a novel fast numerical simulation method,” *IEEE Transactions on Magnetics*, vol. 40, no. 2, pp. 1374-1377, March 2004.

[68]. B. Gupta, B. Ducharne, G. Sebald and T. Uchimoto, “A Space Discretized Ferromagnetic Model for Non-Destructive Eddy Current Evaluation,” *IEEE Transactions on Magnetics*, vol. 54, no. 3, pp. 1-4, March 2018.

[69]. Z. Chen, M. Rebican, N. Yusa and K. Miya, “Fast simulation of ECT signal due to a conductive crack of arbitrary width,” *IEEE Transactions on Magnetics*, vol. 42, no. 4, pp. 683-686, April 2006.

[70]. Z. Badics, H. Komatsu, Y. Matsumoto, K. Aoki, F. Nakayasu and K. Miya, “A thin sheet finite element crack model in eddy current NDE,” *IEEE Transactions on Magnetics*, vol. 30, no. 5, pp. 3080-3083, Sept. 1994.

[71]. Y. Du, S. Xie, X. Li, Z. Chen, T. Uchimoto and T. Takagi, “A Fast Forward

Simulation Scheme for Eddy Current Testing of Crack in a Structure of Carbon Fiber Reinforced Polymer Laminate,” *IEEE Access*, vol. 7, pp. 152278-152288, 2019.

[72]. T. Takagi, Haoyu Huang, H. Fukutomi and J. Tani, “Numerical evaluation of correlation between crack size and eddy current testing signal by a very fast simulator,” *IEEE Transactions on Magnetics*, vol. 34, no. 5, pp. 2581-2584, Sept. 1998.

[73]. H. Huang, T. Takagi, and T. Uchimoto, “A fast numerical calculation for crack modeling in eddy current testing of ferromagnetic materials,” *Journal of Applied Physics*, vol. 94, pp. 5866–5872, Nov. 2003.

[74]. K. Zhao, M. N. Vouvakis and J. F. Lee, “Solving electromagnetic problems using a novel symmetric FEM-BEM approach,” *IEEE Transactions on Magnetics*, vol. 42, no. 4, pp. 583-586, Apr. 2006.

[75]. F. Matsuoka and A. Kameari, “Calculation of three dimensional eddy current by FEM-BEM coupling method,” *IEEE Transactions on Magnetics*, vol. 24, no. 1, pp. 182-185, Jan. 1988.

[76]. T. Steinmetz, N. Godel, G. Wimmer, M. Clemens, S. Kurz and M. Bebenorf, “Efficient symmetric FEM-BEM coupled simulations of electro-quasistatic fields,” *IEEE Transactions on Magnetics*, vol. 44, no. 6, pp. 1346-1349, Jun. 2008.

[77]. Z. Badics, Y. Matsumoto, K. Aoki, F. Nakayasu, M. Uesaka, and K. Miya, “An effective 3-D finite element scheme for computing electromagnetic field distortions due to defects in eddy-current nondestructive evaluation,” *IEEE Transactions on Magnetics*, vol. 33, no. 2, pp. 1012-1020, Mar. 1997.

[78]. G. Rubinacci, A. Tamburrino, S. Ventre, and F. Villone, “A fast 3-D multipole method for eddy-current computation,” *IEEE Transactions on Magnetics*, vol. 40, no. 2, pp. 1290-1293, March 2004.

[79]. M. Lu, A. Peyton and W. Yin, “Acceleration of Frequency Sweeping in Eddy-Current Computation,” *IEEE Transactions on Magnetics*, vol. 53, no. 7, pp. 1-8, July 2017.

[80]. Z. Badics, J. Pávó, S. Bilicz and S. Gyimóthy, “Subdomain Perturbation Finite-

Element Method for Quasi-static Darwin Approximation,” *IEEE Transactions on Magnetics*, vol. 56, no. 1, pp. 1-4, Jan. 2020.

[81]. D. I. Ona, G. Y. Tian, R. Sutthaweeikul and S. M. Naqvi, “Design and optimisation of mutual inductance based pulsed eddy current probe”, *Measurement*, vol. 144, pp. 402-409, Oct. 2019.

[82]. M. Fan, B. Cao, A. I. Sunny, W. Li, G. Tian, and B. Ye, “Pulsed eddy current thickness measurement using phase features immune to liftoff effect,” *NDT & E International*, vol. 86, pp. 123–131, 2017.

[83]. E. Pinotti and E. Puppini, “Simple Lock-In Technique for Thickness Measurement of Metallic Plates,” *IEEE Transactions on Instrumentation and Measurement*, vol. 63, no. 2, pp. 479-484, Feb. 2014.

[84]. W. Yin and A. J. Peyton, “Thickness Measurement of Metallic Plates With an Electromagnetic Sensor Using Phase Signature Analysis,” *IEEE Transactions on Instrumentation and Measurement*, vol. 57, no. 8, pp. 1803-1807, Aug. 2008.

[85]. W. Yin and A. J. Peyton, “Thickness measurement of non-magnetic plates using multi-frequency eddy current sensors,” *NDT & E International*, vol. 40, no. 1, pp. 43-48, 2007.

[86]. M. Fan, B. Cao, P. Yang, W. Li, and G. Tian, “Elimination of liftoff effect using a model-based method for eddy current characterization of a plate,” *NDT & E International*, vol. 74, pp. 66-71, 2015.

[87]. M. Lu, X. Meng, W. Yin, Z. Qu, F. Wu, J. Tang, et al., “Thickness measurement of non-magnetic steel plates using a novel planar triple-coil sensor,” *NDT & E International*, vol. 107, 2019.

[88]. A. V. Egorov, V. V. Polyakov, D. S. Salita, E. A. Kolubaev, et al., “Inspection of aluminum alloys by a multi-frequency eddy current method,” *Defence Technology*, vol. 11, no. 2, pp. 99-103, 2015.

[89]. B. Halleux, B. L. Stirum, and A. I'tchelintsev, “Eddy current measurement of the wall thickness and conductivity of circular non-magnetic conductive tubes,” *NDT & E*

International, vol. 29, no. 2, pp. 103-109, Apr. 1996.

[90]. J. C. Moulder, E. Uzal, and J. H. Rose, "Thickness and conductivity of metallic layers from eddy current measurements," *Review of Scientific Instruments*, vol. 63, no. 6, pp. 3455-3465, Jan. 1992.

[91]. W. Yin, S. J. Dickinson, and A. J. Peyton, "Imaging the continuous conductivity profile within layered metal structures using inductance spectroscopy," *IEEE Sensors Journal*, vol. 5, no. 2, pp. 161–166, Apr. 2005.

[92]. F. Loete, Y. Le Bihan and D. Mencaraglia, "Novel Wideband Eddy Current Device for the Conductivity Measurement of Semiconductors," *IEEE Sensors Journal*, vol. 16, no. 11, pp. 4151-4152, June, 2016.

[93]. Y. Yu, Y. Zou, M. A. Hosani and G. Tian, "Conductivity Invariance Phenomenon of Eddy Current NDT: Investigation, Verification, and Application," *IEEE Transactions on Magnetics*, vol. 53, no. 1, pp. 1-7, Jan. 2017.

[94]. Y. Yu, Y. Zou, M. Jiang and D. Zhang, "Investigation on conductivity invariance in eddy current NDT and its application on magnetic permeability measurement," *2015 IEEE Far East NDT New Technology & Application Forum (FENDT)*, pp. 257-262, 2015.

[95]. M. Lu, R. Huang, W. Yin, Q. Zhao and A. Peyton, "Measurement of Permeability for Ferrous Metallic Plates Using a Novel Lift-Off Compensation Technique on Phase Signature," *IEEE Sensors Journal*, vol. 19, no. 17, pp. 7440-7446, 1 Sept. 2019.

[96]. Z. Song, T. Yamada, H. Shitara, and Y. Takemura, "Detection of damage and crack in railhead by using eddy current testing," *Journal of Electromagnetic Analysis and Applications*, 2011.

[97]. Y. J. Kim, and S. S. Lee, "Eddy current probes of inclined coils for increased detectability of circumferential cracks in tubing," *NDT & E International*, vol. 49, no. 77-82, 2012.

[98]. Z. Zeng, Y. Deng, X. Liu, L. Udpa, S. S. Udpa, B. E. C. Koltenbah, et. al, "EC-GMR Data Analysis for Inspection of Multilayer Airframe Structures," *IEEE*

Transactions on Magnetics, vol. 47, no. 12, pp. 4745-4752, Dec. 2011.

[99]. A. N. Abdalla, K. Ali, J. K. Paw, D. Rifai, and M. A. Faraj, "A novel eddy current testing error compensation technique based on mamdani-type fuzzy coupled differential and absolute probes," *Sensors*, vol. 18, no. 7, pp. 2108, 2018.

[100]. C. Ye, A. Rosell, M. Haq, E. Stitt, L. Udpa and S. Udpa, "EC probe with orthogonal excitation coils and TMR sensor for CFRP inspection," *International Journal of Applied Electromagnetics and Mechanics*, vol. 59, no. 4, pp. 1247-1255, 2019.

[101]. J. R. S. Avila, Z. Chen, H. Xu and W. Yin, "A multi-frequency NDT system for imaging and detection of cracks," *2018 IEEE International Symposium on Circuits and Systems (ISCAS)*, pp. 1-4, 2018.

[102]. Z. Xu, X. Wang and Y. Deng, "Rotating Focused Field Eddy-Current Sensing for Arbitrary Orientation Defects Detection in Carbon Steel," *Sensors*, vol. 20, no. 8, 2020.

[103]. C. Ye, Y. Huang, L. Udpa and S. S. Udpa, "Novel Rotating Current Probe With GMR Array Sensors for Steam Generate Tube Inspection," *IEEE Sensors Journal*, vol. 16, no. 12, pp. 4995-5002, June15, 2016.

[104]. R. Hamia, C. Cordier, and C. Dolabdjian, "Eddy-current non-destructive testing system for the determination of crack orientation," *Ndt & E International*, vol. 61, pp. 24-28, 2014.

[105]. M. Ricci, G. Silipigni, L. Ferrigno, M. Laracca, I. D. Adewale, and G. Y. Tian, "Evaluation of the lift-off robustness of eddy current imaging techniques," *NDT & E International*, vol. 85, pp. 43-52, 2017.

[106]. N. H. Jo, and H. B. Lee, "A novel feature extraction for eddy current testing of steam generator tubes," *NDT & E International*, vol. 42, no. 7, pp. 658-663, 2009.

[107]. Y. Tao, H. Xu, Z. Chen, R. Huang, Q. Ran, Q. Zhao, *et al*, "Automatic feature extraction method for crack detection in eddy current testing," *2019 IEEE International Instrumentation and Measurement Technology Conference (I2MTC)*, pp. 1-6, 2019.

Chapter 3 Support theory

In this chapter, both the analytical method and the numerical method are introduced to calculate the inductance change due to the test sample. It includes Dodd and Deeds formulations for the plate model and the developed finite element method for electromagnetic modelling.

3.1 The inductance calculation based on Dodd & Deeds model

In the field of eddy current testing, the mutual inductance between the excitation coil and the sensing coil is a key indicator of the property of the tested conductive sample. The analytical solution of the coils upon an infinite large testing plate given by Dodd and Deeds has provided a strong theoretical basis.

3.1.1 Inductance calculation for co-axial sensor probe

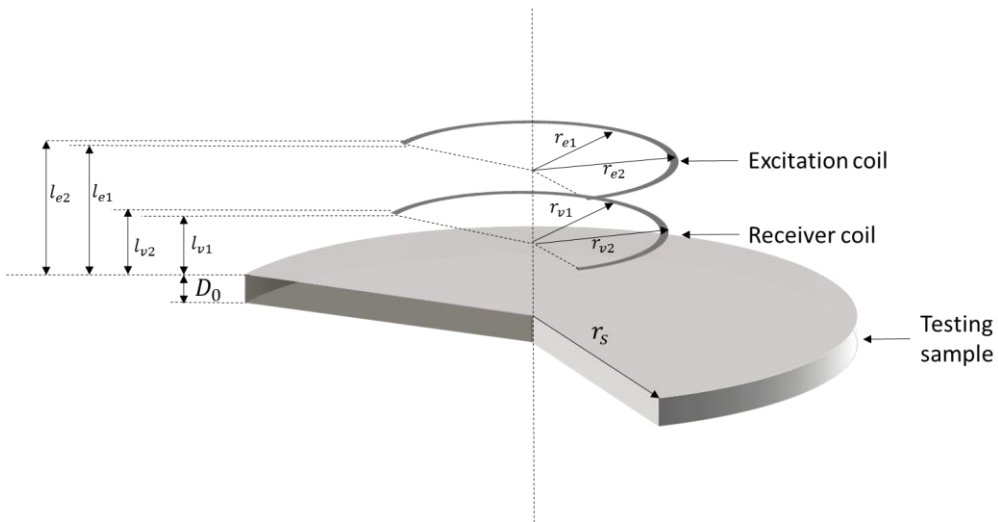


Figure 3.1 A coil above an infinite conductive plate

The co-axial sensor probe is commonly used in the eddy current testing. According to Dodd and Deeds model [1], it considers the sample plate as an infinite conductive plate.

The inductance change due to the presence of the sample plate induced by the sensor probe with two identical coils is calculated. As shown in Figure 3.1, for the model of a coil above the infinite testing plate, the vector potential generated by the excitation coil in the r-z axis plane is,

$$A(r, z) = \frac{I\mu_0 N_e}{2} \int_0^\infty \frac{J_1(\alpha r) P(\alpha)}{\alpha^3} K(z, \alpha) \phi(\alpha) d\alpha \quad 3.1$$

With

$$\phi(\alpha) = \frac{(\alpha_1 + \mu_1 \alpha)(\alpha_1 - \mu_1 \alpha) - (\alpha_1 + \mu_1 \alpha)(\alpha_1 - \mu_1 \alpha)e^{2\alpha_1 D_0}}{-(\alpha_1 - \mu_1 \alpha)(\alpha_1 - \mu_1 \alpha) + (\alpha_1 + \mu_1 \alpha)(\alpha_1 + \mu_1 \alpha)e^{2\alpha_1 D_0}} \quad 3.2$$

$$\alpha_1 = \sqrt{\alpha^2 + j\omega\sigma\mu_0\mu_1} \quad 3.3$$

$$K(z, \alpha) = (2 - e^{\alpha(z-l_{e2})} - e^{-\alpha(z-l_{e1})})/\phi(\alpha) + e^{-\alpha z}(e^{-\alpha l_{e1}} - e^{-\alpha l_{e2}}) \quad 3.4$$

$$P(\alpha) = \int_{\alpha r_{e1}}^{\alpha r_{e2}} \tau J_1(\tau) d\tau \quad 3.5$$

Where: D_0 , μ_1 , and σ denote the thickness, relative permeability, and electrical conductivity of the sample plate. μ_0 represents the permeability of the free space. ω denotes the working angular frequency for the excitation current. I denotes the excitation current. N_e denotes the turns of the excitation coil. r_{e1} and r_{e2} denote the inner and outer radii of the excitation coil. l_{e1} and l_{e2} denote the lower and upper height of the excitation coil. J_1 denotes a first order Bessel function of the first kind. α and τ are the integration variables.

Further, the induced voltage on the receiver coil is the integral of the induced vector potential over the whole receiver coil.

$$V = N_v j\omega \int_s \mathbf{A} ds = \frac{2\pi N_v j\omega}{(l_{v1} - l_{v2})^2 (r_{v1} - r_{v2})^2} \int_{l_{v1}}^{l_{v2}} \int_{r_{v1}}^{r_{v2}} r A(r, z) dr dz \quad 3.6$$

Where: l_{v1} and l_{v2} denote the lower and upper height of the receiver coil. r_{v1} and r_{v2}

denote the inner radius and the outer radius of the receiving coil. N_v denotes the turns of the receiving coil.

Then the received voltage with the presence of the sample plate (V_{sample}) and the received voltage without the presence of the sample plate (in free space, V_{air}) are

$$V_{sample} = \frac{j\omega I \pi \mu_0 N_v N_e}{(l_{v1} - l_{v2})^2 (r_{v1} - r_{v2})^2} \int_0^\infty \frac{P^2(\alpha)}{\alpha^6} (2\alpha(l_{v2} - l_{v1}) - e^{a(l_{v2}-l_{e2})} + e^{a(l_{v1}-l_{e2})} + e^{-a(l_{v2}-l_{e1})} - e^{-a(l_{v1}-l_{e1})} + (e^{-\alpha l_{v1}} - e^{-\alpha l_{v2}})(e^{-\alpha l_{e1}} - e^{-\alpha l_{e2}})\phi(\alpha))d\alpha \quad 3.7$$

$$V_{air} = \frac{j\omega I \pi \mu_0 N_v N_e}{(l_{v1} - l_{v2})^2 (r_{v1} - r_{v2})^2} \int_0^\infty \frac{P^2(\alpha)}{\alpha^6} (2\alpha(l_{v2} - l_{v1}) - e^{a(l_{v2}-l_{e2})} + e^{a(l_{v1}-l_{e2})} + e^{-a(l_{v2}-l_{e1})} - e^{-a(l_{v1}-l_{e1})})d\alpha \quad 3.8$$

Thus, the inductance change due to the presence of the sample plate induced by the sensor probe with two identical coils is (the subtraction between the inductance with the sample and without the sample - i.e. free space),

$$\Delta L(\omega) = \frac{V_{sample} - V_{air}}{j\omega I} \quad 3.9$$

$$= \frac{\pi N_v N_e \mu_0}{(l_{v1} - l_{v2})^2 (r_{v1} - r_{v2})^2} \int_0^\infty \frac{P^2(\alpha)}{\alpha^6} G(\alpha) \phi(\alpha) d\alpha$$

With

$$G(\alpha) = e^{-\alpha(2l+h+g)}(1 - e^{-\alpha h})^2 \quad 3.10$$

$$h = l_{e2} - l_{e1} \quad 3.11$$

Where, l denotes the lift-off and g the gap between the excitation and receiver coils.

Since there is a phase difference between the induced voltage and the injected current, the impedance calculated should be complex. Therefore, the change of the complex

inductance due to the sample plate (subtract to the inductance in the air) can be obtained by dividing the impedance change by the excitation frequency. The schematic diagram for the infinite non-magnetic metallic sample plate is demonstrated in Figure 3.2.

It can be seen that the both parts of the inductance change begin from 0 at low frequency. As the excitation frequency increases, the magnitude of the real part increases until reaching the saturated value. For the imaginary part, the peak value could be achieved at the characteristic frequency, termed as peak frequency, then decreases to reach zero again. While for the magnetic sample plate, there exists a zero-crossing point for the real part of the inductance change.

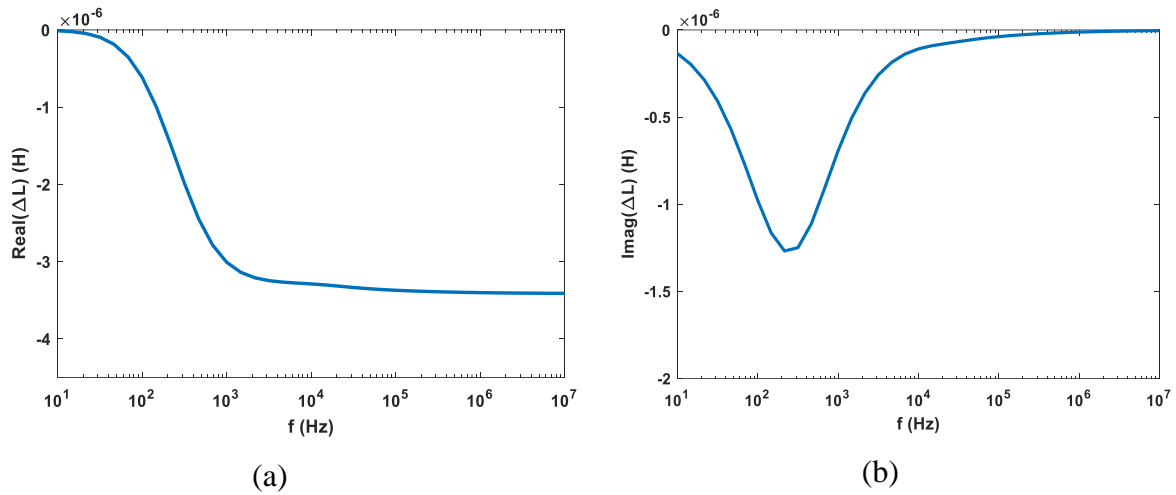


Figure 3.2 Schematic diagram of the sensor system above the infinite non-magnetic metallic sample plate (a) real part (b) imaginary part

The peak frequency is related to the material properties, it can be obtained from $\phi(\alpha)$. Due to the fact that this term changes very slowly with α with regards to other terms, and it reaches its maximum at a characteristic spatial frequency α_0 . Therefore, the inductance change can be approximated as

$$\Delta L(\omega) = \phi(\alpha_0) \Delta L_0 \quad 3.12$$

With

$$\Delta L_0 = \frac{\pi N_v N_e \mu_0}{(l_{v1} - l_{v2})^2 (r_{v1} - r_{v2})^2} \int_0^\infty \frac{P^2(\alpha)}{\alpha^6} G(\alpha) d\alpha \quad 3.13$$

From Equation 3.12 - Equation 3.13, ΔL_0 is the magnitude of the inductance change and is related to the sensor probe parameters. The phase feature depends on the term, $\phi(\alpha_0)$. According to [3], $\phi(\alpha_0)$ can be approximated as,

$$\phi(\alpha_0) = \frac{j \frac{\omega}{\omega_0}}{j \frac{\omega}{\omega_0} + 1 + \frac{2\alpha_0 \alpha_1 D_0}{2\alpha_0^2 D_0 + 2\alpha_0}} \quad 3.14$$

With

$$\omega_0 = \frac{2\alpha_0^2 D_0 + 2\alpha_0}{\sigma \mu_0 D_0} \quad 3.15$$

As can be seen from Equation 3.14 - Equation 3.15, the phase of the inductance change is a first order system. The peak frequency can be approximated by ω_0 and there is a linear trend between the peak frequency and α_0 when the coil diameter is much larger than the plate thickness ($\alpha_0 D_0 \ll 1$). Consequently, the thickness and the conductivity of the sample plate can be deduced from this peak frequency feature.

3.2 FEM based eddy current computation solver

Due to the limitations of the analytical solution, numerical solution has been widely applied in engineering fields. Based on the method of weighted residuals, Galerkin method was developed by simplifying the differential equations into linear equations to obtain the approximation results and has been regarded as a powerful numerical technique.

A. Nodal shape function

Nodal shape functions have been introduced in the finite element analysis and they are continuous within arbitrary element. They are interpolated into relevant nodes to

represent the overall shape of the approximation solutions of the element. It is assumed that the nodal shape function interpolated at node i should be nonzero at the node i and be zero at other nodes. Figure 3.3 shows the linear interpolation functions in one dimensional element.

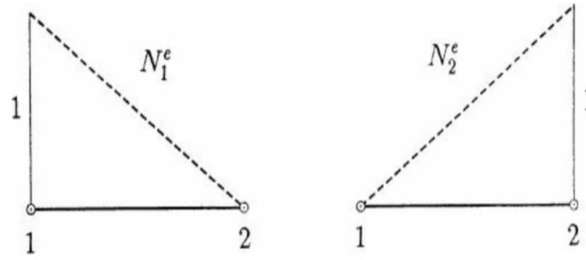


Figure 3.3 Linear interpolation functions in one dimensional element [3]

In order to construct the shape function for the tetrahedral elements, the Silvester-Lagrange polynomial is usually applied. The shape function with the Silvester-Lagrange polynomial is conveniently expressed as

$$P_i^n(\xi) = \begin{cases} \frac{1}{i!} \prod_{l=0}^{i-1} (n\xi - l), & \text{for } 1 \leq i \leq n \\ 1, & \text{for } i = 0 \end{cases} \quad 3.16$$

where: n is the integer parameter and ξ is the normalised coordinate variable.

For the Silvester-Lagrange polynomial, the key feature is that $P_i^n(\xi)$ is unity at the point equals to $\frac{i}{n}$. It is corresponding to the property of the shape function. Besides, the value of n reveals the number of divisions of the interval $[0, 1]$ into uniform subintervals. Based on these features, the Silvester-Lagrange polynomial can be used to construct the interpolatory polynomials.

In order to construct the shape functions, four integers I, J, K and L are used to label each node within the tetrahedral element. The numbering scheme (IJKL) for tetrahedral

element is shown in Figure 3.4.

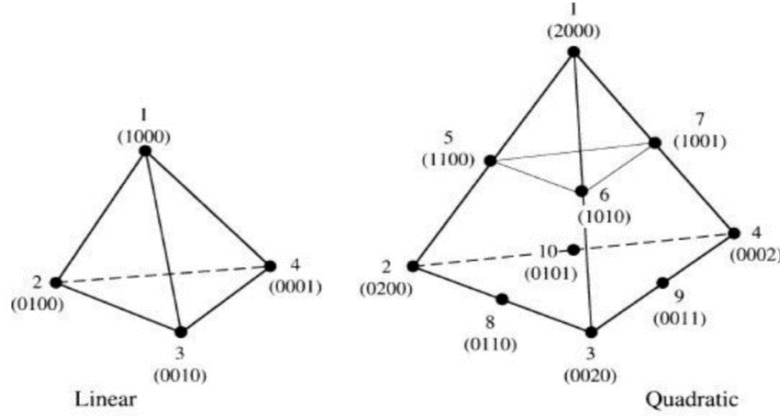


Figure 3.4 The numbering scheme for tetrahedral elements [4]

By multiplying every interpolatory polynomial, the nodal shape function can be written as

$$N_i = P_i^n(\xi)P_j^n(\eta)P_k^n(\zeta)P_l^n(1 - \xi - \eta - \zeta) \quad I + J + K + L = n \quad 3.17$$

B. Edge shape function

For the construction of the first order edge shape function, two factors should be considered: one is that the normal component, which is interpolated by the divergence-conforming vector shape function on the face i , should be vanished along the remaining faces of the element; another is that the tangential component, which is interpolated by the curl-conforming vector shape function on the edge j , should be vanished along the remaining edges of the element. The vector function is defined as

$$\mathbf{W}_{i_1 i_2} = \xi_{i_1} \nabla \xi_{i_2} - \xi_{i_2} \nabla \xi_{i_1} \quad 3.18$$

where: i_1 and i_2 are the terminal nodes of the i^{th} edge, and ranges from 1 to 4.

The vector function $\mathbf{W}_{i_1 i_2}$ has all the features that should be fulfilled for the appropriate vector field. Assumed that the length of vector shape function \mathbf{N}_i should be

1, the vector shape function can be described as

$$\mathbf{N}_i = l_{i_1 i_2} \mathbf{W}_{i_1 i_2} \quad 3.19$$

Figure 3.5 shows the flow of the vector shape function for a surface of the tetrahedral element.

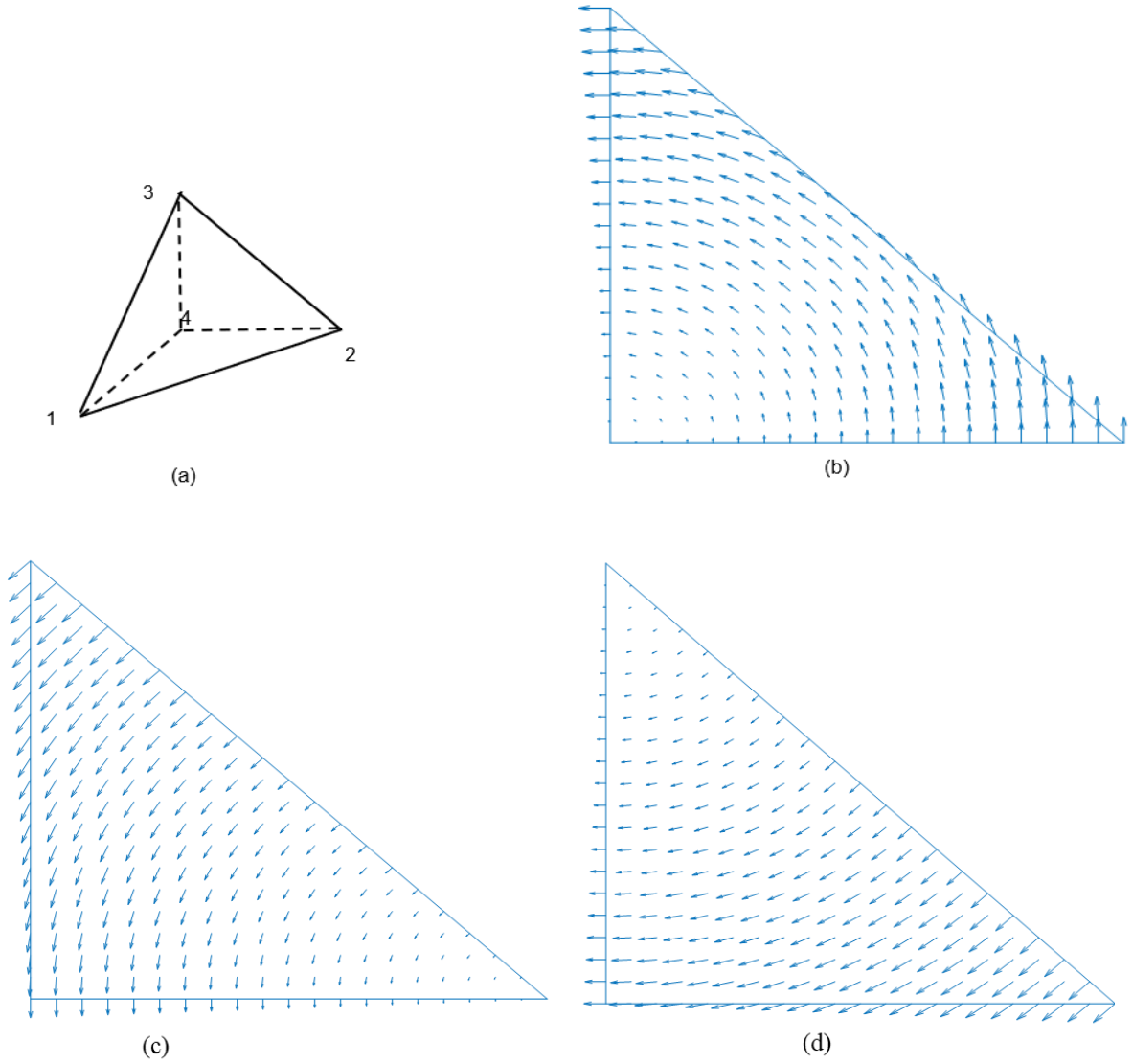


Figure 3.5 (a) The tetrahedral element (b) The vector shape function of edge 23 (c) The vector shape function of edge 34 (d) The vector shape function of edge 24

Higher order vector shape functions are constructed by a combination of the first-order vector shape function and a set of scalar polynomials. The shifted Silvester polynomials,

denoted as $\hat{P}_i^n(\xi)$, are used so as to construct the scalar polynomials. Then the $(p+1)^{\text{th}}$ order vector shape function can be constructed and expressed as [4]

$$\hat{P}_i^n(\xi) = \begin{cases} \frac{1}{(i-1)!} \prod_{l=1}^{i-1} (n\xi - l), & \text{for } 2 \leq i \leq n \\ 1, & \text{for } i = 1 \end{cases} \quad 3.20$$

$$\alpha_{ijkl}^{i_1 i_2, p+1} = \frac{p+2}{p+2-\beta-\gamma} l_{i_1 i_2} \quad 3.21$$

$$\begin{aligned} N_{ijkl}^{12, p+1} &= \alpha_{ijkl}^{12, p+1} \hat{P}_i^{p+2}(\xi_1) \hat{P}_j^{p+2}(\xi_2) P_k^{p+2}(\xi_3) P_l^{p+2}(\xi_4) \mathbf{W}_{12} \\ N_{ijkl}^{13, p+1} &= \alpha_{ijkl}^{13, p+1} \hat{P}_i^{p+2}(\xi_1) P_j^{p+2}(\xi_2) \hat{P}_k^{p+2}(\xi_3) P_l^{p+2}(\xi_4) \mathbf{W}_{13} \\ N_{ijkl}^{14, p+1} &= \alpha_{ijkl}^{14, p+1} \hat{P}_i^{p+2}(\xi_1) P_j^{p+2}(\xi_2) P_k^{p+2}(\xi_3) \hat{P}_l^{p+2}(\xi_4) \mathbf{W}_{14} \\ N_{ijkl}^{23, p+1} &= \alpha_{ijkl}^{23, p+1} P_i^{p+2}(\xi_1) \hat{P}_j^{p+2}(\xi_2) \hat{P}_k^{p+2}(\xi_3) P_l^{p+2}(\xi_4) \mathbf{W}_{23} \\ N_{ijkl}^{24, p+1} &= \alpha_{ijkl}^{24, p+1} P_i^{p+2}(\xi_1) \hat{P}_j^{p+2}(\xi_2) P_k^{p+2}(\xi_3) \hat{P}_l^{p+2}(\xi_4) \mathbf{W}_{24} \\ N_{ijkl}^{34, p+1} &= \alpha_{ijkl}^{34, p+1} P_i^{p+2}(\xi_1) P_j^{p+2}(\xi_2) \hat{P}_k^{p+2}(\xi_3) \hat{P}_l^{p+2}(\xi_4) \mathbf{W}_{34} \end{aligned} \quad 3.22$$

From the equations showed above, it is obvious that, for the point interpolated on the edge, there is a corresponding basis function. Figure 3.6 shows the second order vector shape functions of the tetrahedral element interpolated on the edges of face 234. There are two interpolation functions on each edge.

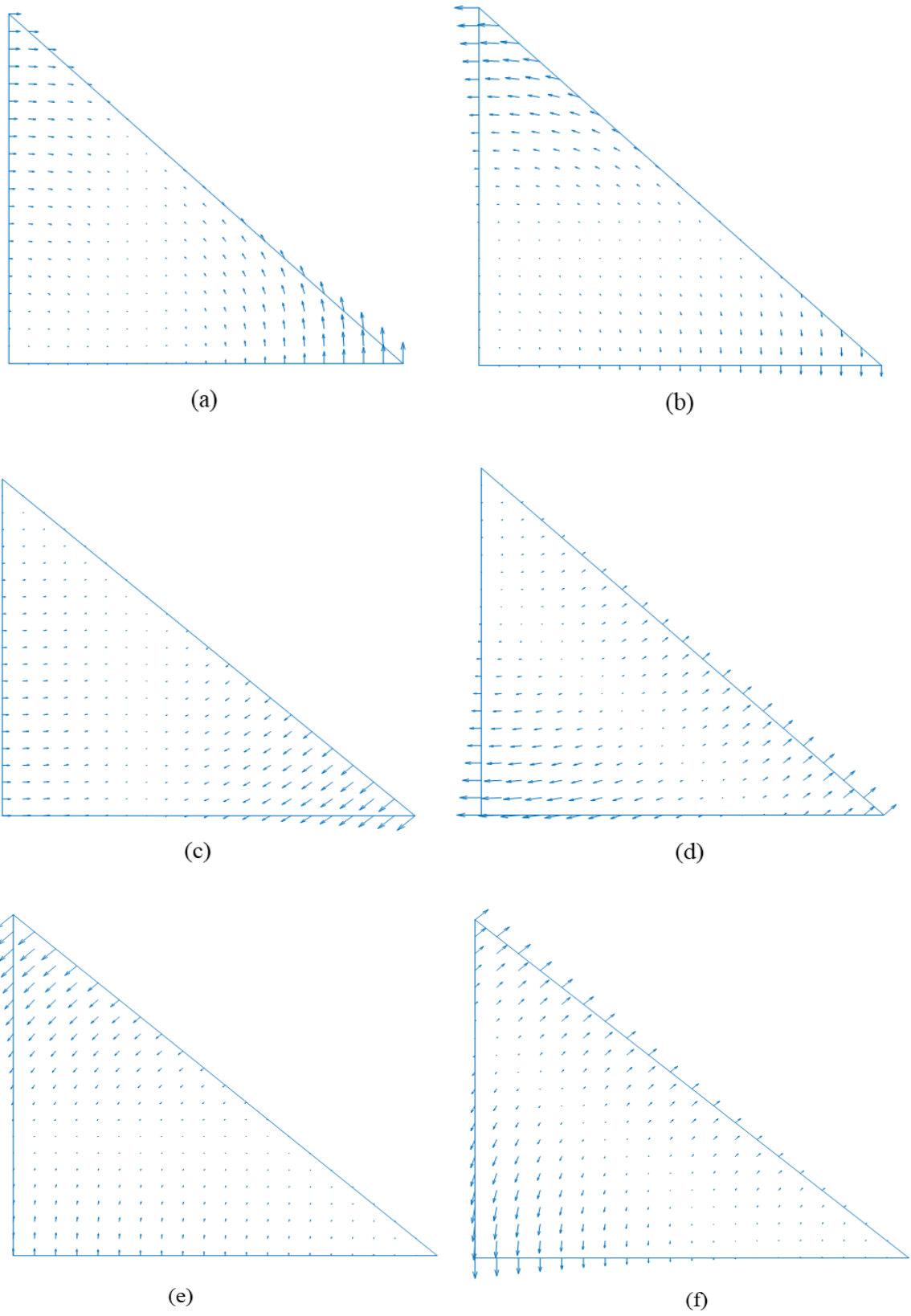


Figure 3.6 Second-order interpolation functions (a) N_{0210}^{23} (b) N_{0120}^{23} (c) N_{0201}^{24} (d) N_{0102}^{24} (e) N_{0021}^{34} (f)

N_{0012}^{34}

C. Galerkin equations

With the aid of the edge shape functions and the nodal shape functions, the unknown vector potential and scalar potential fields can be approximated. In order to construct the shape functions for each tetrahedral element, matrix transformation from global space to local space can be used if isotropy is satisfied for every edge element [5].

$$J = \begin{bmatrix} \frac{\partial x}{\partial \xi} & \frac{\partial y}{\partial \xi} & \frac{\partial z}{\partial \xi} \\ \frac{\partial x}{\partial \eta} & \frac{\partial y}{\partial \eta} & \frac{\partial z}{\partial \eta} \\ \frac{\partial x}{\partial \zeta} & \frac{\partial y}{\partial \zeta} & \frac{\partial z}{\partial \zeta} \end{bmatrix} \quad 3.23$$

$$\lambda_v = J^{-1} \hat{\lambda}_v \quad 3.24$$

$$\lambda_s = J^{-1} \hat{\lambda}_s \quad 3.25$$

$$\nabla \times \lambda_v = \frac{1}{|J|} J^T \nabla \times \hat{\lambda}_v \quad 3.26$$

Where, J denotes the Jacobian matrix, xyz denote the coordinates in the global space, $\xi\eta\zeta$ denote the coordinates in the local space, $\hat{\lambda}_v$ and $\hat{\lambda}_s$ denote the relevant components in the local space and λ_v and λ_s denotes the relevant components in the global space.

Then combine approximated fields with the boundary conditions, Galerkin equations can be obtained, shown as followings:

$$\begin{aligned} \int_{\Omega_c} \nabla \times N_i \cdot v \nabla \times \mathbf{A}^n d\Omega + \int_{\Omega_c} j\omega\sigma N_i \cdot \mathbf{A}^n d\Omega + \int_{\Omega_c} j\omega\sigma N_i \cdot \nabla V^n d\Omega \\ = \int_{\Omega_c} \nabla \times N_i \cdot v_0 \nabla \times \mathbf{A}_s d\Omega \quad i = 1, 2, \dots, 6 \end{aligned} \quad 3.27$$

$$\int_{\Omega_c} j\omega\sigma \nabla L_i \cdot \mathbf{A}^n d\Omega + \int_{\Omega_c} j\omega\sigma \nabla L_i \cdot \nabla V^n d\Omega = 0 \quad 3.28$$

$$i = 1, 2, \dots, 4$$

Where, V^n denotes the scalar potential (voltage) of element n . A^n denotes the induced vector potential corresponding to element n . σ denotes the media electrical conductivity. v_0 denotes the reluctivity in the free space domain. v denotes the reluctivity for the target.

It is noted that, for every arbitrary element n , the matrix Q^n can be expressed by the stiffness matrix form which is the combined by the left-hand terms of Equation 3. 27 and 3. 28.

$$Q^n = \begin{bmatrix} K^n & L^n \\ M^n & N^n \end{bmatrix} \quad 3. 29$$

From the aspect of the whole system, the whole system matrix can be derived by combining Equation 3. 29 to Equation 3. 27 and 3. 28 and expressed as

$$Q \begin{bmatrix} A_1 \\ \vdots \\ A_p \\ V_1 \\ \vdots \\ V_q \end{bmatrix} = \begin{bmatrix} K^{p \times p} & L^{p \times q} \\ M^{q \times p} & N^{q \times q} \end{bmatrix} \begin{bmatrix} A_1 \\ \vdots \\ A_p \\ V_1 \\ \vdots \\ V_q \end{bmatrix} = B \quad 3. 30$$

with

$$K^{p \times p} = K_1^{p \times p} + K_2^{p \times p} \quad 3. 31$$

According to Equation 3. 30 - Equation 3. 31, the K matrix consists of two parts, the K_1 and K_2 matrices. K_1 matrix represents the 1st A term of Equation 3. 27 and it plays a role for the generation of the basic A wave. K_2 represents the 2nd A term of Equation 3. 27 and the eddy current diffusion effect can be revealed by K_2 matrix. L represents the 1st V term of Equation 3. 27, and it monitors the eddy current confined within the sample geometry (Maxwell-Wagner effect). M represents the 1st term of the left-hand side of Equation 3. 28 and N represents the 2nd term of the left-hand side of Equation

3. 28. The magnetostatic field is governed by both of the terms. \mathbf{B} represents the right-hand side of Equation 3. 27 and Equation 3. 28, and it acts as the environmental background field. p represents the order of the edge. q represents the order of the vertex. The pre-conditioning technique is also applied to increase the accuracy of the calculated \mathbf{A} and V of the whole mesh.

After obtaining \mathbf{A} and V of the whole mesh through Equation 3. 30, the electric field can be formed by combining the canonical $\mathbf{A} - V$ formulation with the Coulomb gauge [6]:

$$\mathbf{E}^n = -j\omega\mathbf{A}^n - \nabla V^n \quad 3. 32$$

According to the principle of Lorentz reciprocity in [7], the inductance measured by the sensor can be derived:

$$\Delta L = \frac{1}{j\omega I^2} \int_c \mathbf{E}_a \cdot \mathbf{E}_b \cdot (\sigma_a - \sigma_b) dv \quad 3. 33$$

Where, ΔL represents the variation of the inductance due to the substrate domain of a and b .

Reference

- [1]. C. V. Dodd, W. E. Deeds, J. W. Luquire and W. G. Spoeri, "Some Eddy-Current Problems and Their Integral Solutions", *Oak Ridge National Laboratory*, April 1969.
- [2]. W. Yin and K. Xu, "A Novel Triple-Coil Electromagnetic Sensor for Thickness Measurement Immune to Lift-Off Variations," *IEEE Transactions on Instrumentation and Measurement*, vol. 65, no. 1, pp. 164-169, Jan. 2016.
- [3] W. Yin and A. J Peyton, "Thickness measurement of non-magnetic plates using multi-frequency eddy current sensors," *NDT&E International*, vol. 40, pp. 43-48, 2007.
- [4]. Jianming Jin, "The Finite Element Method in Electromagnetics", IEEE Press, 2014.
- [5]. A. F. Peterson, S. L. Ray and R. Mittra, "Computational methods for

electromagnetics,” Piscataway, *IEEE Press*, 1997.

[6]. Z. Zeng, L. Udpa, S. S. Udpa and M. S. C. Chan, “Reduced magnetic vector potential formulation in the finite element analysis of eddy current nondestructive testing,” *IEEE Transactions on Magnetics*, vol. 45, no. 3, pp. 964-967, 2009.

[7]. C. Ktistis, D. W. Armitage and A. J. Peyton, “Calculation of the forward problem for absolute image reconstruction in MIT,” *Physiological measurement*, vol. 29, no. 6, pp. 455-464, 2008.

Chapter 4 Overview of papers

This chapter summarises the proposed methods in electromagnetic computation and the applications by using the proposed methods are presented.

For the analytical method of calculating impedance of metallic plates with finite planar dimension based on Dodd and Deeds plate model, the proposed method is introducing an initial point of the integral. The mathematical deviation demonstrates the deviation of the initial point for the integration. Both the simulation and experimental results agreed well. The thickness measurement can be carried out and the error of the reconstructed thickness is within 2%.

Moreover, in the permeability measurement for ferrous metallic plates, the lift-off of the sensor affects the prediction of the electromagnetic properties for the sample plates. The proposed method is to eliminate the deviation on the phase of the signal due to the lift-off and based on this compensation, the prediction of permeability is presented. From the results, it can be seen that the estimation error due to the lift-off is reduced.

For the acceleration of the finite element method, a novel method using perturbed matrix inversion method is presented. It applies to the eddy current calculation for crack detection. Numerical tests prove that the proposed method enhanced the computation speed compared with unaccelerated method. Further, it is found that the crack only causes a small perturbation in fields in the surrounding region. Based on this property, a novel crack calculation method is proposed. From the simulation results, it shows that the calculation is greatly shortened with the accelerated rate of 3-34 times which is related to the element number.

4.1 Analytical methods for eddy current testing

4.1.1 The modified analytical method for metallic plates with finite planar dimension

A. Theoretical derivations of the modified analytical solution - the initial integration point α_r

For the air-cored sensor probe, the impedance change due to the presence of an infinite metal plate can be calculated by the Dodd-Deeds model. However, in practical measurements, the sample cannot match with the condition required - 'infinite', thus the Dodd-Deeds model could not be applied to the disk with finite size and certainly not a co-axial hole in the center. Therefore, a modified analytical solution of inductance for the plate with finite dimensions is highly requisite.

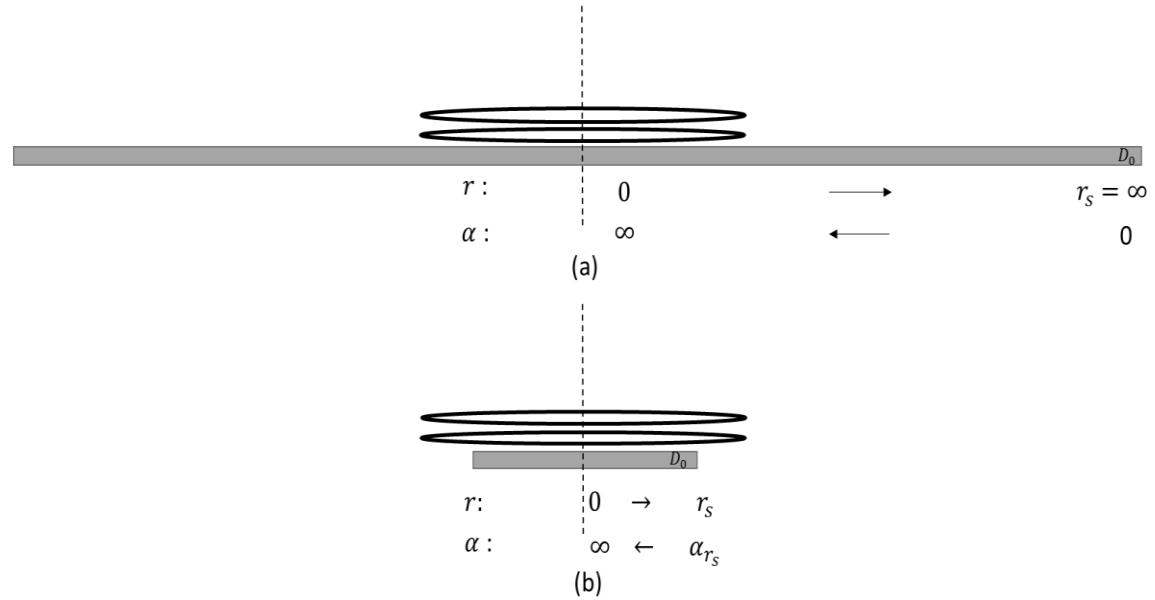


Figure 4.1 Illustration of the integrational path for the proposed method (a) An infinite plate where r ranges from 0 to ∞ (b) A finite plate where r ranges from 0 to r_s

As shown in Figure 4.1, in the Dodd Deeds model, the integration of α ranges from 0

to infinity, where $\alpha = 0$ corresponds to the plate section of the infinite radius ($r = r_s = \infty$) and $\alpha = \infty$ to the centre of the sample plate ($r = 0$). Therefore, in the proposed method, by replacing $\alpha = 0$ with $\alpha = \alpha_{r_s}$, the inductance for a plate with a finite radius can be simulated. The following mathematical manipulation is to explain the rationale behind changing the integration range of α .

By referring to the manipulation of the Dodd Deeds analytical formulations [1], the model of a coil above a plate can be divided into four regions, the magnetic vector potential formulation \mathbf{A} can be represented by a product of two polynomials, $R(r)$ and $Z(z)$.

$$\frac{\partial^2 A}{\partial r^2} + \frac{1}{r} \frac{\partial A}{\partial r} + \frac{\partial^2 A}{\partial z^2} - \frac{A}{r^2} + \omega^2 \mu_i \sigma_i A - j\omega \mu_i \sigma_i A = 0 \quad 4.1$$

$$r \in [0, r_s] \quad 4.2$$

Where, i denotes the i^{th} layer/region conductor.

In Equation 4. 2, the defined range of r for the infinite plate case is from 0 to $r_s = \infty$.

However, for a sample with finite radius, r ranges from 0 to a constant r_s .

Since the magnetic vector potential can be presented as,

$$\mathbf{A} = R(r)Z(z) \quad 4.3$$

By substituting Equation 4. 3 into Equation 4. 1, the field can be expressed as,

$$\frac{1}{R(r)} \frac{\partial^2 R(r)}{\partial r^2} + \frac{1}{rR(r)} \frac{\partial R(r)}{\partial r} + \frac{1}{Z(z)} \frac{\partial^2 Z(z)}{\partial z^2} - \frac{1}{r^2} + \omega^2 \mu_i \sigma_i - j\omega \mu_i \sigma_i = 0 \quad 4.4$$

Using the principle of separation of variables, a separation ‘constant’ α^2 is introduced [1], where α is related to the wave number of plane wave.

$$\frac{1}{Z(z)} \frac{\partial^2 Z(z)}{\partial z^2} = \alpha^2 - \omega^2 \mu_i \sigma_i + j\omega \mu_i \sigma_i \quad 4.5$$

Then substitute Equation 4. 5 into Equation 4. 4, which gives,

$$\alpha^2 = \frac{1}{r^2} - \frac{1}{rR(r)} \frac{\partial R(r)}{\partial r} - \frac{1}{R(r)} \frac{\partial^2 R(r)}{\partial r^2} \quad 4.6$$

According to Equation 4. 6, the solution of $R(r)$ can be expressed in terms of Bessel functions $J_1(\alpha r)$ and $Y_1(\alpha r)$, $R(r)$ can be represented as [1],

$$R(r) = C J_1(\alpha r) + D Y_1(\alpha r) \quad 4.7$$

Due to the divergence of Y_1 at the origin (it tends to infinity when r equals to 0), D should be 0 in all regions. C is a constant value obtained from the boundary conditions, which is related to the coil parameters and the electrical conductivity of the sample plate.

Combining Equations 4. 6 - 4. 7, then we can obtain α^2 ,

$$\begin{aligned} \alpha^2 &= \frac{1}{r^2} - \frac{1}{rC J_1(\alpha r)} \frac{\partial C J_1(\alpha r)}{\partial r} - \frac{1}{C J_1(\alpha r)} \frac{\partial^2 C J_1(\alpha r)}{\partial r^2} \\ &= \frac{1}{r^2} - \frac{\alpha}{r J_1(\alpha r)} \frac{J_0(\alpha r) - J_2(\alpha r)}{2} - \frac{\alpha^2}{J_1(\alpha r)} \frac{-3J_1(\alpha r) + J_3(\alpha r)}{4} \end{aligned} \quad 4.8$$

Where, J_0 , J_2 , and J_3 are the zero, second, and third order Bessel function of the first kind.

Therefore, α can be derived by finding the solution of Equation 4. 9,

$$\alpha^2 - \frac{1}{r^2} + \frac{\alpha}{4r J_1(\alpha r)} \left(2(J_0(\alpha r) - J_2(\alpha r)) - \alpha r(-3J_1(\alpha r) + J_3(\alpha r)) \right) = 0 \quad 4.9$$

By multiplying r^2 on both sides of Equation 4. 9,

$$(\alpha r)^2 - 1 + \frac{\alpha r}{4J_1(\alpha r)} \left(2(J_0(\alpha r) - J_2(\alpha r)) - \alpha r(-3J_1(\alpha r) + J_3(\alpha r)) \right) = 0 \quad 4.10$$

Substitute αr with x , then Equation 4. 10 is converted as,

$$(x)^2 - 1 + \frac{x}{4J_1(x)} \left(2(J_0(x) - J_2(x)) - x(-3J_1(x) + J_3(x)) \right) = 0 \quad 4.11$$

Assuming x_0 is the solution of the above equation, then the integral range of α is related to the defined variable r , which can be written as $\alpha = \frac{x_0}{r}$, i.e. α is inversely proportional to r . Taking the example of a plate with an infinite planar dimension, the defined range of r is from 0 to ∞ (referring to Equation 4. 1 and Equation 4. 2). By referring to Equation 4. 11, the corresponding range of α is from $\alpha|_{r=0} = \infty$ to $\alpha|_{r=\infty} = 0$. For a plate with a finite radius, r ranges from 0 to r_s , the corresponding range of α is from $\alpha|_{r=0} = \infty$ to a constant value $\alpha|_{r=r_s} = \alpha_{r_s} = \frac{x_0}{r_s} = \frac{3.518}{r_s}$. 3.518 is the first zero obtained from Equation 4. 11, it covers all the domain for different sample plate with finite dimension.

Therefore, for a finite size sample, the vector potential involves the integration from $\alpha|_{r=r_s} = \alpha_{r_s}$ to $\alpha|_{r=0} = \infty$.

$$A = \frac{I\mu_0 N_e}{2} \int_{\alpha_{r_s}}^{\infty} \frac{J_1(\alpha r) P(\alpha)}{\alpha^3} K(r, z, \alpha) \phi(\alpha) d\alpha \quad 4.12$$

Further, the inductance change due to the presence of the finite-size plate is,

$$\Delta L(\omega) = \frac{\pi N_v N_e \mu_0}{(l_{v1} - l_{v2})^2 (r_{v1} - r_{v2})^2} \int_{\alpha_{r_s}}^{\infty} \frac{P^2(\alpha)}{\alpha^6} G(\alpha) \phi(\alpha) d\alpha \quad 4.13$$

$$\text{with } \alpha_{r_s} = \frac{3.518}{r_s}$$

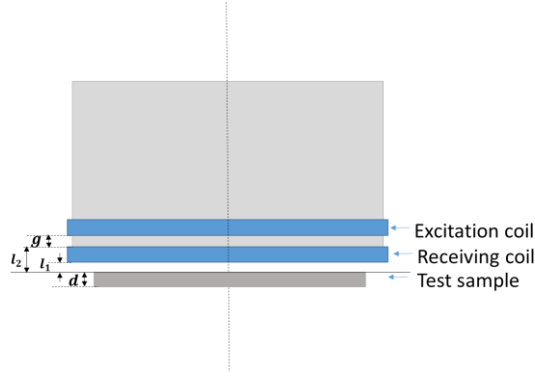
Where: r_s is the radius of the sample.

It can be seen that the integral limit of Equation 4. 13 is different to the case of the

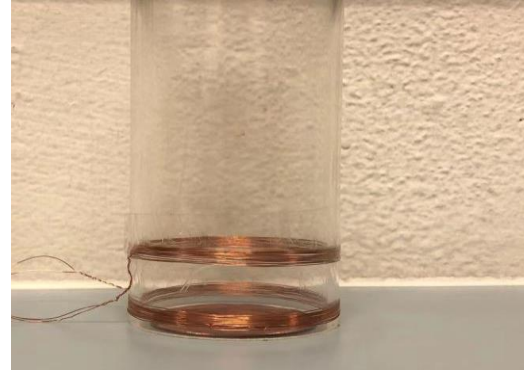
infinite-size plate in Equation 3.9. For the finite sample plate, the new formulation integrates all the contributions of plane wave that is interactive with the sample (by integrating over the effective region of α , where α is related to the wave number of plane wave). The assumption is that the proposed formulation currently works for non-magnetic thin sample plates.

B. Experimental and simulation setup

Both the experimental measurements (by using the impedance analyser) and the simulations (by using the modified analytical solution and the software (COMSOL)) have been carried out to validate the theoretical deviations. In the process of the measurements, the air-cored co-axial sensor was located co-axially with circular planar samples, as shown in Figure 4.2. The parameters are listed in Table 4.1. Samples of copper and aluminium plates were selected because of availability. The conductivities of these two materials are 57 MS/m, and 35 MS/m. The copper plate has a thickness of 1 mm and range of diameters (from 25 mm to 45 mm in steps of 5 mm), while the aluminium plate has a diameter of 40 mm and thickness range from 22 μm to 132 μm . The copper plates were used to verify the derived theory while the aluminium plates with different thicknesses were used for the further application of the thickness measurement. The impedance analyser can operate from 100 Hz to 510 kHz in a logarithmic step of 0.02735 with high precision and the excitation voltage in the measurement was set to 0.3 V. To test the effect of different sensor geometries, three sensors of the different radii (28 mm, 40 mm, and 52 mm) have been used.

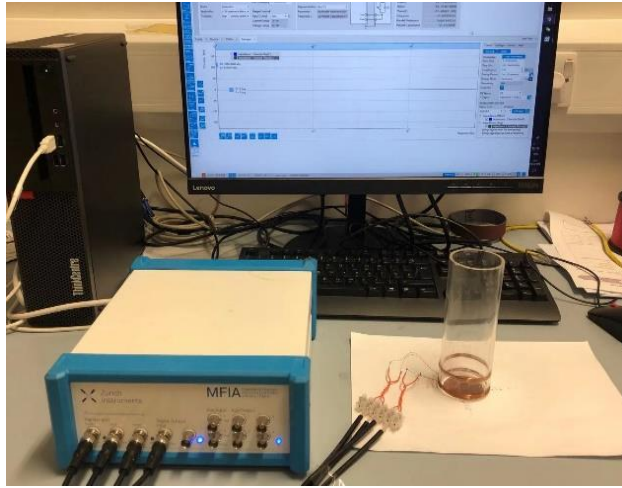


(a)

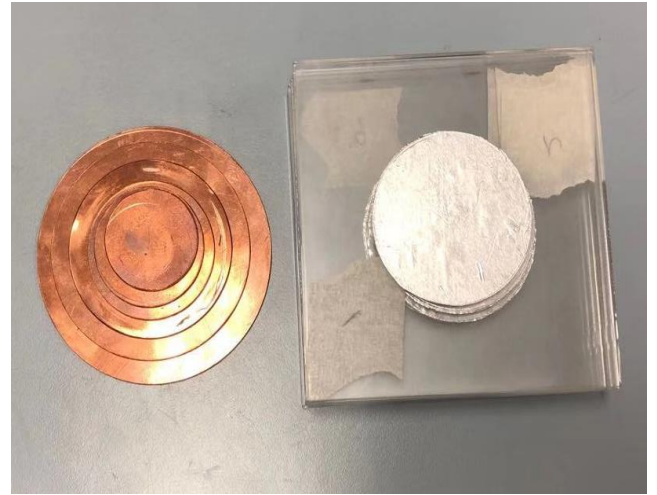


(b)

Figure 4.2 Air-cored sensor above the tested plate(a) schematic setup (b) actual setup



(a)



(b)

Figure 4.3 Experimental setup (a) measurement setup (b) circular sample plates

From Figure 4.6 to Figure 4.10, the mutual impedance (ΔZ) between the excitation coil and the receiving coil measured via the Zurich impedance analyser (Figure 4.3 (a)) are presented. Due to the phase difference between the induced voltage and the excitation current, the tested impedance should be complex. Therefore, the inductance can be presented by dividing the mutual impedance by the excitation frequency in the experimental measurements, as shown in Equation 4. 14 - Equation 4. 16.

$$\Delta Z = R + j\omega\Delta L \quad 4. 14$$

$$\Delta L = \operatorname{Re}\left(\frac{Z_{\text{sample}} - Z_{\text{air}}}{j\omega}\right) \quad 4.15$$

$$-R\omega^{-1} = \operatorname{Im}\left(\frac{Z_{\text{sample}} - Z_{\text{air}}}{j\omega}\right) \quad 4.16$$

Where: Z_{sample} denotes the impedance caused by the metallic sample plate and Z_{air} denotes the impedance in the air.

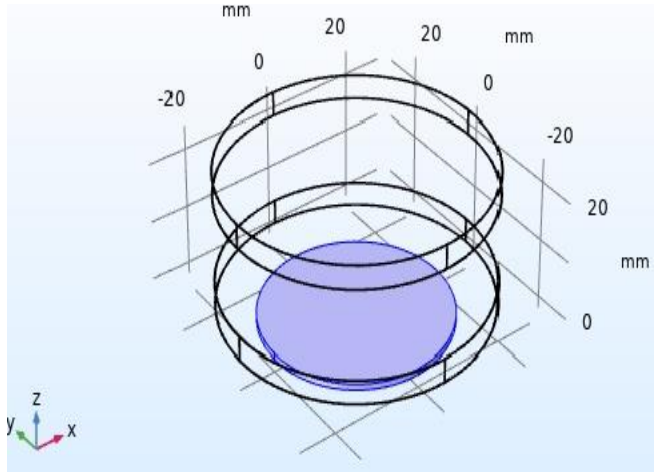
Table 4.1 Sensor Parameters

Inner and outer radii of the excitation coil (r_{e1} / r_{e2})	28 mm/28.25 mm 40 mm/40.25 mm 52 mm/52.25 mm
Inner and outer radii of the sensing coil (r_{v1} / r_{v2})	28 mm/28.25 mm 40 mm/40.25 mm 52 mm/52.25 mm
Height of the excitation coil ($l_{e2} - l_{e1}$)	4 mm
Height of the sensing coil ($l_{v2} - l_{v1}$)	4 mm
Turns of excitation coil and receiving coil (N_e / N_v)	15/15
Plate thickness (D_0)	1 mm for copper, 22 μm – 132 μm for aluminium
The gap between two coils (g)	15 mm

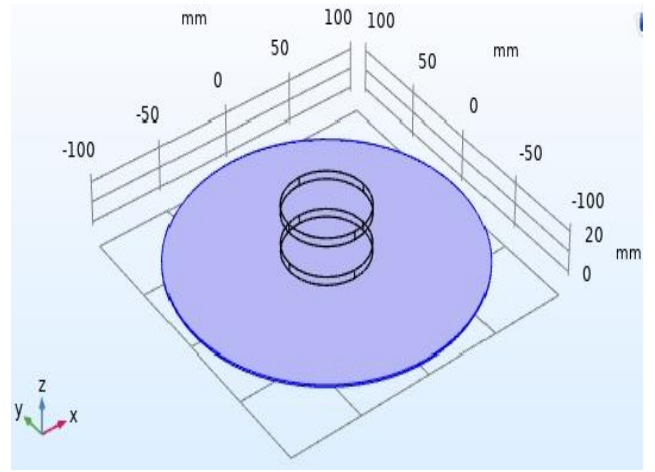
C. Results

C.1 Validation of the modified analytical solution

As illustrated in Figure 4.1, compared with the infinite planar plate, the main difference for the finite region analytical solution is that it starts at different points for the integral path. Firstly, both the analytical solution and the simulation software (COMSOL) were compared to validate the proposed method. The simulated models are shown in Figure 4.4. Figure 4.5 shows the inductance change caused by the copper plate.

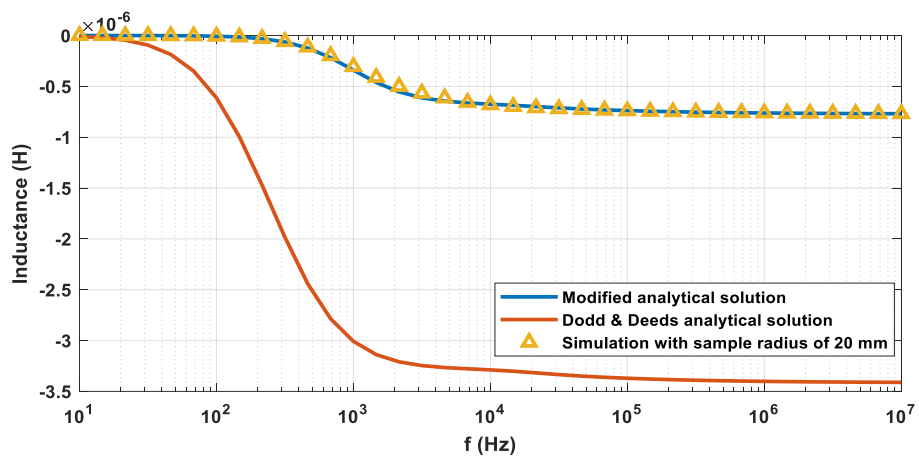


(a)

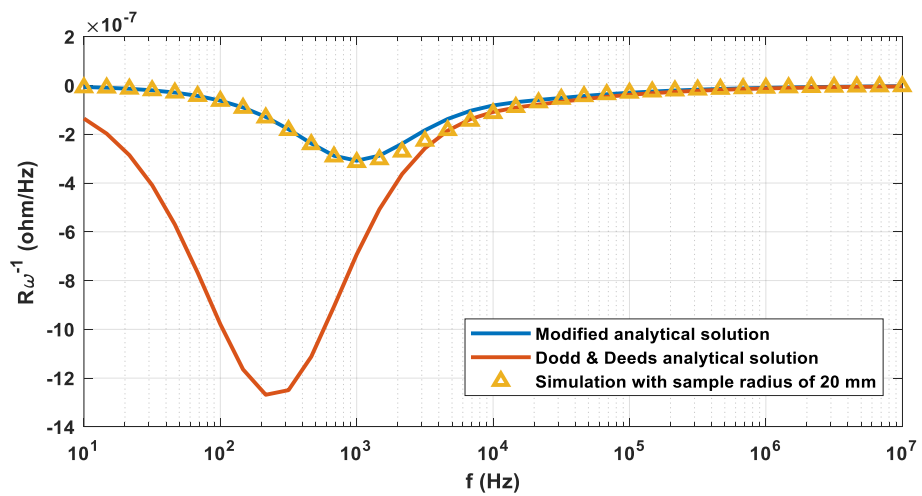


(b)

Figure 4.4 The simulated model (a) the plate with a radius of 20 mm (84 k elements) (b) the plate with a radius of 100 mm (142 k elements)



(a)



(b)

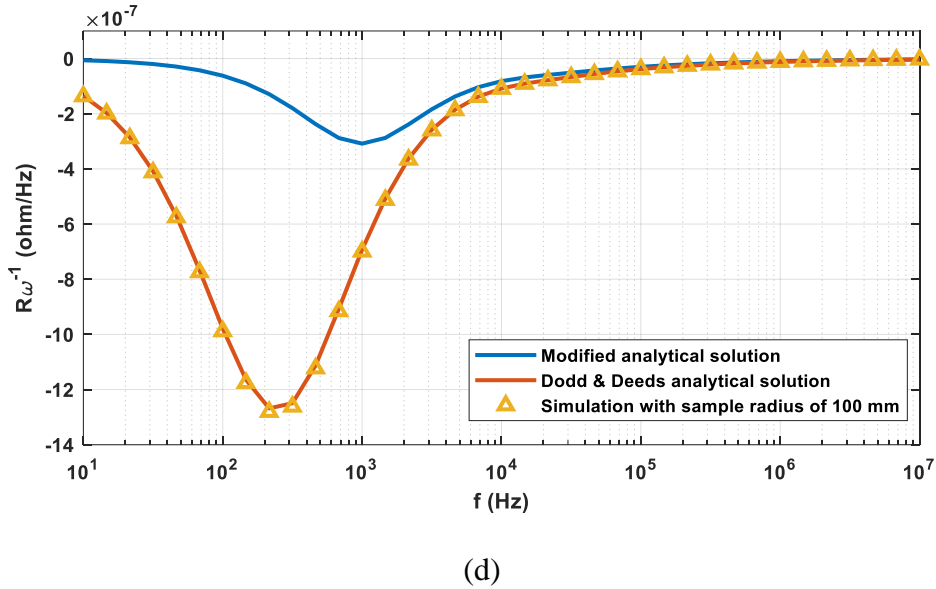
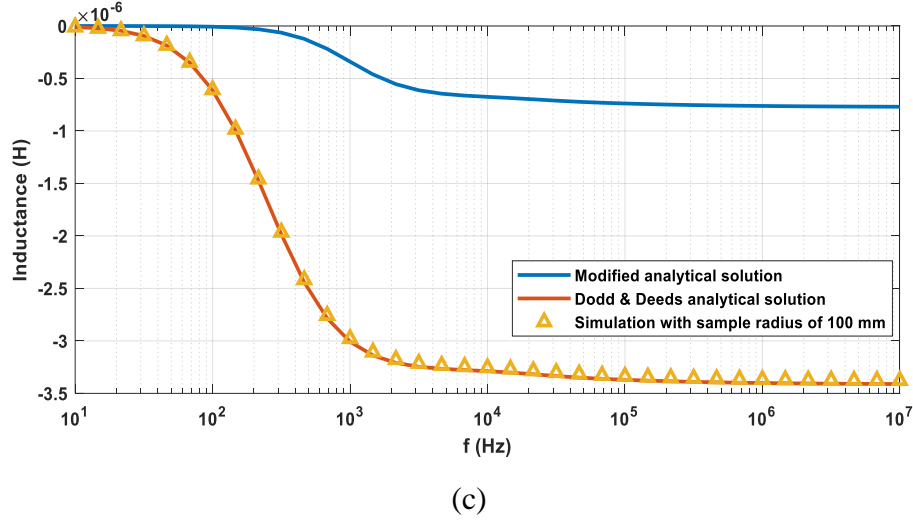


Figure 4.5 (a)The inductance change caused by copper plates with sample radius of 20 mm (b) The change of $R\omega^{-1}$ caused by copper plates with sample radius of 20 mm (c)The inductance change caused by copper plates with sample radius of 100 mm (d) The change of $R\omega^{-1}$ caused by copper plates with sample radius of 100 mm

Figure 4.5 shows the inductance change caused by the copper plate. It can be observed that, for both metallic plates, the results are matched under the sweeping frequency ranging from 10 Hz to 10 MHz. Since the test samples are non-magnetic, there is no zero-crossing point for the inductance change. As the frequency increases, it would finally reach a saturated value for the inductance change and approach zero for the detected resistance-frequency combined term $R\omega^{-1}$. A peak frequency feature can be

observed from $R\omega^{-1}$, which is found to be shifted rightwards as the size of the sample decreases. This is possibly because the magnetic flux interacts less with the plate for the sample with a smaller radius.

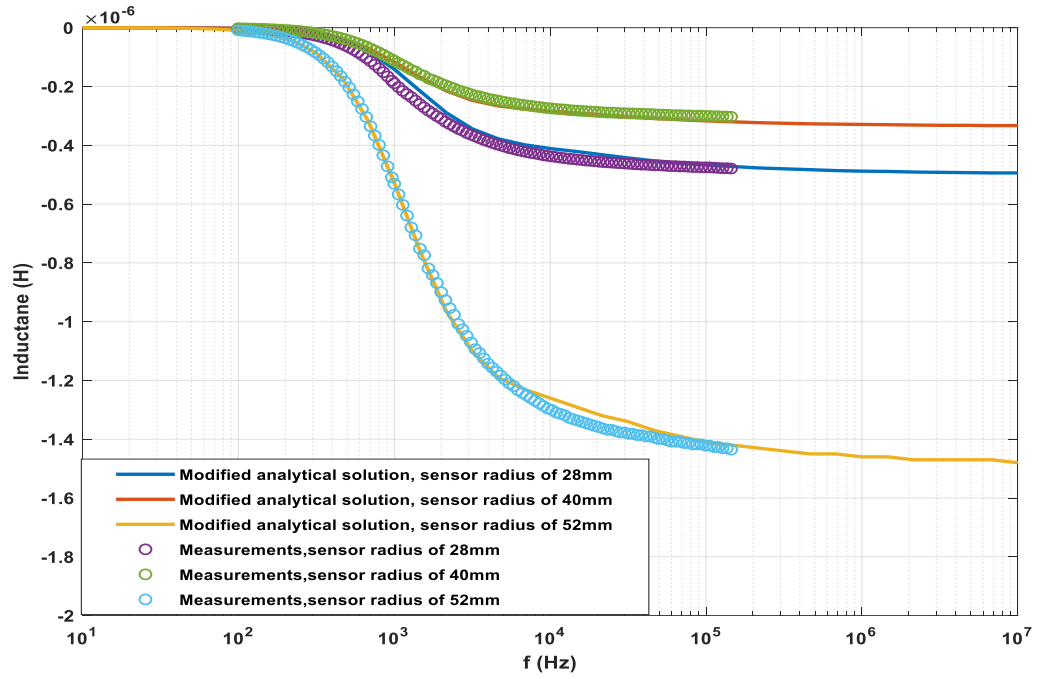
C.2 Effect of the sensor coil dimensions

The modified analytical solution is associated with the initial point of α . Hence, some measurements have been carried out to determine the value of α_r . Figure 4.6 and Figure 4.7 depict the inductance change of both measured results and modified analytical solutions under the same three sensors with the radii of 28 mm, 40 mm, and 52 mm respectively, but different sample radii.

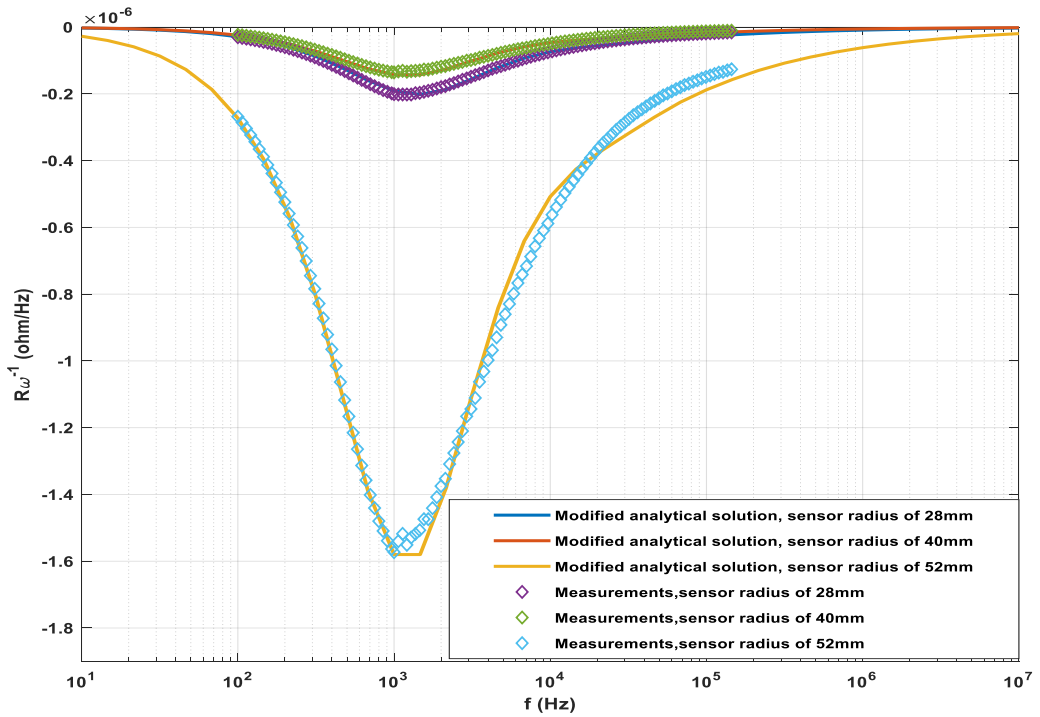
From the results of both simulations and measurements, the value of the initial point α_{r_s} is immune to the sensor size. That is, for a fixed-size test sample, no matter what size of the sensor, α_{r_s} remains unchanged (since α_{r_s} is merely related to the size of the sample, referring to Equation 4. 10). Besides, the value of α_{r_s} reduces with the increase of the sample radius, which is consistent with the theoretical derivations.

C.3 Effect of the sample size

From previous experiments, it can be noticed that α_{r_s} is not related to the size of the sensor. Further, samples with different radii were measured under the same sensor with the sensor radius of 40 mm. Figure 4.8 shows the results of both modified analytical solutions and measurements for copper plates with different radii. The results are matched by finding the appropriate α_{r_s} . The value of α_{r_s} under different sample radii is shown in Figure 4.9.

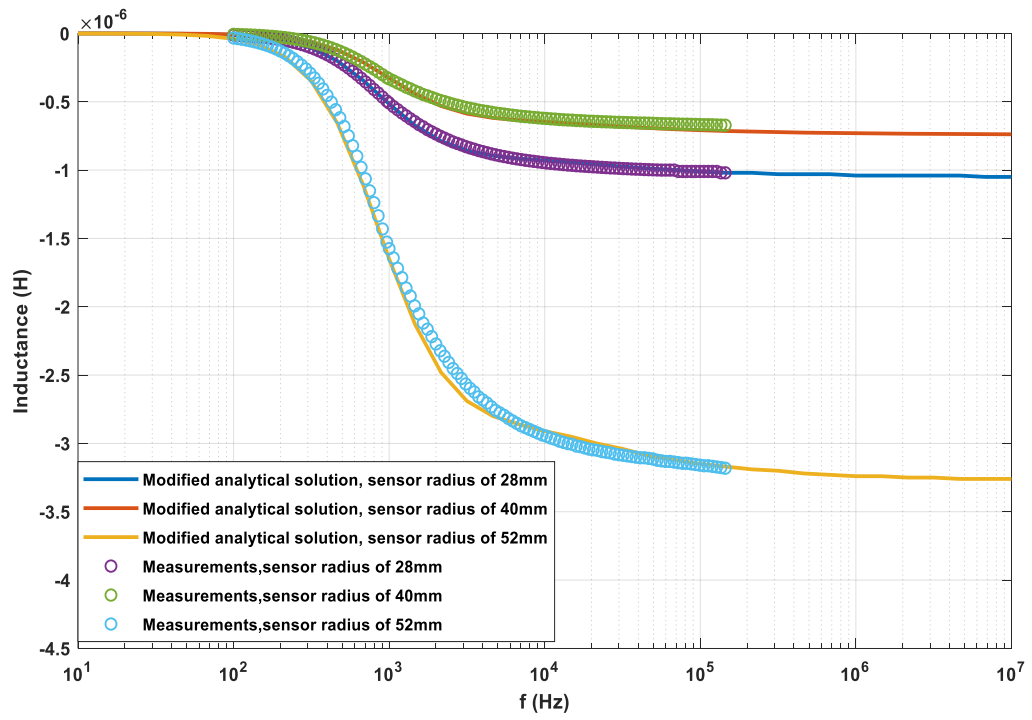


(a)

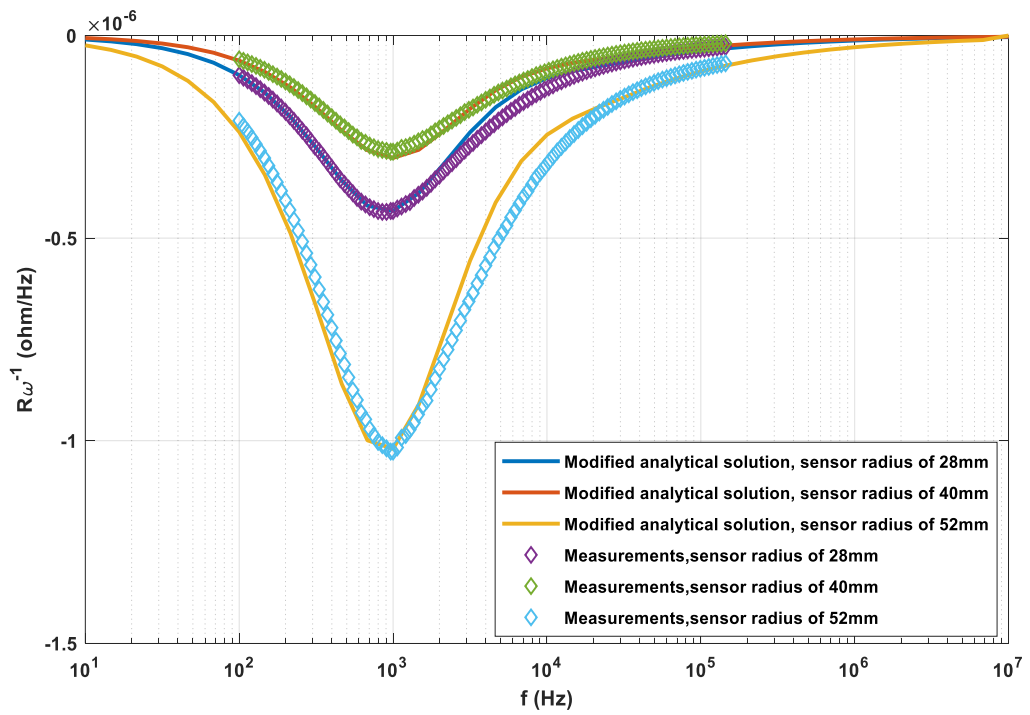


(b)

Figure 4.6 (a) The inductance change caused by copper plates with the radius of 17.5 mm (b) $R\omega^{-1}$ caused by copper plates with the radius of 17.5 mm

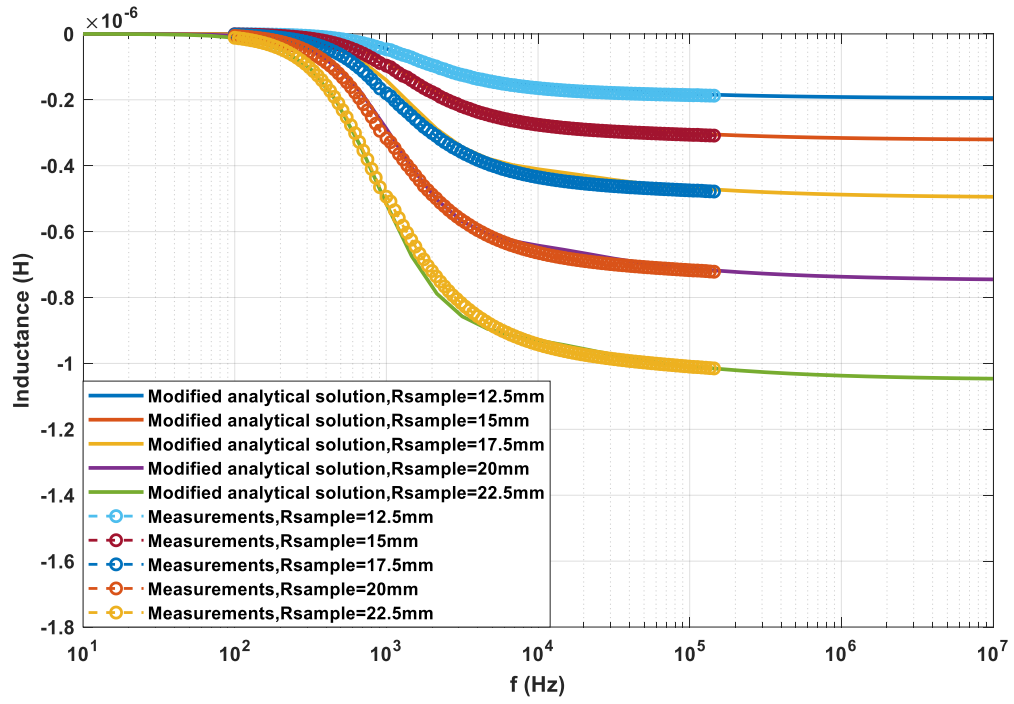


(a)

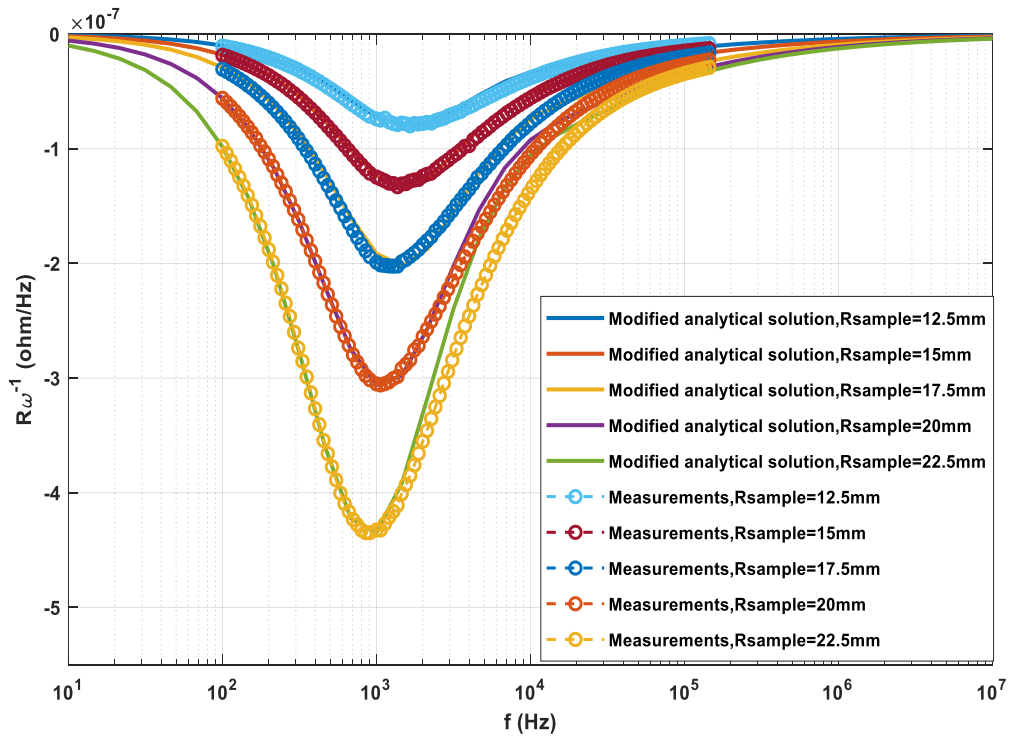


(b)

Figure 4.7 (a) The inductance change caused by copper plates with the radius of 22.5 mm (b) The change of $R\omega^{-1}$ caused by copper plates with the radius of 22.5 mm



(a)



(b)

Figure 4.8 (a) The inductance changes under various radius of the copper samples (b) The change of

$R\omega^{-1}$ under various radius of the copper samples

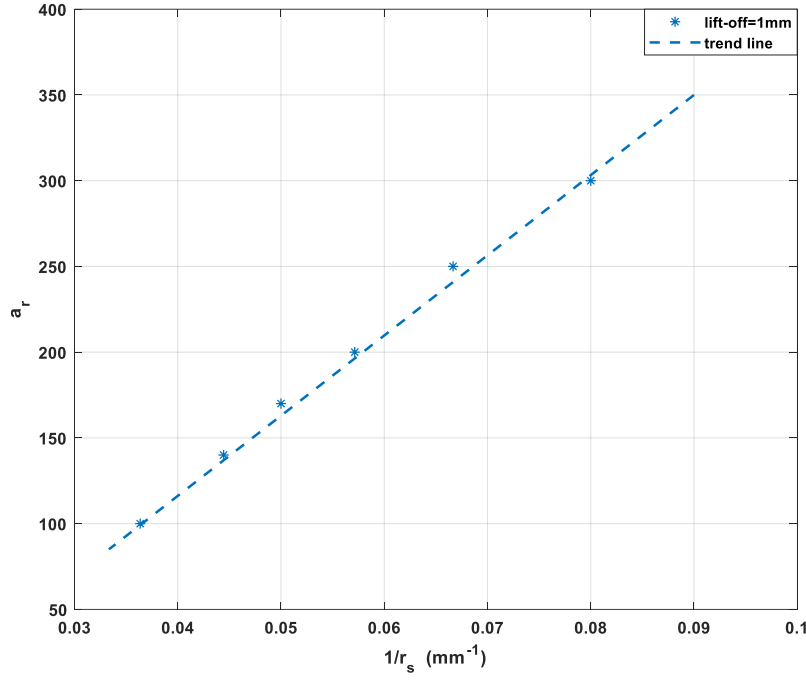


Figure 4.9 Relationship between α_{r_s} and the reciprocal of sample radius

As can be seen from Figure 4.9, the value of α_{r_s} is proportional to the reciprocal of the sample radius (i.e. $\alpha_{r_s} = \text{const.} \times \frac{1}{r_s}$) and, from the experimental experience, the constant is ~ 3.518 .

D. Thickness measurement based on the modified analytical solution

The proposed method can be used to test the thickness of plate samples with the same radius. Since α_{r_s} is immune to the sensor radius but related to the sample radius, it can be set to an appropriate fixed value. In our previous studies, the peak frequency caused from $R\omega^{-1}$ is associated with the sample thickness and the sample conductivity. Applying this principle with the same material samples used in the testing, the larger the thickness, the lower the peak frequency. Consequently, the thickness of the test samples can be estimated by matching the peak frequency of the modified analytical solution (Prior to the measurement, a look-up table is obtained from the modified analytical solution which contains the peak frequency information for different

thicknesses under the same conductivity. By referring to the table, the thickness of the sample can be predicted.).

In the measurements, the thickness of the aluminium sample varies from 22 μm to 132 μm . The operation frequency ranges from 1 kHz to 505 kHz. As Figure 4.10 depicts, the result of the modified analytical solution matches well with the measurement. Besides, the peak frequency by utilising both original analytical solution and modified analytical solution is listed in Table 4.2. It can be seen that there is a huge difference for finite planar dimension samples compared with original analytical solution. Moreover, the principle of the thickness reconstruction is fitting the peak frequency of the simulation to that of the measurement, therefore, it leads to a larger error for thickness prediction as shown in Table 4.2 and Figure 4.11. The fitting of peak frequency feature is one of commonly used methods for sample properties reconstruction [2-5]. As in our previous papers [5], we use a first order function to approximate the curve and fit the experimental and simulated curves in a least squared sense. Once the first order system is obtained, its peak frequency can be obtained easily. Table 4.3 illustrates the estimated thickness from the modified analytical solution and the error between the actual and estimated thickness. The thickness reconstruction for the sample plate is finding the simulated peak frequency of the multi-frequency inductance curve (via Equation 4. 13) that is closest to the measured peak frequency while changing the thickness. It can be seen from Table 4.3, the error from the testing can be achieved within 2%. Figure 4.11 demonstrates the estimation results from both methods and the error caused by using the infinite model – the original Dodd Deeds is significantly inaccurate.

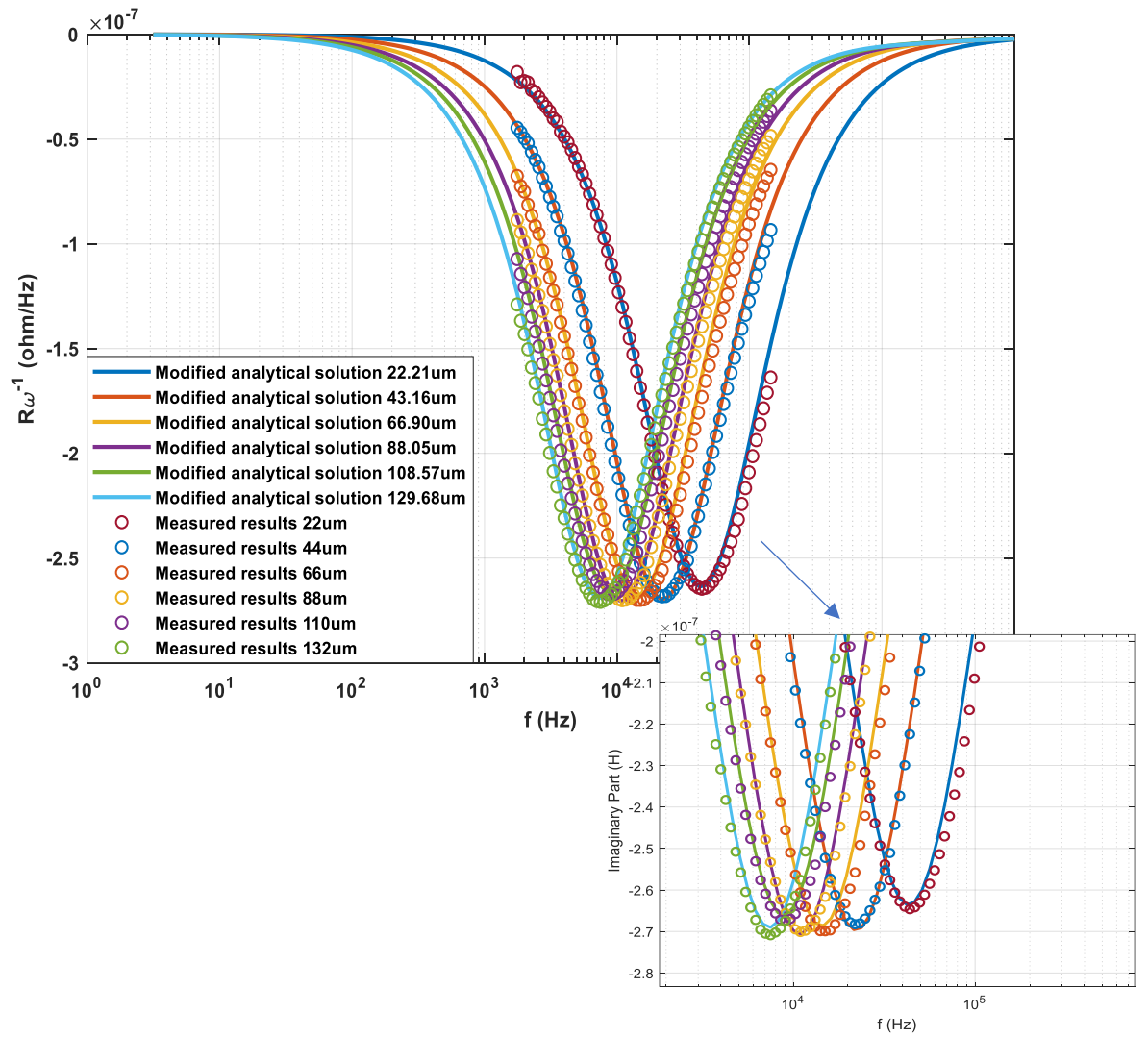


Figure 4.10 The change of $R\omega^{-1}$ under varying thickness samples

Table 4.2 Peak frequency of Dodd Deeds analytical solution and modified analytical solution for the aluminium plates

Sample thickness (μm)	Peak frequency (kHz)	
	Dodd Deeds analytical solution	Modified analytical solution
22	13.335	42.170
44	6.190	23.714
66	4.217	14.678
88	3.162	11.007
110	2.610	9.085
132	1.957	7.499

Table 4.3 Actual and estimated thickness for the aluminium plates using peak frequency feature

Material	Actual thickness (μm)	Estimated thickness (μm)	Error (%)
Aluminium	22	22.21	0.95
	44	43.16	-1.91
	66	66.90	1.36
	88	88.05	0.06
	110	108.57	-1.30
	132	129.68	-1.76

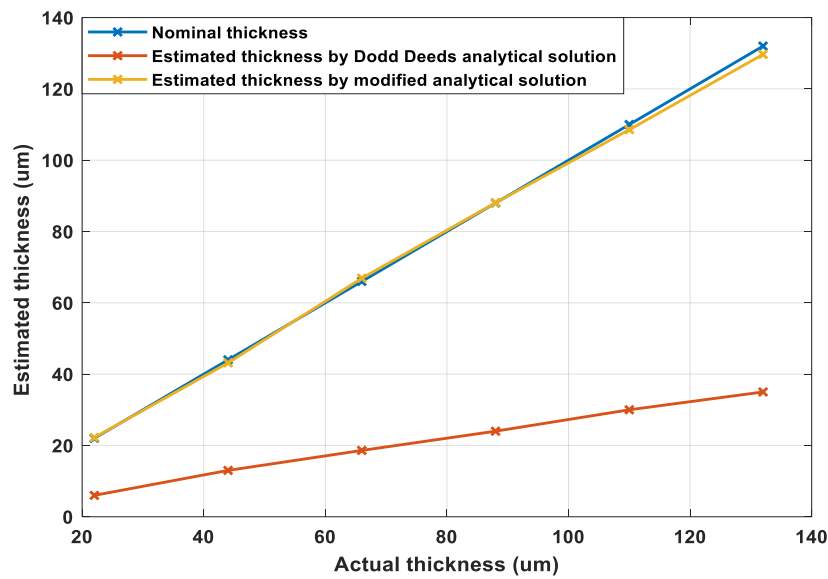


Figure 4.11 Estimated thickness by Dodd Deeds analytical solution and modified analytical solution

4.1.2 A novel lift-off compensation technique on phase signature

A. EM sensor setup

As can be seen from Figure 4.12 and Table 4.4, considering sensors accessibility for experiments and analytical simulations, EM sensor was designed to be 2 co-axially coupled air-cored loop coils: excitation coils and pick-up coils with identical size turns and materials (copper coil). In Table 4.4, a series of lift-off spacers are used to test the

lift-off influences on the impedance phase.

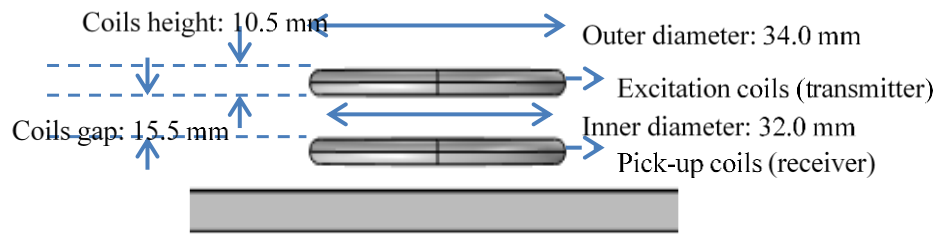


Figure 4.12 EM Sensor

Table 4.4 Probes properties

	Values
$2r_1$ (Inner diameter)/mm	32.0
$2r_2$ (Outer diameter)/mm	34.0
l_o (lift-offs)/mm	0.8, 2.3, 3.8
h (coils height)/mm	10.5
g (coils gap)/mm	15.5
Number of turns $N_1 = N_2$ (N_1 - Transmitter; N_2 - Receiver)	30

B. Method

For the coil above the magnetic material, there has a zero-crossing point in the real part of the inductance change and the corresponding frequency is termed as the zero-crossing frequency. For the magnetic sample plate, the magnetic field generated by the excitation coil interacts with the magnetic plate in two ways. Initially, the magnetic plate is magnetised due to the primary magnetic field. This process increases the inductance in the system so that the real part of the inductance change starts from a positive value. Besides, it also induces the eddy current in the plate which reduces the inductance change in the system. In low frequencies, the magnetization process dominants while in high frequencies, the eddy current effect dominants. Therefore, there is a zero-crossing point and the corresponded frequency (zero-crossing frequency)

can be obtained. From our previous researches [6]-[8], the magnitude of the detected response impedance and zero-crossing frequency were found to grow with reduced sensor lift-offs. It is also observed that the impedance phase rises up slightly with reduced lift-offs. Consequently, it is speculated that a novel approach could be deduced for compensating the impedance phase error due to sensor lift-offs with the signal amplitude and zero-crossing frequency. The derivations process for compensating the zero-crossing frequency ω_0 was carried out in [9]. Procedure of the proposed algorithm for impedance phase compensation is summarized in Figure 4.13.

For the previous work, the compensated zero-crossing frequency is $\omega_0 = \pi^2 \omega_1 / (\pi^2 + 4 \ln (\Delta L_0 / \Delta L_m))$. Where, ω_0 denotes the zero-crossing frequency after compensation; ω_1 is zero-crossing frequency under current unknown lift-off; ΔL_0 is the inductance amplitude under the high-frequency (when the response signal barely changes with frequencies) with unknown lift-offs; ΔL_m is the inductance amplitude under same frequencies with the smallest lift-off.

In Figure 4.13, l_0 denotes the unknown lift-off; θ_r denotes the measured phase angle under any frequency ω and an unknown lift-off; $\Delta\theta$ denotes the impedance phase angle change caused by the unknown lift-off, which should be compensated. θ denotes impedance phase angle (i.e. $\theta = \theta_r - \Delta\theta$) after compensation.

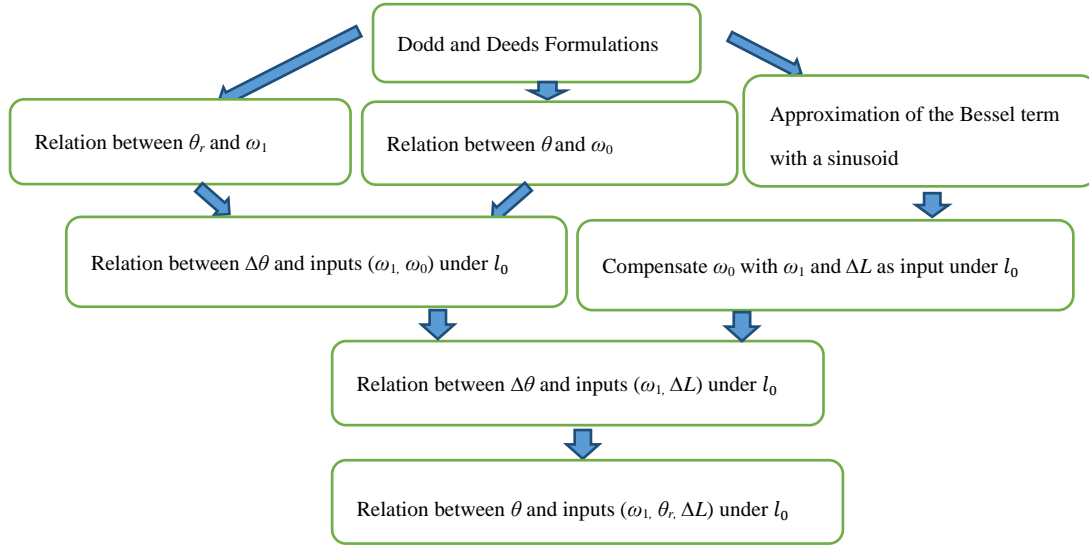


Figure 4.13 The procedure of impedance phase compensating deduction

Considering a magnetic steel sample, at low excitation frequency (100 Hz), the eddy current is restrained around the surface of the sample. Due to the eddy current skin effect, the magnetic sample can be regarded as a conductive half-space [7], therefore, the phase related term (Equation 3. 2) can be expressed as,

$$\varphi(\alpha_0) = \frac{\mu_r \alpha_0 - \sqrt{\alpha_0^2 + j\omega\sigma\mu_r\mu_0}}{\mu_r \alpha_0 + \sqrt{\alpha_0^2 + j\omega\sigma\mu_r\mu_0}} \quad 4.17$$

$$\varphi(\alpha_{0r}) = \frac{\mu_r \alpha_{0r} - \sqrt{\alpha_{0r}^2 + j\omega\sigma\mu_r\mu_0}}{\mu_r \alpha_{0r} + \sqrt{\alpha_{0r}^2 + j\omega\sigma\mu_r\mu_0}} \quad 4.18$$

For the metallic plates with $u_r \gg 1$ (ferrous plates), the compensated phase related term $\varphi(\alpha_0)$ and measured phase related term $\varphi(\alpha_{0r})$ under unknown lift-off equal,

$$\varphi(\alpha_0) = \frac{1 - \sqrt{1/\mu_r^2 + j\omega\sigma\mu_0/\mu_r\alpha_0^2}}{1 + \sqrt{1/\mu_r^2 + j\omega\sigma\mu_0/\mu_r\alpha_0^2}} \quad 4.19$$

$$\varphi(\alpha_{0r}) = \frac{1 - \sqrt{1/\mu_r^2 + j\omega\sigma\mu_0/\mu_r\alpha_{0r}^2}}{1 + \sqrt{1/\mu_r^2 + j\omega\sigma\mu_0/\mu_r\alpha_{0r}^2}} \quad 4.20$$

Here, α_0 is a spatial frequency indicating the geometry feature of the sensor.

Neglecting $1/\mu_r^2$ term in above equation and assigning $\omega_0 = \mu_r \alpha_0^2 / \mu_0 \sigma$, $\omega_1 = \mu_r \alpha_{0r}^2 / \mu_0 \sigma$. The compensated and measured phase related term under unknown lift-off can be expressed as followings,

$$\varphi(\alpha_0) = \frac{1 - \sqrt{j\omega/\omega_0}}{1 + \sqrt{j\omega/\omega_0}} = \frac{1 - \frac{\sqrt{2\omega/\omega_0}}{2}(1+j)}{1 + \frac{\sqrt{2\omega/\omega_0}}{2}(1+j)} \quad 4.21$$

$$\varphi(\alpha_{0r}) = \frac{1 - \sqrt{j\omega/\omega_1}}{1 + \sqrt{j\omega/\omega_1}} = \frac{1 - \frac{\sqrt{2\omega/\omega_1}}{2}(1+j)}{1 + \frac{\sqrt{2\omega/\omega_1}}{2}(1+j)} \quad 4.22$$

Then, the measured phase angle under unknown lift-off should be,

$$\theta_r = \tan^{-1} \left(\frac{\text{Im}(Z_r)}{\text{Re}(Z_r)} \right) = \tan^{-1} \left(\frac{\text{Im}(\varphi(\alpha_{0r}))}{\text{Re}(\varphi(\alpha_{0r}))} \right) = \tan^{-1} \left(\frac{\frac{\sqrt{2\omega_1}}{\omega}}{1 - \frac{\omega_1}{\omega}} \right) \quad 4.23$$

Similarly, the compensated phase angle can be derived from ω_0 ,

$$\theta = \tan^{-1} \left(\frac{\sqrt{2\omega_0/\omega}}{1 - \omega_0/\omega} \right) \quad 4.24$$

Therefore, the phase change angle caused by the lift-off should be,

$$\Delta\theta = \theta_r - \theta = \tan^{-1} \left(\frac{\sqrt{2\omega_1/\omega}}{1 - \omega_1/\omega} \right) - \tan^{-1} \left(\frac{\sqrt{2\omega_0/\omega}}{1 - \omega_0/\omega} \right) \quad 4.25$$

Then, the compensated phase angle should be,

$$\theta = \theta_r - \Delta\theta = \theta_r - \tan^{-1} \left(\frac{\sqrt{2\omega_1/\omega}}{1 - \omega_1/\omega} \right) + \tan^{-1} \left(\frac{\sqrt{2\omega_0/\omega}}{1 - \omega_0/\omega} \right) \quad 4.26$$

As shown in the appendix, the relation between ω_0 and ω_1 is $\omega_0 = \pi^2 \omega_1 / (\pi^2 + 4 \ln(\Delta L_0 / \Delta L_m))$. And the mathematic derivation details of this compensated zero-crossing frequency are shown at the end of the paper.

Finally, the impedance phase angle after compensation is evaluated from ω_1 , ΔL_0 , and ΔL_m .

$$\begin{aligned} \theta = \theta_r - \Delta\theta = \theta_r - \tan^{-1}\left(\frac{\sqrt{2\omega_1/\omega}}{1 - \omega_1/\omega}\right) \\ + \tan^{-1}\left(\frac{\sqrt{2\omega_1/\left(1 + \frac{4}{\pi^2} \ln\left(\frac{\Delta L_0}{\Delta L_m}\right)\right)\omega}}{1 - \omega_1/\left(1 + \frac{4}{\pi^2} \ln\left(\frac{\Delta L_0}{\Delta L_m}\right)\right)\omega}\right) \end{aligned} \quad 4.27$$

Assigning $G(\omega) = \tan^{-1}(\sqrt{2\omega_1/\omega}/(1 - \omega_1/\omega))$, through some mathematic manipulations, the compensated phase angle can be obtained.

$$\theta = \theta_r - \Delta\theta = \theta_r - G(\omega) + G\left(\left(1 + \frac{4}{\pi^2} \ln\left(\frac{\Delta L_0}{\Delta L_m}\right)\right)\omega\right) \quad 4.28$$

With

$$G(\omega) = \tan^{-1}\left(\frac{\sqrt{2\omega_1/\omega}}{1 - \omega_1/\omega}\right) \quad 4.29$$

Where, ΔL_0 is the inductance amplitude under the high -frequency (when the response signal barely changes with frequencies) with unknown lift-offs; while ΔL_m is obtained from Equation 4. 44 by utilising the inductance amplitude under same frequencies with the smallest lift-off (here this lift-off in measurement setup is 0.8 mm).

It can be seen in Equation 4. 29 that with the measured phase, inductance magnitude and zero-crossing frequencies from the measurements at an unknown lift-off as inputs, impedance phase angles θ after compensating (phase with zero lift-offs) could be obtained using the compensation scheme proposed above. For instance, if the sensor is put on a lift-off approaching 0, $\ln(\Delta L_0/\Delta L_m)$ should equal 0. As a result, the corresponding compensated result θ_0 calculated from Equation 4. 28 equals θ_r , which is reasonable under a negligible lift-off.

C. Analytical solutions and measurements

C.1 Analytical solutions

For the analytical solutions, Dodd Deeds approach was utilized to compute the sensor's detected response signal - impedance. The sample was chosen to be a duplex-phase specimen - DP600 (specimen's properties and size data are shown in Table 4.5 Properties of Duplex-phase specimens) under varying lift-offs of 0.8 mm, 2.3 mm, and 3.8mm. The analytical solver is scripted and operated on MATLAB coding platform, which is utilized for the evaluation of inductance ΔL (Equation 4. 30 – Equation 4. 35 in the appendix) and the compensated phase using Equation 4. 29.

C.2 Measurements

In order to measure the impedance/inductance phase of the samples, a symmetric air-cored electromagnetic sensor was designed for steel micro-structure monitoring in the Continuous Annealing & Processing Line (CAPL). As can be seen from Figure 4.14, the excitation coil sits in the middle and two receive coils at bottom and top respectively. Receiver coil 2 is used as the test coils; receiver coil 1 is served as a reference coil. In the paper, only the signal of receiver coil 2 is recorded and served as the response output signal. All the coils have the same diameters, i.e. an inner diameter of 32.0 mm and an outer diameter of 34.0 mm. Each of the coils has 30 turns, and the coil separation is 35.0 mm. SI 1260 impedance analyser has been utilized to measure the air-cored sensor induced signal response – mutual impedance or inductance of the sensor influenced by the tested samples. The working frequency range of the instrument is set from 310 Hz to 3 MHz. Moreover, all the samples are tested under a series of lift-offs of 0.8, 2.3, and 3.8 mm.

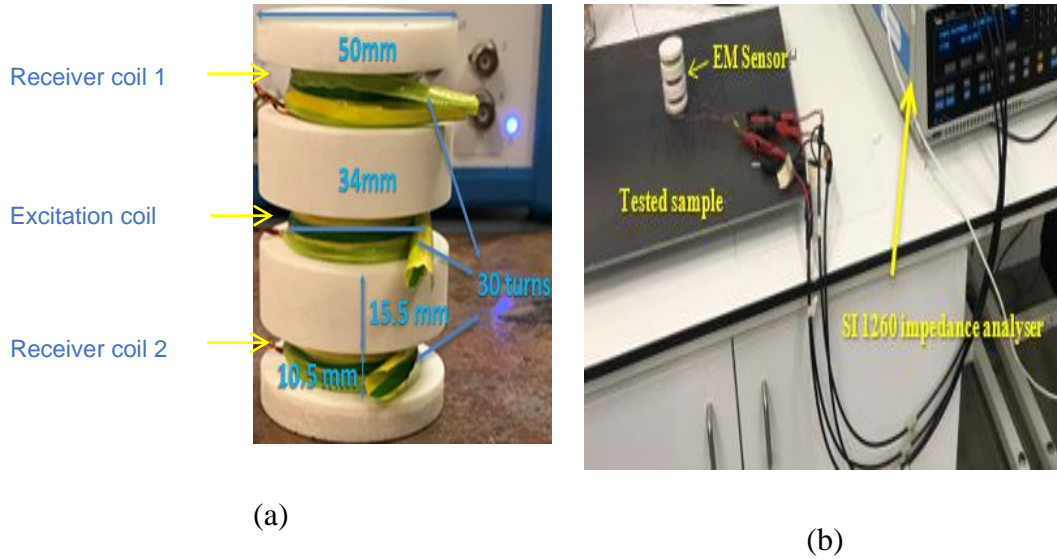
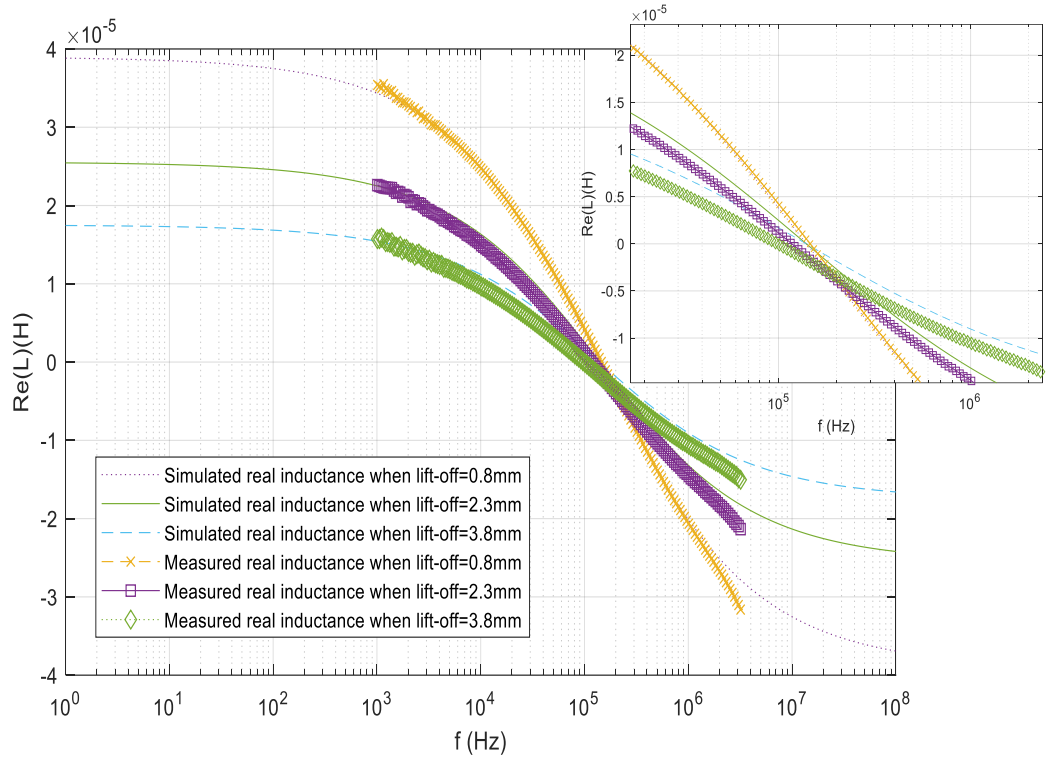


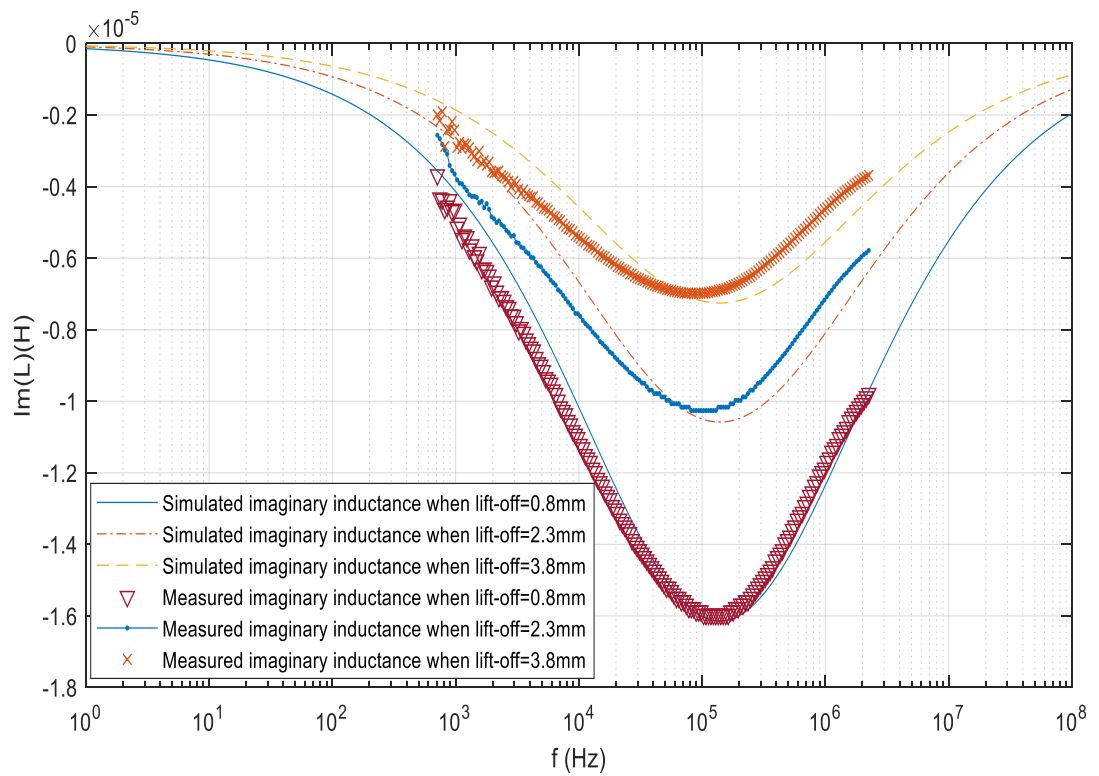
Figure 4.14 Measurement setup a) EM air-cored Sensor configuration b) SI 1260 impedance analyser

C.3 Results

Figure 4.15 exhibits both the real part and imaginary part of the simulations and measurements of sensor-plates system mutual inductance multi-frequency spectra. In Figure 4.15, it is obviously that inductance curves magnitude drops off with increased lift-offs. Meanwhile, the zero-crossing frequency decreases with increased lift-offs. Some singular points may be encountered during the measurements which are due to the signal noise of SI 1260 impedance analyser, especially under the low frequency. Besides, it can be noticed that there is a discrepancy under high frequencies in the real part of the inductance change. This is mainly due to the capacitive effect between the two coils and the tested specimen. It could lead to resonance effect and skew the measurement results in particular in high frequencies.



(a)



(b)

Figure 4.15 Real and imaginary part of inductance under varying lift-offs - 0.8 mm, 2.3 mm, and

3.8mm (a) real part (b) imaginary part

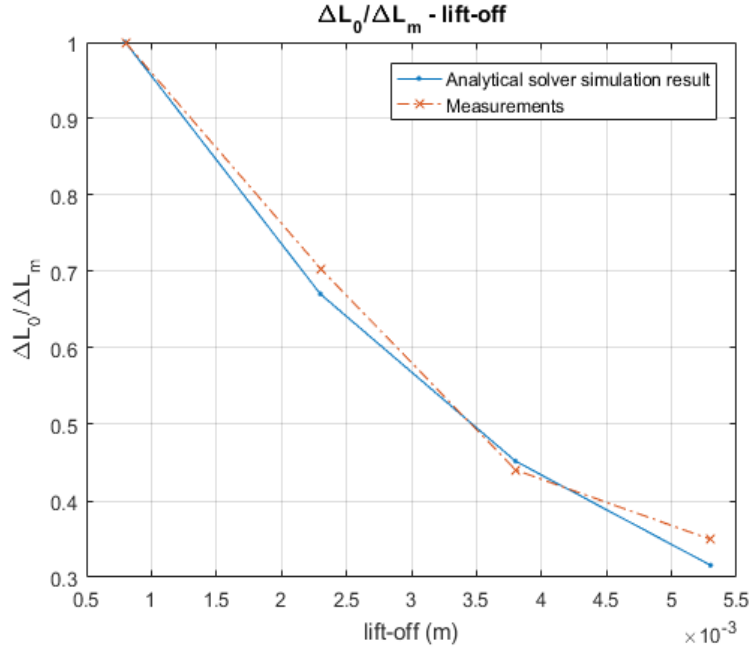


Figure 4.16 Trend of inductance term L_0/L_m (for DP 600 specimen) for different lift-offs

In Figure 4.16, it is observed that the inductance term $\Delta L_0/\Delta L_m$ decreases with increased lift-offs. Consequently, the relative loss of the inductance $\Delta L_0/\Delta L_m$ can be used for the compensation of inductance or impedance phase due to lift-offs, which can be used to compensate the drop in phase with rising lift-offs. Here, ΔL_m is the sample's inductance with end point frequency (the last frequency sample for both simulations and measurements) for the smallest lift-off (0.8 mm under the sensor setup in Figure 4.14).

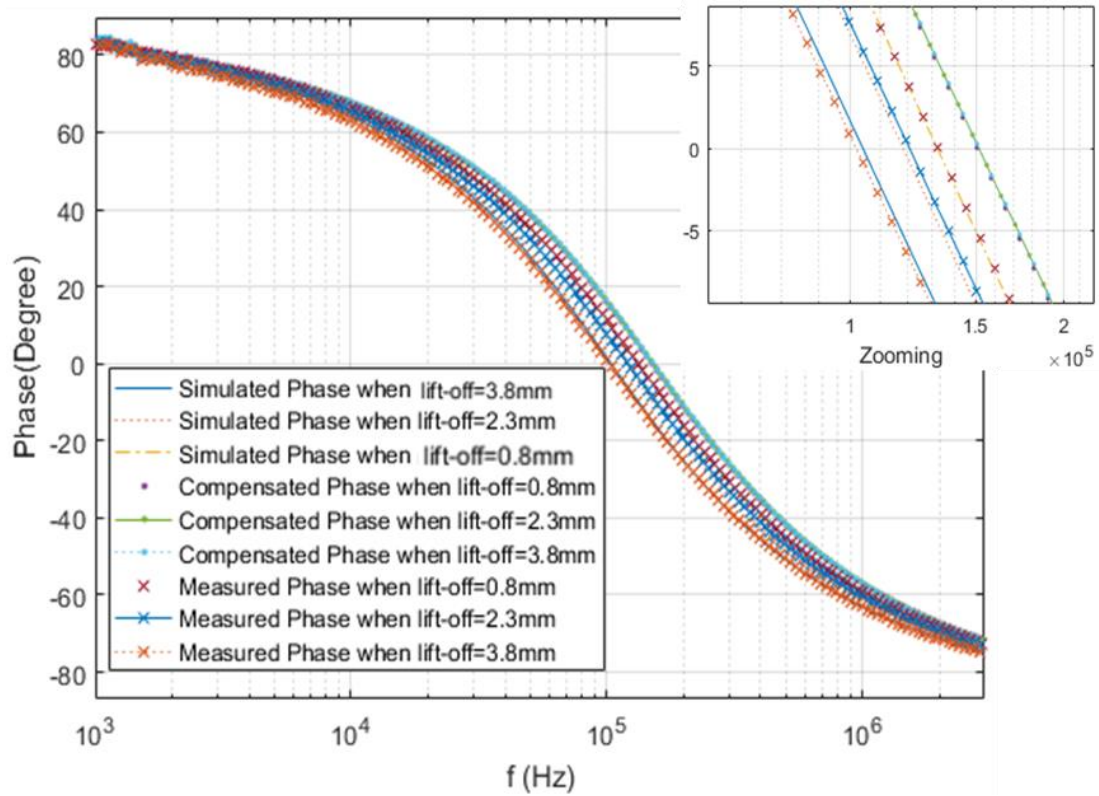


Figure 4.17 shows the simulations, measurements, and the phase multi-frequency spectra after the proposed compensation algorithm (Equation 4. 28 and Equation 4. 29). It can be seen that both the simulated and measured phase decrease as increased lift-offs. In addition, the compensated phase is barely affected by the lift-off. Based on the compensated phase, ferrous plate magnetic permeability could be easily predicted via the measured response of the sensor. The ferrous metallic plates' magnetic permeability measurement technique is validated via the comparison of modelling and measured data for the mentioned sensor next to dual-phase (DP) steels with various values of magnetic permeability.

DP800	0.8	144	138.48	142.37	3.83%	1.13%
	2.3	144	136.76	142.12	5.03%	1.31%
	3.8	144	133.31	141.94	7.42%	1.43%
DP1000	0.8	122	117.68	120.72	3.54%	1.05%
	2.3	122	115.27	120.57	5.52%	1.17%
	3.8	122	111.98	120.15	8.21%	1.52%

In principle, the magnetic permeability reconstruction for the tested specimens is finding the simulated multi-frequency inductance/impedance curve (via Equation 4. 30 - Equation 4. 35 in appendix) that is closest to the measured multi-frequency spectra data (after the proposed compensation algorithms - Equation 4. 28 and Equation 4. 29) while changing the permeability. In order to validate the proposed magnetic permeability reconstruction technique via the compensated phase, multi-frequency inductances of two ferrous specimens have been tested (specimens' properties and size data are shown in Table 4.5). In the measurement process, 120 logarithmically spaced frequencies samples range from 310 Hz to 3 MHz have been chosen as the operation frequencies. In addition, both DP steel specimens have identical size of $500 \times 400 \times 7.0$ mm. Consequently, magnetic permeability comparisons for compensated phase and the measured phase without compensation is shown in Table 4.6.

It can be concluded from Table 4.6 that the magnetic permeability reconstruction shows a better performance through the proposed impedance or inductance phase compensation scheme (Equation 4. 28 and Equation 4. 29).

In practical application, the lift-offs range may be different. However, it has been found that the error of the measured permeability is always within a small value of 5%.

Appendix

The deviations of the compensated zero-crossing frequency (ZCF) ω_0 from the measured ZCF and inductance (ω_1 and ΔL) under a lift-off of l_0 :

The inductance due to the appearance of the sample is the subtraction of the sensor

tested inductance when sensor is put on a specimen ($L(\omega)$) and that when sensor is in empty region ($L_A(\omega)$): $\Delta L(\omega) = L(\omega) - L_A(\omega)$.

Dodd Deeds formulations are listed as follows:

$$\Delta L(\omega) = K \int_0^\infty \frac{P^2(\alpha)}{\alpha^6} A(\alpha) \phi(\alpha) d\alpha \quad 4.30$$

Where,

$$A(\alpha) = e^{-\alpha(G+h+2l_0)}(1 - e^{-\alpha h})^2 \quad 4.31$$

$$\begin{aligned} \phi(\alpha) &= \frac{(\mu_r \alpha - \alpha_1)}{(\mu_r \alpha + \alpha_1)} = \frac{\mu_r \alpha - \sqrt{\alpha^2 + j\omega\sigma\mu_r\mu_0}}{\mu_r \alpha + \sqrt{\alpha^2 + j\omega\sigma\mu_r\mu_0}} \\ &= \frac{1 - \sqrt{1/\mu_r^2 + j\omega\sigma\mu_0/\mu_r\alpha^2}}{1 + \sqrt{1/\mu_r^2 + j\omega\sigma\mu_0/\mu_r\alpha^2}} \end{aligned} \quad 4.32$$

$$K = \frac{\pi\mu_0 N^2}{h^2(r_1 - r_2)^2} \quad 4.33$$

$$P(\alpha) = \int_{\alpha r_1}^{\alpha r_2} x J_1(x) dx \quad 4.34$$

$$\alpha_1 = \sqrt{\alpha^2 + j\omega\sigma\mu_r\mu_0} \quad 4.35$$

l_0 is sensor's lift-off; h is sensor's coil height; N is sensor's coil turn number; r_1 and r_2 are inner and outer radii of sensor's coil; μ_r is the specimen's relative permeability. μ_0 is the vacuum permeability; G is the distance between the excitation coil and receiving coil.

In Equation 4.30, since the $\phi(\alpha)$ term barely change with α (compared with $A(\alpha)$ and $P(\alpha)$), ϕ could be estimated as Equation 4.37,

$$\Delta L(\omega) = \phi(\alpha_0) \Delta L_0 \quad 4.36$$

α_0 is the spatial frequency, which is a constant controlled by the sensor configuration.

From Equation 4. 36, the phase of tested inductance or impedance is merely controlled via $\phi(\alpha_0)$.

$$\phi(\alpha_0) = \frac{-\sqrt{1/\mu_r^2 + j\mu_0\sigma\omega/\mu_r\alpha_0^2} + 1}{\sqrt{1/\mu_r^2 + j\mu_0\sigma\omega/\mu_r\alpha_0^2} + 1} \quad 4. 37$$

Neglect $1/\mu_r^2$ in Equation 4. 37,

$$\phi(\alpha_0) = \frac{-\sqrt{j\mu_0\sigma\omega/\mu_r\alpha_0^2} + 1}{\sqrt{j\mu_0\sigma\omega/\mu_r\alpha_0^2} + 1} \quad 4. 38$$

In Equation 4. 38, it can be observed that $\phi(\alpha_0)$ is sample and sensor related (controlled by σ and μ_r). Assign $\frac{\mu_r\alpha_0^2}{\mu_0\sigma}$ with ω_1 , Equation 4. 38 can be expressed as,

$$\phi(\alpha_0) = \frac{-\sqrt{j\omega/\omega_1} + 1}{\sqrt{j\omega/\omega_1} + 1} \quad 4. 39$$

In Equation 4. 36, ΔL_0 denotes the magnitude of the tested inductance, which is solely controlled by the sensor configuration (cannot affected by the specimen properties).

From our previously work, a simple function $\sin^2\left(\frac{\alpha\pi}{2\alpha_0}\right)$ with its maximum at α_0 is used to approximate ΔL_0 [6].

$$\Delta L_0 \approx \Delta L_m e^{-2\alpha l_0} \sin^2\left(\frac{\alpha\pi}{2\alpha_0}\right) \quad 4. 40$$

Where ΔL_m is the sample's inductance with start point frequency (the first frequency sample for both simulations and measurements) for zero lift-off (0 mm under the sensor setup).

The revised α should maximize $e^{-2\alpha l_0} \sin^2\left(\frac{\alpha\pi}{2\alpha_0}\right)$ and therefore $e^{-\alpha l_0} \sin\left(\frac{\alpha\pi}{2\alpha_0}\right)$.

In our previous work [9], the shift in α_0 caused by the lift-off effect - α_{0r} can be derived as,

$$\alpha_{0r} = \alpha_0 - \frac{4\alpha_0^2 l_0}{\pi^2} \quad 4.41$$

Therefore, the revised ω_1 becomes

$$\omega_1 = \frac{(\alpha_0^2 \pi^4 - 8\pi^2 \alpha_0^3 l_0 + 16\alpha_0^4 l_0^2) \mu_r}{\pi^4 \sigma \mu_0} \quad 4.42$$

Combining Equation 4.40 with Equation 4.41, ΔL_0 becomes

$$\begin{aligned} \Delta L_0 &= \Delta L_m e^{-2(\alpha_0 - \frac{4\alpha_0^2 l_0}{\pi^2}) l_0} \cos^2\left(\frac{2\alpha_0 l_0}{\pi}\right) \\ &= \Delta L_m e^{-2(\alpha_0 - \frac{4\alpha_0^2 l_0}{\pi^2}) l_0} \left(\frac{\cos(\frac{4\alpha_0 l_0}{\pi}) + 1}{2}\right) \end{aligned} \quad 4.43$$

Considering $\alpha_0 l_0 \ll 1$ and based on small-angle approximation $\cos(\theta) \approx 1 - \theta^2/2$, $\cos(4\alpha_0 l_0/\pi)$ is substituted with $1 - (4\alpha_0 l_0/\pi)^2/2$.

ΔL_0 becomes $\Delta L_0 = \Delta L_m e^{-2(\alpha_0 - \frac{4\alpha_0^2 l_0}{\pi^2}) l_0} (1 - \frac{4\alpha_0^2 l_0^2}{\pi^2})$, substituting $(1 - \frac{4\alpha_0^2 l_0^2}{\pi^2})$ with $e^{-\frac{4\alpha_0^2 l_0^2}{\pi^2}}$,

$$\Delta L_0 = \Delta L_m e^{-2(\alpha_0 - \frac{4\alpha_0^2 l_0}{\pi^2}) l_0} e^{-\frac{4\alpha_0^2 l_0^2}{\pi^2}} = \Delta L_m e^{-2(\alpha_0 - \frac{2\alpha_0^2 l_0}{\pi^2}) l_0} \quad 4.44$$

Then,

$$\ln \frac{\Delta L_0}{\Delta L_m} = -2(\alpha_0 - \frac{2\alpha_0^2 l_0}{\pi^2}) l_0 \quad 4.45$$

And further derivation from Equation 4.45:

$$4\alpha_0^2 l_0^2 - 2\pi^2 \alpha_0 l_0 - \pi^2 \ln \frac{\Delta L_0}{\Delta L_m} = 0 \quad 4.46$$

This is now a quadratic equation with $\alpha_0 l_0$ as its variable.

Therefore, the solution for $\alpha_0 l_0$ is

$$\alpha_0 l_0 = \frac{\pi^2 - \sqrt{\pi^4 + 4\pi^2 \ln \frac{\Delta L_0}{\Delta L_m}}}{4} \quad 4.47$$

Since $\alpha_0 l_0 \ll 1$, the other solution, the other solution $\alpha_0 l_0 = \frac{\pi^2 + \sqrt{\pi^4 + 4\pi^2 \ln \frac{\Delta L_0}{\Delta L_m}}}{4}$ therefore is discarded.

From Equation 4.47, lift-off can be estimated as

$$l_0 = \frac{\pi^2 - \sqrt{\pi^4 + 4\pi^2 \ln \frac{\Delta L_0}{\Delta L_m}}}{4\alpha_0} \quad 4.48$$

Combining Equation 4.42 with Equation 4.48,

$$\omega_1 = \frac{\alpha_0^2 \left(\pi^2 + 4 \ln \frac{\Delta L_0}{\Delta L_m} \right) \mu_r}{\pi^2 \sigma \mu_0} \quad 4.49$$

Further derivation from 4.49 - $\alpha_0^2 (\pi^2 + 4 \ln \frac{\Delta L_0}{\Delta L_m}) \mu_r - \pi^2 \sigma \mu_0 \omega_1 = 0$

And the solution is

$$\alpha_0 = \sqrt{\frac{\pi^2 \sigma \mu_0 \omega_1}{\left(\pi^2 + 4 \ln \frac{\Delta L_0}{\Delta L_m} \right) \mu_r}} \quad 4.50$$

Thus, the zero-crossing frequency can be compensated as following,

$$\omega_0 = \frac{\mu_r \alpha_0^2}{\mu_0 \sigma} = \frac{\pi^2 \omega_1}{\left(\pi^2 + 4 \ln \frac{\Delta L_0}{\Delta L_m} \right)} \quad 4.51$$

4.2 FEM solver for eddy current computation

4.2.1 Acceleration based on perturbed matrix inversion

A. Method

Fast eddy current computation is vital for non-destructive testing. The perturbed matrix inversion (PMI) method was used for solving the linear system of equations in FEM when a small defect is present on the sample. As described in Equation 3. 27 and Equation 3. 28, it can be regarded as solving a large system of algebraic equations. Assume that a small defect is present on the sample, the system matrix is a slightly varied matrix to the sample without the defect. The variation matrix (or the perturbation matrix) due to the defect can be expressed as

$$D = \begin{bmatrix} -K2' & -L' \\ -M' & -N' \end{bmatrix} \quad 4. 52$$

Where: $K2'$ and L' present the change from the second and third terms due to the perturbation in Equation 3. 27. M' and N' present the change from the first and second terms due to the perturbation in Equation 3. 28.

According to the Sherman-Morrison-Woodbury formula, the inversion can be expressed as

$$(Q + D)^{-1} = Q^{-1} - Q^{-1}(Q^{-1} + D^{-1})^{-1}Q^{-1} \quad 4. 53$$

Simplify the notation by denoting Q^{-1} as Q_i , then Equation 4. 53 can be simplified as [10]

$$(Q + D)^{-1} = Q_i - Q_i D (I + Q_i D)^{-1} Q_i \quad 4. 54$$

Consequently, the solution can be obtained through the PMI method. All the computations were operated on the platform ThinkCentre M910s, with 16GB RAM and Intel Core i7-6700 processor.

B. Model

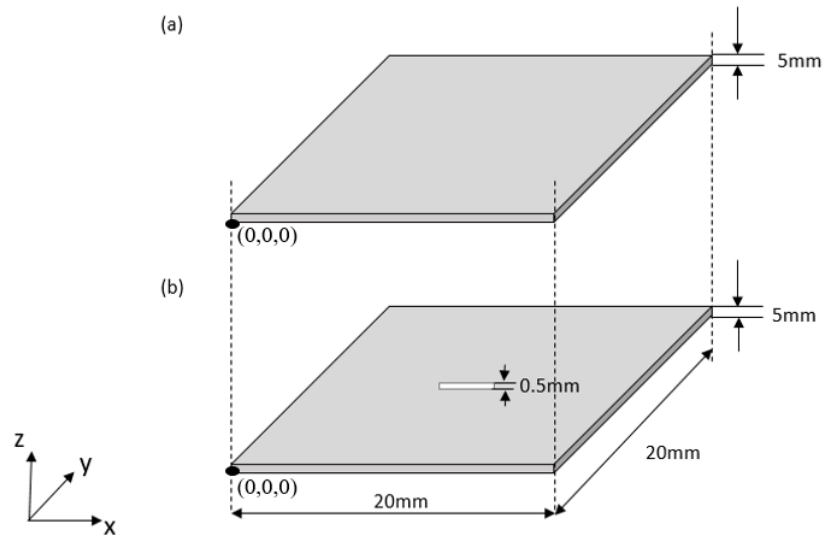


Figure 4.18 Model Geometry (a) metal plate (b) metal plate with the defect

In Figure 4.18, the objects have been modelled as an unflawed metallic plate and a metallic plate with a defect in the centre. For both metal plates in (a) and (b), the length, width and height are 20 mm, 20 mm and 5 mm respectively. For the metal plate with the defect in (b), the simulated defect is placed in the centre with a length of 5 mm, a width of 0.5 mm and a height of 3 mm. Two blocks are centred at (10, 10, 3.5) mm. To validate the solver, two materials are chosen for the metal plates, one is aluminium with the electrical conductivity of 35 MS/m at 20 degrees, and another is copper with the electrical conductivity of 57 MS/m at 20 degrees.

In the simulation, as shown in Figure 4.19 and Table 4.7, a coaxial sensor is used in the simulation process. Both the radius of the excitation coil and the receiving coil are set to 0.5 mm. The lift-off of the sensor is 0.05 mm and the gap between the excitation coil and the receiving coil is 0.2 mm. The magnitude of the injection current in excitation coil is 1 A. During the simulation for crack inspection, the coils are moving in parallel along the y-axis (from (10, 0, 5) mm to (10, 20, 5) mm if there is no lift-off).

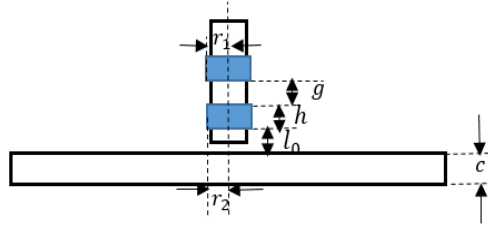


Figure 4.19 Sensor Configuration

Table 4.7 Sensor Parameters

Radius of excitation coil r_1	0.5 mm
Radius of receiving coil r_2	0.5 mm
Height of coil h	0.25 mm
Gap between two coils g	0.2 mm
Lift off l_0	0.05 mm
Thickness of the plate c	5 mm

C. Test of the accelerated FEM

According to the Dodd Deeds formulas, the inductance variation due to the sample plates (aluminium and copper) without defect can be calculated, shown in Figure 4.20 and Figure 4.21. The sweeping frequency changes from 10 Hz to 1 MHz in the analytical solution.

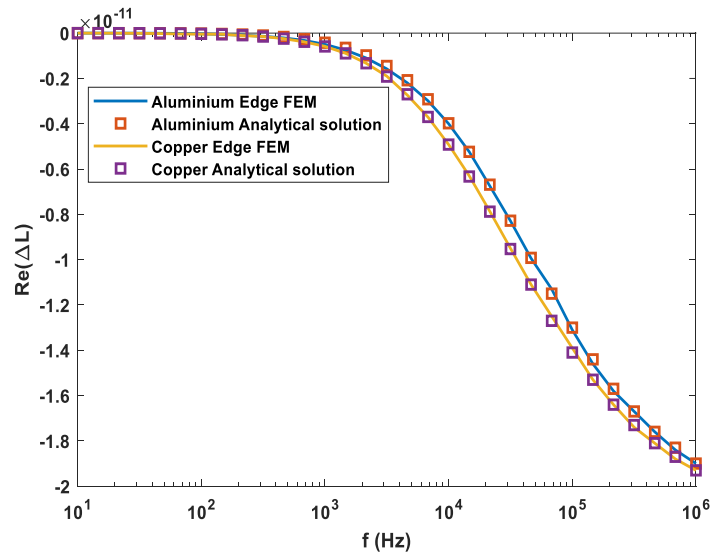


Figure 4.20 The real part of the inductance due to the aluminium and copper plate without defect

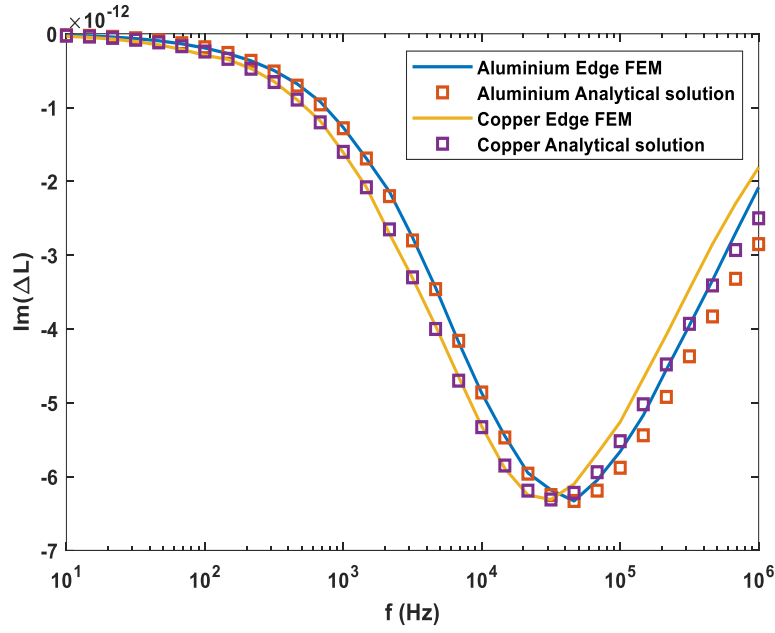


Figure 4.21 The imaginary part of the inductance caused by the aluminium and copper plate without defect

It can be seen from the figures above that edge FEM simulation and analytical results are matched well with each other under the frequency range from 10 Hz to 100 kHz. Compared with the results from the aluminium plate, the characteristic frequency reduces when the copper plate was used, which is in accordance with the relationship between the conductivity and the characteristic frequency. In addition, given that the solution from analytical formulas is the results for the plate with infinite width and length, for the imaginary part of the inductance results, there exists some error as the frequency sweeping from 100 kHz to 1 MHz.

D. Acceleration Performance in Crack Scanning

As the perturbation matrix due to the presence of the defect on the sample was assigned to be the perturbation matrix D , the acceleration performance from the PMI approach can be obtained in order to detect the presence of the defect. The result of the PMI approach was compared with that calculated from the conventional conjugate gradient squared (CGS) method. The frequency was set to 10 Hz. The defect depths of the

sample plate are 1 mm, 2 mm and 3 mm respectively. The results are shown in the following subsections.

D.1 Verification of the PMI-based Acceleration Solver

Figure 4.22 and Figure 4.23 demonstrate the changes of induced voltage on the receiver coil as the sensor scans along the y axis above the sample plates (Figure 4.18(b)) with three different depths of the defects under the same frequency and lift-off. It can be seen that CGM and PMI methods agree well. As expected, the maximum value (peak value) of the voltage occurs at the center of the sample where the defect is located. The deeper the defect is, the larger the change in the induced voltage. There is a larger drop as defect depth increases from 1 mm to 2 mm than from 2 mm to 3 mm, which is due to the strength of eddy current decreases as the depth increases. Compared with the results from the aluminum plate, the change of the received voltage from the copper plate is slightly larger which is due to a higher conductivity for copper.

Figure 4.24 illustrates the effect of the lift-off for the crack detection simulated from the copper plate with a 3 mm depth defect in the middle of the plate. The lift-off of the sensor is 0.05 mm and 0.5 mm respectively. The results from both methods agree well and the peaks of the voltage change are located at the same place. With the increase of the lift-off, the peak value decreases around 2.5 times which also proves the lift-off is one of the crucial factors in the crack detection process.

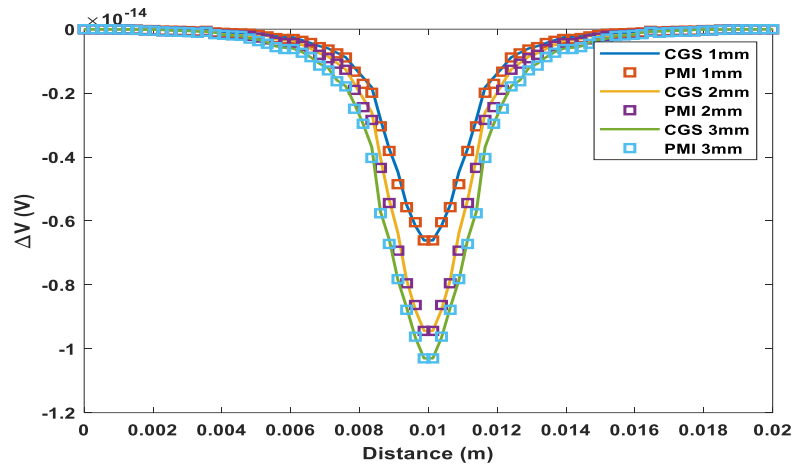


Figure 4.22 Computation results for the aluminum plate with different depths of defect, lift-off is 0.05 mm

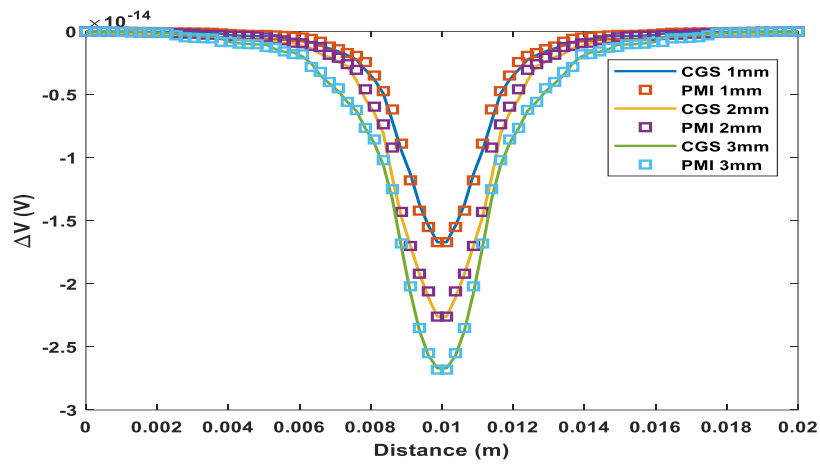


Figure 4.23 Computation results for the copper plate with different depths of defect, lift-off is 0.05 mm

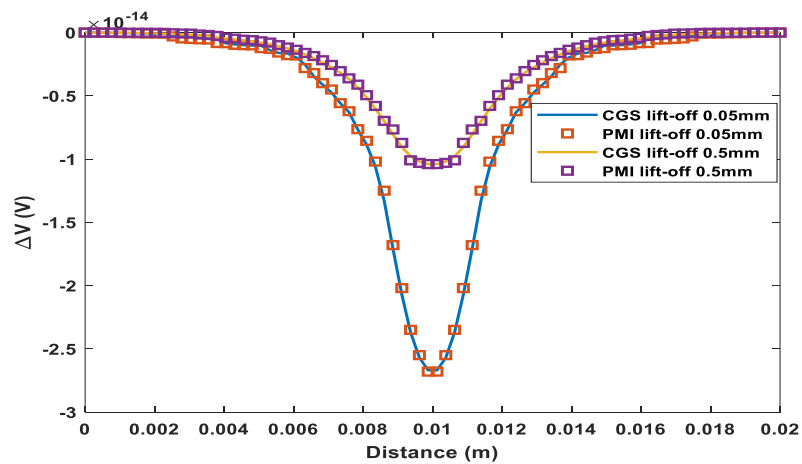


Figure 4.24 Computation results for the copper plate with different lift-offs

D.2 Effect of Sampling Point Density during Scanning

The effect of the sampling point density for crack detection is presented in Figure 4.25. The aluminium plate with a 3 mm depth of defect was used in the simulation process. The computation time varies from 100 s to 300 s for each scanning process by using the PMI method while it consumes 300 s to 900 s by using the conventional CGS method as the scanning sample points increasing from 50 to 150 in the step of 4. It can be noticed that the computation speed of the PMI method is about 3 times faster than the conventional CGS method. As shown in Figure 4.25, the computation time for both methods are increasing linearly with the increase of the sampling point density. Besides, the time shrinks more significantly for high density of sampling points by using the accelerated method.

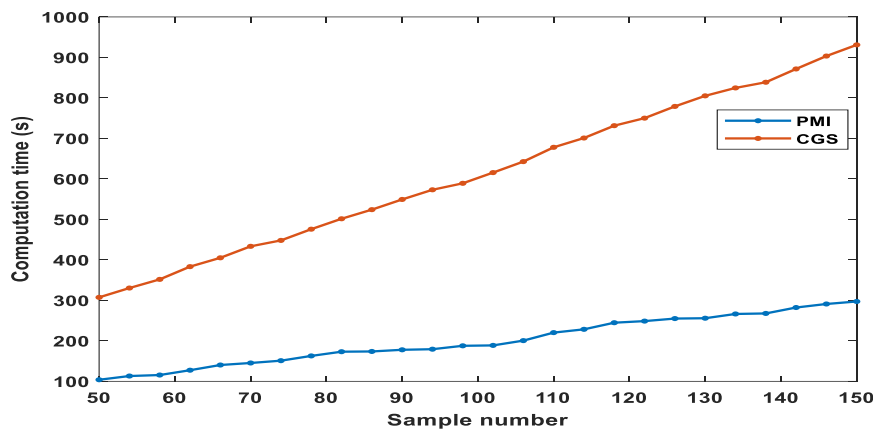


Figure 4.25 Computation time of PMI method and CGS method for different scanning sample numbers

D.3 Effect of Frequency

As shown in Figure 4.26, the relationship between the frequency used in the simulation and the computation time is plotted. The frequency used ranges from 10 Hz to 10 kHz in a logarithmic scale in the simulation process. After adopting the PMI method, the scanning speed is much faster than the conventional CGS method. The computation time used for PMI and conventional CGS methods almost remains stable regardless of

frequency settings, around 200 s, and 550 s respectively. It can be concluded that the acceleration efficiency remains almost the same concerning the frequency in the scanning process.

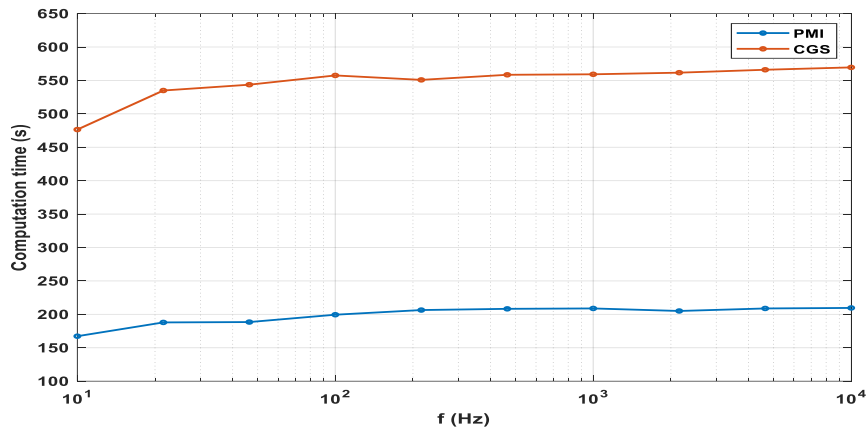


Figure 4.26 Computation time of PMI method and CGS method under different frequencies

D.4 Effect of Defect Depth

As can be seen from Table 4.8, for the PMI method, the computation time slightly increases as the defect depth increases to 3 mm when aluminium plate was used while the speed almost maintains stable when the copper plate is used. Meanwhile, for the CGS method, the computation time increases as the depth increases for both materials. It can be noticed that the acceleration efficiency under the defect depth of 3 mm is slightly higher than that under the defect depth of 1 mm and 2 mm.

Table 4.8 CGS method and PMI method computation time for different defect depths

Defect Depth	Computation Time (s)			
	Aluminium		Copper	
	PMI	CGS	PMI	CGS
1mm	165.64	436.32	166.12	446.55
2mm	168.64	449.51	167.97	450.31
3mm	170.96	458.12	167.79	455.75

4.2.2 Accelerated calculation for the algebraic system due to small perturbation

A. Method

The final solution of the FEM problem results in a large algebraic equation system, as shown in Equation 3. 30. Now considering that there is a small crack in the tested sample, the original system matrix (crack free sample) can be expressed with the matrices affected/unaffected by the small perturbation, shown as

$$\begin{bmatrix} K_1 & K_2 & L_1 & L_2 \\ K_3 & K_4 & L_3 & L_4 \\ M_1 & M_2 & N_1 & N_2 \\ M_3 & M_4 & N_3 & N_4 \end{bmatrix} \begin{bmatrix} \mathbf{A}_u \\ \mathbf{A}_c \\ \mathbf{V}_u \\ \mathbf{V}_c \end{bmatrix} = \begin{bmatrix} X_{u1} \\ X_{c1} \\ X_{u2} \\ X_{c2} \end{bmatrix} \quad 4. 55$$

Then reordering Equation 4. 55, four new submatrices (Q_{11} , Q_{12} , Q_{21} and Q_{22}) can be used to present the current crack free system matrix and given as

$$\begin{bmatrix} K_1 & L_1 & K_2 & L_2 \\ M_1 & N_1 & M_2 & N_2 \\ K_3 & L_3 & K_4 & L_4 \\ M_3 & N_3 & M_4 & N_4 \end{bmatrix} \begin{bmatrix} \mathbf{A}_u \\ \mathbf{V}_u \\ \mathbf{A}_c \\ \mathbf{V}_c \end{bmatrix} = \begin{bmatrix} X_{u1} \\ X_{u2} \\ X_{c1} \\ X_{c2} \end{bmatrix} \quad 4. 56$$

$$\begin{bmatrix} Q_{11} & Q_{12} \\ Q_{21} & Q_{22} \end{bmatrix} \begin{bmatrix} \mathbf{S}_u \\ \mathbf{S}_c \end{bmatrix} = \begin{bmatrix} \mathbf{X}_u \\ \mathbf{X}_c \end{bmatrix} \quad 4. 57$$

Where:

$$Q_{11} = \begin{bmatrix} K_1 & L_1 \\ M_1 & N_1 \end{bmatrix}, Q_{12} = \begin{bmatrix} K_2 & L_2 \\ M_2 & N_2 \end{bmatrix}, Q_{21} = \begin{bmatrix} K_3 & L_3 \\ M_3 & N_3 \end{bmatrix}, Q_{22} = \begin{bmatrix} K_4 & L_4 \\ M_4 & N_4 \end{bmatrix}, \mathbf{S}_u = \begin{bmatrix} \mathbf{A}_u \\ \mathbf{V}_u \end{bmatrix}, \mathbf{S}_c = \begin{bmatrix} \mathbf{A}_c \\ \mathbf{V}_c \end{bmatrix}, \mathbf{X}_u = \begin{bmatrix} X_{u1} \\ X_{u2} \end{bmatrix}, \mathbf{X}_c = \begin{bmatrix} X_{c1} \\ X_{c2} \end{bmatrix} \quad 4. 58$$

Here submatrix Q_{11} represents the domain of elements which has no influence due to the existence of the crack while submatrices Q_{12} , Q_{21} and Q_{22} represent the domain of elements near the crack and are affected by this small perturbation. Submatrices Q_{12} and Q_{21} are transposed. Matrix \mathbf{X} is the right-hand side matrix of the system which is

partitioned into two column matrices X_u and X_c and matrix S is the solution for the matrix system, consisting of two submatrices S_u and S_c . Then the system equations change to

$$Q_{11}S_u + Q_{12}S_c = X_u \quad 4. 59$$

$$Q_{21}S_u + Q_{22}S_c = X_c \quad 4. 60$$

Now due to the presence of the crack, the left-hand side of the crack free sample system matrix is very slightly perturbed. then the system equations with the small perturbation turn to

$$Q_{11} S_u' + (Q_{12} + \Delta Q_{12})S_c' = X_u \quad 4. 61$$

$$(Q_{21} + \Delta Q_{21})S_u' + (Q_{22} + \Delta Q_{22})S_c' = X_c \quad 4. 62$$

Where: ΔQ_{12} , ΔQ_{21} and ΔQ_{22} are the submatrices affected due to the small perturbation. S_u' and S_c' are the solution for the new system equations.

Since that the element domain of submatrix Q_{11} is hardly affected by the presence of the small perturbation, the vector and scalar potential solution of S_u' for this domain is regarded equal to the unperturbed solution without the crack in the sample plate, which gives

$$S_u' \approx S_u \quad 4. 63$$

Using Equation 4. 63 and Equation 4. 62, the solution S_c' can be derived from equation (4.29)

$$S_c' = (Q_{22} + \Delta Q_{22})^{-1}(-\Delta Q_{21}S_u + Q_{22}S_c) \quad 4. 64$$

The solution S_c' should also satisfy Equation 4. 61. By referring to [10], and assume that Q_{22_i} is the inversion matrix of Q_{22} , then

$$(Q_{22} + \Delta Q_{22})^{-1} = Q_{22i} - Q_{22i}\Delta Q_{22}(I + Q_{22i}\Delta Q_{22})^{-1}Q_{22i} \quad 4. 65$$

Substitute Equation 4. 65 to Equation 4. 64, it turns to

$$S_c' = (Q_{22i} - Q_{22i}\Delta Q_{22}(I + Q_{22i}\Delta Q_{22})^{-1}Q_{22i})(-\Delta Q_{21}S_u + Q_{22}S_c) \quad 4. 66$$

Now substitute Equation 4. 63 and Equation 4. 64 to the left-hand side of Equation 4. 61 and it gives

$$Q_{11} S_u' + (Q_{12} + \Delta Q_{12})S_c' = Q_{11}S_u + (Q_{12} + \Delta Q_{12})(S_c - HS_u + G(I + G)^{-1}HS_u - G(I + G)^{-1}S_c) \quad 4. 67$$

Where:

$$G = Q_{22i}\Delta Q_{22}, H = Q_{22i}\Delta Q_{21} \quad 4. 68$$

The matrices ΔQ_{12} , G and H are perturbed matrices with small element values, terms containing these matrices can be eliminated, then Equation 4. 67 can be approximated as Equation 4. 69, which is satisfied with the right-hand side of Equation 4. 59.

$$Q_{11} S_u' + (Q_{12} + \Delta Q_{12})S_c' \approx Q_{11}S_u + Q_{12}S_c = X_u \quad 4. 69$$

Consequently, Equation 4. 61 is valid. Therefore, the final solution of equation system with the perturbation of the crack can be approximately calculated as

$$\begin{cases} S_u' = S_u \\ (Q_{22} + \Delta Q_{22})S_c' = X_c - (Q_{21} + \Delta Q_{21})S_u \end{cases} \quad 4. 70$$

After obtaining both the vector potential and scalar potential, the eddy current, the voltage and the inductance change can be calculated respectively.

B. Simulation setup

An EM sensor probe is designed for the simulations to verify the proposed method. As shown in Figure 4.27, the sensor probe is the co-axial type sensor. The coil parameters are listed in Table 4.9. The exciting coil and receiving coil have identical radius and

height with single turn. The sensor probe is placed 0.5 mm above the sample plate and the gap between the coils is 0.5 mm. The excitation current with the magnitude of 1 A and the frequency of 1 kHz is injected into the exciting coil, the induced inductance with the presence of the sample plate can be received from the receiving coil. The conductivity and thickness of the sample plate is set to 57 MS/m and 2 mm respectively. It can be seen from Figure 4.28 that there are different shapes of crack would be tested. These cracks are generated in the middle of the sample plate.

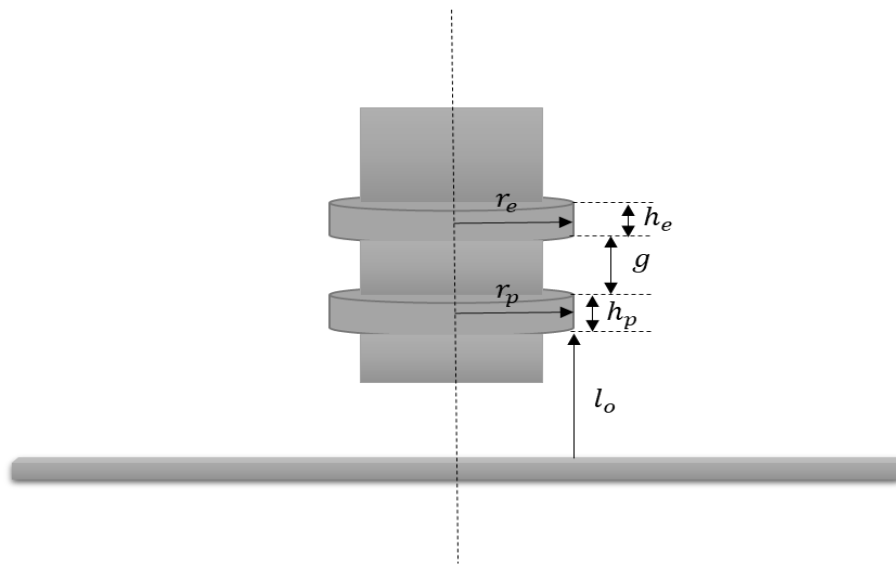


Figure 4.27 The configuration of EM sensor probe

Table 4.9 Coil Parameters

Exciting coil	Radius (r_e)	3 mm
	Height (h_e)	0.3 mm
Receiving coil	Radius (r_p)	3 mm
	Height (h_p)	0.3 mm
Lift off l_o	0.5 mm	
Gap between the exciting coil and receiving coil g	0.5 mm	
Thickness of the sample plate c	2 mm	
Working frequency f	1 kHz	

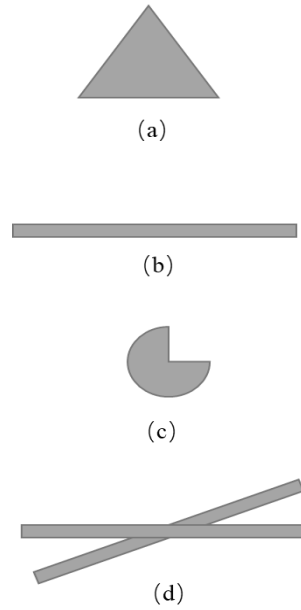


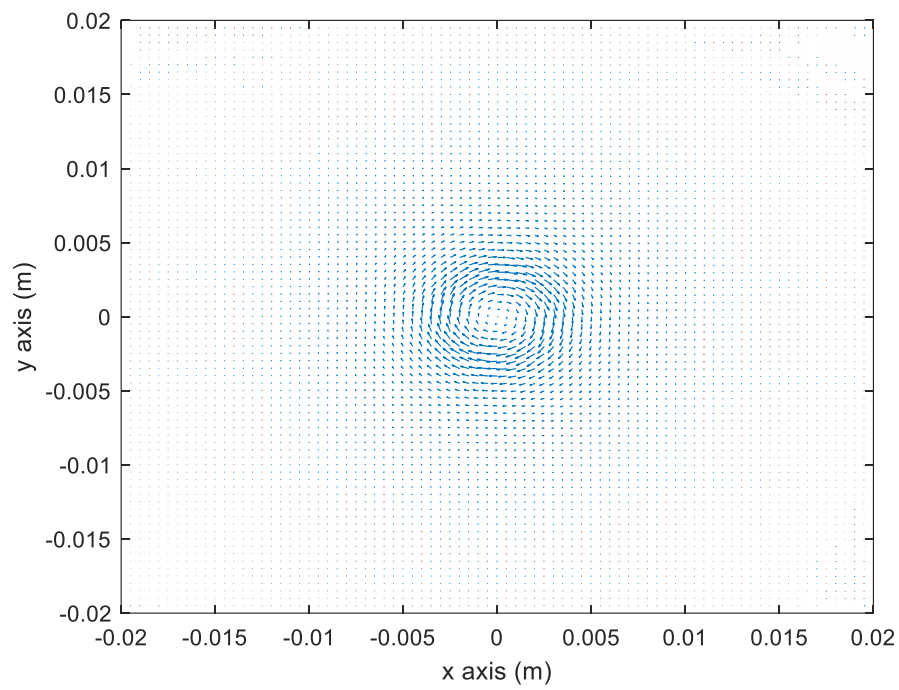
Figure 4.28 Crack shapes (a) Triangle (b) Rectangle (c) Circular sector (d) X shape

C. Results

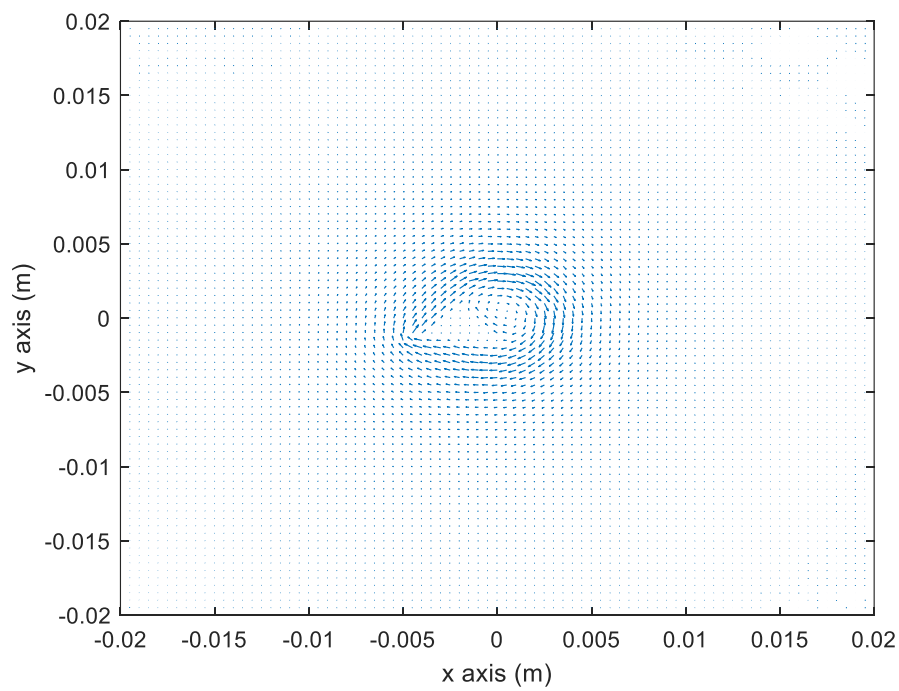
C.1 Verification of FE analysis

The movement of eddy current is a key point in the inspection of eddy current testing. It would be disturbed due to the presence of the crack. As shown in Figure 4.29, eddy current flows on the sample plate without crack or with different shapes of crack. It can be seen that the eddy current is rotational as there is no crack on the sample plate. Then when it encounters with a crack, it will be flow around the edge of the crack but the overall trend remains the same. From the vector diagram of the eddy current, the crack shape can be seen clearly and same compared with Figure 4.28. The inductance change due to the sample plate with a rectangle crack under different element number was calculated. As listed in Table 4.10, the deviation is within 5% and the speed of the computation is significantly improved, i.e., the time for the calculation is shortened 3.79 times as the total element number is 10 k with the variation of 2.56 % while 34.24 times as the total element number is 139 k with the variation of 3.56%. Figure 4.30 shows the relative residual of varying iteration number under different element number and it can

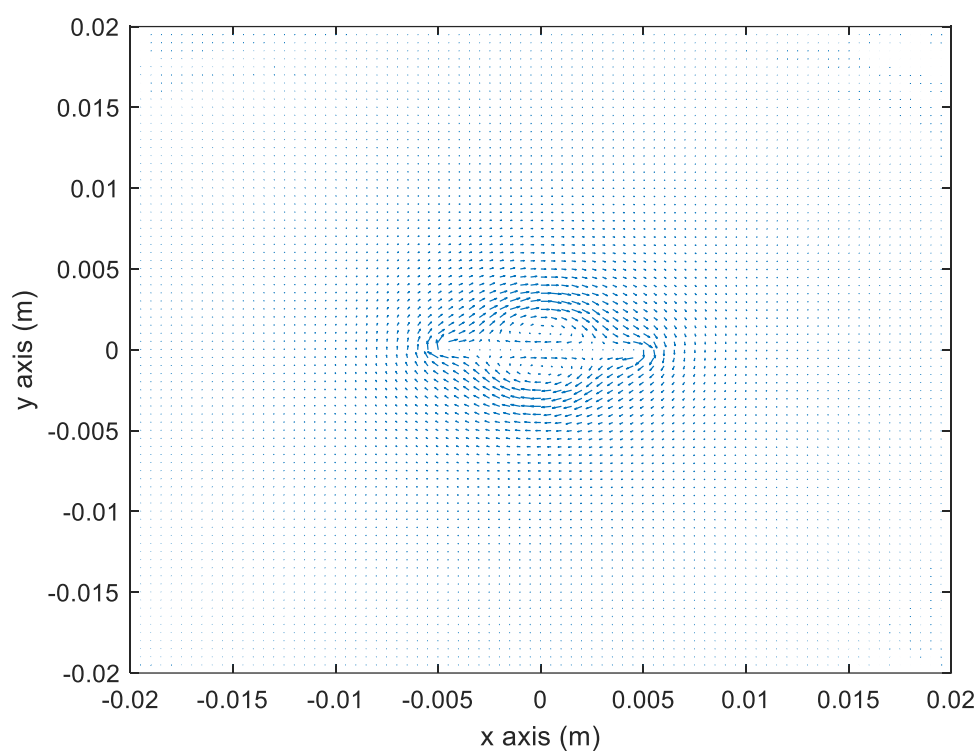
be also revealed that it needs less iteration cycles to achieve the convergence.



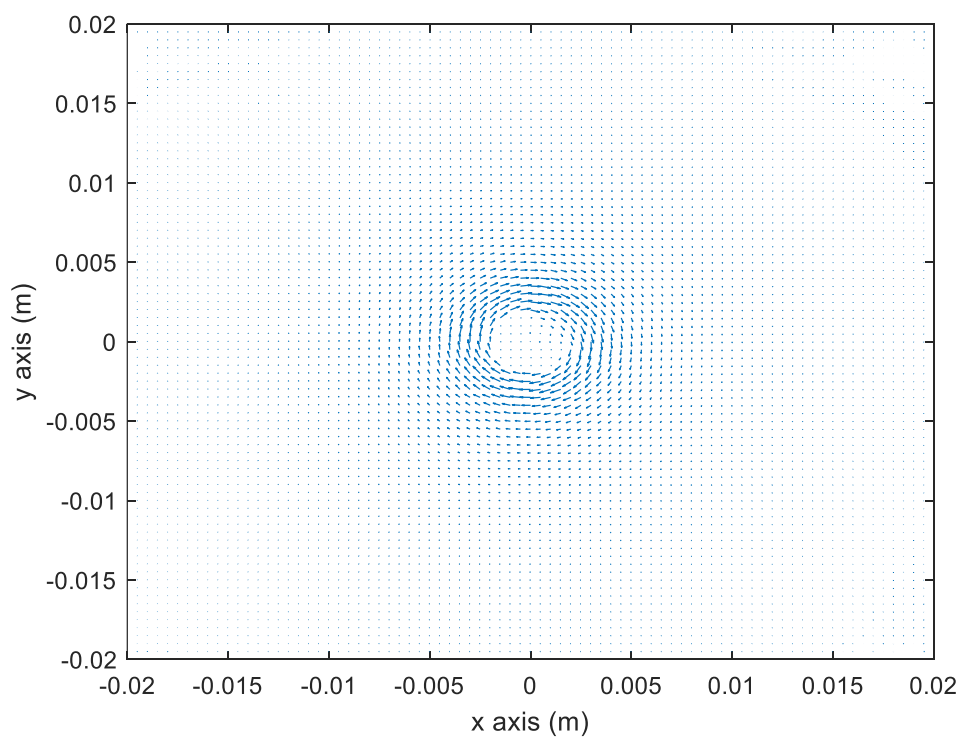
(a)



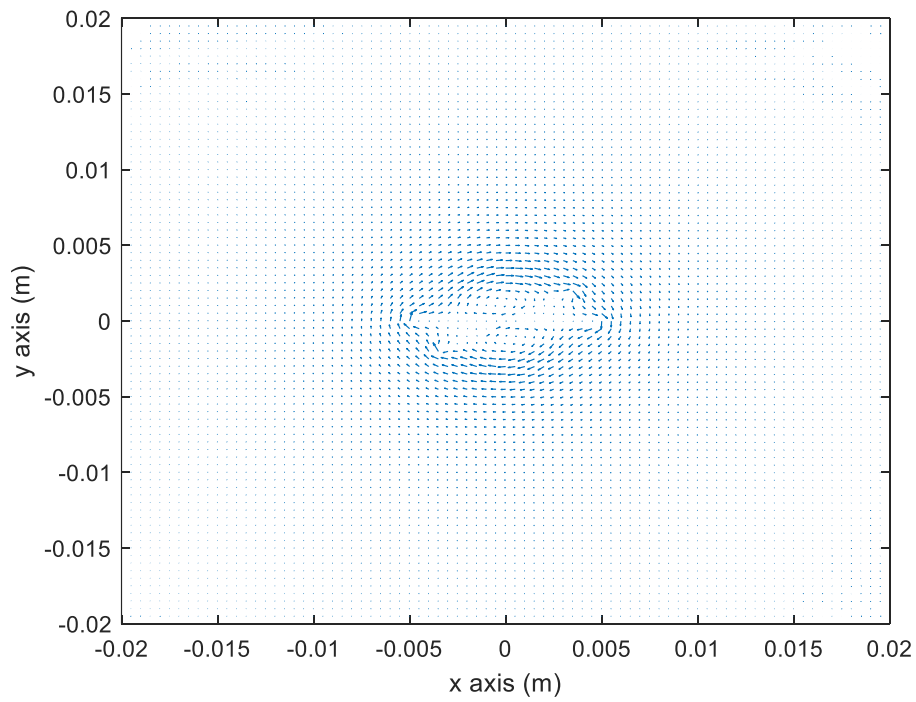
(b)



(c)



(d)



(e)

Figure 4.29 Eddy current (a) without crack and with crack (b) triangle (c) rectangle (d) circular sector

(e) X shape

Table 4.10 The accelerated rate and deviation of the inductance change due to the sample plate under different element number

Element Number	Calculation time of the method without acceleration (s)	Calculation time of the proposed method (s)	Accelerated rate (times)	Calculation deviation (%)
10 k	7.69	2.03	3.79	2.56
51 k	57.74	3.56	16.22	3.22
139 k	306.79	8.96	34.24	3.56

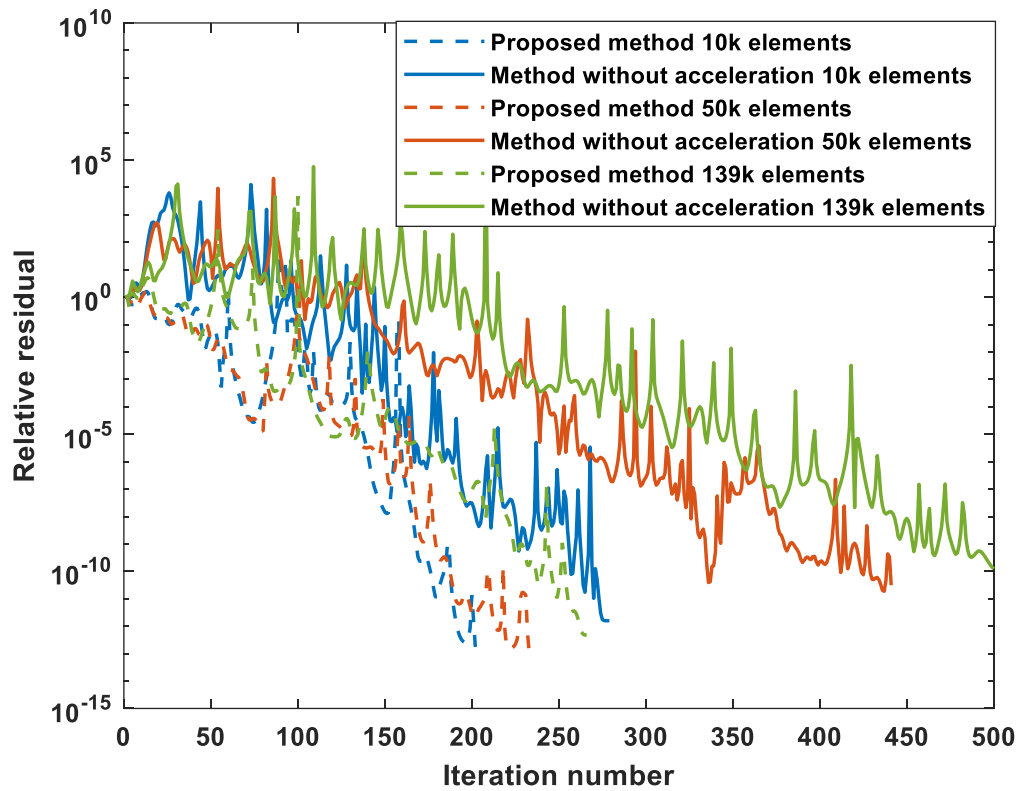
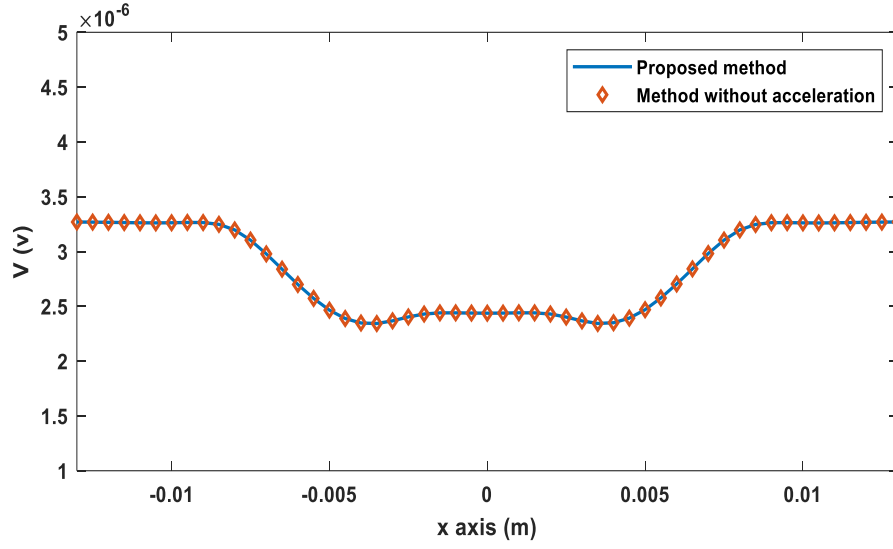


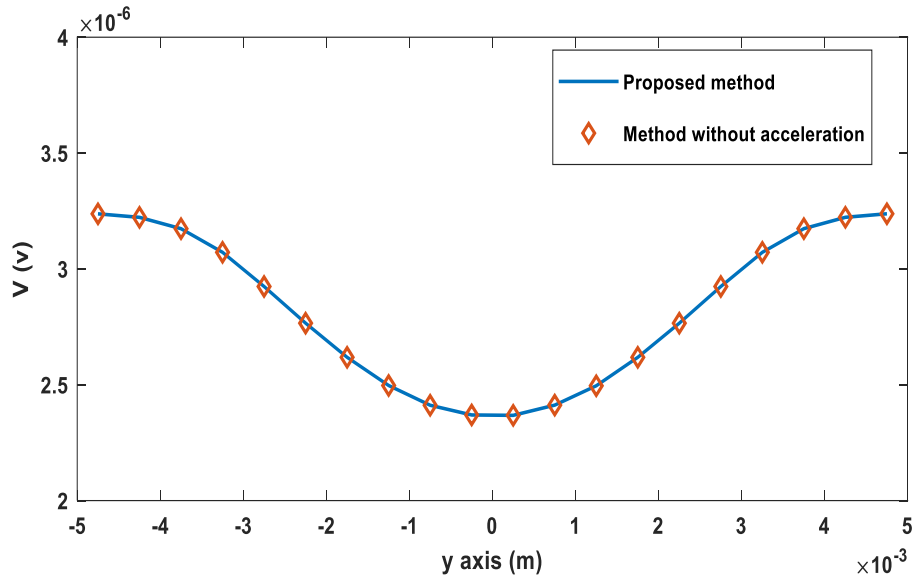
Figure 4.30 Relative residual under different element number

C.2 Crack scanning

FE calculation can be used in the detection for the crack. As depicted in Figure 4.31, the sensor probe scans a crack with the length of 10 mm and the width of 0.5 mm in the centre of the sample plate (same with the sample plate with a rectangle crack, shown in Figure 4.28(b) and Figure 4.29(c)) and it scans along x and y axis respectively. The results agreed with the simulation results without using the acceleration method and, as listed in Table 4.11, the speed is enhanced approx. 7 folds. It can be noted that the sensor probe closes to the crack, the received voltage is decreasing then stays stable and the voltage increases until it leaves the crack. This phenomenon is due to the perturbation of the crack, the distribution of the eddy current changes on the sample plate which results in the change of the magnetic field.



(a)



(b)

Figure 4.31 The sensor probe scans across the crack along (a) x axis (b) y axis

Table 4.11 The computation time for one step

Scanning direction	Calculation time (s)	
	Proposed method	Method without acceleration
X axis	5.47	35.92
Y axis	5.68	36.08

Figure 4.32 shows the experimental setup consisting of an EM instrument, a sensor

probe and the sample plate. Then the detected data would be transmitted to the host PC. Here a differential sensor probe was made for detecting different depths of the crack from 0.1 mm to 2 mm with the increment of 0.1 mm. The crack has the length of 10 mm and the width of 0.1 mm. The sensor parameters are listed in Table 4.12. The lift-off of the sensor probe was 1 mm and the working frequency was 20 kHz. The conductivity and the thickness of the sample plate are 1.4 MS/m and 2 mm respectively.



Figure 4.32 Experimental setup

Table 4.12 Experiment sensor parameters

Excitation coil	Length (mm)	8
	Width (mm)	4
	Height (mm)	10
	Turns N	20
Receiving coil	Radius (mm)	0.5
	Turns N	250
	Length (mm)	10
	Width (mm)	0.1
Surface crack	Depth (mm)	0.1 to 2 mm in step of 0.1 mm
Lift-off l_0 (mm)		1
Excitation frequency (kHz)		20
Plate thickness (mm)		2
Plate conductivity (MS/m)		1.4

The received and simulated data are plotted in Figure 4.33. The simulated results are agreed with the measured ones. It can be seen that, when the sensor probe scan across the crack, there is a sine relationship between the scanning distance and the received voltage of the measured and simulated data. The peak voltage is related to the depth of the crack, i.e., the deeper the crack depth, the larger the received result. The peak voltage can be used to predict the depth of the crack. Besides, it can be deduced that the length of the crack is 10 mm which is consistent with the sample crack.

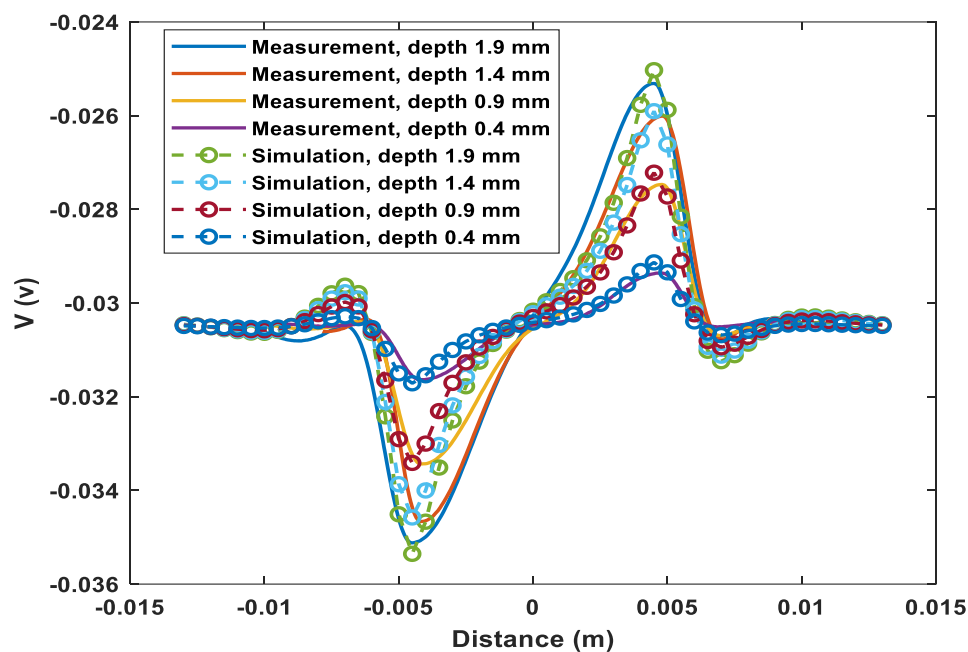


Figure 4.33 Measured and simulated results under different depths

Reference

- [1]. C. V. Dodd, W. E. Deeds, J. W. Luquire and W. G. Spoeri, "Some Eddy-Current Problems and Their Integral Solutions", *Oak Ridge National Laboratory*, April 1969.
- [2]. W. Yin and A. J. Peyton, "Thickness measurement of non-magnetic plates using multi-frequency eddy current sensors," *NDT & E International*, vol. 40, no. 1, pp. 43-

48, 2007.

- [3]. W. Yin and K. Xu, "A Novel Triple-Coil Electromagnetic Sensor for Thickness Measurement Immune to Lift-Off Variations," *IEEE Transactions on Instrumentation and Measurement*, vol. 65, no. 1, pp. 164-169, Jan. 2016.
- [4]. M. Lu, L. Yin, A. J. Peyton and W. Yin, "A Novel Compensation Algorithm for Thickness Measurement Immune to Lift-Off Variations Using Eddy Current Method," *IEEE Transactions on Instrumentation and Measurement*, vol. 65, no. 12, pp. 2773-2779, Dec. 2016.
- [5]. W. Yin, A. J. Peyton and S. J. Dickinson, "Simultaneous measurement of distance and thickness of a thin metal plate with an electromagnetic sensor using a simplified model," *IEEE Transactions on Instrumentation and Measurement*, vol. 53, no. 4, pp. 1335-1338, 2004.
- [6]. M. Lu, W. Zhu, L. Yin, A. J. Peyton, W. Yin and Z. Qu, "Reducing the Lift-Off Effect on Permeability Measurement for Magnetic Plates From Multifrequency Induction Data," *IEEE Transactions on Instrumentation and Measurement*, vol. 67, no. 1, pp. 167-174, Jan. 2018.
- [7]. W. Zhu, W. Yin, A. Peyton, and H. Ploegaert, "Modelling and experimental study of an electromagnetic sensor with an H-shaped ferrite core used for monitoring the hot transformation of steel in an industrial environment," *NDT & E International*, vol. 44, no. 7, pp. 547-552, 2011.
- [8]. W. Yin, X. J. Hao, A. J. Peyton, M. Strangwood, and C. L. Davis, "Measurement of permeability and ferrite/austenite phase fraction using a multi-frequency electromagnetic sensor," *NDT & E International*, vol. 42, no. 1, pp. 64-68, 2009.
- [9]. M. Lu, L. Yin, A. Peyton, and W. Yin, "A novel compensation algorithm for thickness measurement immune to lift-off variations using eddy current method," *IEEE Transactions on Instrumentation and Measurement*, vol. 65, no. 12, pp. 2773-2779, 2016.
- [10]. H. Arsham, J. Grad and G. Jaklič, "Algorithm for Perturbed Matrix Inversion

Problem," *Applied Mathematics and Computation*, vol. 188, pp. 801–807, 2007.

Chapter 5 Thickness measurement of metallic plates with finite planar dimension using eddy current method

Ruochen Huang, Mingyang Lu, Anthony Peyton, Wuliang Yin

IEEE Transactions on Instrumentation and Measurement, vol. 69, no. 10, 2020.

In this chapter, a modified analytical solution based on the Dodd - Deeds model is proposed. It is applied for the metallic sample with a finite dimension. In this method, it is found that the radius of the sample is related to the integral point of analytical algorithm, therefore, for the sample with finite dimension, a new initial integral point is introduced to calculate the inductance change using eddy current sensor. Both the experiment and simulation have been carried out to verify the proposed method. Moreover, it can also be used for the thickness measurement and the retrieved thickness for the sample plate is within the error of 2%.

Thickness Measurement of Metallic Plates With Finite Planar Dimension Using Eddy Current Method

Ruochen Huang[✉], Mingyang Lu[✉], Anthony Peyton[✉], and Wuliang Yin[✉], *Senior Member, IEEE*

Abstract—Until now, the Dodd–Deeds model has been used to evaluate the inductance change in an air-cored sensor in the presence of an infinitely large conducting plate. In practice, it can be applied to the sample relatively larger than the radius of the sensor coil (normally >3–5 times larger), which can be regarded as a plate sample with infinite planar size. However, in various practical applications, the size of the tested sample may not satisfy this condition. In this article, a modified analytical solution based on the Dodd–Deeds model is proposed, which has introduced a new initial integration point instead of 0 for the analytical inductance of the finite-size metallic plate. Theoretical derivation has been presented for the derivation of the initial integration point. Moreover, an inversely proportional relation can be observed between the initial integration point and the radius of the test sample. The simulation and experimental measurements for the thickness of several finite-size metallic samples have been carried out for the verification of the proposed method.

Index Terms—Eddy current testing, finite region, magnetic induction, nondestructive testing, thickness measurement.

I. INTRODUCTION

IN RECENT decades, nondestructive testing techniques have been developed for the need of sample evaluation. Compared with ultrasonic [1], [2] and X-ray [3] testing, eddy current testing is also one of the most widely used techniques in the field of nondestructive testing. As a noncontact detection method, eddy current testing has proved its reliability in a wide range of applications, such as defect inspection, conductivity and permeability measurements, and process monitoring [4]–[12]. Other than these applications, thickness measurement is also a significant application. Meanwhile, the analytical solutions proposed by Dodd and Deeds have been serving for decades for solving various

kinds of eddy current sensing problems such as thickness measurement of metallic plates [13].

Tai *et al.* [14] developed a self-designed instrument based on the pulsed eddy current to measure the sample thickness using a look-up table. The potential of multifrequency eddy current testing has also been explored. It has been found that the phase signature from the sensing coil can be used to measure the thickness of the metal sample [15], [16]. In [17], with the robust feature between the peak frequency and the sample thickness, the accuracy of the reconstructed thickness could be achieved within 3%. However, the error can arise with increased lift-offs. Various approaches from the time domain to the frequency domain have been exploited to address this issue [18]–[26]. Using the multifrequency spectra, a simplified model has been derived from the Dodd–Deeds analytical solution to compensate the error effect caused by the lift-off [18], [19]. In addition, an equivalent effect—a proportional relationship between the conductivity and thickness—has been found in thin plates [27]. Furthermore, Lu *et al.* [28] proposed a single-frequency measurement method with a planar sensor, which has a potential of on-line real-time measurement. However, these approaches are based on the condition that the size of the test samples is much larger (normally >3–5 times larger) than that of the sensor coils. Moreover, the truncated region eigenfunction expansion (TREE) method has been commonly used to make the computation numerically to solve it efficiently [29]. With the complicated and cumbersome boundary conditions for the small disk samples, TREE method can also be utilized for the computation of the impedance. However, with our modified analytical solution, the inductance/impedance can be accurately and efficiently simulated for the small sample.

In this article, to address the issue of the finite-size sample, we proposed a modified analytical solution for the inductance of a coil in the presence of a sample with a finite circular planar region. For this proposed method, the tested sample should be coaxial with the sensor. Through theoretical manipulations, the initial point of the integral, α_r , can be determined by the radius of the test sample. Moreover, experiments and simulations for the thickness measurements of several samples have been carried out for the verification of this feature. Sections II–IV present the mathematical derivations and experimental verifications of the proposed method.

Manuscript received January 19, 2020; accepted April 3, 2020. Date of publication April 13, 2020; date of current version September 15, 2020. This work was supported by the U.K. Engineering and Physical Sciences Research Council (EPSRC) under Grant EPP027237/1 [title: Real-time In-line Microstructural Engineering (RIME)]. The Associate Editor coordinating the review process was Subhas Chandra Mukhopadhyay. (*Corresponding authors: Mingyang Lu; Wuliang Yin.*)

The authors are with the School of Electrical and Electronic Engineering, The University of Manchester, Manchester M13 9PL, U.K. (e-mail: mingyang.lu@manchester.ac.uk; wuliang.yin@manchester.ac.uk).

Color versions of one or more of the figures in this article are available online at <http://ieeexplore.ieee.org>.

Digital Object Identifier 10.1109/TIM.2020.2987413

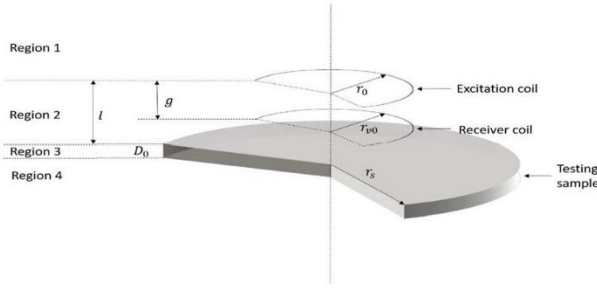


Fig. 1. Coil above an infinite conductive plate.

II. THEORETICAL DERIVATIONS OF THE MODIFIED ANALYTICAL SOLUTION—THE INITIAL INTEGRATION POINT α_r

In the field of eddy current testing, the mutual inductance between the excitation coil and the sensing coil is a key indicator of the property of the tested conductive sample. The analytical solution of a coil upon an infinite large testing plate given by Dodd and Deeds has provided a strong theoretical basis. However, this model can only be adopted in the condition that the size of the testing plate is three to five times larger than that of the sensor coil. However, in many practical applications, the size of the test sample may not satisfy this condition. Therefore, a modified analytical solution of inductance for the plate with finite dimensions is highly requisite.

As shown in Fig. 1, for the model of a coil above the infinite testing plate, the vector potential generated by the excitation coil in the r - z axis is [13]

$$A(r, z) = \frac{I\mu_0 N_e}{2} \int_0^\infty \frac{J_1(\alpha r) P(\alpha)}{\alpha^3} K(r, z, \alpha) \phi(\alpha) d\alpha \quad (1)$$

where

$$\phi(\alpha) = \frac{(\alpha_1 + \mu_1 \alpha)(\alpha_1 - \mu_1 \alpha) - (\alpha_1 + \mu_1 \alpha)(\alpha_1 - \mu_1 \alpha) e^{2\alpha_1 D_0}}{-(\alpha_1 - \mu_1 \alpha)(\alpha_1 - \mu_1 \alpha) + (\alpha_1 + \mu_1 \alpha)(\alpha_1 + \mu_1 \alpha) e^{2\alpha_1 D_0}} \quad (2)$$

$$\alpha_1 = \sqrt{\alpha^2 + j\omega\sigma\mu_1\mu_0} \quad (3)$$

$$K(r, z, \alpha) = 2 - e^{-\alpha(z-l_{e2})} - e^{-\alpha(z-l_{e1})} + e^{-\alpha z}(e^{-\alpha l_{e1}} - e^{-\alpha l_{e2}}) \quad (4)$$

$$P(\alpha) = \int_{\alpha r_{e1}}^{\alpha r_{e2}} \tau J_1(\tau) d\tau. \quad (5)$$

Furthermore, the induced voltage on the receiver coil is the integral of the induced vector potential over the whole receiver coil

$$V = N_v j\omega \int_s \mathbf{A} ds = \frac{N_v j\omega 2\pi r_{v0}}{(l_{v1} - l_{v2})^2 (r_{v1} - r_{v2})^2} \int_{l_{v1}}^{l_{v2}} \int_{r_{v1}}^{r_{v2}} r A(r, z) dr dz \quad (6)$$

$$r_{v0} = \frac{r_{v1} + r_{v2}}{2}. \quad (7)$$

Thus, the inductance change due to the presence of the sample is (the subtraction between the inductance with the

sample and without the sample, i.e., free space [11])

$$\Delta L(\omega) = \frac{V|_{\sigma, \mu_1} - V|_{\sigma=0, \mu_0}}{j\omega I} = \frac{\pi r_0 N_e N_v \mu_0}{(l_{v1} - l_{v2})^2 (r_{v1} - r_{v2})^2} \int_0^\infty \frac{P^2(\alpha)}{\alpha^6} e^{-\alpha(2l+h+g)} (1 - e^{-2\alpha h}) \phi(\alpha) d\alpha. \quad (8)$$

$$h = l_{e2} - l_{e1}. \quad (9)$$

D_0 , μ_1 , and σ denote the thickness, relative permeability, and electrical conductivity of the sample, respectively. μ_0 represents the permeability of the free space. N_e and N_v denote the turns of the excitation and receiver coil, respectively. r_{e1} and r_{e2} denote the inner and outer radii of the excitation coil, respectively. r_{v1} and r_{v2} denote the inner and outer radii of the receiver coil, respectively. l_{e1} and l_{e2} denote the lower and upper height of the excitation coil, respectively. l_{v1} and l_{v2} denote the lower and upper height of the receiver coil, respectively. l denotes the lift-off and g the gap between the excitation and receiver coils. J_1 denotes a first-order Bessel function of the first kind. α and τ are the integration variables.

As shown in Fig. 2, in the Dodd–Deeds model, the integration of α ranges from 0 to infinity, where $\alpha = 0$ corresponds to the plate section of the infinite radius ($r = r_s = \infty$) and $\alpha = \infty$ to the center of the sample plate ($r = 0$). Therefore, in the proposed method, by replacing $\alpha = 0$ with $\alpha = \alpha_r$, the inductance for a plate with a finite radius can be simulated. The following mathematical manipulation is to explain the rationale behind changing the integration range of α .

By referring to the manipulation of the Dodd–Deeds analytical formulations [13], the model of a coil above a plate can be divided into four regions, as shown in Fig. 1. For each region, the magnetic vector potential formulation \mathbf{A} can be represented by a product of two polynomials, $R(r)$ and $Z(z)$

$$\frac{\partial^2 A}{\partial r^2} + \frac{1}{r} \frac{\partial A}{\partial r} + \frac{\partial^2 A}{\partial z^2} - \frac{A}{r^2} + \omega^2 \mu_i \sigma_i A - j\omega \mu_i \sigma_i A = 0 \quad (10)$$

$$r \in [0, r_s] \quad (11)$$

where i denotes the i th layer/region conductor.

In (11), the defined range of r for the infinite plate case is from 0 to $r_s = \infty$. However, for a sample with finite radius, r ranges from 0 to a constant r_s .

By substituting \mathbf{A} with $R(r)Z(z)$, the field can be expressed as

$$\frac{1}{R(r)} \frac{\partial^2 R(r)}{\partial r^2} + \frac{1}{r R(r)} \frac{\partial R(r)}{\partial r} + \frac{1}{Z(z)} \frac{\partial^2 Z(z)}{\partial z^2} - \frac{1}{r^2} + \omega^2 \mu_i \sigma_i - j\omega \mu_i \sigma_i = 0. \quad (12)$$

Using the principle of separation of variables, a separation “constant” α^2 is introduced [13]

$$\frac{1}{Z(z)} \frac{\partial^2 Z(z)}{\partial z^2} = \alpha^2 - \omega^2 \mu_i \sigma_i + j\omega \mu_i \sigma_i. \quad (13)$$

Then substitute (13) into (12), which gives

$$\alpha^2 = \frac{1}{r^2} - \frac{1}{r R(r)} \frac{\partial R(r)}{\partial r} - \frac{1}{R(r)} \frac{\partial^2 R(r)}{\partial r^2}. \quad (14)$$

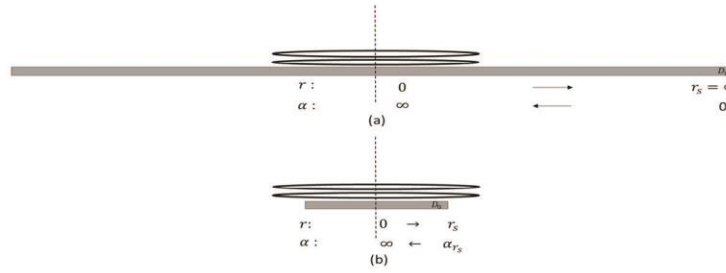


Fig. 2. Illustration of the integrational path for the proposed method. (a) Infinite plate where r ranges from 0 to ∞ . (b) Finite plate where r ranges from 0 to r_s .

Since the solution of $R(r)$ can be expressed in terms of Bessel functions, $R(r)$ can be represented as [13]

$$R(r) = CJ_1(ar) + DY_1(ar). \quad (15)$$

Due to the divergence of Y_1 at the origin, $D=0$ in all regions.

Combining (14) and (15), we can obtain α^2

$$\alpha^2 = \frac{1}{r^2} - \frac{\alpha}{4rJ_1(ar)}(2(J_0(ar) - J_2(ar)) - ar(-3J_1(ar) + J_3(ar))) \quad (16)$$

where J_0 , J_2 , and J_3 are the zero-, second-, and third-order Bessel function of the first kind.

Therefore, α can be derived by finding the solution of the following equation:

$$\alpha^2 - \frac{1}{r^2} + \frac{\alpha}{4rJ_1(ar)}(2(J_0(ar) - J_2(ar)) - ar(-3J_1(ar) + J_3(ar))) = 0. \quad (17)$$

By multiplying r^2 on both sides of (17)

$$(ar)^2 - 1 + \frac{ar}{4J_1(ar)}(2(J_0(ar) - J_2(ar)) - ar(-3J_1(ar) + J_3(ar))) = 0. \quad (18)$$

Substitute ar with x , then equation (18) is converted as

$$(x)^2 - 1 + \frac{x}{4J_1(x)}(2(J_0(x) - J_2(x)) - x(-3J_1(x) + J_3(x))) = 0. \quad (19)$$

Assuming x_0 is the solution of the above equation, the integral range of α is related to the defined variable r , which can be written as $\alpha = x_0/r$, that is, α is inversely proportional to r . Taking the example of a plate with an infinite planar dimension, the defined range of r is from 0 to ∞ [referring to (10) and (11)]. By referring to (19), the corresponding range of α is from $\alpha|_{r=0} = \infty$ to $\alpha|_{r=\infty} = 0$. For a plate with a finite radius, r ranges from 0 to r_s , and the corresponding range of α is from $\alpha|_{r=0} = \infty$ to a constant value $\alpha|_{r=r_s} = \alpha_{r_s} = x_0/r_s = 3.518/r_s$.

Therefore, for a finite-size sample, the vector potential involves the integration from $\alpha|_{r=r_s} = \alpha_{r_s}$ to $\alpha|_{r=0} = \infty$.

$$A = \frac{I\mu_0 N_e}{2} \int_{\alpha_{r_s}}^{\infty} \frac{J_1(ar)P(a)}{\alpha^3} K(r, z, a) \phi(a) da. \quad (20)$$

Furthermore, the inductance change due to the presence of the finite-size plate is

$$\Delta L(\omega) = \frac{\pi r_0 N_b N_e \mu_0}{(l_{v1} - l_{v2})^2 (r_{v1} - r_{v2})} \int_{\alpha_{r_s}}^{\infty} \frac{P^2(a)}{\alpha^6} e^{-\alpha(2l+h+g)} (1 - e^{-2ah}) \phi(a) da \quad (21)$$

with $\alpha_{r_s} = 3.518/r_s$ where r_s is the radius of the sample.

It can be seen that the integral limit of (21) is different to the case of the infinite-size plate (8).

III. EXPERIMENTAL AND SIMULATION SETUP

In this article, both the experimental measurements (using the impedance analyzer) and the simulations [using the modified analytical solution and the software (COMSOL)] have been carried out to validate the theoretical deviations. In the process of the measurements, the air-cored coaxial sensor was located coaxially with circular planar samples, as shown in Fig. 3. Samples of copper and aluminum plates were selected because of availability. The conductivities of these two materials are 57 and 35 MS/m. The copper plate has a thickness of 1 mm and a range of diameters (from 25 to 45 mm in steps of 5 mm), while the aluminum plate has a diameter of 40 mm and thickness range from 22 to 132 μm . The copper plates were used to verify the derived theory, while the aluminum plates with different thicknesses were used for further application of the thickness measurement. The impedance analyzer can operate from 100 Hz to 510 kHz in a logarithmic step of 0.02735 with high precision and the excitation voltage in the measurement was set to 0.3 V. To test the effect of different sensor geometries, three sensors of the different radii (28, 40, and 52 mm) have been used. The experimental and sensor setup are shown in Fig. 4 and Table I.

From Figs. 6–11, the mutual impedance (ΔZ) between the excitation coil and the receiving coil measured through the Zurich impedance analyzer [Fig. 4(a)] are presented. Due to the phase difference between the induced voltage and the excitation current, the tested impedance should be complex. Therefore, the inductance can be presented by dividing the mutual impedance by the excitation frequency in the experimental measurements, as shown in the following equations:

$$\Delta Z = R + j\omega \Delta L \quad (22)$$

$$\Delta L = \text{Re} \left(\frac{Z_{\text{sample}} - Z_{\text{air}}}{j\omega} \right) \quad (23)$$

$$R\omega^{-1} = -\text{Im} \left(\frac{Z_{\text{sample}} - Z_{\text{air}}}{j\omega} \right) j \quad (24)$$

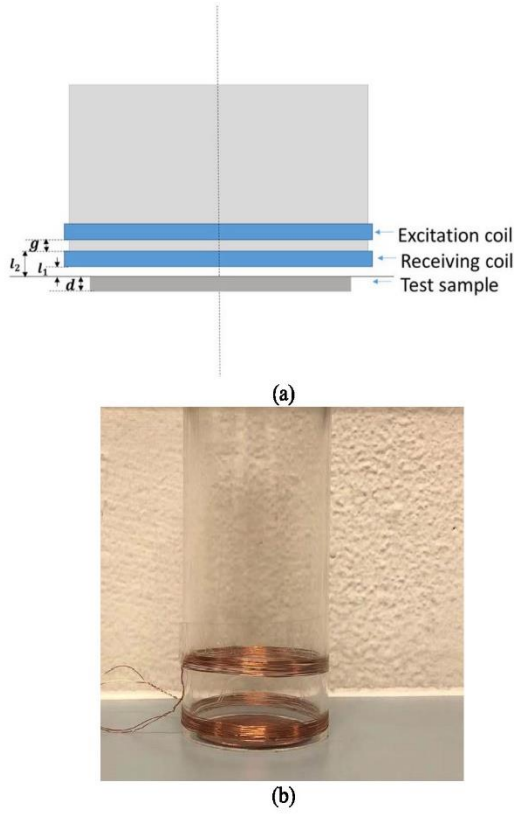


Fig. 3. Air-cored sensor above the tested plate. (a) Schematic setup. (b) Actual setup.

TABLE I
SENSOR PARAMETERS

Inner and outer radii of the excitation coil (r_{e1} / r_{e2})	28 mm/28.25 mm 40 mm/40.25 mm 52 mm/52.25 mm
Inner and outer radii of the sensing coil (r_{v1} / r_{v2})	28 mm/28.25 mm 40 mm/40.25 mm 52 mm/52.25 mm
Height of the excitation coil ($l_{e2} - l_{e1}$)	4 mm
Height of the sensing coil ($l_{v2} - l_{v1}$)	4 mm
Turns of excitation coil and receiving coil (N_e / N_v)	15/15
Plate thickness (D_0)	1 mm for copper, 22 μ m – 132 μ m for aluminium
The gap between two coils (g)	15 mm

where Z_{sample} denotes the impedance caused by the metallic sample plate and Z_{air} denotes the impedance in the air.

IV. RESULTS

A. Validation of the Modified Analytical Solution

As illustrated in Fig. 2, compared with the infinite planar plate, the main difference for the finite region analytical solution is that it starts at different points for the integral path. First, both the analytical solution and the simulation software (COMSOL) were compared to validate the proposed method. The simulated models are shown in Fig. 5. Fig. 6 shows the inductance change caused by the copper plate.

It can be observed that for both metallic plates, the results are matched under the sweeping frequency ranging from 10 Hz

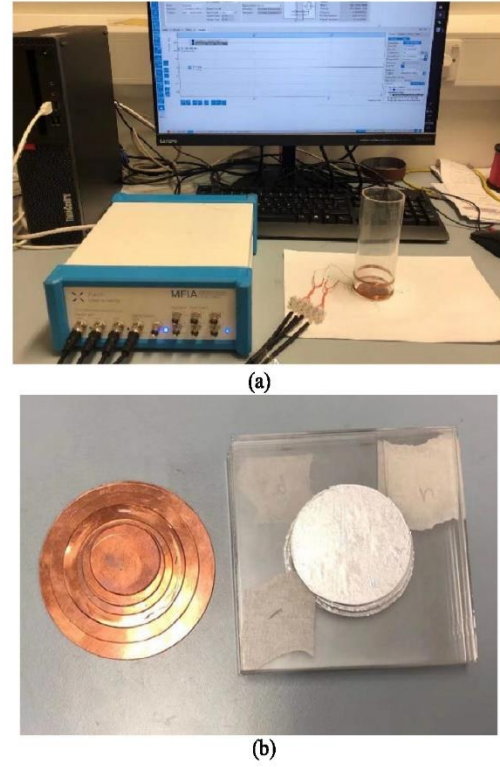


Fig. 4. Experimental setup. (a) Measurement setup. (b) Circular sample plates.

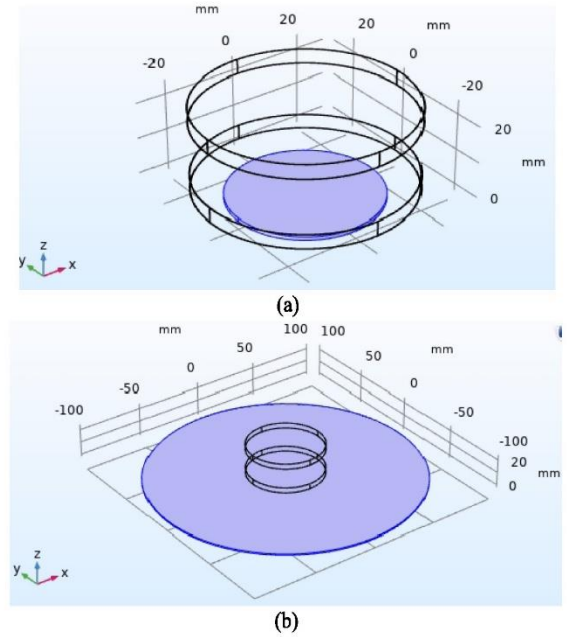


Fig. 5. Simulated model. (a) Plate with a radius of 20 mm (84k elements). (b) Plate with a radius of 100 mm (142k elements).

to 10 MHz. Since the test samples are nonmagnetic, there is no zero-crossing point for the inductance change. As the frequency increases, it would finally reach a saturated value for the inductance change and approach zero for the detected resistance–frequency combined term $R\omega^{-1}$. A peak frequency feature can be observed from $R\omega^{-1}$, which is found to be shifted rightward as the size of the sample decreases. This is possibly because the magnetic flux interacts less with the plate for the sample with a smaller radius.

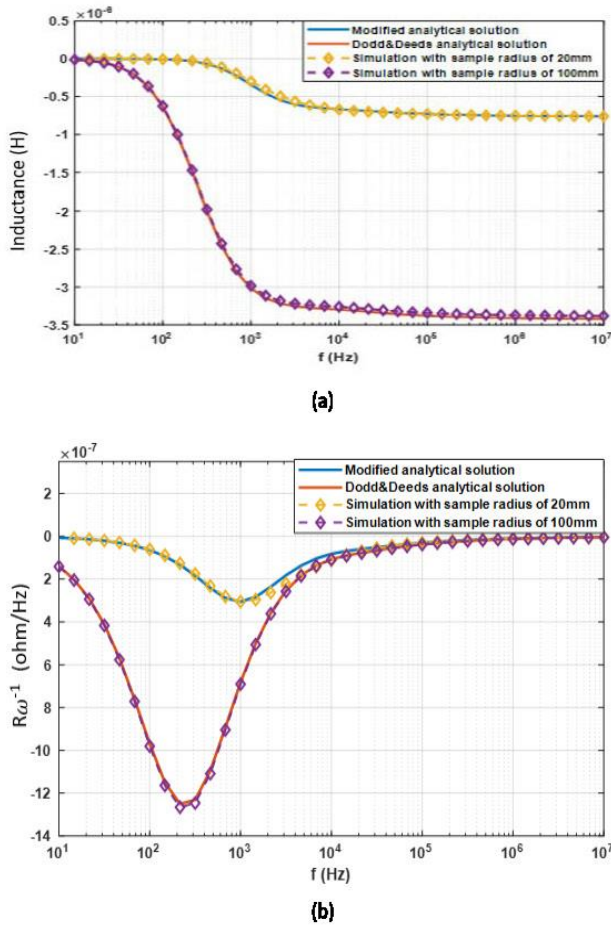


Fig. 6. (a) Inductance change caused by copper plates. (b) Change in $R\omega^{-1}$ caused by copper plates.

B. Effect of the Sensor Coil Dimensions

The modified analytical solution is associated with the initial point of α . Hence, some measurements have been carried out to determine the value of α_r . Figs. 7 and 8 depict the inductance change in both the measured results and the modified analytical solutions under the same three sensors with the radii of 28, 40, and 52 mm, respectively, but different sample radii.

From the results of both simulations and measurements, the value of the initial point α_{r_s} is immune to the sensor size. That is, for a fixed-size test sample, no matter what size of the sensor, α_{r_s} remains unchanged [since α_{r_s} is merely related to the size of the sample, referring to (18)]. Besides, the value of α_{r_s} reduces with the increase in the sample radius, which is consistent with the theoretical derivations.

C. Effect of the Sample Size

From previous experiments, it can be noticed that α_{r_s} is not related to the size of the sensor. Furthermore, samples with different radii were measured under the same sensor with the sensor radius of 40 mm. Fig. 9 shows the results of both the modified analytical solutions and measurements for copper plates with different radii. The results are matched by finding the appropriate α_{r_s} . The value of α_{r_s} under different sample radii is shown in Fig. 10.

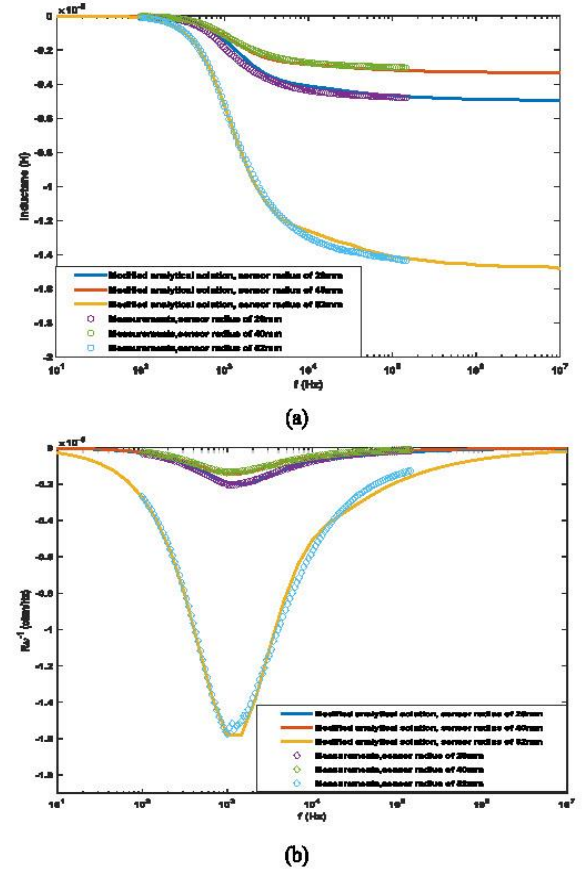


Fig. 7. (a) Inductance change caused by copper plates with the radius of 17.5 mm. (b) $R\omega^{-1}$ caused by copper plates with the radius of 17.5 mm.

As can be seen from Fig. 10, the value of α_{r_s} is proportional to the reciprocal of the sample radius (i.e., $\alpha_{r_s} = \text{const.} \times 1/r_s$) and, from the experimental experience, the constant is ~ 3.518 .

D. Thickness Measurement Based on the Modified Analytical Solution

The proposed method can be used to test the thickness of plate samples with the same radius. Since α_{r_s} is immune to the sensor radius but related to the sample radius, it can be set to an appropriate fixed value. In our previous studies, the peak frequency caused from $R\omega^{-1}$ is associated with the sample thickness and the sample conductivity. Applying this principle with the same material samples used in the testing, the larger the thickness, the lower the peak frequency. Consequently, the thickness of the test samples can be estimated by matching the peak frequency of the modified analytical solution. (Prior to the measurement, a look-up table is obtained from the modified analytical solution which contains the peak frequency information for different thicknesses under the same conductivity. By referring to the table, the thickness of the sample can be predicted.)

In the measurements, the thickness of the aluminum sample varies from 22 to 132 μm . The operation frequency ranges from 1 to 505 kHz. As Fig. 11 depicts the result of the modified analytical solution matches well with the measurement. Besides, the peak frequency using both the original analytical solution and the modified analytical solution

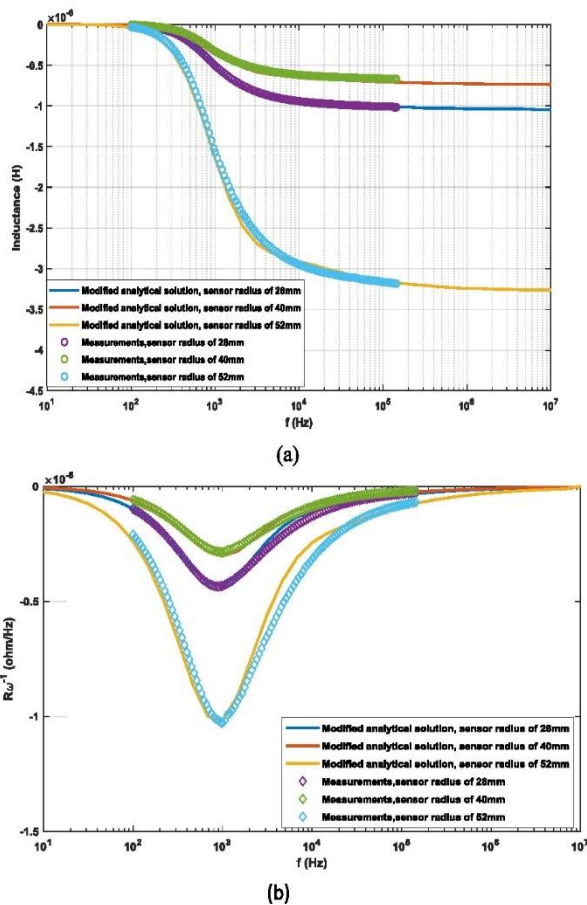


Fig. 8. (a) Inductance change caused by copper plates with the radius of 22.5 mm. (b) Change in $R\omega^{-1}$ caused by copper plates with the radius of 22.5 mm.

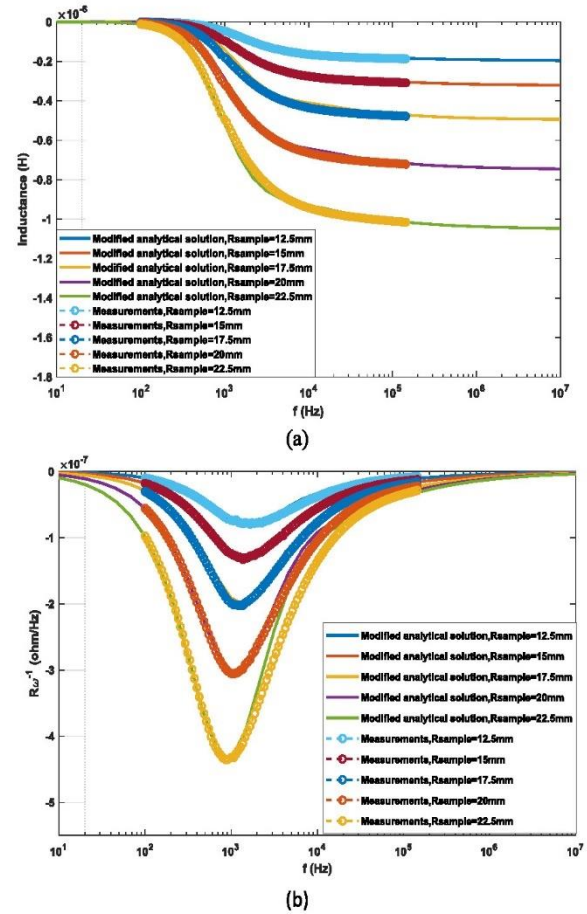


Fig. 9. (a) Inductance changes under various radii of the copper samples. (b) Change in $R\omega^{-1}$ under various radii of the copper samples.

TABLE II

PEAK FREQUENCY OF DODD–DEEDS ANALYTICAL SOLUTION AND MODIFIED ANALYTICAL SOLUTION FOR THE ALUMINUM PLATES

Sample thickness (μm)	Peak frequency (kHz)	
	Dodd Deeds analytical solution	Modified analytical solution
22	13.335	42.170
44	6.190	23.714
66	4.217	14.678
88	3.162	11.007
110	2.610	9.085
132	1.957	7.499

TABLE III

ACTUAL AND ESTIMATED THICKNESS FOR THE ALUMINUM PLATES

Material	Actual thickness (μm)	Estimated thickness (μm)	Error (%)
Aluminium	22	22.21	0.95
	44	43.16	-1.91
	66	66.90	1.36
	88	88.05	0.06
	110	108.57	-1.30
	132	129.68	-1.76

is listed in Table II. It can be seen that there is a huge difference for finite planar dimension samples compared with the original analytical solution. Moreover, the principle of the thickness reconstruction is fitting the peak frequency of

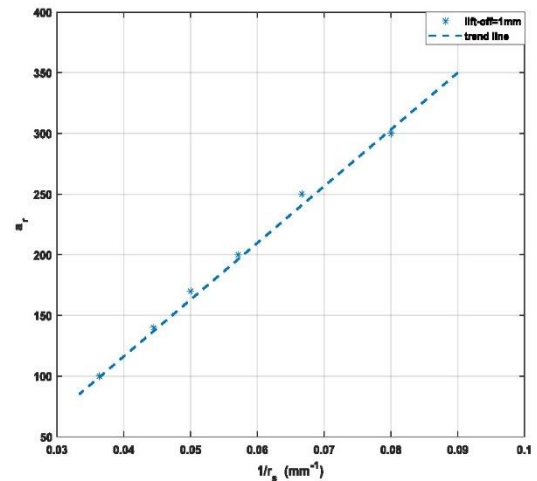


Fig. 10. Relationship between α_{TS} and the reciprocal of sample radius.

the simulation to that of the measurement, and therefore, it leads to a larger error for thickness prediction as shown in Table III and Fig. 12. The fitting of the peak frequency feature is one of the commonly used methods for sample properties' reconstruction [17]–[19], [30]. As in [30], we use a first-order function to approximate the curve and fit the experimental and simulated curves in a least squared sense. Once the first-order system is obtained, its peak frequency can be obtained easily. Table III illustrates the estimated thickness

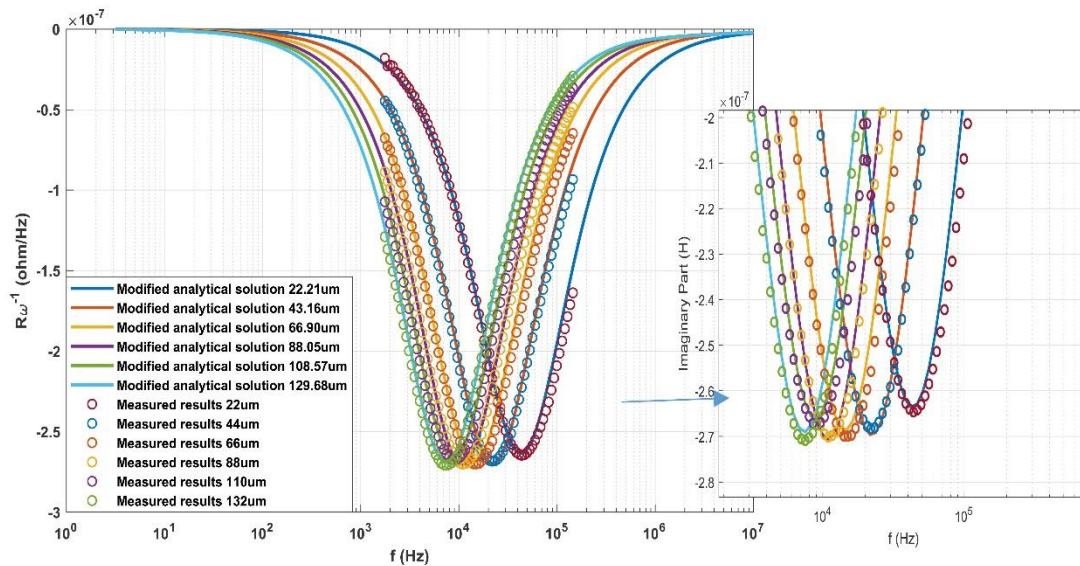


Fig. 11. Change of $R\omega^{-1}$ under varying thickness samples.

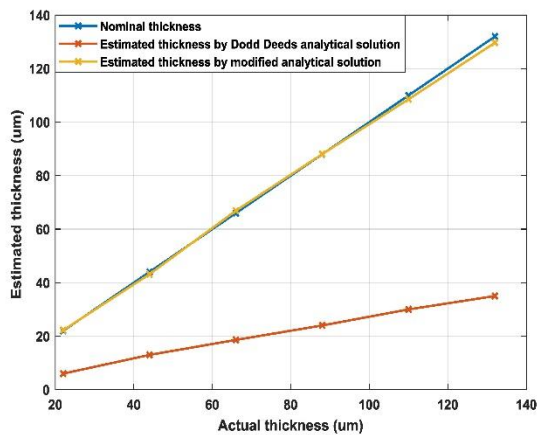


Fig. 12. Estimated thickness by Dodd Deeds analytical solution and modified analytical solution.

from the modified analytical solution and the error between the actual and the estimated thicknesses. It can be seen from Table III that the error from testing can be achieved within 2%. Fig. 12 demonstrates the estimation results from both methods and the error caused using the infinite model—the original Dodd–Deeds is significantly inaccurate.

V. CONCLUSION

This article has proposed a modified analytical solution for the metallic sample with a finite dimension. Based on this method, an eddy current thickness measurement technique has been presented. Previously, it was found that the Dodd–Deeds analytical solution cannot be applied to the situation when the radius of the testing sample does not exceed three to five times of the sensor coil. In this article, an alternative initial integral point α_{r_s} has been found in the modified analytical solution for the finite-size samples. From the results of measurements and modified analytical solutions, it is shown that α_{r_s} is related to the size of the testing sample, instead of the size of the sensor. Moreover, α_{r_s} has been found to be inversely proportional to

the size of the testing sample. Using this method, the thickness of the circular sample can be accurately reconstructed with a small error within 2%.

In this method, the peak frequency feature (instead of the magnitude) is used to reconstruct the thickness of the sample. Before measuring, the conductivity of the sample material is taken as known. Besides, the samples have to be cylindrical, and for noncylindrical shapes, the analytical solution is not valid. The results from the measurements are obtained based on the coil-sample coaxially assembled condition. Error will be induced due to axial offset situation.

REFERENCES

- [1] A. M. T. Hassan and S. W. Jones, "Non-destructive testing of ultra high performance fibre reinforced concrete (UHPFRC): A feasibility study for using ultrasonic and resonant frequency testing techniques," *Construct. Building Mater.*, vol. 35, pp. 361–367, Oct. 2012.
- [2] I. N. Prassianakis and N. I. Prassianakis, "Ultrasonic testing of non-metallic materials: Concrete and marble," *Theor. Appl. Fract. Mech.*, vol. 42, no. 2, pp. 191–198, Nov. 2004.
- [3] R. Hanke, T. Fuchs, and N. Uhlmann, "X-ray based methods for non-destructive testing and material characterization," *Nucl. Instrum. Methods Phys. Res. A, Accel., Spectrometers, Detectors Associated Equip.*, vol. 591, no. 1, pp. 14–18, Jun. 2008.
- [4] D. J. Harrison, L. D. Jones, and S. K. Burke, "Benchmark problems for defect size and shape determination in eddy-current nondestructive evaluation," *J. Nondestruct. Eval.*, vol. 15, no. 1, pp. 21–34, Mar. 1996.
- [5] A. Bernieri, G. Betta, L. Ferrigno, and M. Laracca, "Crack depth estimation by using a multi-frequency ECT method," *IEEE Trans. Instrum. Meas.*, vol. 62, no. 3, pp. 544–552, Mar. 2013.
- [6] A. Sophian, G. Y. Tian, D. Taylor, and J. Rudlin, "A feature extraction technique based on principal component analysis for pulsed eddy current NDT," *NDT E Int.*, vol. 36, no. 1, pp. 37–41, Jan. 2003.
- [7] G. Y. Tian and A. Sophian, "Defect classification using a new feature for pulsed eddy current sensors," *NDT E Int.*, vol. 38, no. 1, pp. 77–82, Jan. 2005.
- [8] J. C. Moulder, E. Uzal, and J. H. Rose, "Thickness and conductivity of metallic layers from eddy current measurements," *Rev. Sci. Instrum.*, vol. 63, no. 6, pp. 3455–3465, Jun. 1992.
- [9] X. Ma, A. J. Peyton, and Y. Y. Zhao, "Eddy current measurements of electrical conductivity and magnetic permeability of porous metals," *NDT E Int.*, vol. 39, no. 7, pp. 562–568, Oct. 2006.
- [10] X. Chen and Y. Lei, "Electrical conductivity measurement of ferromagnetic metallic materials using pulsed eddy current method," *NDT E Int.*, vol. 75, pp. 33–38, Oct. 2015.

- [11] M. Lu, R. Huang, W. Yin, Q. Zhao, and A. Peyton, "Measurement of permeability for ferrous metallic plates using a novel lift-off compensation technique on phase signature," *IEEE Sensors J.*, vol. 19, no. 17, pp. 7440–7446, Sep. 2019.
- [12] W. Yin, A. J. Peyton, G. Zysko, and R. Denno, "Simultaneous noncontact measurement of water level and conductivity," *IEEE Trans. Instrum. Meas.*, vol. 57, no. 11, pp. 2665–2669, Nov. 2008.
- [13] C. V. Dodd and W. E. Deeds, "Analytical solutions to eddy-current probe-coil problems," *J. Appl. Phys.*, vol. 39, no. 6, pp. 2829–2838, 1968.
- [14] C. Tai, J. H. Rose, and J. C. Moulder, "Thickness and conductivity of metallic layers from pulsed eddy-current measurements," *Rev. Sci. Instrum.*, vol. 67, no. 11, pp. 3965–3972, Nov. 1996.
- [15] E. Pinotti and E. Puppini, "Simple lock-in technique for thickness measurement of metallic plates," *IEEE Trans. Instrum. Meas.*, vol. 63, no. 2, pp. 479–484, Feb. 2014.
- [16] W. Yin and A. J. Peyton, "Thickness measurement of metallic plates with an electromagnetic sensor using phase signature analysis," *IEEE Trans. Instrum. Meas.*, vol. 57, no. 8, pp. 1803–1807, Aug. 2008.
- [17] W. Yin and A. J. Peyton, "Thickness measurement of non-magnetic plates using multi-frequency eddy current sensors," *NDT E Int.*, vol. 40, no. 1, pp. 43–48, Jan. 2007.
- [18] W. Yin and K. Xu, "A novel triple-coil electromagnetic sensor for thickness measurement immune to lift-off variations," *IEEE Trans. Instrum. Meas.*, vol. 65, no. 1, pp. 164–169, Jan. 2016.
- [19] M. Lu, L. Yin, A. J. Peyton, and W. Yin, "A novel compensation algorithm for thickness measurement immune to lift-off variations using eddy current method," *IEEE Trans. Instrum. Meas.*, vol. 65, no. 12, pp. 2773–2779, Dec. 2016.
- [20] J. Kral, R. Smid, H. M. G. Ramos, and A. L. Ribeiro, "The lift-off effect in eddy currents on thickness modeling and measurement," *IEEE Trans. Instrum. Meas.*, vol. 62, no. 7, pp. 2043–2049, Jul. 2013.
- [21] A. L. Ribeiro, H. G. Ramos, and J. C. Arez, "Lift-off insensitive thickness measurement of aluminum plates using harmonic eddy current excitation and a GMR sensor," *Measurement*, vol. 45, no. 9, pp. 2246–2253, Nov. 2012.
- [22] J. R. S. Avila, M. Lu, R. Huang, Z. Chen, S. Zhu, and W. Yin, "Accurate measurements of plate thickness with variable lift-off using a combined inductive and capacitive sensor," *NDT E Int.*, vol. 110, Mar. 2020, Art. no. 102202.
- [23] M. Lu, Y. Xie, W. Zhu, A. Peyton, and W. Yin, "Determination of the magnetic permeability, electrical conductivity, and thickness of ferrite metallic plates using a multifrequency electromagnetic sensing system," *IEEE Trans. Ind. Informat.*, vol. 15, no. 7, pp. 4111–4119, Jul. 2019.
- [24] M. Lu, X. Meng, L. Chen, R. Huang, W. Yin, and A. Peyton, "Measurement of ferromagnetic slabs permeability based on a novel planar triple-coil sensor," *IEEE Sensors J.*, vol. 20, no. 6, pp. 2904–2910, Mar. 2020.
- [25] M. Lu *et al.*, "Conductivity lift-off invariance and measurement of permeability for ferrite metallic plates," *NDT E Int.*, vol. 95, pp. 36–44, Apr. 2018.
- [26] M. Lu, W. Zhu, L. Yin, A. J. Peyton, W. Yin, and Z. Qu, "Reducing the lift-off effect on permeability measurement for magnetic plates from multifrequency induction data," *IEEE Trans. Instrum. Meas.*, vol. 67, no. 1, pp. 167–174, Jan. 2018.
- [27] W. Yin *et al.*, "An equivalent-effect phenomenon in eddy current non-destructive testing of thin structures," *IEEE Access*, vol. 7, pp. 70296–70307, 2019.
- [28] M. Lu *et al.*, "Thickness measurement of non-magnetic steel plates using a novel planar triple-coil sensor," *NDT E Int.*, vol. 107, Oct. 2019, Art. no. 102148.
- [29] T. P. Theodoulidis and J. R. Bowler, "The truncated region eigenfunction expansion method for the solution of boundary value problems in eddy current nondestructive evaluation," in *Proc. AIP Conf.*, 2005, vol. 760, no. 1, pp. 403–408.
- [30] W. Yin, A. J. Peyton, and S. J. Dickinson, "Simultaneous measurement of distance and thickness of a thin metal plate with an electromagnetic sensor using a simplified model," *IEEE Trans. Instrum. Meas.*, vol. 53, no. 4, pp. 1335–1338, Aug. 2004.



Ruochen Huang is currently pursuing the Ph.D. degree with School of Electrical and Electronics Engineering, The University of Manchester, Manchester, U.K., under the supervision of Wuliang Yin.

He is mainly working on finite-element method (FEM) modeling software packages for electromagnetic (EM) simulations.



Mingyang Lu received the B.S. and Ph.D. degrees with the School of Electrical and Electronic Engineering, The University of Manchester, Manchester, U.K., in 2014 and 2018, respectively, under the supervision of Wuliang Yin.

He is mainly working on developing a finite-element method (FEM) software to solve electromagnetic (EM) simulation taking into account random geometry and material properties (including microstructure). He is currently a Research Associate with The University of Manchester. He has

authored or coauthored more than 30 publications. His current research interests include modeling magnetic induction effects, FEM modeling software packages on EM simulations, and inversion of EM properties for metallic structure.



Anthony Peyton received the B.Sc. degree in electrical engineering and electronics and the Ph.D. degree from the University of Manchester Institute of Science and Technology (UMIST), Manchester, U.K., in 1983 and 1986, respectively.

He was a Principal Engineer with Kratos Analytical Ltd., Manchester, from 1986 to 1989, where he was involved in developing precision electronic instrumentation systems for magnetic sector and quadrupole mass spectrometers. He joined the Process Tomography Group, UMIST, where he was a lecturer. In 1996, he joined Lancaster University, Lancaster, U.K., as a Senior Lecturer, where he was a Reader in electronic instrumentation in 2001, and a Professor in 2004. Since 2004, he has been a Professor of electromagnetic tomography engineering with The University of Manchester, Manchester. His current research interests include instrumentation, applied sensor systems, and electromagnetics.



Wuliang Yin (Senior Member, IEEE) received the B.Sc. degree and the M.Sc. degrees in electronic measurement and instrumentation from Tianjin University, Tianjin, China, in 1992 and 1995, respectively, and the Ph.D. degree in automotive electronics from Tsinghua University, Beijing, China, in 1999.

He was appointed as a Mettler Toledo (MT) Sponsored Lecturer with the Department of Electrical and Electronic Engineering, School of Engineering, The University of Manchester, Manchester, U.K., in 2012, and was promoted to a Senior Lecturer in 2016. He has authored one book, more than 230 articles, and was granted more than ten patents in the area of electromagnetic sensing and imaging.

Dr. Yin was a recipient of the 2014 and 2015 Williams Award from the Institute of Materials, Minerals and Mining and the Science and Technology Award from the Chinese Ministry of Education in 2000.

Chapter 6 Measurement of permeability for ferrous metallic plates using a novel lift-off compensation technique on phase signature

Mingyang Lu, **Ruochen Huang**, Wuliang Yin, Qian Zhao, Anthony Peyton

IEEE Sensors Journal, vol. 19, no. 17, 2019.

In this chapter, a novel algorithm is proposed to eliminate the deviation of the phase for ferrous sample plates caused by the lift-off of the sensor probe. The algorithm is based on two basic features. Firstly, in the multi-frequency spectra, the phase of the impedance will grow with the decreased lift-off. Secondly, the amplitude of the detected induced response (impedance) will rise up with small sensor lift-offs. Based on this sophisticated phase compensating algorithm, the phase without the effect of the unknown lift-off can be reconstructed and the magnetic permeability of the ferrous plate can be estimated from the measured impedance.

Measurement of Permeability for Ferrous Metallic Plates Using a Novel Lift-Off Compensation Technique on Phase Signature

Mingyang Lu¹, Ruochen Huang, Wuliang Yin², *Senior Member, IEEE*, Qian Zhao, and Anthony Peyton³

Abstract—Lift-off of sensor affects the prediction of electromagnetic properties for both ferrous and non-ferrous steel plates. In this paper, we developed a strategy to address this issue for ferrous plates. With increased lift-off, the phase of the measured impedance for steel plates reduces. Meanwhile, the magnitude of the impedance signal decreases. Based on these facts, a phase compensation algorithm is developed which corrects the phase change due to lift-off considering the magnitude of the impedance signal. Further, a new magnetic permeability prediction technique is presented, which has been validated by analytical and measured results. With this new technique, the error in permeability prediction is less than 2% within the range of lift-offs tested.

Index Terms—Measurement of magnetic permeability, new compensation algorithm, phase signature, Eddy current sensor, lift-off variation, ferrous plates.

I. INTRODUCTION

ELECTROMAGNETIC (EM) technique has been applied for various implications, for example, electrical conductivity perdition, magnetic permeability measurement, surface crack detection, and non-destructive online welding [1]–[6]. Nevertheless, sensors lift-offs can influence the performance of these EM implications. Novel sensor setup, induced responses post-demodulation, and measurement approaches [7]–[9] were used to decrease the error caused by sensors lift-offs. Currently, a few types of research have proposed some new techniques based on the impedance phase feature of the measured multi-frequency spectra to compensate measurements error due to lift-offs [10]. Although the phase can usually be deduced from some analytical approaches such as Dodd Deeds method and finite edge-element technique, most of them commonly require sophisticated and tedious calculations which are inefficient and impossible for some simultaneous testing techniques such as online measurements and welding post-inspection [11]. Consequently, more efficient and compendious methods are imperative to compute the multi-frequency

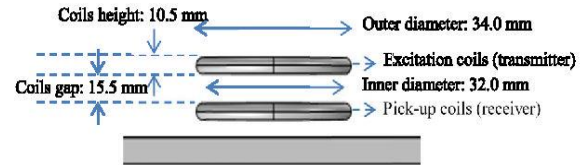


Fig. 1. EM sensor.

impedance phase, which can be used for various EM applications such as the steels parameters reconstruction and surface crack inspection. Although the proposed approach from [10] was verified to be able to reduce the sensors lift-offs effects on the output multi-frequency impedance phase, the phase error caused by the lift-offs is non-negligible under more precise non-contact measurement with significant lift-offs. Moreover, most of the aforementioned works are related to non-magnetic specimens or just utilize simple characteristics of impedance phase of ferrous specimens.

This paper proposes a novel algorithm to reduce the error of impedance phase for ferrous steels due to sensors lift-offs. The algorithm is based on two basic features. For one side, multi-frequency impedance phases will grow with reduced lift-offs. For the other side, the amplitude of the detected induced response (impedance) will rise up with small sensor lift-offs. Based on this sophisticated phase compensating algorithm, ferrous plate magnetic permeability can be deduced from the measured impedance. Comparing the analytical and measured results for some duplex-phase (DP) steels specimens with various magnetic permeability, this approach has been proved to be accurate enough for the measurement of ferrous plate's magnetic permeability.

II. EM SENSORS SETUP

As can be seen from figure 1 and table 1, considering sensors accessibility for experiments and analytical simulations, EM sensor was designed to be 2 co-axially coupled air-cored loop coils: excitation coils and pick-up coils with identical size turns and materials (copper coil). In table 1, a series of lift-off spacers are used to test the lift-off influences on the impedance phase.

III. COMPENSATION OF IMPEDANCE PHASE ERROR DUE TO LIFT-OFFS

From our previous researches, the magnitude of the detected response impedance and a frequency feature - zero-crossing frequency were found to grow with reduced sensor lift-offs [12]–[14]. It is also observed that the impedance phase rise

Manuscript received March 16, 2019; revised April 26, 2019; accepted May 9, 2019. Date of publication May 13, 2019; date of current version August 6, 2019. This work was supported in part by the Shanxi Province Scientific International Cooperation Project of China under Grant 201803D421038. The associate editor coordinating the review of this paper and approving it for publication was Dr. Francis P. Hindle. (Corresponding author: Wuliang Yin.)

M. Lu, R. Huang, and A. Peyton are with the School of Electrical and Electronic Engineering, The University of Manchester, Manchester M13 9PL, U.K.

W. Yin is with the School of Electrical and Electronic Engineering, The University of Manchester, Manchester M13 9PL, U.K., and also with the School of Instrument and Electronics, North University of China, Taiyuan 030051, China (e-mail: wuliang.yin@manchester.ac.uk).

Q. Zhao is with the College of Engineering, Qufu Normal University, Qufu 273165, China.

Digital Object Identifier 10.1109/JSEN.2019.2916431

1558-1748 © 2019 IEEE. Personal use is permitted, but republication/redistribution requires IEEE permission.

See http://www.ieee.org/publications_standards/publications/rights/index.html for more information.

TABLE I
 PROBES PROPERTIES

	Values
$2r_i$ (Inner diameter)/mm	32.0
$2r_o$ (Outer diameter)/mm	34.0
l_0 (lift-offs)/mm	0.8, 2.3, 3.8
h (coils height)/mm	10.5
g (coils gap)/mm	15.5
Number of turns $N_1 = N_2$	30
(N_1 - Transmitter; N_2 - Receiver)	

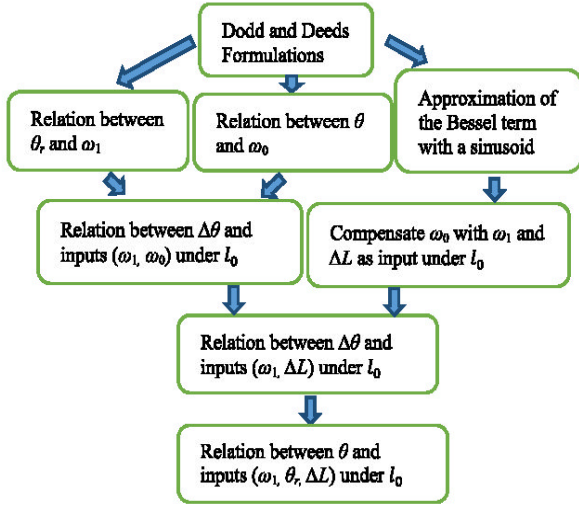


Fig. 2. The procedure of impedance phase compensating deduction.

up slightly with reduced lift-offs. Consequently, it is speculated that a novel approach could be deduced for compensating the impedance phase error due to sensor lift-offs with the signal amplitude and zero-crossing frequency. The derivations process for compensating the zero-crossing frequency ω_0 was carried out in [13]. Procedure of the proposed algorithm for impedance phase compensation is summarized in figure 2.

For the previous work, the compensated zero-crossing frequency is $\omega_0 = \pi^2 \omega_1 / (\pi^2 + 4 \ln(\Delta L_0 / \Delta L_m))$. Where, ω_0 denotes the zero-crossing frequency after compensation; ω_1 is zero-crossing frequency under current unknown lift-off; ΔL_0 is the inductance amplitude under the high-frequency (when the response signal barely changes with frequencies) with unknown lift-offs; ΔL_m is the inductance amplitude under same frequencies with the smallest lift-off.

In figure 2, l_0 denotes the unknown lift-off; θ_r denotes the measured phase under any frequency ω and an unknown lift-off; $\Delta \theta$ denotes the impedance phase change caused by the unknown lift-off, which should be compensated. θ denotes impedance phase (i.e. $\theta = \theta_r - \Delta \theta$) after compensation.

Derivation process of the phase compensation algorithm:

For the metallic plates with $u_r \gg 1$ (ferrous plates), the compensated phase $\varphi(\alpha_0)$ and measured phase $\varphi(\alpha_{0r})$ under unknown lift-off equal,

$$\varphi(\alpha_0) = \frac{1 - \sqrt{1/\mu_r^2 + j\omega\sigma\mu_0/\mu_r\alpha_0^2}}{1 + \sqrt{1/\mu_r^2 + j\omega\sigma\mu_0/\mu_r\alpha_0^2}} \quad (1)$$

$$\varphi(\alpha_{0r}) = \frac{1 - \sqrt{1/\mu_r^2 + j\omega\sigma\mu_0/\mu_r\alpha_{0r}^2}}{1 + \sqrt{1/\mu_r^2 + j\omega\sigma\mu_0/\mu_r\alpha_{0r}^2}} \quad (2)$$

Here, α_0 is a spatial frequency indicating the geometry feature of the sensor. [6], [12], [13], and [14]

Neglecting $1/\mu_r^2$ term in above equation and assigning $\omega_0 = \mu_r\alpha_0^2/\mu_0\sigma$, $\omega_1 = \mu_r\alpha_{0r}^2/\mu_0\sigma$

The compensated phase φ and measured φ under unknown lift-off can be expressed as followings,

$$\varphi(\alpha_0) = \frac{1 - \sqrt{j\omega/\omega_0}}{1 + \sqrt{j\omega/\omega_0}} = \frac{1 - \frac{\sqrt{2\omega/\omega_0}}{2}(1+j)}{1 + \frac{\sqrt{2\omega/\omega_0}}{2}(1+j)} \quad (3)$$

$$\varphi(\alpha_{0r}) = \frac{1 - \sqrt{j\omega/\omega_1}}{1 + \sqrt{j\omega/\omega_1}} = \frac{1 - \frac{\sqrt{2\omega/\omega_1}}{2}(1+j)}{1 + \frac{\sqrt{2\omega/\omega_1}}{2}(1+j)} \quad (4)$$

Then, the measured phase under unknown lift-off should be,

$$\begin{aligned} \theta_r &= \tan^{-1} \left(\frac{\text{Im}(Z_r)}{\text{Re}(Z_r)} \right) = \tan^{-1} \left(\frac{-\text{Re}(L_r)}{\text{Im}(L_r)} \right) \\ &= \tan^{-1} \left(\frac{-\text{Re}(\phi(\alpha_{0r}))}{\text{Im}(\phi(\alpha_{0r}))} \right) \\ &= \tan^{-1} \left(\frac{\sqrt{2\omega_1/\omega}}{1 - \omega_1/\omega} \right) \end{aligned} \quad (5)$$

Similarly, the compensated phase can be derived from ω_0 ,

$$\theta = \tan^{-1} \left(\frac{\sqrt{2\omega_0/\omega}}{1 - \omega_0/\omega} \right) \quad (6)$$

Therefore, the phase change caused by the lift-off should be,

$$\begin{aligned} \Delta \theta &= \theta_r - \theta \\ &= \tan^{-1} \left(\frac{\sqrt{2\omega_1/\omega}}{1 - \omega_1/\omega} \right) - \tan^{-1} \left(\frac{\sqrt{2\omega_0/\omega}}{1 - \omega_0/\omega} \right) \end{aligned} \quad (7)$$

Then, the compensated phase should be,

$$\begin{aligned} \theta &= \theta_r - \Delta \theta \\ &= \theta_r - \tan^{-1} \left(\frac{\sqrt{2\omega_1/\omega}}{1 - \omega_1/\omega} \right) + \tan^{-1} \left(\frac{\sqrt{2\omega_0/\omega}}{1 - \omega_0/\omega} \right) \end{aligned} \quad (8)$$

As shown in the appendix, the relation between ω_0 and ω_1 is $\omega_0 = \pi^2 \omega_1 / (\pi^2 + 4 \ln(\Delta L_0 / \Delta L_m))$. And the mathematic derivation details of this compensated zero-crossing frequency are shown at the end of the paper.

Finally, the impedance phase after compensation is evaluated from ω_1 , ΔL_0 , and ΔL_m .

$$\begin{aligned} \theta &= \theta_r - \Delta \theta \\ &= \theta_r - \tan^{-1} \left(\frac{\sqrt{2\omega_1/\omega}}{1 - \omega_1/\omega} \right) \\ &\quad + \tan^{-1} \left(\frac{\sqrt{2\omega_1/\left(1 + \frac{4}{\pi^2} \ln\left(\frac{\Delta L_0}{\Delta L_m}\right)\right)\omega}}{1 - \omega_1/\left(1 + \frac{4}{\pi^2} \ln\left(\frac{\Delta L_0}{\Delta L_m}\right)\right)\omega} \right) \end{aligned} \quad (9)$$

Assigning $G(\omega) = \tan^{-1}(\sqrt{2\omega_1/\omega}/(1 - \omega_1/\omega))$, through some mathematic manipulations, the compensated phase can

TABLE II
PROPERTIES OF DUPLEX-PHASE SPECIMENS

Specimens	Electrical conductivity (MS/m)	Relative permeability	Planar size (mm)	Thickness (mm)
DP600	4.13	222	500 × 400	7.0
DP800	3.81	144	500 × 400	7.0
DP1000	3.80	122	500 × 400	7.0

be obtained.

$$\begin{aligned}\theta &= \theta_r - \Delta\theta \\ &= \theta_r - G(\omega) + G\left(\left(1 + \frac{4}{\pi^2} \ln\left(\frac{\Delta L_0}{\Delta L_m}\right)\right)\omega\right)\end{aligned}\quad (10)$$

With,

$$G(\omega) = \tan^{-1}\left(\frac{\sqrt{2\omega_1/\omega}}{1 - \omega_1/\omega}\right)\quad (11)$$

where, ΔL_0 is the inductance amplitude under the high-frequency (when the response signal barely changes with frequencies) with unknown lift-offs; while ΔL_m is the inductance amplitude under same frequencies with the smallest lift-off (here this lift-off in measurement setup is 0.8 mm).

It can be seen in equation 11 that with the measured phase, inductance magnitude and zero-crossing frequencies from the measurements at an unknown lift-off as inputs, impedance phases θ after compensating (phase with zero lift-offs) could be obtained using the compensation scheme proposed above. For instance, if the sensor is put on a lift-off approaching 0, $\ln(\Delta L_0/\Delta L_m)$ should equal 0. As a result, the corresponding compensated result θ_0 calculated from equation 10 equals θ_r , which is reasonable under a negligible lift-off.

IV. ANALYTICAL SOLUTIONS AND MEASUREMENTS

In order to validate the feasibility of the deduced phase compensating approach, measurements and analytical solution have been made to compare impedance phases with various sensor lift-offs. The co-relation between impedance and inductance are shown in followings:

$$\Delta L = \frac{Z - Z_{air}}{j\omega}\quad (12)$$

$$\omega = 2\pi f\quad (13)$$

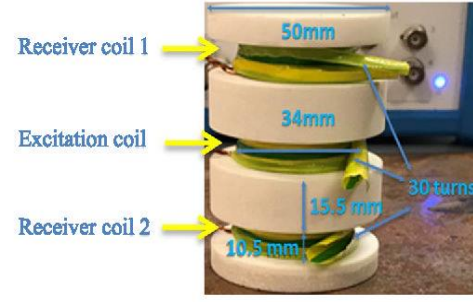
Here, Z represents the sensor mutual impedance with specimens; Z_{air} denotes the mutual impedance between the sensor's transmitter and receiver without specimens; f is the operation frequency.

Then, the impedance phase can be evaluated,

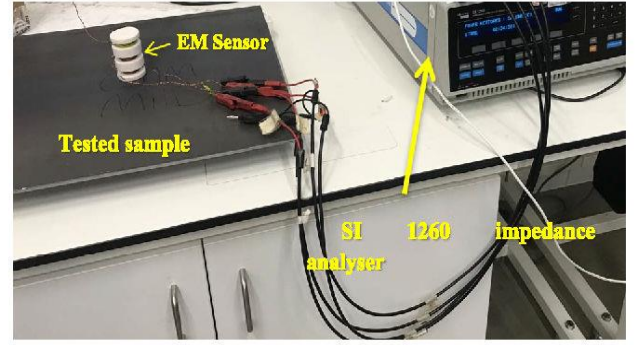
$$\theta = \tan^{-1}\left(\frac{\text{Im}(Z - Z_{air})}{\text{Re}(Z - Z_{air})}\right) = \tan^{-1}\left(\frac{-\text{Re}(\Delta L)}{\text{Im}(\Delta L)}\right)\quad (14)$$

A. Analytical Solutions

For the analytical solutions, Dodd Deeds approach [11] was utilized to compute the sensor's detected response signal - impedance. The sample was chosen to be a duplex-phase specimen - DP600 (specimen's properties and size data are shown in Table 2) under varying lift-offs of 0.8 mm, 2.3 mm,



(a)



(b)

Fig. 3. Measurement setup a) EM air-cored sensor configuration b) SI 1260 impedance analyser.

and 3.8mm. The analytical solver is scripted and operated on MATLAB coding platform, which is utilized for the evaluation of inductance ΔL (equations 15 - 20 in the appendix) and the compensated phase using equation 10.

B. Measurements

In order to measure the impedance/inductance phase of the samples, a symmetric air-cored electromagnetic sensor was designed for steel micro-structure monitoring in the Continuous Annealing & Processing Line (CAPL). As can be seen from Fig. 3, the excitation coil sits in the middle and two receive coils at bottom and top respectively. The geometry profile of the sensor is illustrated in Table 1. Receive coil 2 is used as the test coils; receive coil 1 is served as a reference coil. In the paper, only receive 2 coil signal is recorded and served as the response output signal. All the coils have the same diameters, i.e. an inner diameter of 32.0 mm and an outer diameter of 34.0 mm. Each of the coils has 30 turns, and the coil separation is 35.0 mm. SI 1260 impedance analyser has been utilized to measure the air-core sensor induced signal response - mutual impedance or inductance of the sensor influenced by the tested samples. The working frequency range of the instrument is set from 310 Hz to 3 MHz. Moreover, all the samples are tested under a series lift-offs of 0.8, 2.3, and 3.8 mm.

C. Results

Figure 4 exhibits both the real part and imaginary part of the simulations and measurements of sensor-plates system mutual inductance multi-frequency spectra. In figure 4, it is obviously that inductance curves magnitude drop off with increased lift-offs. Meanwhile, the zero-crossing frequency decreases with

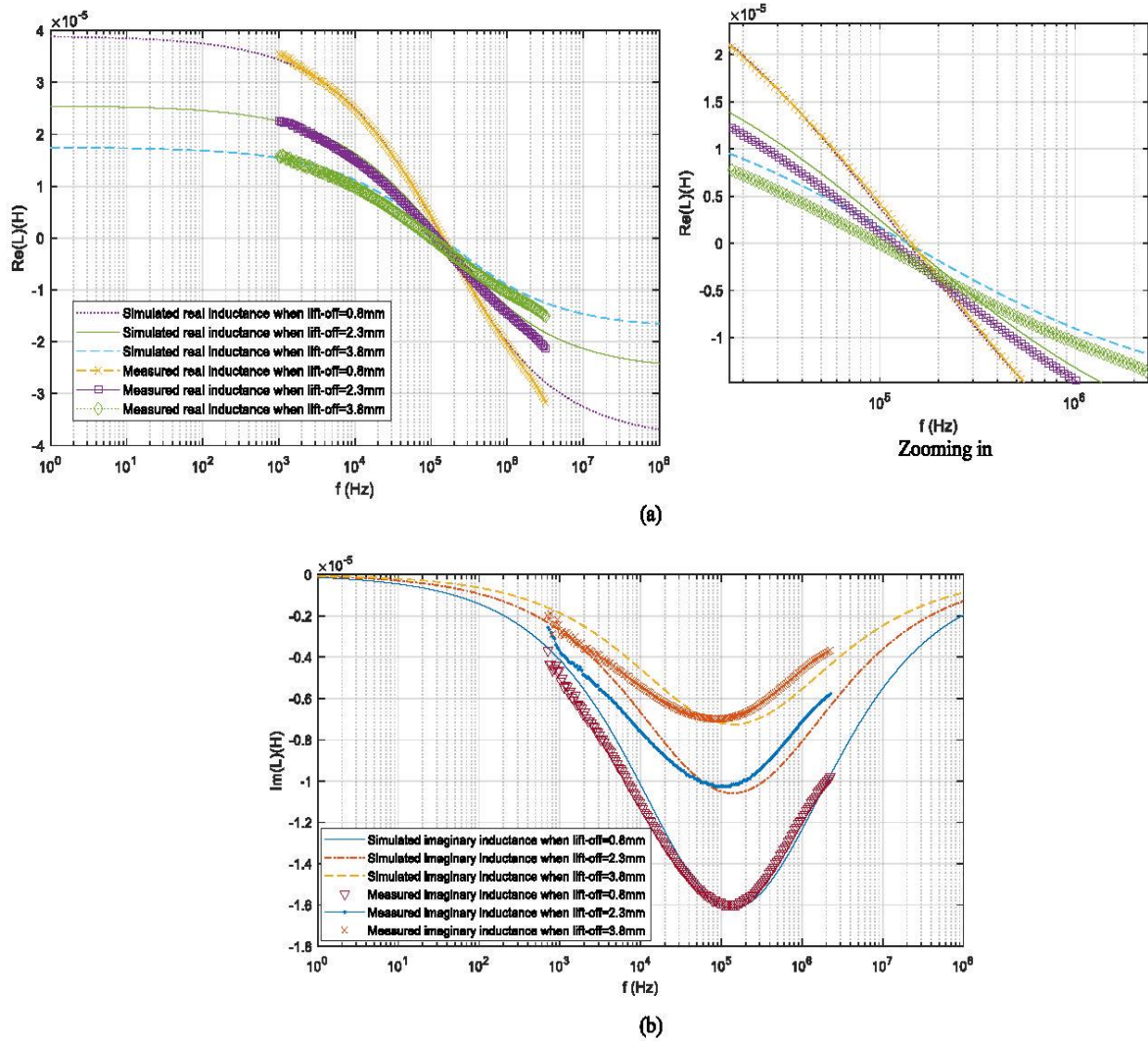


Fig. 4. Real and imaginary part of inductance under varying lift-offs —0.8 mm, 2.3 mm, and 3.8mm (a) real part and (b) imaginary part.

increased lift-offs. Some singular points may be encountered during the measurements which are due to the signal noise of SI 1260 impedance analyser, especially under the low frequency.

In figure 5, it is observed that the inductance term $\Delta L_0/\Delta L_m$ decreases with increased lift-offs. Consequently, the relative loss of the inductance $\Delta L_0/\Delta L_m$ can be used for the compensation of inductance or impedance phase due to lift-offs, which can be used to compensate the drop in phase with rising lift-offs. Here, ΔL_m is the sample's inductance (as shown in equation 12) with end point frequency (the last frequency sample for both simulations and measurements) for the smallest lift-off (0.8 mm under the sensor setup in figure 3).

Figure 6 shows the simulations, measurements, and the phase multi-frequency spectra after the proposed compensation algorithm (equation 10 and 11). It can be seen that both the simulated and measured phase decrease as increased lift-offs. In addition, the compensated phase is barely affected by the lift-off. Based on the compensated phase, ferrous plate magnetic permeability could be easily predicted via the measured response of the sensor. The ferrous metallic plates' magnetic permeability measurement technique is validated

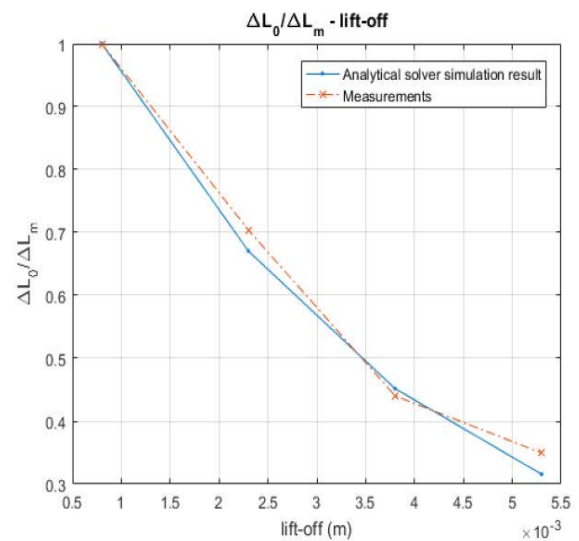


Fig. 5. Trend of inductance term $\Delta L_0/\Delta L_m$ (for DP 600 specimen) for different lift-offs.

via the comparison of modelling and measured data for the mentioned sensor next to dual-phase (DP) steels with various values of magnetic permeability.

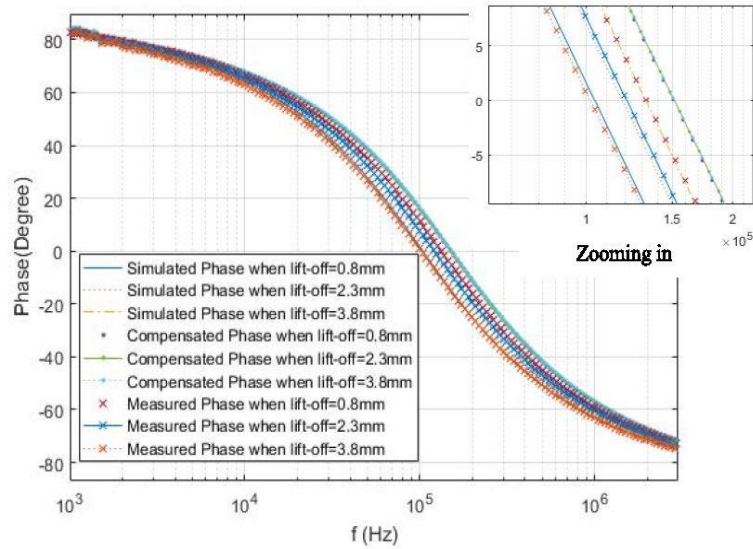


Fig. 6. Compensation performance both on simulations and measurements with 0.8, 2.3, 3.8 mm lift-offs.

TABLE III
RELATIVE PERMEABILITY MEASUREMENTS FOR DIFFERENT LIFT-OFFS

Plates	Lift-offs (mm)	Actual relative permeability	Relative permeability without compensation	Relative permeability inferred from compensated phase	Relative error for non-compensated permeability	Relative error for compensated permeability
DP800	0.8	144	138.48	142.37	3.83%	1.13%
	2.3	144	136.76	142.12	5.03%	1.31%
	3.8	144	133.31	141.94	7.42%	1.43%
DP1000	0.8	122	117.68	120.72	3.54%	1.05%
	2.3	122	115.27	120.57	5.52%	1.17%
	3.8	122	111.98	120.15	8.21%	1.52%

In principle, the magnetic permeability reconstruction for the tested specimens is finding the simulated multi-frequency inductance/impedance curve (via equations 15 - 20 in appendix) that is closest to the measured multi-frequency spectra data (after the proposed compensation algorithms - equation 10 and 11) while changing the permeability. In order to validate the proposed magnetic permeability reconstruction technique via the compensated phase, multi-frequency inductances of two ferrous specimens have been tested (specimens' properties and size data are shown in Table 2). In the measurement process, 120 logarithmically spaced frequencies samples range from 310 Hz to 3 MHz have been chosen as the operation frequencies. In addition, both DP steel specimens have identical size of $500 \times 400 \times 7.0$ mm. Consequently, magnetic permeability comparisons for compensated phase and the measured phase without compensation is shown in table 3.

It can be concluded from table 3 that the magnetic permeability reconstruction shows a better performance through the proposed impedance or inductance phase compensation scheme (equation 10 and 11).

In practical application, the lift-offs range may be different. However, it has been found that the error of the measured permeability is always within a small value of 5%.

V. CONCLUSIONS

In this paper, a compensation technique is developed for the relief of lift-off effects on impedance phase for metallic

ferrous plates. From the results, it can be easily observed that both phase and signal (impedance/inductance) magnitude decreases as lift-off increases. And the measured inductance or impedance can be used for the compensation of impedance phase loss due to lift-offs via the proposed algorithms. Based on the proposed phase compensation approach, a magnetic permeability measurement technique was proposed that is also virtually independent of lift-offs. The results have been verified with both measurements and simulations of selected cases.

APPENDIX

Inferring the compensated zero-crossing frequency (ZCF) ω_0 from the measured ZCF and inductance (ω_1 and ΔL) under a lift-off of l_0 :

Dodd Deeds method has been chosen as the forward simulation solver for the calculation of the inductance due to the appearance of the sample when tested by an axially symmetric air-cored sensor [10].

The inductance due to the appearance of the sample is the subtraction of the sensor tested inductance when sensor is put on a specimen ($L(\omega)$) and that when sensor is in empty region ($L_A(\omega)$): $\Delta L(\omega) = L(\omega) - L_A(\omega)$.

Dodd Deeds formulations are listed as follows:

$$\Delta L(\omega) = K \int_0^\infty \frac{P^2(\alpha)}{\alpha^6} A(\alpha) \phi(\alpha) d\alpha \quad (15)$$

where,

$$A(\alpha) = (1 - e^{-2ah})e^{-\alpha(G+h+2l_0)} \quad (16)$$

$$\begin{aligned} \phi(\alpha) &= \frac{(\mu_r \alpha - \alpha_1)}{(\mu_r \alpha + \alpha_1)} = \frac{\mu_r \alpha - \sqrt{\alpha^2 + j\omega\sigma\mu_r\mu_0}}{\mu_r \alpha + \sqrt{\alpha^2 + j\omega\sigma\mu_r\mu_0}} \\ &= \frac{1 - \sqrt{1/\mu_r^2 + j\omega\sigma\mu_0/\mu_r\alpha^2}}{1 + \sqrt{1/\mu_r^2 + j\omega\sigma\mu_0/\mu_r\alpha^2}} \end{aligned} \quad (17)$$

$$K = \frac{\pi\mu_0 N^2}{h^2(r_1 - r_2)^2} \quad (18)$$

$$P(\alpha) = \int_{\alpha r_1}^{\alpha r_2} x J_1(x) dx \quad (19)$$

$$\alpha_1 = \sqrt{\alpha^2 + j\omega\sigma\mu_r\mu_0} \quad (20)$$

l_0 is sensor's lift-off; h is sensor's coil height; N is sensor's coil turn number; r_1 and r_2 are inner and outer radii of sensor's coil; μ_r is the specimen's relative permeability. μ_0 is the vacuum permeability; G is the distance between the excitation coil and receiving coil.

In equation (15), since the $\phi(\alpha)$ term barely change with α (compared with $A(\alpha)$ and $P(\alpha)$), ϕ could be estimated as equation (22),

$$\Delta L(\omega) = \phi(\alpha_0)\Delta L_0 \quad (21)$$

α_0 is the spatial frequency, which is a constant controlled by sensor configuration.

From equation (21), the phase of tested inductance or impedance is merely controlled via $\phi(\alpha_0)$.

Where,

$$\phi(\alpha_0) = \frac{-\sqrt{1/\mu_r^2 + j(\mu_0/\mu_r)\sigma\omega\alpha_0^2} + 1}{\sqrt{1/\mu_r^2 + j(\mu_0/\mu_r)\sigma\omega\alpha_0^2} + 1} \quad (22)$$

Neglect $1/\mu_r^2$ in equation (22),

$$\phi(\alpha_0) = \frac{-\sqrt{j(\mu_0/\mu_r)\sigma\omega\alpha_0^2} + 1}{\sqrt{j(\mu_0/\mu_r)\sigma\omega\alpha_0^2} + 1} \quad (23)$$

In equation (23), it can be observed that $\phi(\alpha_0)$ is sample and sensor related (controlled by σ and μ_r).

Assign $\frac{\mu_r\alpha_0^2}{\mu_0\sigma}$ with ω_1 , equation (23) can be expressed as,

$$\phi(\alpha_0) = \frac{-\sqrt{j\omega/\omega_1} + 1}{\sqrt{j\omega/\omega_1} + 1} \quad (24)$$

In equation (21), ΔL_0 denotes the magnitude of the tested inductance, which is solely controlled by the sensor configuration (cannot be affected by the specimen properties).

From our previously work, a simple function $\sin^2\left(\frac{\alpha\pi}{2\alpha_0}\right)$ with its maximum at α_0 is used to approximate ΔL_0 [13],

$$\Delta L_0 \approx \Delta L_m e^{-2\alpha l_0} \sin^2\left(\frac{\alpha\pi}{2\alpha_0}\right) \quad (25)$$

where ΔL_m is the sample's inductance (as shown in equation 12) with start point frequency (the first frequency sample for both simulations and measurements) for the smallest lift-off (0.8 mm under the sensor setup in figure 3)

The revised α should maximize $e^{-2\alpha l_0} \sin^2\left(\frac{\alpha\pi}{2\alpha_0}\right)$ and therefore $e^{-\alpha l_0} \sin\left(\frac{\alpha\pi}{2\alpha_0}\right)$.

In our previous work [13], the shift in α_0 caused by lift-off effect - α_{0r} can be derived as,

$$\alpha_{0r} = \alpha_0 - \frac{4\alpha_0^2 l_0}{\pi^2} \quad (26)$$

Therefore, the revised ω_1 becomes

$$\omega_1 = \frac{(\alpha_0^2 \pi^4 - 8\pi^2 \alpha_0^3 l_0 + 16\alpha_0^4 l_0^2) \mu_r}{\pi^4 \sigma \mu_0} \quad (27)$$

Combining (25) with (26), ΔL_0 becomes

$$\begin{aligned} \Delta L_0 &= \Delta L_m e^{-2(\alpha_0 - \frac{4\alpha_0^2 l_0}{\pi^2})l_0} \cos^2\left(\frac{2\alpha_0 l_0}{\pi}\right) \\ &= \Delta L_m e^{-2(\alpha_0 - \frac{4\alpha_0^2 l_0}{\pi^2})l_0} \left(\frac{\cos(\frac{4\alpha_0 l_0}{\pi}) + 1}{2}\right) \end{aligned}$$

Considering $\alpha_0 l_0 \ll 1$ and based on small-angle approximation $\cos(\theta) \approx 1 - \theta^2/2$, $\cos(4\alpha_0 l_0/\pi)$ is substituted with $1 - (4\alpha_0 l_0/\pi)^2/2$.

ΔL_0 becomes, $\Delta L_0 = \Delta L_m e^{-2(\alpha_0 - \frac{4\alpha_0^2 l_0}{\pi^2})l_0} (1 - \frac{4\alpha_0^2 l_0^2}{\pi^2})$

Substituting $\left(1 - \frac{4\alpha_0^2 l_0^2}{\pi^2}\right)$ with $e^{-\frac{4\alpha_0^2 l_0^2}{\pi^2}}$

$$\begin{aligned} \Delta L_0 &= \Delta L_m e^{-2(\alpha_0 - \frac{4\alpha_0^2 l_0}{\pi^2})l_0} e^{-\frac{4\alpha_0^2 l_0^2}{\pi^2}} \\ &= \Delta L_m e^{-2(\alpha_0 - \frac{2\alpha_0^2 l_0}{\pi^2})l_0} \end{aligned} \quad (28)$$

Then,

$$\ln \frac{\Delta L_0}{\Delta L_m} = -2(\alpha_0 - \frac{2\alpha_0^2 l_0}{\pi^2})l_0 \quad (29)$$

And further derivation from (29):

$$4\alpha_0^2 l_0^2 - 2\pi^2 \alpha_0 l_0 - \pi^2 \ln \frac{\Delta L_0}{\Delta L_m} = 0 \quad (30)$$

This is now a quadratic equation with $\alpha_0 l_0$ as its variable. Therefore, the solution for $\alpha_0 l_0$ is

$$\alpha_0 l_0 = \frac{\pi^2 - \sqrt{\pi^4 + 4\pi^2 \ln \frac{\Delta L_0}{\Delta L_m}}}{4} \quad (31)$$

Since $\alpha_0 l_0 \ll 1$, the other solution, the other solution $\alpha_0 l_0 = \frac{\pi^2 + \sqrt{\pi^4 + 4\pi^2 \ln \frac{\Delta L_0}{\Delta L_m}}}{4}$ therefore is discarded.

From equation (31), lift-off can be estimated as

$$l_0 = \frac{\pi^2 + \sqrt{\pi^4 + 4\pi^2 \ln \frac{\Delta L_0}{\Delta L_m}}}{4\alpha_0} \quad (32)$$

Combining (27) with (32),

$$\omega_1 = \frac{\alpha_0^2 \left(\pi^2 + 4 \ln \frac{\Delta L_0}{\Delta L_m}\right) \mu_r}{\pi^2 \sigma \mu_0} \quad (33)$$

Further derivation from equation (33),

$$\alpha_0^2 (\pi^2 + 4 \ln \frac{\Delta L_0}{\Delta L_m}) \mu_r - \pi^2 \sigma \mu_0 \omega_1 = 0$$

And the solution is

$$\alpha_0 = \sqrt{\frac{\pi^2 \sigma \mu_0 \omega_1}{\left(\pi^2 + 4 \ln \frac{\Delta L_0}{\Delta L_m}\right) \mu_r}} \quad (34)$$

Thus, the zero-crossing frequency can be compensated as following,

$$\omega_0 = \frac{\mu_r \alpha_0^2}{\mu_0 \sigma} = \frac{\pi^2 \omega_1}{\left(\pi^2 + 4 \ln \frac{\Delta L_0}{\Delta L_m}\right)} \quad (35)$$

REFERENCES

- [1] Y. He, G. Y. Tian, H. Zhang, M. Alamin, A. Simm, and P. Jackson, "Steel corrosion characterization using pulsed eddy current systems," *IEEE Sensors J.*, vol. 12, no. 6, pp. 2113–2120, Jun. 2012.
- [2] G. Y. Tian, A. Sophian, D. Taylor, and J. Rudlin, "Multiple sensors on pulsed eddy-current detection for 3-D subsurface crack assessment," *IEEE Sensors J.*, vol. 5, no. 1, pp. 90–96, Feb. 2005.
- [3] J. R. S. Avila, K. Y. How, M. Lu, and W. Yin, "A novel dual modality sensor with sensitivities to permittivity, conductivity, and permeability," *IEEE Sensors J.*, vol. 18, no. 1, pp. 356–362, Jan. 2018.
- [4] C. Ye, Y. Huang, L. Udpa, S. Udpa, and A. Tamburrino, "Magnetoresistive sensor with magnetic balance measurement for inspection of defects under magnetically permeable fasteners," *IEEE Sensors J.*, vol. 16, no. 8, pp. 2331–2338, Apr. 2016.
- [5] M. Lu, Y. Xie, W. Zhu, A. Peyton, and W. Yin, "Determination of the magnetic permeability, electrical conductivity, and thickness of ferrite metallic plates using a multi-frequency electromagnetic sensing system," *IEEE Trans. Ind. Informat.*, vol. 1, no. 1, pp. 1–8. doi: 10.1109/TII.2018.2885406.
- [6] W. Yin, S. J. Dickinson, and A. J. Peyton, "Imaging the continuous conductivity profile within layered metal structures using inductance spectroscopy," *IEEE Sensors J.*, vol. 5, no. 2, pp. 161–166, Apr. 2005.
- [7] H. Hoshikawa and K. Koyama, "A new eddy current surface probe without lift-off noise," in *Proc. 10th APCNDT*, Brisbane, QLD, Australia, p. 8575, 2001.
- [8] D. Kim, L. Udpa, and S. S. Udpa, "Lift-off invariance transformations for eddy current nondestructive evaluation signals," in *Proc. AIP Conf.*, vol. 615, 2002, pp. 615–622.
- [9] D. F. He and M. Yoshizawa, "Dual-frequency eddy current NDE based on high- T_c RF SQUID," *Phys. C, Supercond.*, vol. 383, no. 3, pp. 223–226, Dec. 2002.
- [10] W. Yin, R. Binns, S. J. Dickinson, C. Davis, and A. J. Peyton, "Analysis of the liftoff effect of phase spectra for eddy current sensors," *IEEE Trans. Instrum. Meas.*, vol. 56, no. 6, pp. 2775–2781, Dec. 2007.
- [11] C. V. Dodd and W. E. Deeds, "Analytical solutions to eddy-current probe-coil problems," *J. Appl. Phys.*, vol. 39, no. 6, pp. 2829–2839, 1968.
- [12] W. Yin and K. Xu, "A novel triple-coil electromagnetic sensor for thickness measurement immune to lift-off variations," *IEEE Trans. Instrum. Meas.*, vol. 65, no. 1, pp. 164–169, Jan. 2016.
- [13] M. Lu, L. Yin, A. Peyton, and W. Yin, "A novel compensation algorithm for thickness measurement immune to lift-off variations using eddy current method," *IEEE Trans. Instrum. Meas.*, vol. 65, no. 12, pp. 2773–2779, Dec. 2016.
- [14] M. Lu, W. Zhu, L. Yin, A. J. Peyton, W. Yin, and Z. Qu, "Reducing the lift-off effect on permeability measurement for magnetic plates from multifrequency induction data," *IEEE Trans. Instrum. Meas.*, vol. 67, no. 1, pp. 167–174, Jan. 2018.

Chapter 7 A Novel Perturbed Matrix Inversion Based Method for the Acceleration of Finite Element Analysis in Crack-Scanning Eddy Current NDT

Ruochen Huang, Mingyang Lu, Anthony Peyton, Wuliang Yin

IEEE Access, 2020.

The finite element method is commonly used to calculate the EM field of eddy current sensors and inspect the surface crack of metals. However, FEM takes hours of computation time due to the significant number of mesh elements. In this chapter, an accelerated method based on the perturbed matrix inversion method is proposed. For the calculation of the crack detection, it only needs the inversion for a much smaller matrix, consequently, it reduces the computation time by three folds. This method is proved by the numerical tests.

A Novel Perturbed Matrix Inversion Based Method for the Acceleration of Finite Element Analysis in Crack-Scanning Eddy Current NDT

RUOCHEN HUANG^{1,2}, MINGYANG LU^{1,2}, ANTHONY PEYTON²,
AND WULIANG YIN^{1,2}, (Senior Member, IEEE)

¹College of Electronic Information and Automation, Tianjin University of Science and Technology, Tianjin 300222, China

²School of Electrical and Electronic Engineering, The University of Manchester, Manchester M13 9PL, U.K.

Corresponding author: Wuliang Yin (wuliang.yin@manchester.ac.uk)

This work was supported in part by the UK Engineering and Physical Sciences Research Council (EPSRC) under Grant EP/P027237/1, and in part by the Real-time In-line Microstructural Engineering (RIME).

ABSTRACT Non-destructive testing (NDT) has a promising capability for crack detection. In this paper, a novel method for accelerating eddy current calculation for crack detection using the finite element method (FEM) is presented. This method exploits the fact that, due to the presence of a small defect, the stiffness matrix in FEM for a sample plate with the defect can be regarded as a summation of the stiffness matrix Q from the sample plate without the presence of the defect and the perturbation matrix D from the defect. The inversion of the stiffness matrix for a sample plate with the defect can, therefore, be obtained using the perturbed matrix inversion (PMI) method. PMI method only requires the inversion of a much smaller matrix and therefore improves the speed of the computation process. Numerical tests verified the effectiveness of the proposed method in shortening the computation time for crack scanning in FEM.

INDEX TERMS Finite-element method (FEM), eddy current calculation, perturbed matrix inversion, computation acceleration, crack scanning.

I. INTRODUCTION

The emergence of high-speed and high-capacity electronic computers and the rapid development of the numerical analysis algorithms offer favourable conditions and a solid foundation for the development of computational electromagnetics. So far, when it comes to the numerical analysis for electromagnetics, it can be mainly divided into two kinds of methods, one is the finite element method (FEM) [1], and the other is the boundary element method (BEM) [2]. Both of them are universally adopted to obtain the solution with accuracy and efficiency [3]. FEM can be utilised for electromagnetic analysis of specimens with arbitrary geometry and media information and is commonly used in non-destructive evaluation (NDE). It discretises the whole sample model to masses of subdomains. Moreover, shape functions are interpolated to approximate the unknown fields. By integrating the equations

of all elements, it is regarded as finding the numerical solution of the discretized formulations [4], [5].

In recent years, to hasten the calculation of electromagnetic (EM) problems, various approaches have been put forward. They can be summarised into two kinds, that is, the improvements in the eddy current algorithm as well as the advancement of finding the solution.

From the aspects of improving the formulation/strategy, a novel multi-layered conductive structures (MCS) model was developed in [6] for electromagnetic non-destructive evaluation techniques. Instead of using the integration model, the computation was simplified by applying the series expression based on the truncated region eigenfunction expansion (TREE) method. Compared with the conventional FEM, the computation speed has been hastened over a hundred times when using the TREE method. However, this method is usually applied in certain layer-isotropic materials. In addition, a fast simulator based on the precomputed unflawed database approach was proposed in [7] for the evaluation of the crack size. Due to the advantage of its detectability,

The associate editor coordinating the review of this manuscript and approving it for publication was Chong Leong Gan.

this method can be used for crack reconstruction. Other researchers have also explored fast computation for non-destructive testing for crack inspection [8-11]. It has been found that some terms in the formula are independent of the crack and can be calculated ahead of time, then stored in a database. As a result, the computation burden can be significantly reduced. In [12], Noritaka et al. have developed a novel algorithm by using the Tabu search for reconstruction of the crack. Although the algorithm is expected to be time-consuming, it is compatible with parallel computation so that the time reduces dramatically. Moreover, the FEM-BEM approach has been greatly applied [3], [13], [14], which combines the boundary element region with the finite element region to obtain a solution of the non-uniform material distribution. For the sake of accelerating the computation speed for FEM, SuiteSparse [15] and GRID [16] were also developed to solve systems of linear equations.

To further advance the numerical solution process, in our previous works, a fast FEM approach has been proposed. The principle of the acceleration is introducing a preconditioner [17], [18] for the evaluation of eddy current formulation. In addition, an equivalent-effect phenomenon has also been proposed for the electromagnetic computation of thin structures [19].

In this paper, a fast edge-element FEM technique for scanning sensors over a sample plate with defects is presented.

This method is based on the perturbed matrix inversion (PMI) method to evaluate the change of the eddy current due to a small defect and its effectiveness in improving the computation speed has been verified through numerical experiments.

II. A-V EDGE-ELEMENT FORMULATION AND PERTURBED MATRIX INVERSION

A. A-V EDGE-ELEMENT FORMULATION

Eddy currents can be induced by the time-varying magnetic field within a conducting target. With the aid of the edge shape functions and the nodal shape functions, the unknown vector potential and scalar potential fields can be approximated. In order to construct the shape functions for each tetrahedral element, matrix transformation from global space to local space can be used if isotropy is satisfied for every edge element [20].

$$J = \begin{bmatrix} \frac{\partial x}{\partial \xi} & \frac{\partial y}{\partial \xi} & \frac{\partial z}{\partial \xi} \\ \frac{\partial x}{\partial \eta} & \frac{\partial y}{\partial \eta} & \frac{\partial z}{\partial \eta} \\ \frac{\partial x}{\partial \zeta} & \frac{\partial y}{\partial \zeta} & \frac{\partial z}{\partial \zeta} \end{bmatrix} \quad (1)$$

$$\lambda_v = J^{-1} \hat{\lambda}_v \quad (2)$$

$$\lambda_s = J^{-1} \hat{\lambda}_s \quad (3)$$

$$\nabla \times \lambda_v = \frac{1}{|J|} J^T \nabla \times \hat{\lambda}_v \quad (4)$$

where, J denotes the Jacobian matrix, xyz denote the coordinates in the global space, $\xi\eta\zeta$ denote the coordinates in the

local space, $\hat{\lambda}_v$ and $\hat{\lambda}_s$ denote the relevant components in the local space and λ_v and λ_s denotes the relevant components in the global space.

Then combine approximated fields with the boundary conditions, Galerkin equations can be obtained, shown as followings:

$$\int_{\Omega_c} \nabla \times N_i \cdot v \nabla \times \mathbf{A}^n d\Omega + \int_{\Omega_c} j\omega\sigma N_i \cdot \mathbf{A}^n d\Omega + \int_{\Omega_c} \sigma N_i \cdot \nabla V^n d\Omega = \int_{\Omega_c} \nabla \times N_i \cdot v_0 \nabla \times \mathbf{A}_s d\Omega \quad i = 1, 2, \dots, 6 \quad (5)$$

$$\int_{\Omega_c} j\omega\sigma \nabla L_i \cdot \mathbf{A}^n d\Omega + \int_{\Omega_c} \sigma \nabla L_i \cdot \nabla V^n d\Omega = 0 \quad i = 1, 2, \dots, 4 \quad (6)$$

where, V^n denotes the scalar potential (voltage) of element n . \mathbf{A}^n denotes the induced vector potential corresponding to element n . σ denotes the media electrical conductivity. v_0 denotes the reluctivity in the free space domain. v denotes the reluctivity for the target.

It is noted that, for every arbitrary element n , the matrix Q^n can be expressed by the stiffness matrix form which is the combined by the left-hand terms of equations (5) and (6).

$$Q^n = \begin{bmatrix} K^n & L^n \\ M^n & N^n \end{bmatrix} \quad (7)$$

From the aspect of the whole system, the whole system matrix can be derived by combining equation (7) to equations (5)-(6) and expressed as

$$Q \begin{bmatrix} \begin{bmatrix} \mathbf{A}_1 \\ \vdots \\ \mathbf{A}_p \\ V_1 \\ \vdots \\ V_q \end{bmatrix} \end{bmatrix} = \begin{bmatrix} K^{p \times p} & L^{p \times q} \\ M^{q \times p} & N^{q \times q} \end{bmatrix} \begin{bmatrix} \begin{bmatrix} \mathbf{A}_1 \\ \vdots \\ \mathbf{A}_p \\ V_1 \\ \vdots \\ V_q \end{bmatrix} \end{bmatrix} = B \text{ with, } K^{p \times p} = K_1^{p \times p} + K_2^{p \times p} \quad (8)$$

According to equation (8), the K matrix consists of two parts, the K_1 and K_2 matrices. K_1 matrix represents the 1st A term of equation (5) and it plays a role for the generation of the basic A wave. K_2 represents the 2nd A term of equation (5) and the eddy current diffusion effect can be revealed by K_2 matrix. L represents the 1st V term of equation (5), and it monitors the eddy current confined within the sample geometry (Maxwell-Wagner effect). M represents the 1st term of the left-hand side of equation (6) and N represents the 2nd term of the left-hand side of equation (6). The magnetostatic field is governed by both of the terms. B represents the right-hand side of equations (5) and (6), and it acts as the environmental background field. p represents the order of the edge. q represents the order of the vertex. The pre-conditioning technique is also applied to increase the accuracy of the calculated A and V of the whole mesh.

After obtaining A and V of the whole mesh through equation (8), the electric field can be formed by combining the

canonical $\mathbf{A} - V$ formulation with the Coulomb gauge [21]:

$$\mathbf{E}^n = -j\omega\mathbf{A}^n - \nabla V^n \quad (9)$$

According to the principle of Lorentz reciprocity in [22], the inductance measured by the sensor can be derived:

$$\Delta L = \frac{1}{j\omega I^2} \int_c \mathbf{E}_a \cdot \mathbf{J}_b dv = \frac{1}{j\omega I^2} \int_c \mathbf{E}_a \cdot \mathbf{E}_b \cdot (\sigma_a - \sigma_b) dv \quad (10)$$

where, ΔL represents the variation of the inductance due to the substrate domain of a and b .

B. ACCELERATION BASED ON PERTURBED MATRIX INVERSION

Fast eddy current computation is vital for non-destructive testing. The perturbed matrix inversion (PMI) method was used for solving the linear system of equations in FEM when a small defect is present on the sample. As described in equation (8), it can be regarded as solving a large system of algebraic equations. Assume that a small defect is present on the sample, the system matrix is a slightly varied matrix to the sample without the defect. The variation matrix (or the perturbation matrix) due to the defect can be expressed as

$$D = \begin{bmatrix} -K' & -L' \\ -M' & -N' \end{bmatrix} \quad (11)$$

According to the Sherman-Morrison-Woodbury formula, the inversion can be expressed as

$$(Q + D)^{-1} = Q^{-1} - Q^{-1}(Q^{-1} + D^{-1})^{-1}Q^{-1} \quad (12)$$

Then substitute Q^{-1} with Q' , then equation 11 can be simplified as [23]

$$(Q + D)^{-1} = Q' - Q'D(I + Q'D)^{-1}Q' \quad (13)$$

Consequently, the solution can be obtained through the PMI method. All the computations were operated on the platform ThinkCentre M910s, with 16GB RAM and Intel Core i7-6700 processor.

III. NUMERICAL EXPERIMENTS AND VERIFICATION OF THE PMI METHOD

A. MODELS

In Fig. 1, the objects have been modelled as an unflawed metallic plate and a metallic plate with a defect in the centre. For both metal plates in (a) and (b), the length, width and height are 20 mm, 20 mm and 5 mm respectively. For the metal plate with the defect in (b), the simulated defect is placed in the centre with a length of 5 mm, a length of 0.5 mm and a height of 3 mm. Two blocks are centred at (10, 10, 2.5) mm. To validate the solver, two materials are chosen for the metal plates, one is aluminium with the electrical conductivity of 35 MS/m at 20 degrees, and another is copper with the electrical conductivity of 57 MS/m at 20 degrees.

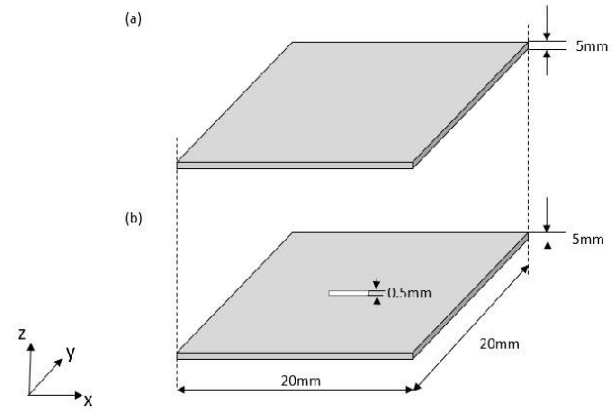


FIGURE 1. Model geometry (a) metal plate (b) metal plate with the defect.

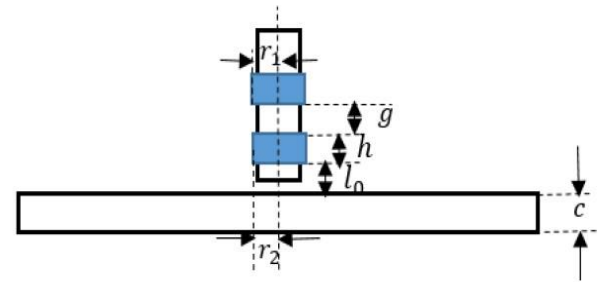


FIGURE 2. Sensor configuration.

TABLE 1. Sensor parameters.

Radius of excitation coil r_1	0.5 mm
Radius of receiving coil r_2	0.5 mm
Height of coil h	0.25 mm
Gap between two coils g	0.2 mm
Lift off l_0	0.05 mm
Thickness of the plate c	5 mm

B. SENSOR CONFIGURATION

The sensor schematic and the sensor parameters are exhibited in figure 2 and table 1, a coaxial sensor is used in the simulation process. Both the radius of the excitation coil and the receiving coil are set to 0.5 mm. The lift-off of the sensor is 0.05 mm and the gap between the excitation coil and the receiving coil is 0.2 mm. The magnitude of the injection current in excitation coil is 1 A. During the simulation for crack inspection, the coils are moving in parallel along the y-axis (from (10, 0, 5) mm to (10, 20, 5) mm).

C. TEST OF THE ACCELERATED FEM

According to the Dodd Deeds formulas, the inductance variation due to the sample plates (aluminium and copper) without defect can be calculated, shown in figure 3 and figure 4. The sweeping frequency changes from 10 Hz to 1 MHz in the analytical solution.

It can be seen from the figures above that edge FEM simulation and analytical results are matched well with each other under the frequency range from 10 Hz to 100 kHz. Compared with the results from the aluminium plate, the characteristic frequency reduces when the copper plate was used, which is

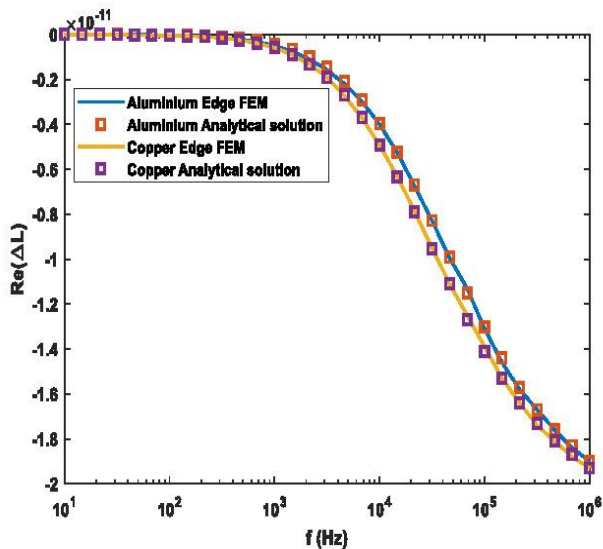


FIGURE 3. The real part of the inductance due to the aluminium and copper plate without defect.

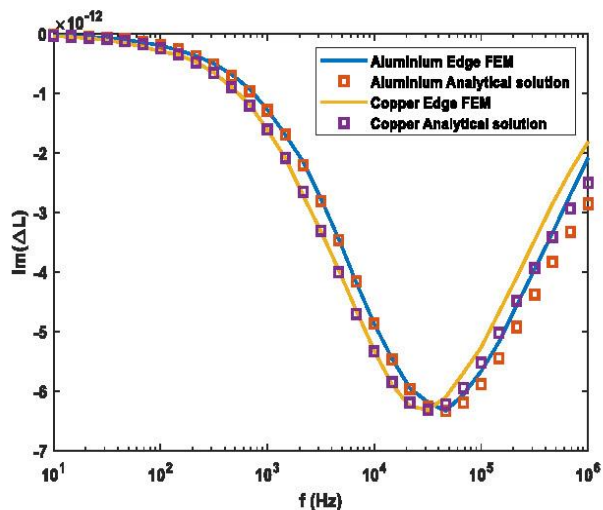


FIGURE 4. The imaginary part of the inductance caused by the aluminium and copper plate without defect.

in accordance with the relationship between the conductivity and the characteristic frequency. In addition, given that the solution from analytical formulas is the results for the plate with infinite width and length, for the imaginary part of the inductance results, there exists some error as the frequency sweeping from 100 kHz to 1 MHz.

D. ACCELERATION PERFORMANCE IN CRACK SCANNING

As the perturbation matrix due to the presence of the defect on the sample was assigned to be the perturbation matrix D , the acceleration performance from the PMI approach can be obtained in order to detect the presence of the defect. The result of the PMI approach was compared with that calculated from the conventional conjugate gradient squared (CGS) method. The frequency was set to 10 Hz. The defect depths of the sample plate are 1 mm, 2 mm and 3 mm respectively. The results are shown in the following subsections.

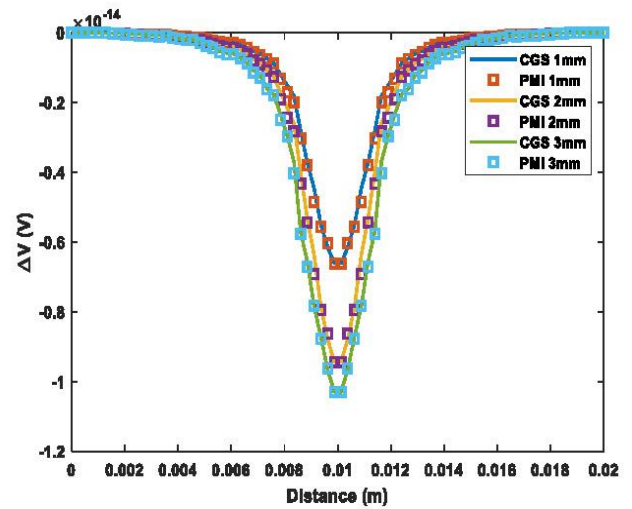


FIGURE 5. Computation results for the aluminum plate with different depths of defect, lift-off is 0.05 mm.

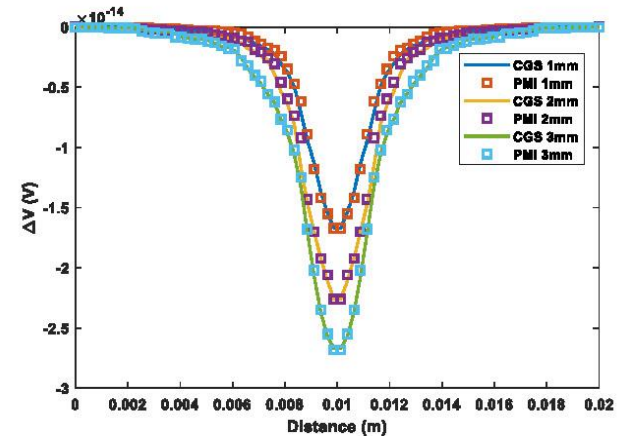


FIGURE 6. Computation results for the copper plate with different depths of defect, lift-off is 0.05 mm.

1) VERIFICATION OF THE PMI-BASED ACCELERATION SOLVER

Figures 5 and 6 demonstrate the changes of induced voltage on the receiver coil as the sensor scans along the y axis above the sample plates (figure 1(b)) with three different depths of the defects under the same frequency and lift-off. It can be seen that CGM and PMI methods agree well. As expected, the maximum value (peak value) of the voltage occurs at the center of the sample where the defect is located. The deeper the defect is, the larger the change in the induced voltage. There is a larger drop as defect depth increases from 1 mm to 2 mm than from 2 mm to 3 mm, which is due to the strength of eddy current decreases as the depth increases. Compared with the results from the aluminum plate, the change of the received voltage from the copper plate is slightly larger which is due to a higher conductivity for copper.

Figure 7 illustrates the effect of the lift-off for the crack detection simulated from the copper plate with a 3 mm depth defect in the middle of the plate. The lift-off of the sensor is 0.05 mm and 0.5 mm respectively. The results from both methods agree well and the peaks of the voltage change are located at the same place. With the increase of the lift-off,

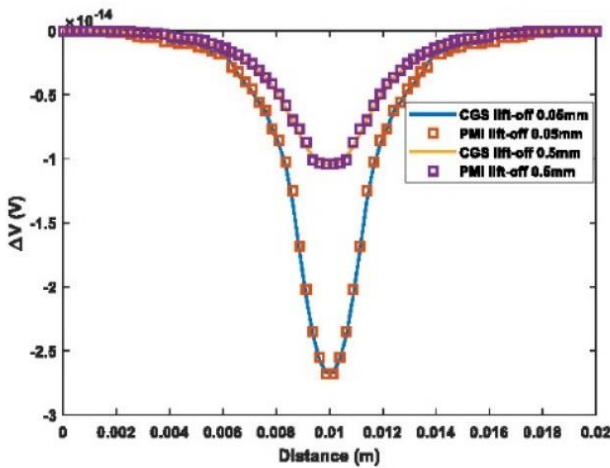


FIGURE 7. Computation results for the copper plate with different lift-offs.

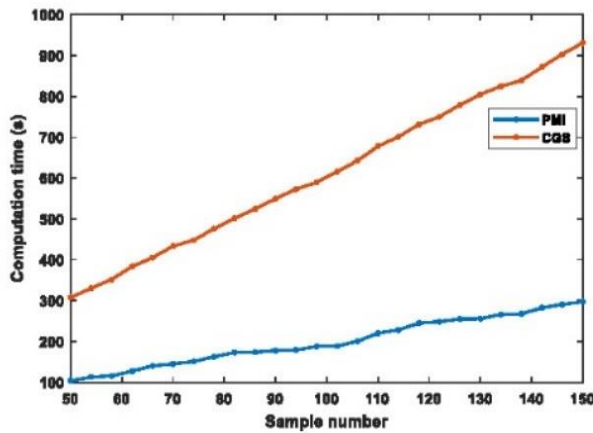


FIGURE 8. Computation time of PMI method and CGS method for different scanning sample numbers.

the peak value decreases around 2.5 times which also proves the lift-off is one of the crucial factors in the crack detection process.

2) EFFECT OF SAMPLING POINT DENSITY DURING SCANNING

The effect of the sampling point density for crack detection is presented in Fig. 8. The aluminium plate with a 3 mm depth of defect was used in the simulation process. The computation time varies from 100 s to 300 s for each scanning process by using the PMI method while it consumes 300 s to 900 s by using the conventional CGS method as the scanning sample points increasing from 50 to 150 in the step of 4. It can be noticed that the computation speed of the PMI method is about 3 times faster than the conventional CGS method. As the sampling point density increases, the time needed is increasing linearly and the time for high density of sampling points shrinks a lot as using the accelerated method.

3) EFFECT OF FREQUENCY

As shown in Fig. 9, the relationship between the frequency used in the simulation and the computation time is plotted. The frequency used ranges from 10 Hz to 10 kHz in a logarithmic scale in the simulation process. After adopting

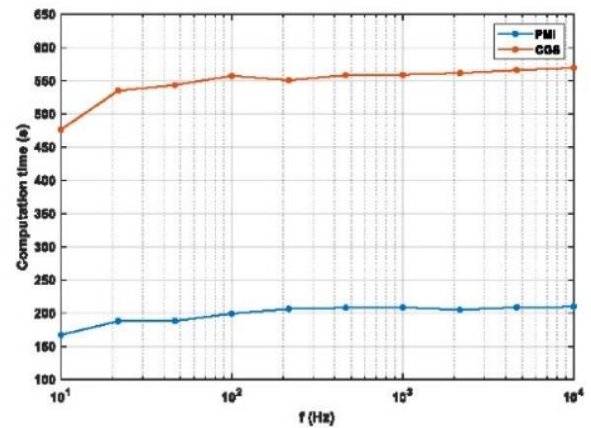


FIGURE 9. Computation time of PMI method and CGS method under different frequencies.

TABLE 2. CGS method and PMI method computation time for different defect depths.

Defect Depth	Computation Time (s)			
	Aluminium		Copper	
1mm	PMI	CGS	PMI	CGS
1mm	165.64	436.32	166.12	446.55
2mm	168.64	449.51	167.97	450.31
3mm	170.96	458.12	167.79	455.75

the PMI method, the scanning speed is much faster than the conventional CGS method. The computation time used for PMI and conventional CGS methods almost remains stable regardless of frequency settings, around 200 s, and 550 s respectively. It can be concluded that the acceleration efficiency remains almost the same concerning the frequency in the scanning process.

4) EFFECT OF DEFECT DEPTH

As can be seen from table 2, for the PMI method, the computation time slightly increases as the defect depth increases to 3 mm when aluminium plate was used while the speed almost maintains stable when the copper plate is used. Meanwhile, for the CGS method, the computation time increases no matter which material is used. It can be noticed that the acceleration efficiency under the defect depth of 3 mm is slightly higher than that under the defect depth of 1 mm and 2 mm.

IV. CONCLUSION

This paper has proposed a method to accelerate the computation for the crack detection in FEM eddy current calculation by using a PMI method. Based on the perturbed matrix inversion (PMI) method, the effect of the perturbation matrix caused by the defect can be easily taken into account without inverting a full matrix.

From the results of the numerical tests, a good agreement can be found between the edge FEM and the analytical solution by Dodd and Deeds, which verifies the accuracy of the FEM solver. Besides, the PMI method agrees with the conventional CGS method but has higher computational efficiency. In numerical tests, two materials (aluminium and copper) are modelled. The results from both materials showed

that the computation time by the PMI method was shortened about 3 times compared with that by the conventional CGS method. Moreover, the acceleration efficiency is slightly related to the crack depth due to the degree of perturbation on the stiffness matrix with different crack depths, but it remains almost the same for the frequency used in the scanning process. It should be noted that the initial inversed stiffness matrix Q needs to be calculated prior in order for this method to be effective.

APPENDIX

Firstly, the Dodd Deeds formulation is applied in order to obtain the variation of the inductance between the transmitter and receiver due to the presence of the testing sample [24], [25]. The complex inductance variation can be represented as

$$\Delta L(\omega) = L(\omega) - L_A(\omega) \quad (14)$$

where: $L(\omega)$ and $L_A(\omega)$ denotes the inductance with and without the presence of the sample.

The equations of Dodd Deeds analytical formulation are shown in followings:

$$\Delta L(\omega) = K \int_0^\infty \frac{P^2(\alpha)}{\alpha^6} A(\alpha) \varphi(\alpha) d\alpha \quad (15)$$

$$\varphi(\alpha) = \frac{(\alpha_1 + \alpha)(\alpha_1 - \alpha) - (\alpha_1 + \alpha)(\alpha_1 - \alpha)e^{2\alpha_1 c}}{-(\alpha_1 - \alpha)(\alpha_1 - \alpha) + (\alpha_1 + \alpha)(\alpha_1 + \alpha)e^{2\alpha_1 c}} \quad (16)$$

$$\alpha_1 = \sqrt{\alpha^2 + j\omega\sigma\mu_0} \quad (17)$$

$$K = \frac{\pi\mu_0 N^2}{h^2(r_1 - r_2)^2} \quad (18)$$

$$P(\alpha) = \int_{\alpha r_1}^{\alpha r_2} x J_1(x) dx \quad (19)$$

$$A(\alpha) = e^{-\alpha(2l_0 + h + g)}(e^{-2\alpha h} + 1) \quad (20)$$

where, c represents the sample thickness. σ represents the sample conductivity. μ_0 represents the magnetic permeability in the vacuum space. r_1 and r_2 represent the inner and outer radii of the probe. h and l_0 represent the probe height and the lift-off of the sensor probe. N represents the coil turns.

ACKNOWLEDGMENT

(Ruochen Huang and Mingyang Lu are co-first authors.)

REFERENCES

- [1] A. J. Otto, N. Marais, E. Lezar, and D. B. Davidson, "Using the FEniCS package for FEM solutions in electromagnetics," *IEEE Antennas Propag. Mag.*, vol. 54, no. 4, pp. 206–223, Aug. 2012.
- [2] M. Lu, Q. Zhao, P. Hu, W. Yin, and A. J. Peyton, "Prediction of the asymptotical magnetic polarization tensors for cylindrical samples using the boundary element method," in *Proc. IEEE Sensors Appl. Symp. (SAS)*, Apr. 2015, pp. 1–4.
- [3] K. Zhao, M. Vouvakis, and J.-F. Lee, "Solving electromagnetic problems using a novel symmetric FEM-BEM approach," *IEEE Trans. Magn.*, vol. 42, no. 4, pp. 583–586, Apr. 2006.
- [4] J. N. Reddy, *An Introduction to the Finite Element Method*. New York, NY, USA: McGraw-Hill, 1993.
- [5] J. Jin, *The Finite Element Method in Electromagnetics*. Piscataway, NJ, USA: IEEE Press, 2014.
- [6] Y. Li, T. Theodoulidis, and G. Y. Tian, "Magnetic field-based eddy-current modeling for multilayered specimens," *IEEE Trans. Magn.*, vol. 43, no. 11, pp. 4010–4015, Nov. 2007.
- [7] T. Takagi, H. Huang, H. Fukutomi, and J. Tani, "Numerical evaluation of correlation between crack size and eddy current testing signal by a very fast simulator," *IEEE Trans. Magn.*, vol. 34, no. 5, pp. 2581–2584, 1998.
- [8] S. Xie, Z. Chen, T. Takagi, and T. Uchimoto, "Development of a very fast simulator for pulsed eddy current testing signals of local wall thinning," *NDT&E Int.*, vol. 51, pp. 45–50, Oct. 2012.
- [9] S. Xie, Z. Chen, T. Takagi, and T. Uchimoto, "Efficient numerical solver for simulation of pulsed eddy-current testing signals," *IEEE Trans. Magn.*, vol. 47, no. 11, pp. 4582–4591, Nov. 2011.
- [10] Z. Chen, G. Preda, O. Mihalache, and K. Miya, "Reconstruction of crack shapes from the MFLT signals by using a rapid forward solver and an optimization approach," *IEEE Trans. Magn.*, vol. 38, no. 2, pp. 1025–1028, Mar. 2002.
- [11] Z. Chen, N. Yusa, and K. Miya, "Some advances in numerical analysis techniques for quantitative electromagnetic nondestructive evaluation," *Nondestruct. Test. Eval.*, vol. 24, nos. 1–2, pp. 69–102, Mar. 2009.
- [12] N. Yusa, Z. Chen, K. Miya, T. Uchimoto, and T. Takagi, "Large-scale parallel computation for the reconstruction of natural stress corrosion cracks from eddy current testing signals," *NDT&E Int.*, vol. 36, no. 7, pp. 449–459, Oct. 2003.
- [13] F. Matsuoka and A. Kameari, "Calculation of three dimensional eddy current by FEM-BEM coupling method," *IEEE Trans. Magn.*, vol. MAG-24, no. 1, pp. 182–185, Jan. 1988.
- [14] T. Steinmetz, N. Godel, G. Wimmer, M. Clemens, S. Kurz, and M. Bebenorf, "Efficient symmetric FEM-BEM coupled simulations of electro-quasistatic fields," *IEEE Trans. Magn.*, vol. 44, no. 6, pp. 1346–1349, Jun. 2008.
- [15] J. Georgii and R. Westermann, "A streaming approach for sparse matrix products and its application in Galerkin multigrid methods," *Electron. Trans. Numer. Anal.*, vol. 37, pp. 263–275, Jan. 2010.
- [16] J. Fritschy, L. Horeh, D. S. Holder, and R. H. Bayford, "Using the GRID to improve the computation speed of electrical impedance tomography (EIT) reconstruction algorithms," *Physiol. Meas.*, vol. 26, no. 2, pp. S209–S215, Apr. 2005.
- [17] M. Lu, A. Peyton, and W. Yin, "Acceleration of frequency sweeping in eddy-current computation," *IEEE Trans. Magn.*, vol. 53, no. 7, pp. 1–8, Jul. 2017.
- [18] W. Yin, M. Lu, L. Yin, Q. Zhao, X. Meng, Z. Zhang, and A. Peyton, "Acceleration of eddy current computation for scanning probes," *Insight*, vol. 60, no. 10, pp. 547–555, Oct. 2018.
- [19] W. Yin, J. Tang, M. Lu, H. Xu, R. Huang, Q. Zhao, Z. Zhang, and A. Peyton, "An equivalent-effect phenomenon in eddy current non-destructive testing of thin structures," *IEEE Access*, vol. 7, pp. 70296–70307, 2019.
- [20] A. F. Peterson, S. L. Ray, and R. Mittra, *Computational Methods for Electromagnetics*. Piscataway, NJ, USA: IEEE Press, 1997.
- [21] Z. Zeng, L. Udupa, S. Udupa, and M. Chan, "Reduced magnetic vector potential formulation in the finite element analysis of eddy current non-destructive testing," *IEEE Trans. Magn.*, vol. 45, no. 3, pp. 964–967, Mar. 2009.
- [22] C. Ktistis, D. W. Armitage, and A. J. Peyton, "Calculation of the forward problem for absolute image reconstruction in MIT," *Physiol. Meas.*, vol. 29, no. 6, pp. S455–S464, Jun. 2008.
- [23] H. Arsham, J. Grad, and G. Jaklič, "Perturbed matrix inversion with application to LP simplex method," *Appl. Math. Comput.*, vol. 188, no. 1, pp. 801–807, May 2007.
- [24] C. Dodd and W. Deeds, "Analytical solutions to eddy-current probe coil problems," *J. Appl. Phys.*, vol. 39, no. 6, pp. 2829–2839, May 1968.
- [25] S. K. Burke and R. J. Ditchburn, "Mutual impedance of planar eddy-current driver-pickup spiral coils," *Res. in Nondestruct. Eval.*, vol. 19, no. 1, pp. 1–19, Jan. 2008.



RUOCHEN HUANG is currently pursuing the Ph.D. degree with Wuliang in the School of Electrical and Electronics Engineering, The University of Manchester, mainly working on finite-element method (FEM) modeling software packages for electromagnetic (EM) simulations.



MINGYANG LU received the B.S. and Ph.D. degrees from the School of Electrical and Electronic Engineering, The University of Manchester, in 2014 and 2018, respectively, mainly working on developing a finite-element method (FEM) software to solve electromagnetic (EM) simulation taking into account random geometry and material properties (including microstructure), under the supervision of Wuliang Yin. He is currently a Research Associate with The University of Manchester, U.K. He has authored or coauthored over 30 publications. His current research interests include modeling magnetic induction effects, finite-element method (FEM) modeling software packages on electromagnetic (EM) simulations, and inversion of EM properties for metallic structure.



ANTHONY PEYTON received the B.Sc. degree in electrical engineering and electronics and the Ph.D. degree from the Institute of Science and Technology (UMIST), The University of Manchester, Manchester, U.K., in 1983 and 1986, respectively. He was a Principal Engineer with Kratos Analytical Ltd., Manchester, from 1986 to 1989, where he was involved in developing precision electronic instrumentation systems for magnetic sector and quadrupole mass spectrometers. He joined the Process Tomography Group, UMIST, where he was a Lecturer. In 1996, he was a Senior Lecturer with Lancaster University, Lancaster, U.K., where he was a Reader in electronic instrumentation, in 2001, and a Professor, in 2004. Since 2004, he has been a Professor of electromagnetic tomography engineering with The University of Manchester. His current research interests include instrumentation, applied sensor systems, and electromagnetics.



WULIANG YIN (Senior Member, IEEE) received the B.Sc. and M.Sc. degrees in electronic measurement and instrumentation from Tianjin University, Tianjin, China, in 1992 and 1995, respectively, and the Ph.D. degree in automotive electronics from Tsinghua University, Beijing, China, in 1999. He was appointed as a Mettler Toledo (MT) Sponsored Lecturer with the Department of Electrical and Electronic Engineering, School of Engineering, The University of Manchester, Manchester, U.K., in 2012, and was promoted to a Senior Lecturer, in 2016. He has authored one book and more than 230 articles, and was granted more than ten patents in the area of electromagnetic sensing and imaging. He was a recipient of the 2014 and 2015 Williams Award from the Institute of Materials, Minerals and Mining and the Science and Technology Award from the Chinese Ministry of Education, in 2000.

• • •

Chapter 8 A novel acceleration method for eddy current crack computation using finite element analysis

Ruochen Huang, Mingyang Lu, Ziqi Chen, Yuchun Shao, Gang Hu, Anthony Peyton, Wuliang Yin

NDT & E International, submitted.

In this chapter, due to the fact that a small crack only causes a small perturbation of the fields in the surrounding region. Based on this feature and by solving the field of crack surrounding region, a novel crack calculation acceleration method is proposed. Both the eddy current and the inductance change due to the sample plate are calculated and it shows that the more the element number, the more the computation speed increases. The experiment of crack scanning has also been conducted and the results agree with the simulation results.

A novel acceleration method for eddy current crack computation using finite element analysis

Ruochen Huang^a, Mingyang Lu^a, Ziqi Chen^a, Yuchun Shao^a, Gang Hu^a, Anthony Peyton^a, Wuliang Yin^{a*}

^aSchool of Electrical and Electronic Engineering, University of Manchester, Manchester, M13 9PL, UK

Ruochen.huang@postgrad.manchester.ac.uk

Mingyang.lu@manchester.ac.uk

Ziqi.chen@manchester.ac.uk

Yuchun.shao@postgrad.manchester.ac.uk

Gang.hu@postgrad.manchester.ac.uk

A.peyton@manchester.ac.uk

Wuliang.yin@manchester.ac.uk

*Corresponding author: Wuliang.yin@manchester.ac.uk

Abstract

Finite element analysis plays an essential role in the field of eddy current computation and analysis for non-destructive testing applications. There are some analytical solutions that can be used to solve eddy current problems, however, in most cases, there is no suitable analytical method, i.e., the test sample with arbitrary geometry or with arbitrary shape of crack. Therefore, finite element method is a fundamental tool in conducting the investigations. A key feature of using finite element method for eddy

current simulation is being versatile but slow. In this paper, exploiting the fact that the crack only causes a small perturbation in fields in the surrounding region, a novel crack calculation acceleration method is proposed. The algorithm proves that the calculation can be mainly executed within the perturbation domain. Both numerical and experimental tests have been conducted for verification. The speed of the calculation is enhanced greatly (up to 34 folds in the tested cases) while deviation from the full solution is within 5%. Moreover, the measured results have a good agreement with the simulated ones under different depths of crack.

Keywords: finite element method, crack detection, eddy current, acceleration.

Introduction

Non-destructive techniques have been widely applied in the industrial applications due to its merits, i.e., non-contact, reliability and no damage to the target [1-2]. Eddy current testing, as one of the categories, is commonly utilised to measure the product characteristics, i.e., electrical conductivity and magnetic permeability [3-5], predict the coating thickness [6-8] and detect the crack existing in the target sample [9-10]. As known, due to the aging and long-time running, the presence of the crack can lead to severe consequences and financial losses. Thus, the facilities would be examined regularly to prevent from unexpected failure [11-12].

Many researches have been investigated and carried out to detect the crack using the eddy current testing methods. In [13], Nafiah, *et al.* used the features extracting from the scanning data to develop different models (multiple linear regression model, hierarchical linear model and artificial neural network) to predict the depth and angle of the crack. From the results, it was found that ANN model has the most accurate performance compared with other models. A sensor probe with orthogonal transmitters was made to produce different excitation current for crack detection and proved to be feasible [14]. Besides, Liu, *et al.* designed a non-encircling sensor structure with L

shape using electromagnetic tomography to achieve the reconstruction of rail defect inspection [15]. In [16], Yang *et al.* considered the uniform sensitivity property of the rotational electromagnetic field and applied it into the detection for the crack with arbitrary angle. However, both sensor design and data analysis require accurate modelling of the eddy current phenomena.

To precisely simulate the eddy current problem due to the effect of the crack, there are various methods and can be generally divided into three groups, that is, analytical methods, finite element methods and integral equation techniques. Analytical methods are generally fast and convenient for computing eddy current in some special cases, i.e., an infinitely long-slot crack [17] and co-axial hole [18]. For example, Lu, *et al.* developed the analytical solution for triple-coil drive-pickup EC sensor probe to identify the orientation of the surface crack [19]. Compared with analytical methods, finite element methods and integral equation techniques have the capability to solve the eddy current problem for arbitrary geometry of crack or target sample and the sensor setup.

In solving the problem caused by the presence of the crack using the integral formulation, volume integral [20-23] can be considered for the scattered field. The dyadic kernel was applied by Bowler and Jenkins, the direct and reflected field can be calculated due to the perturbation of the open crack and meets the continuity for the boundary [20]. Supported by the dedicated kernel which lessens massive computations for the number of unknown variables, the eddy current problem due to the existence of the edge crack in the conductive quarter region can be addressed [23]. Besides, the crack with negligible width can also be treated as a surface with jump in the electromagnetic field between the crack and the conductor [24]. The boundary condition for the crack in the thin skin regime introduced by Bowler and Harfield satisfied with the 2-D Laplace equation and the impedance change can be derived [25].

Several researches for the development of the finite element methods for different cases

have been conducted for decades, including curved plates simulation [26], ferromagnetic modelling [27-28] and conductive defect simulation [29]. Since the received field is affected by the crack, the perturbed field can be calculated by improving the formulations in most works. In order to ease the burden from the mesh discretization, Badics, *et al.* introduced a thin sheet crack model for the crack which satisfies the condition that the crack width is much smaller than other dimensions of the crack [30]. In [29], to tackle the effect caused by the conductive crack, the parallel component of the received signal can be calculated with the condition that the width of a crack is less than the prepared database.

Due to the fact that the massive computation time is required to achieve high accuracy from the simulation, reducing the running time is essential and several significant progresses have been made during these decades in this aspect. Prestored database method [27, 31-33] and FEM-BEM hybrid method [22, 31] are popular in solving this kind of problem. Du, *et al.* proposed a fast calculation solver based on the FEM-BEM method and database for ECT simulations and the running time was significantly shortened with the guarantee of the accuracy [31]. Combining the finite element method with the existing analytical methods for the unflawed area, the distorted field due to the defect can be directly obtained [34]. The adaptive fast multipole method offers the possibility to shrink the operations in the computation process and Rubinacci, *et al.*, proved its robustness in [35]. Moreover, new shape functions were presented by Morozov adapting the eddy current caused by the crack and a small part from the entire system was inverted to obtain the perturbed signal which lessens the burden of the computation [22]. Lu, *et al.* proposed an accelerated method by using the optimized initial guess from previous frequency calculation which reduces the iteration numbers for the simulation [36]. With the aid of Darwin approximation, the subdomain perturbation (SDP) formulation can be usefully adopted to simulate the near field for eddy current problem both the accuracy from the low frequency aspects and the computation speed [37].

In this paper, to address this issue, a fast crack calculation method is proposed. Due to the presence of the crack, the system is mainly affected around the crack area. Utilising this feature, the solution due to the perturbation by the crack can be calculated. The theoretical manipulations have been presented in the following part and numerical and experimental tests have been carried out for the verification of the proposed method.

Theoretical manipulations for crack calculation

A. Edge element analysis based on FEM

Finite element method (FEM) is a powerful tool in electromagnetic computing and is widely used in the field of non-destructive testing. The FEM program based on A-V Edge-Element Formulation was scripted in MATLAB by utilising the constructed mesh models (mesh information, including coordinates of subdomain elements) of the tested sample. Taking the boundary conditions into account, the Galerkin method is employed to compute the scalar potential (V) and vector potential (\mathbf{A}) of the whole domain. For each tetrahedral subdomain element, the equations are shown as follows:

$$\begin{aligned} & \int_{\Omega_c} \nabla \times \mathbf{N}_i \cdot \nu \nabla \times \mathbf{A}^n d\Omega + \int_{\Omega_c} j\omega\sigma \mathbf{N}_i \cdot \mathbf{A}^n d\Omega + \int_{\Omega_c} j\omega\sigma \mathbf{N}_i \cdot \nabla V^n d\Omega \\ & = \int_{\Omega_c} \nabla \times \mathbf{N}_i \cdot \nu_0 \nabla \times \mathbf{A}_s d\Omega \quad i = 1, 2, \dots, 6 \end{aligned} \quad (1)$$

$$\int_{\Omega_c} j\omega\sigma \nabla L_i \cdot \mathbf{A}^n d\Omega + \int_{\Omega_c} j\omega\sigma \nabla L_i \cdot \nabla V^n d\Omega = 0 \quad i = 1, 2, \dots, 4 \quad (2)$$

Where: \mathbf{N}_i denotes the i th edge shape (interpolation) function; L_i denotes the i th nodal shape (interpolation) function; Ω_c denotes the conductive region of the model; ν and σ denote the reluctivity and the conductivity of the tested sample; ν_0 denotes reluctivity in the vacuum.

Considering the uniqueness of shape (interpolation) functions for individual tetrahedral element, the coordinate transformation is used to convert the global coordinates (λ_v, λ_s) to the local coordinates ($\hat{\lambda}_v, \hat{\lambda}_s$), in order to reduce the burden for computation.

Consequently, the shape functions can be expressed as

$$J = \begin{bmatrix} \frac{\partial x}{\partial \xi} & \frac{\partial y}{\partial \xi} & \frac{\partial z}{\partial \xi} \\ \frac{\partial x}{\partial \eta} & \frac{\partial y}{\partial \eta} & \frac{\partial z}{\partial \eta} \\ \frac{\partial x}{\partial \zeta} & \frac{\partial y}{\partial \zeta} & \frac{\partial z}{\partial \zeta} \end{bmatrix} \quad (3)$$

$$\lambda_v = J^{-1} \hat{\lambda}_v \quad (4)$$

$$\lambda_s = J^{-1} \hat{\lambda}_s \quad (5)$$

$$\nabla \times \lambda_v = \frac{1}{|J|} J^T \nabla \times \hat{\lambda}_v \quad (6)$$

Where, J is the Jacobian matrix, λ_v is the vector component in the global coordinates, λ_s is the scalar component in the global coordinates, $\hat{\lambda}_v$ is the vector component in the local coordinates, $\hat{\lambda}_s$ is the scalar component in the local coordinates.

Combining equations (1) and (2), the whole system matrix can be derived as a linear system of algebraic equations with the support of the stiffness matrix Q .

$$Q = \begin{bmatrix} K^{p \times p} & L^{p \times q} \\ M^{q \times p} & N^{q \times q} \end{bmatrix} \quad (7)$$

$$Q \begin{bmatrix} \begin{bmatrix} A_1 \\ \vdots \\ A_p \end{bmatrix} \\ \begin{bmatrix} V_1 \\ \vdots \\ V_q \end{bmatrix} \end{bmatrix} = X \quad (8)$$

Here, p denotes the number of edges and q denotes the number of vertex nodes. K , which is related to the summation of the first two terms of equation (1), mainly dominates by the vector field and contributes to the generation of the vector potential. L is the third term of equation (2), controlling the flow of the eddy current as it encounters with the notch. M and N are the terms of left-hand side of equation (2), satisfying the conditions of magnetostatic field. X is the terms of right-hand side of

equation (1) and (2), providing the background field of the entire system. Therefore, the magnetic vector potential field \mathbf{A} along all the edges and electric scalar potential field V on all the vertex of the entire system can be calculated by equation (9). Then, the eddy current produced in the tested sample is equal as

$$\mathbf{J}_s = \sigma \mathbf{E} = -j\omega\sigma\mathbf{A} - \sigma\nabla V \quad (9)$$

Where, \mathbf{E} is the electric field contributed by both the vector and scalar potential field.

As stated in paper [38], the calculated inductance change (ΔL) due to the sample can be given as

$$\Delta L = \frac{1}{j\omega I^2} \int_c \mathbf{E}_a \cdot \mathbf{E}_b \cdot (\sigma_a - \sigma_b) dv \quad (10)$$

Here the inductance change is derived from the substrate domain of a and b .

B. Accelerated calculation for the algebraic system due to small perturbation

The final solution of the FEM problem results in a large algebraic equation system, as shown in equation (8). Considering that there is a small crack in the tested sample, the original system matrix (crack free sample) can be expressed with the matrices affected/unaffected by the small perturbation, shown as

$$\begin{bmatrix} K_1 & K_2 & L_1 & L_2 \\ K_3 & K_4 & L_3 & L_4 \\ M_1 & M_2 & N_1 & N_2 \\ M_3 & M_4 & N_3 & N_4 \end{bmatrix} \begin{bmatrix} \mathbf{A}_u \\ \mathbf{A}_c \\ V_u \\ V_c \end{bmatrix} = \begin{bmatrix} X_{u1} \\ X_{c1} \\ X_{u2} \\ X_{c2} \end{bmatrix} \quad (11)$$

Then reordering equation (11), four new submatrices (Q_{11} , Q_{12} , Q_{21} and Q_{22}) can be used to present the current crack free system matrix and given as

$$\begin{bmatrix} K_1 & L_1 & K_2 & L_2 \\ M_1 & N_1 & M_2 & N_2 \\ K_3 & L_3 & K_4 & L_4 \\ M_3 & N_3 & M_4 & N_4 \end{bmatrix} \begin{bmatrix} \mathbf{A}_u \\ V_u \\ \mathbf{A}_c \\ V_c \end{bmatrix} = \begin{bmatrix} X_{u1} \\ X_{u2} \\ X_{c1} \\ X_{c2} \end{bmatrix} \quad (12)$$

$$\begin{bmatrix} Q_{11} & Q_{12} \\ Q_{21} & Q_{22} \end{bmatrix} \begin{bmatrix} S_u \\ S_c \end{bmatrix} = \begin{bmatrix} X_u \\ X_c \end{bmatrix} \quad (13)$$

Where: $Q_{11} = \begin{bmatrix} K_1 & L_1 \\ M_1 & N_1 \end{bmatrix}$, $Q_{12} = \begin{bmatrix} K_2 & L_2 \\ M_2 & N_2 \end{bmatrix}$, $Q_{21} = \begin{bmatrix} K_3 & L_3 \\ M_3 & N_3 \end{bmatrix}$, $Q_{22} = \begin{bmatrix} K_4 & L_4 \\ M_4 & N_4 \end{bmatrix}$, $S_u = \begin{bmatrix} A_u \\ V_u \end{bmatrix}$, $S_c = \begin{bmatrix} A_c \\ V_c \end{bmatrix}$, $X_u = \begin{bmatrix} X_{u1} \\ X_{u2} \end{bmatrix}$, $X_c = \begin{bmatrix} X_{c1} \\ X_{c2} \end{bmatrix}$

Here submatrix Q_{11} represents the domain of elements which has no influence due to the existence of the crack while submatrices Q_{12} , Q_{21} and Q_{22} represent the domain of elements near the crack and are affected by this small perturbation. Submatrices Q_{12} and Q_{21} are transposed. Matrix X is the right-hand side matrix of the system which is partitioned into two column matrices X_u and X_c and matrix S is the solution for the matrix system, consisting of two submatrices S_u and S_c . Then the system equations change to

$$Q_{11}S_u + Q_{12}S_c = X_u \quad (14)$$

$$Q_{21}S_u + Q_{22}S_c = X_c \quad (15)$$

Now due to the presence of the crack, the left-hand side of the crack free sample system matrix is very slightly perturbed. then the system equations with the small perturbation turn to

$$Q_{11} S_u' + (Q_{12} + \Delta Q_{12})S_c' = X_u \quad (16)$$

$$(Q_{21} + \Delta Q_{21})S_u' + (Q_{22} + \Delta Q_{22})S_c' = X_c \quad (17)$$

Where: ΔQ_{12} , ΔQ_{21} and ΔQ_{22} are the submatrices affected due to the small perturbation. S_u' and S_c' are the solution for the new system equations.

Since that the element domain of submatrix Q_{11} is hardly affected by the presence of the small perturbation, the vector and scalar solution of S_u' for this domain is regarded equal to the unperturbed solution without the crack in the sample plate, which gives

$$S_u' \approx S_u \quad (18)$$

Using equations (18) and (15), the solution S_c' can be derived from equation (17).

$$S_c' = (Q_{22} + \Delta Q_{22})^{-1}(-\Delta Q_{21}S_u + Q_{22}S_c) \quad (19)$$

The solution S_c' should also satisfy equation (16). It can be proved as below.

By referring to [39], and assume that Q_{22i} is the inversion matrix of Q_{22} , then

$$(Q_{22} + \Delta Q_{22})^{-1} = Q_{22i} - Q_{22i}\Delta Q_{22}(I + Q_{22i}\Delta Q_{22})^{-1}Q_{22i} \quad (20)$$

Substitute equation (20) to equation (19), it turns to

$$S_c' = S_c - Q_{22i}\Delta Q_{21}S_u + Q_{22i}\Delta Q_{22}(I + Q_{22i}\Delta Q_{22})^{-1}Q_{22i}\Delta Q_{21}S_u - Q_{22i}\Delta Q_{22}(I + Q_{22i}\Delta Q_{22})^{-1}S_c \quad (21)$$

Now substitute equations (18) and (21) to the left-hand side of equation (16) and assume that $G = Q_{22i}\Delta Q_{22}$, $H = Q_{22i}\Delta Q_{21}$, it gives

$$Q_{11} S_u' + (Q_{12} + \Delta Q_{12})S_c' = Q_{11}S_u + (Q_{12} + \Delta Q_{12})(S_c - HS_u + G(I + G)^{-1}HS_u - G(I + G)^{-1}S_c) \quad (22)$$

The matrices ΔQ_{12} , G and H are perturbed matrices with small element values, terms containing these matrices can be eliminated, then equation (22) can be approximated as equation (23), which is satisfied with the right-hand side of equation (14).

$$Q_{11} S_u' + (Q_{12} + \Delta Q_{12})S_c' \approx Q_{11}S_u + Q_{12}S_c = X_u \quad (23)$$

Consequently, equation (16) is valid. Therefore, the final solution of equation system (16-17) with the perturbation of the crack can be approximately calculated as

$$\begin{cases} S_u' = S_u \\ (Q_{22} + \Delta Q_{22})S_c' = X_c - (Q_{21} + \Delta Q_{21})S_u \end{cases} \quad (24)$$

Combine the proposed method with the conjugate gradient squared method, the vector

and scalar potential can be calculated.

Simulation setup

An EM sensor probe is designed for the simulations to verify the proposed method. As shown in Fig. 1, the sensor probe is the co-axial type sensor. As listed in Table 1, the exciting coil and receiving coil have identical radius and height. The sensor probe is placed 0.5 mm above the sample plate and the gap between the coils is 0.5 mm. The excitation current with the magnitude of 1 A and the frequency of 1 kHz is injected into the exciting coil, the induced inductance with the presence of the sample plate can be received from the receiving coil. The conductivity and thickness of the sample plate is set to 57 MS/m and 2 mm respectively. It can be seen from Fig. 2 that there are different shapes of crack would be tested. These cracks are generated in the middle of the sample plate.

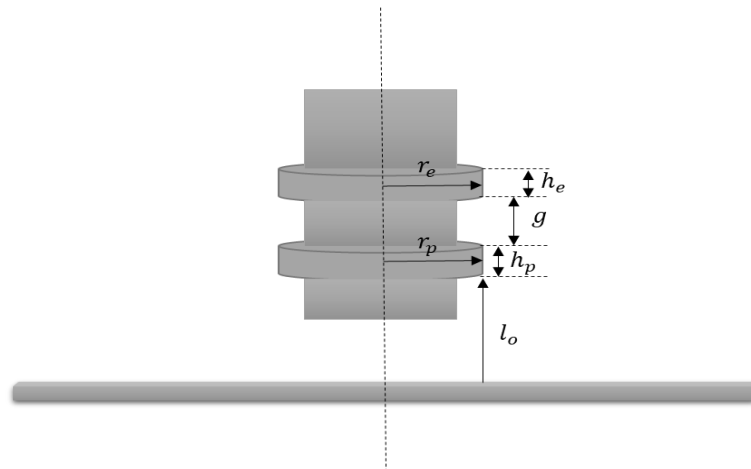


Fig. 1 The configuration of EM sensor probe

TABLE I

Coil Parameters

Exciting coil	Radius (r_e)	3 mm
	Height (h_e)	0.3 mm
Receiving coil	Radius (r_p)	3 mm
	Height (h_p)	0.3 mm
Lift off l_o	0.5 mm	
Gap between the exciting coil and	0.5 mm	

receiving coil g	
Thickness of the sample plate c	2 mm
Working frequency f	1 kHz

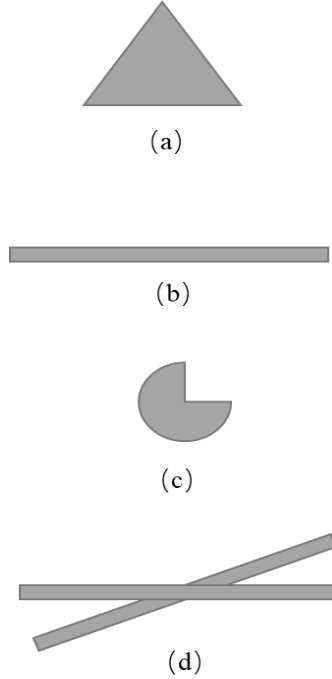


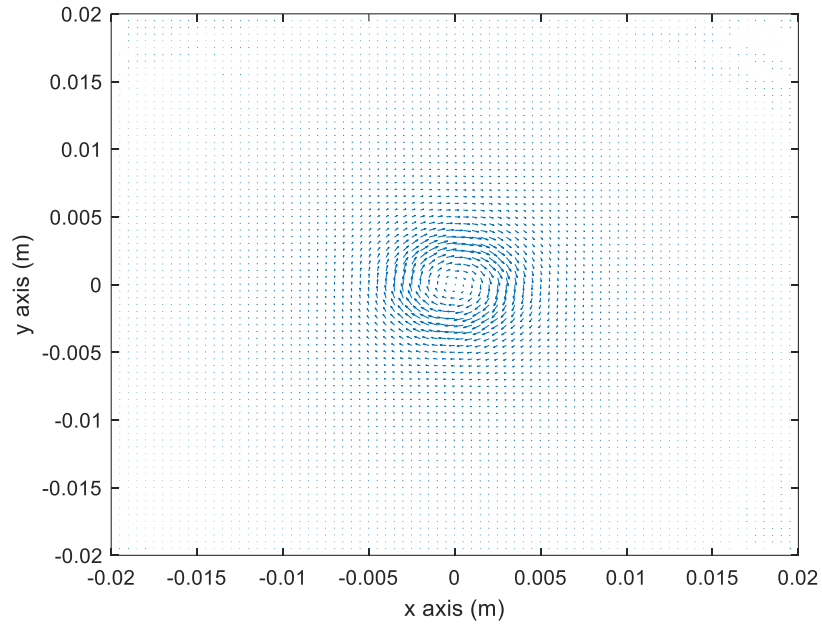
Fig. 2 Crack shapes (a) Triangle (b) Rectangle (c) Circular sector (d) X shape

Results

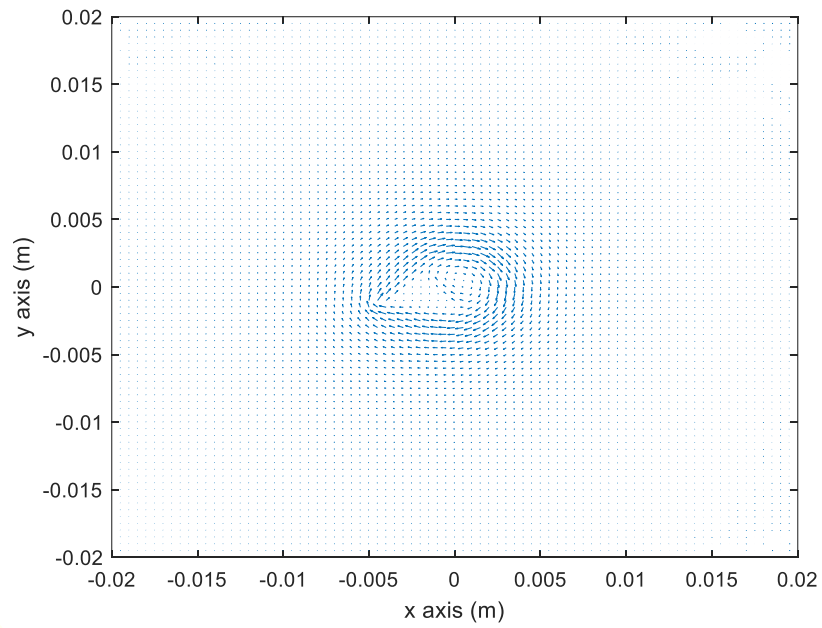
A. Verification of FE analysis

The movement of eddy current is a key point in the inspection of eddy current testing. It would be disturbed due to the presence of the crack. As shown in Fig. 3, eddy current flows on the sample plate without crack or with different shapes of crack. It can be seen that the eddy current is rotational as there is no crack on the sample plate. Then when it encounters with a crack, it will be flow around the edge of the crack but the overall trend remains the same. From the vector diagram of the eddy current, the crack shape can be seen clearly and same compared with Fig. 2. The inductance change due to the sample plate with a rectangle crack under different element number was calculated. As listed in Table II, the deviation is within 5% and the speed of the computation is significantly improved, i.e., the time for the calculation is shortened 3.79 times as the total element number is 10 k with the variation of 2.56 % while 34.24 times as the total

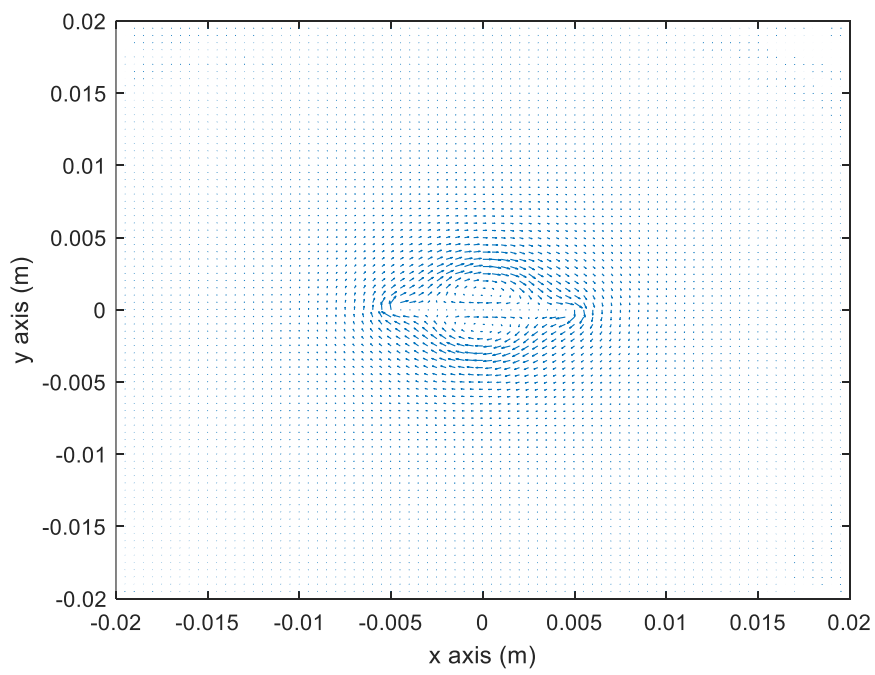
element number is 139 k with the variation of 3.56%. Fig. 4 shows the relative residual of varying iteration number under different element number and it can be also revealed that it needs less iteration cycles to achieve the convergence.



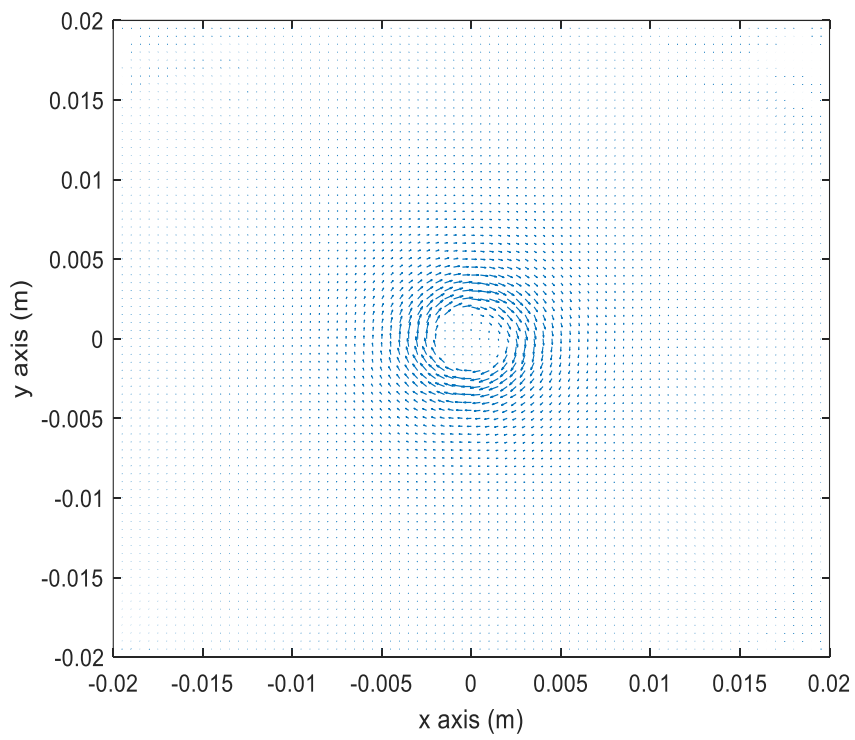
(a)



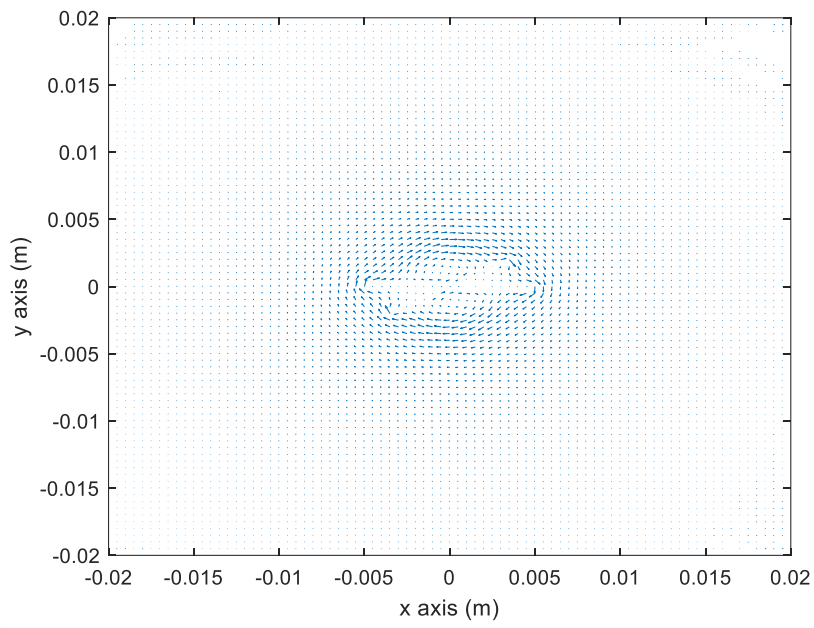
(b)



(c)



(d)



(e)

Fig. 3 Eddy current (a) without crack and with crack (b) triangle (c) rectangle (d) circular sector (e) X shape

TABLE II

The accelerated rate and deviation of the inductance change due to the sample plate under different element number

Element Number	Calculation time of the method without acceleration (s)	Calculation time of the proposed method (s)	Accelerated rate (times)	Calculation deviation (%)
10 k	7.69	2.03	3.79	2.56
51 k	57.74	3.56	16.22	3.22
139 k	306.79	8.96	34.24	3.56

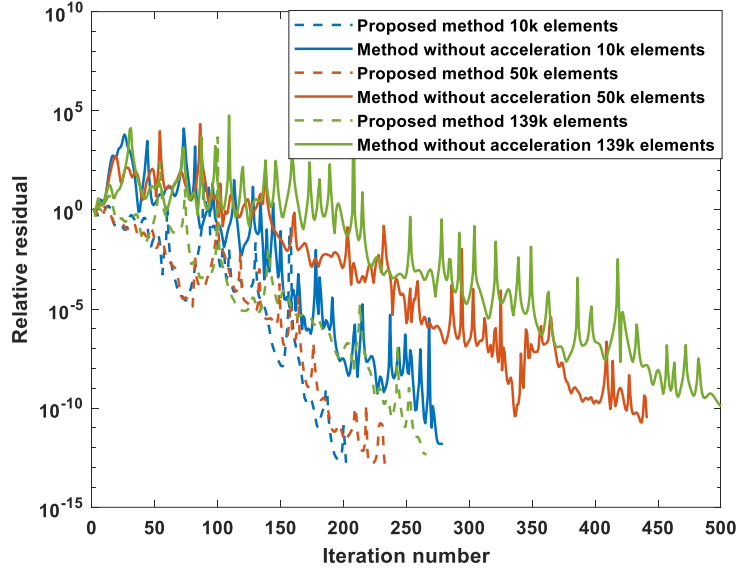
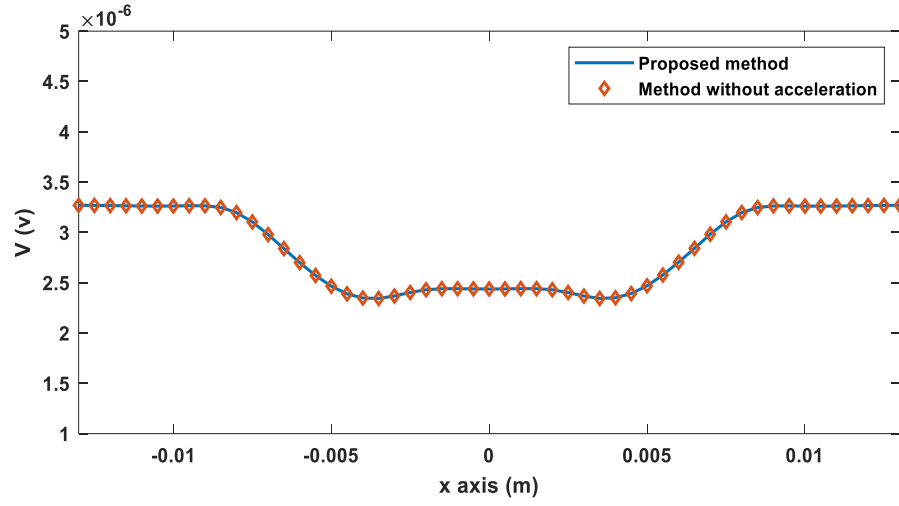


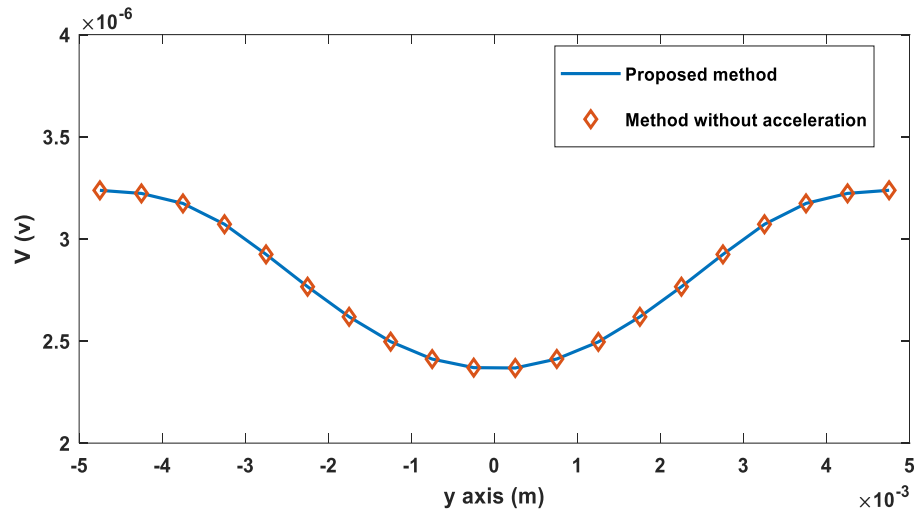
Fig. 4 Relative residual under different element number

B. Crack scanning

FE calculation can be used in the detection for the crack. As depicted in Fig. 5, the sensor probe scans a crack with the length of 10 mm and the width of 0.5 mm in the centre of the sample plate (same with the sample plate with a rectangle crack, shown in Fig. 2(b) and Fig. 3(c)) and it scans along x and y axis respectively. The results agreed with the simulation results without using the acceleration method and, as listed in Table III, the speed is enhanced approx. 7 folds. It can be noted that the sensor probe closes to the crack, the received voltage is decreasing then stays stable and the voltage increases until it leaves the crack. This phenomenon is due to the perturbation of the crack, the distribution of the eddy current changes on the sample plate which results in the change of the magnetic field.



(a)



(b)

Fig. 5 The sensor probe scans across the crack along (a) x axis (b) y axis

TABLE III

The computation time for one step

Scanning direction	Calculation time (s)	
	Proposed method	Method without acceleration
X axis	5.47	35.92
Y axis	5.68	36.08

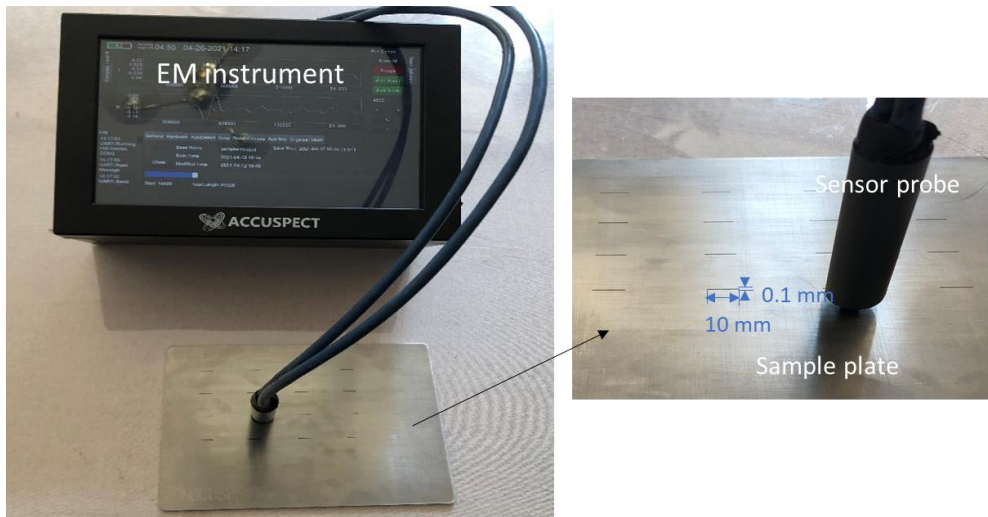


Fig. 6 Experimental setup

TABLE IV

Experiment sensor parameters

Excitation coil	Length (mm)	8
	Width (mm)	4
	Height (mm)	10
	Turns N	20
Receiving coil	Radius (mm)	0.5
	Turns N	250
Lift-off l_0 (mm)		1
Excitation frequency (kHz)		20

Figure 6 shows the experimental setup consisting of an EM instrument, a sensor probe and the sample plate. Then the detected data would be transmitted to the host PC. Here a differential sensor probe was made for detecting different depths of the crack from 0.1 mm to 2 mm with the increment of 0.1 mm. The crack has the length of 10 mm and the width of 0.1 mm. The sensor parameters are listed in Table IV. The lift-off of the sensor probe was 1 mm and the working frequency was 20 kHz. The conductivity and the thickness of the sample plate are 1.4 MS/m and 2 mm respectively. The received and simulated data are plotted in Fig. 7. The simulated results are agreed with the measured ones. It can be seen that, when the sensor probe scan across the crack, there is a sine relationship between the scanning distance and the received voltage of the measured and simulated data. The peak voltage is related to the depth of the crack, i.e., the deep the crack, the larger the received result. The peak voltage can be used to predict the depth of the crack. Besides, it can be deduced that the length of the crack is 10 mm

which is consistent with the sample crack.

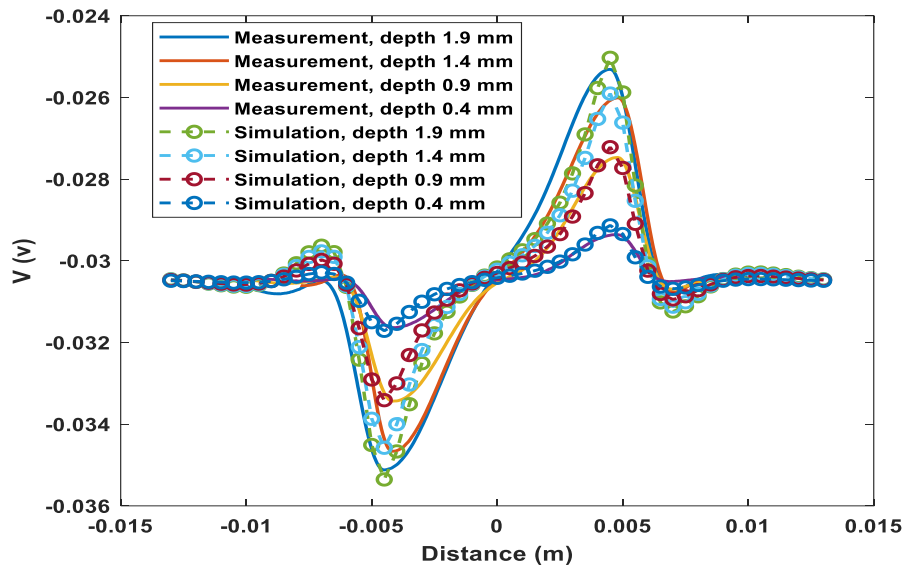


Fig. 7 Measured and simulated results under different depths

Conclusions

In this paper, an acceleration method using finite element method is proposed. Instead of calculating the entire domain for the tested sample, it computes for the region affected by the crack from the crack free region in the simulation. The algorithm is proved effective in greatly shortening the computation time. For this method, the larger the element number of the tested sample, the more the computation speed increases. The accuracy has been verified by numerical tests and it can also be applied for the detection of the crack.

Acknowledgement

This work was supported by [UK Engineering and Physical Sciences Research Council (EPSRC)] [grant number: EP/P027237/1] [title: Real-time In-line Microstructural Engineering (RIME)].

Reference

- [1] M. Lu, X. Meng, R. Huang, L. Chen, A. Peyton and W. Yin, "Measuring Lift-Off Distance and Electromagnetic Property of Metal Using Dual-Frequency Linearity Feature," *IEEE Transactions on Instrumentation and Measurement*, vol. 70, pp. 1-9, 2021.
- [2] D. Wu, W. Chen, J. Yang and F. Yang, "Self-resonance eddy-current testing method in noncontact detection of carbon fiber reinforced plastics," *Composite Structures*, vol. 259, 113247, 2021.
- [3] X. Chen, Y. Lei, "Electrical conductivity measurement of ferromagnetic metallic materials using pulsed eddy current method," *NDT & E International*, vol. 75, pp. 33-38, 2015.
- [4] X. Ma, A.J. Peyton, and Y.Y. Zhao, "Eddy current measurements of electrical conductivity and magnetic permeability of porous metals," *NDT & E International*, vol. 39, no. 7, pp. 562-568, 2006.
- [5] M. Lu, R. Huang, W. Yin, Q. Zhao and A. Peyton, "Measurement of Permeability for Ferrous Metallic Plates Using a Novel Lift-Off Compensation Technique on Phase Signature," *IEEE Sensors Journal*, vol. 19, no. 17, pp. 7440-7446, 1 Sept.1, 2019.
- [6] M. Lu, X. Meng, R. Huang, L. Chen, A. Peyton, W. Yin and Z. Qu, "Thickness measurement of circular metallic film using single-frequency eddy current sensor," *NDT & E International*, vol. 119, 102420, 2021.
- [7] W. Yin, R. Huang, M. Lu, Z. Zhang and A. Peyton, "Measurements of Thickness for Metallic Plates With Co-Axial Holes Using a Novel Analytical Method With the Modified Integration Range," *IEEE Access*, vol. 8, pp. 198301-198306, 2020.
- [8] Y. Yu, D. Zhang, C. Lai and G. Tian, "Quantitative Approach for Thickness and Conductivity Measurement of Monolayer Coating by Dual-Frequency Eddy Current Technique," *IEEE Transactions on Instrumentation and Measurement*, vol. 66, no. 7, pp. 1874-1882, July 2017.

- [9] B. Helifa, A. Oulhadj, A. Benbelghit, I. K. Lefkaier, F. Boubenider and D. Boutassouna, "Detection and measurement of surface cracks in ferromagnetic materials using eddy current testing," *NDT & E International*, vol. 39, no. 5, pp. 384-390, 2006.
- [10] P., Xu, S. Huang and W. Zhao, "A new differential eddy current testing sensor used for detecting crack extension direction," *Ndt & E International*, vol. 44, no. 4, pp. 339-343, 2011.
- [11] N. Yusa, S. Perrin, K. Mizuno, Z. Chen, and K. Miya, "Eddy current inspection of closed fatigue and stress corrosion cracks," *Measurement Science and Technology*, vol. 18, no. 11, pp. 3403-3408, 2007.
- [12] N. Yusa, S. Perrin, K. Mizuno, and K. Miya, "Numerical modeling of general cracks from the viewpoint of eddy current simulations," *NDT & E International*, vol. 40, no. 8, pp. 577-583, 2007.
- [13] F. Nafiah, A. Sophian, M. R. Khan, I. M Z. Abidin, "Quantitative evaluation of crack depths and angles for pulsed eddy current non-destructive testing," *NDT & E International*, vol. 102, pp. 180-188, 2019.
- [14] C. Ye, A. Rosell, M. Haq, E. Stitt, L. Udpa and S. Udpa, "EC probe with orthogonal excitation coils and TMR sensor for CFRP inspection," *International Journal of Applied Electromagnetics and Mechanics*, vol. 59, no. 4, 1247-1255, 2019.
- [15] Z. Liu, W. Li, F. Xue, J. Xiafang, B. Bu and Z. Yi, "Electromagnetic Tomography Rail Defect Inspection," *IEEE Transactions on Magnetics*, vol. 51, no. 10, pp. 1-7, Oct. 2015.
- [16] G. Yang, G. Dib, L. Udpa, A. Tamburrino and S. S. Udpa, "Rotating Field EC-GMR Sensor for Crack Detection at Fastener Site in Layered Structures," *IEEE Sensors Journal*, vol. 15, no. 1, pp. 463-470, Jan. 2015.
- [17] T. Theodoulidis, "Analytical model for tilted coils in eddy-current nondestructive inspection," *IEEE Transactions on Magnetics*, vol. 41, no. 9, pp. 2447-2454, Sept. 2005.
- [18] R. Huang, M. Lu, X. He, A. Peyton and W. Yin, "Measuring Coaxial Hole Size of Finite-Size Metallic Disk Based on a Dual-Constraint Integration Feature Using

Multifrequency Eddy Current Testing,” *IEEE Transactions on Instrumentation and Measurement*, vol. 70, pp. 1-7, 2021.

[19] M. Lu, X. Meng, R. Huang, L. Chen et al., "Determination of Surface Crack Orientation Based on Thin-Skin Regime Using Triple-Coil Drive–Pickup Eddy-Current Sensor," *IEEE Transactions on Instrumentation and Measurement*, vol. 70, pp. 1-9, 2021.

[20] J. R. Bowler, S. A. Jenkins, L. D. Sabbagh, and H. A. Sabbagh, “Eddy-current probe impedance due to a volumetric flaw,” *Journal of Applied Physics*, vol. 70, no. 3, pp. 1107-1114, 1991.

[21] A. Skarlatos, G. Pichenot, D. Lesselier, M. Lambert, and B. Duchene, “Electromagnetic modeling of a damaged ferromagnetic metal tube by a volume integral equation formulation,” *IEEE transactions on magnetics*, vol. 44, no. 5, pp. 623-632, 2008.

[22] M. Morozov, G. Rubinacci, A. Tamburrino and S. Ventre, “Numerical models of volumetric insulating cracks in eddy-current testing with experimental validation,” *IEEE Transactions on Magnetism*, vol. 42, no. 5, pp. 1568-1576, May 2006.

[23] J.R. Bowler, T. P. Theodoulidis, and N. Poulakis. “Eddy current probe signals due to a crack at a right-angled corner.” *IEEE transactions on magnetics*, vol. 48, no.12, pp. 4735-4746, 2012.

[24] J. R. Bowler, “Eddy-current interaction with an ideal crack. I. The forward problem,” *Journal of Applied Physics*, vol. 75, no. 12, pp. 8128-8137, 1994.

[25] J. R. Bowler and N. Harfield, “Thin-skin eddy-current interaction with semielliptical and epicyclic cracks,” *IEEE Transactions on Magnetism*, vol. 36, no. 1, pp. 281-291, Jan. 2000.

[26] Y. Le Bihan, “3-D finite-element analysis of eddy-current evaluation of curved plates,” *IEEE Transactions on Magnetism*, vol. 38, no. 2, pp. 1161-1164, March 2002.

[27] Haoyu Huang, T. Takagi and T. Uchimoto, “Crack shape reconstruction in ferromagnetic materials using a novel fast numerical simulation method,” *IEEE*

Transactions on Magnetism, vol. 40, no. 2, pp. 1374-1377, March 2004.

[28] B. Gupta, B. Ducharme, G. Sebald and T. Uchimoto, "A Space Discretized Ferromagnetic Model for Non-Destructive Eddy Current Evaluation," *IEEE Transactions on Magnetism*, vol. 54, no. 3, pp. 1-4, March 2018.

[29] Z. Chen, M. Rebican, N. Yusa and K. Miya, "Fast simulation of ECT signal due to a conductive crack of arbitrary width," *IEEE Transactions on Magnetism*, vol. 42, no. 4, pp. 683-686, April 2006.

[30] Z. Badics, H. Komatsu, Y. Matsumoto, K. Aoki, F. Nakayasu and K. Miya, "A thin sheet finite element crack model in eddy current NDE," *IEEE Transactions on Magnetism*, vol. 30, no. 5, pp. 3080-3083, Sept. 1994.

[31] Y. Du, S. Xie, X. Li, Z. Chen, T. Uchimoto and T. Takagi, "A Fast Forward Simulation Scheme for Eddy Current Testing of Crack in a Structure of Carbon Fiber Reinforced Polymer Laminate," *IEEE Access*, vol. 7, pp. 152278-152288, 2019.

[32] T. Takagi, Haoyu Huang, H. Fukutomi and J. Tani, "Numerical evaluation of correlation between crack size and eddy current testing signal by a very fast simulator," *IEEE Transactions on Magnetism*, vol. 34, no. 5, pp. 2581-2584, Sept. 1998.

[33] H. Huang, T. Takagi, and T. Uchimoto, "A fast numerical calculation for crack modeling in eddy current testing of ferromagnetic materials," *Journal of Applied Physics*, vol. 94, pp. 5866-5872, Nov. 2003.

[34] Z. Badics, Y. Matsumoto, K. Aoki, F. Nakayasu, M. Uesaka and K. Miya, "An effective 3-D finite element scheme for computing electromagnetic field distortions due to defects in eddy-current nondestructive evaluation," *IEEE Transactions on Magnetism*, vol. 33, no. 2, pp. 1012-1020, Mar. 1997.

[35] G. Rubinacci, A. Tamburrino, S. Ventre and F. Villone, "A fast 3-D multipole method for eddy-current computation," *IEEE Transactions on Magnetism*, vol. 40, no. 2, pp. 1290-1293, March 2004.

[36] M. Lu, A. Peyton and W. Yin, "Acceleration of Frequency Sweeping in Eddy-Current Computation," *IEEE Transactions on Magnetism*, vol. 53, no. 7, pp. 1-8, July

2017.

[37] Z. Badics, J. Pávó, S. Bilicz and S. Gyimóthy, “Subdomain Perturbation Finite-Element Method for Quasi-static Darwin Approximation,” *IEEE Transactions on Magnetics*, vol. 56, no. 1, pp. 1-4, Jan. 2020.

[38] C. Ktistis, D. W. Armitage and A. J. Peyton, “Calculation of the forward problem for absolute image reconstruction in MIT,” *Physiological measurement*, vol. 29, no. 6, pp. 455-464, 2008.

[39] H. Arsham, J. Grad and G. Jaklič, “Algorithm for Perturbed Matrix Inversion Problem,” *Applied Mathematics and Computation*, vol. 188, pp. 801–807, 2007.

Chapter 9 Conclusions and future works

This chapter summarises the conclusions from previous chapters, followed by the recommendation of future works.

9.1 Conclusions

In this study, it concentrates on the electromagnetic calculations in eddy current problems. Electromagnetic simulations are significant in the first stage of the industrial applications, which lay a solid foundation for the inversions of sample profile. Analytical solutions and finite element methods are the two kinds of methods commonly applied in eddy current testing techniques. Although the analytical solutions proposed by Dodd and Deeds can solve many types of the models, there are still some issues needed to be addressed, such as the conductive sample with finite dimension. To address this problem, the proposed novel method for simulations for this occasion and the thickness measurement have been carried out. Another issue in the testing is the effect due to the lift-off of the sensor probe. For the permeability measurement, the method to reduce the error on the phase of the signal due to the lift-off is proposed. For finite element method, in order to increase the computation time in the simulation, the customised solver can be accelerated by using the proposed methods for the crack detection techniques, which are verified by both simulations and experiments.

9.1.1 Analytical solution based on Dodd and Deeds plate model

A. Thickness measurement technique based on modified analytical method

In this section, a modified analytical solution for the metallic sample with a finite dimension is proposed. Based on this method, an eddy current thickness measurement

technique has been presented. Previously, it has been found that the Dodd Deeds analytical solution cannot be applied to the situation when the radius of the testing sample does not exceed 3-5 times of the sensor coil. In this thesis, an alternative initial integral point α_{r_s} has been found in the modified analytical solution for the finite-size samples. From the results of measurements and modified analytical solutions, it is shown that α_{r_s} is related to the size of the testing sample, instead of the size of the sensor. Moreover, α_{r_s} has been found to be inversely proportional to the size of the testing sample. By utilising this method, the thickness of the circular sample can be accurately reconstructed with a small error within 2%.

In this method, the peak frequency feature (instead of the magnitude) is used to reconstruct the thickness of the sample. Before measuring, the conductivity of the sample material is taken as known. Besides, the samples have to be cylindrical, for non-cylindrical shapes, the analytical solution is not valid. The results from the measurements are obtained based on the coil-sample co-axially assembled condition. Error will be induced due to axial offset situation.

B. Measurement of Permeability for Ferrous Metallic Plates

In this section, a compensation technique is developed for the relief of lift-off effects on impedance phase for metallic ferrous plates. From the results, it can be easily observed that both phase and signal (impedance/inductance) magnitude decrease as lift-off increases. And the measured inductance or impedance can be used for the compensation of impedance phase loss due to lift-offs via the proposed algorithms. Based on the proposed phase compensation approach, a magnetic permeability measurement technique was proposed that is also virtually independent of lift-offs. The results have been verified with both measurements and simulations of selected cases.

9.1.2 Finite element method

A. Acceleration method based on perturbed matrix inversion method

In this section, a method to accelerate the computation for the crack detection is proposed in FEM eddy current calculation by using a PMI method. Based on the perturbed matrix inversion (PMI) method, the effect of the perturbation matrix caused by the defect can be easily taken into account without inverting a full matrix.

From the results of the numerical tests, a good agreement can be found between the edge FEM and the analytical solution by Dodd and Deeds, which verifies the accuracy of the FEM solver. Besides, the PMI method agrees with the conventional CGS method but has higher computational efficiency. In numerical tests, two materials (aluminium and copper) are modelled. The results from both materials showed that the computation time by the PMI method was shortened about 3 times compared with that by the conventional CGS method. Moreover, the acceleration efficiency is slightly related to the crack depth due to the degree of perturbation on the stiffness matrix with different crack depths, but it remains almost the same for the frequency used in the scanning process.

B. Acceleration method based on a small perturbation of the crack

In this section, an acceleration method using finite element method is proposed. From the fact that the crack only causes a small perturbation in fields in the surrounding region, it computes for the region affected by the crack from the crack free region in the simulation. By using the proposed algorithm, the eddy current disturbed by the crack can be effectively simulated. The eddy current flows around the edge of the crack when it is blocked by the crack. Besides, from the simulation results, the algorithm is shown effective in greatly shortening the computation time (i.e., 3 times for 10k elements and 34 times for 139k elements). The accuracy has been verified by numerical tests with

the deviation up to 5% and it can be applied for the detection of the crack.

In recent decades, approaches to hasten the calculation of electromagnetic problem can be summarized into two kinds, that is, the improvements in the eddy current formulations and the advancement of finding the solution. Some researchers proposed novel formulations to address the crack perturbation problem with some approximations/techniques, i.e., zero-thickness defect [1], dedicated kernel [2], FEM-BEM combined method [3-4]. In this study, the formulations proposed by Biro [5] are used to solve the electromagnetic problem and improve the computation in the numerical solution process. In [6], some terms in the proposed formulations remain unchanged (unaffected by the crack) so that they can be precalculated and stored in a database. It can be used repeatedly for arbitrary geometry of the crack, consequently, it saves the computation time. By introducing a preconditioner – the optimized initial guess, a fast FEM approach was proposed for the evaluation of eddy current formulation [7]. In this method, using the proposed computation algorithm with the unperturbed field, it effectively shrinks the time needed for the crack inspection due to the small perturbation. Moreover, compared with the acceleration method using PMI method, it is more prospective for solving a large-scale crack detection model. The larger the element number of the tested sample, the more the computation speed increases. It further improved the computation efficiency due to the perturbation of the crack.

Overall, the study aims have been achieved by using both analytical method and finite element method. With the support of Dodd and Deed method, the thickness measurement for finite dimension plate can be conducted with small error. Besides, the permeability of the sample plate can be estimated without the lift-off effect. Further, based on the finite element method, the proposed methods for solving the crack perturbation problems can be employed to accelerate the computation speed.

9.2 Future works

Based on the conclusions stated in this study, future works are recommended for the further study of electromagnetic calculations.

- (1) The modified analytical methods for the inductance calculation due to the sample plate with finite dimension can be used for co-axial testing. The condition for the axial offset between the sample and the sensor probe can lead to some error and it is worth considering in the future.
- (2) The analytical method used in the study is the plate model. In the future, more other kinds of the model can also be considered by using the eddy current testing methods, i.e. cylindrical model, spherical model.
- (3) In the industrial manufacture, the sensor probe is commonly a ferrite-cored sensor probe with higher resolution. In this study, the air-cored sensor is used for the testing. Therefore, the analytical solution for the ferrite-cored sensor can be studied and applied to the measurements.
- (4) So far, the measurements are based on the multi-frequency eddy current testing methods. The potential of the pulsed eddy current testing can be investigated. The half-bridge circuit used in the pulsed eddy current testing is modified to produce larger current so that signal to noise ratio of the system can be improved and suitable for measuring plates of larger thickness. Further, the circuit can be manufactured and tested, then the material properties profiling by using the pulsed eddy current method can be studied.
- (5) The proposed accelerated method using finite element method needs the pre-computed field database. The preparation time is related to the generated mesh. In the future work, by utilising the analytical solutions for the unperturbed field, the time for the preparation of the database can be significantly shortened.

(6) For the solver based on the finite element method, there are some errors when the test sample is magnetic material. It may be due to the skin depth effect which needs very dense mesh to obtain accurate results. Therefore, a novel method can be considered to reduce the error due to the skin depth effect. Further, the sensor with ferrite core can also be considered in the simulation.

Reference

- [1]. J. Pavo and K. Miya, "Reconstruction of crack shape by optimization using eddy current field measurement," *IEEE Transactions on Magnetics*, vol. 30, no. 5, pp. 3407–3410, Sep. 1994.
- [2]. J. R. Bowler, T. P. Theodoulidis, and N. Poulakis. "Eddy current probe signals due to a crack at a right-angled corner." *IEEE Transactions on Magnetics*, vol. 48, no.12, pp. 4735-4746, 2012.
- [3]. Y. Du, S. Xie, X. Li, Z. Chen, T. Uchimoto and T. Takagi, "A Fast Forward Simulation Scheme for Eddy Current Testing of Crack in a Structure of Carbon Fiber Reinforced Polymer Laminate," *IEEE Access*, vol. 7, pp. 152278-152288, 2019.
- [4]. K. Zhao, M. N. Vouvakis and J. F. Lee, "Solving electromagnetic problems using a novel symmetric FEM-BEM approach," *IEEE Transactions on Magnetics*, vol. 42, no. 4, pp. 583-586, Apr. 2006.
- [5]. O. Bíró, "Edge element formulations of eddy current problems," *Computer Methods in Applied Mechanics and Engineering*, vol. 169, no. 3–4, pp. 391-405, 12 February 1999.
- [6]. H. Huang, T. Takagi, and T. Uchimoto, "A fast numerical calculation for crack modeling in eddy current testing of ferromagnetic materials," *Journal of Applied Physics*, vol. 94, pp. 5866–5872, Nov. 2003.
- [7]. W. Yin, M. Lu, L. Yin, Q. Zhao, X. Meng, Z. Zhang, A. Peyton, "Acceleration of eddy current computation for scanning probes," *Insight-Non-Destructive Testing and Condition Monitoring*, vol. 60, no. 10, pp. 547-555, 2018.